Dissertation

submitted to the

Combined Faculty of Mathematics, Engineering and Natural Sciences

of Heidelberg University, Germany

for the degree of

Doctor of Natural Sciences

Put forward by

ALINA BÖCKER

born in: Leverkusen, Germany

Oral examination: 19.07.2022

TRACING THE CENTRAL STELLAR MASS ASSEMBLY OF GALAXIES IN A COSMOLOGICAL CONTEXT

Insights from Observations and Simulations

Referees:

Dr. Nadine Neumayer

Priv. Doz. Dr. Andreas Koch-Hansen

I hope you would be proud!

Image on the previous page shows NGC 2775 in the constellation of Cancer.
Credit: ESA/Hubble & NASA, J. Lee and the PHANGS-HST Team, Acknowledgement: Judy Schmidt (Geckzilla)

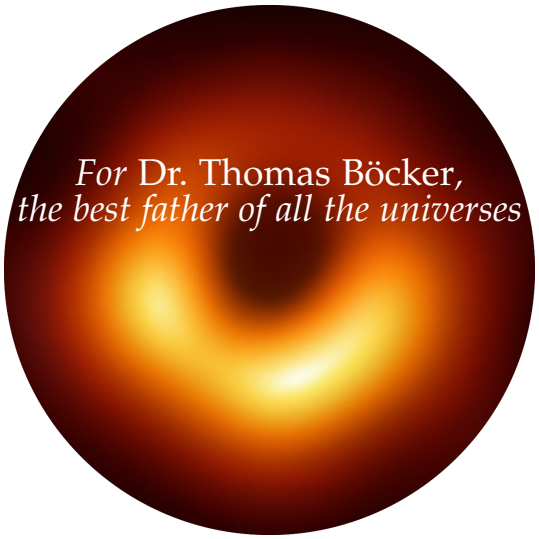

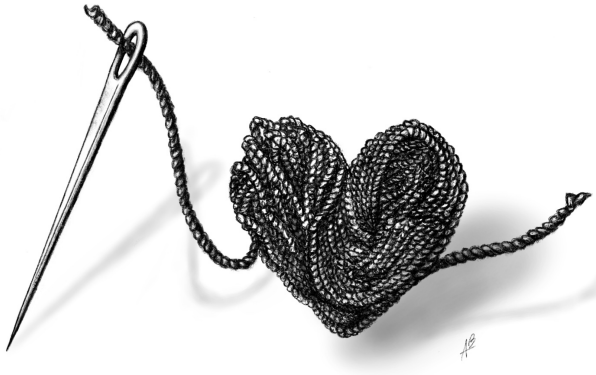

For my grandmother Maria Böcker *(1933-2020),*
the toughest woman I have ever known

For my grandfather Alfred Franzkowiak *(1933-2021),*
who had lost a lot but still continued

The first image on the previous page shows M 87's SMBH (or more precisely its shadow) was imaged by Event Horizon Telescope Collaboration et al. (2019). **Credit**: EHT Collaboration
Danke für all die M 87 Stärkungsdrücki, Papi.
The other two images are drawn by me.

ABSTRACT

Galaxies grow in stellar mass either by turning their gas into stars, or by merging with other galaxies. Disentangling the relative contribution of these processes is essential to understand both the emergence of today's diverse galaxy population and the cosmology in which galaxies form and evolve. In principle, the distribution of ages and metallicities of a galaxy's stellar populations is informative about its assembly history. However, this rich information content is not yet systematically obtained for the majority of galaxies, as they are not resolved on a star-by-star basis. In this thesis, I build on a methodology that can extract age-metallicity distributions from observed integrated spectra alone. I verified that such a technique is robust by using observations of a nearby stellar system, where additionally the ages and metallicities of individually resolved stars are known. Using state-of-the-art cosmological, hydrodynamical simulations, I showed that interactions with other galaxies dictate the assembly of stars in the central few hundred parsecs of galaxies, which are thus ideal regions to study merger histories. The joint analysis of integrated spectra of galaxy centers from real and mock observations confirms the recovery of signatures in ages and metallicities reminiscent of past merger events. These promising results pave the way in measuring galaxy merger statistics from current and future spectroscopic data to understand their role in shaping galaxy properties over cosmic time.

ZUSAMMENFASSUNG

Galaxien nehmen an stellarer Masse zu, indem sie entweder ihr Gas in Sterne umwandeln, oder mit anderen Galaxien verschmelzen. Den relativen Beitrag dieser Prozesse zu entschlüsseln ist essenziell, um sowohl das Zustandekommen der heutigen vielfältigen Galaxienpopulation als auch die Kosmologie zu verstehen, in der Galaxien entstehen und sich entwickeln. Die Verteilung der Alter und Metallizitäten der stellaren Populationen einer Galaxie gibt im Allgemeinen Aufschluss über ihre Entstehungsgeschichte. Dieser reiche Informationsgehalt ist jedoch für die meisten Galaxien noch nicht systematisch verfügbar, da sie nicht Stern für Stern aufgelöst werden können. In dieser Arbeit baue ich auf einer Methode auf, mit der Alters-Metallizitäts-Verteilungen allein aus beobachteten integrierten Spektren extrahiert werden können. Anhand von Beobachtungen eines nahegelegenen Sternsystems, bei dem zusätzlich das Alter und die Metallizität der einzeln aufgelösten Sterne bekannt sind, habe ich die Robustheit einer solchen Methode bestätigt. Mithilfe modernster kosmologischer, hydrodynamischer Simulationen konnte ich zeigen, dass die Wechselwirkungen mit anderen Galaxien die Sternentstehung in den Zentren von Galaxien bestimmen, was sie zu idealen Regionen macht, um Galaxienverschmelzungen zu untersuchen. Die gleichzeitige Analyse integrierter Spektren von Galaxienzentren aus realen und realistisch simulierten Beobachtungen zeigt, dass Signaturen in Sternenpopulation extrahiert werden können, die aufgrund ihrer Alter und Metallizitäten typisch sind für vergangene Galaxienverschmelzungen. Diese vielversprechenden Ergebnisse ebnen den Weg für die Messung von Statistiken über Galaxienverschmelzungen mithilfe von aktuellen und zukünftigen spektroskopischen Daten, womit deren Einfluss auf Galaxieneigenschaften über die kosmische Zeit verstanden werden kann.

ACKNOWLEDGEMENTS

When I started my PhD almost four years ago, I did not think it would come with so many challenges on so many different levels. The scientific challenge was certainly one that I expected, whereas others, more emotional ones, hit me at full force. Along the way I had many people that supported and helped me through both the scientific and emotional ups and downs, which I would like to thank dearly:

Nadine Neumayer : Thank you for taking me on as a PhD student, for supporting me towards any research direction that I wanted to explore, for always making time to talk about science or other obstacles, for enabling me to visit collaborators and to participate in many conferences, for doing submission parties with Neige and have nice talks over lunch. I am also happy that I could co-organize Galaxy Coffee with you - I really enjoyed it and learned a lot.

Annalisa Pillepich : Thank you for becoming a collaborator and supervisor along the way, for having weekly meetings about TNG50, for giving me scientific challenges and broadening my horizon about simulations.

Ryan Leaman : Thank you for always helping me when I am stuck, for coming up and sharing key science ideas and for going through things I have written, often sentence by sentence, to convey the message perfectly. I aspire your knowledge in so many different areas of astronomy, your innovative research and your enthusiasm about science that always motivates me. You have taught me a lot and without you I would not be the scientist I am today.

Ignacio Martín-Navarro : Thank you for having so many science coffees with me during your stay at MPIA, helping me with all things related to stellar populations and teaching me how to finish projects. I also very much appreciate that you continuously checked in on me by email and zoom during these past two years. Nacho, I trusted the process and now I am ready to come to Tenerife!

Alice Zocchi : Thank you so much for reading through and commenting on the majority of this thesis on such short notice. The first time we met I had to write my applications and you immediately helped me with them, which I so much appreciate. I love your positive energy, which is so great and contagious, and I am happy we met!

Jesús Falcón-Barroso : Thank you for providing your scientific support so naturally. It gave me the push to move forward from my perhaps lowest point during this thesis and I am very grateful for that.

Glenn van de Ven : Thank you for always letting me come visit you either in Munich or Vienna, for being in my thesis committee, for giving enthusiastic and fresh input ideas about my research and of course for riding the roller coaster with me.

Andreas Koch-Hansen : Thank you for being in my thesis committee and for agreeing to referee this thesis.

Francisco Aros : Dr. Franceesadsaessco, I am so happy that we met and became such good friends. I think without our daily whatsapp conversations I would have gone insane during the pandemic - and even now we manage with six hours of time difference. Thank you for always being there, sending me moral support gifs, for having nerdy and serious chats, for sharing amazing Chilean culture (food and swear words) and for answering my annoying questions about jeans modelling. And now: play the Nyan Cat!

Neige Frankel : Thank you for being such a great office mate and friend, for asking questions (scientific or otherwise) that I would have never thought about myself and which always give me another perspective on things; and for convincing me to go hiking, which I now love. I am grateful for our walks to the castle in Schriesheim when I was not feeling well emotionally, and our conversations over hot tea on the way and cake when we came back. In particular, I will never forget our icy adventure! Thank you also for giving comments on parts of this thesis.

Thomas Jackson : Thank you for finding my science interesting and in engaging me for new projects. I really enjoyed our retreat, as well as hiking and skiing together. I look forward to continuing our science projects, conversations and other adventures!

Melanie Kaasinen : Thank you for always being so nice, supportive and welcoming. I very much enjoyed our zoom parties with the others and the hike in the Pyrenees! I also really admire your engagement in the scientific community!

Zo Ebelt : Unsere gemeinsame Zeit in Heidelberg wird mir immer in Erinnerung bleiben. Es war so toll immer mit dir zu kochen, zu backen, zu kletten und zu zocken. Auch unser Kochen über zoom ist legendär. Ich bin immer glücklich, wenn wir gemeinsam etwas unternehmen!

Katalin Herres : Danke, dass du immer für mich da bist und ich dir wirklich alles erzählen kann. Ich liebe unsere Lacher.

Romana Tyralla : Mani, du begleitest mich jetzt schon seit ich ein Baby bin und hast mir immer deine Unterstützung und Liebe geschenkt. Ich bin so froh, dass du in meinem Leben bist.

Thomas Böcker : Papa, manchmal kann ich nicht glauben, dass es nur noch wir zwei sind. Ich wüsste wirklich nicht, was ich ohne dich machen sollte, und ich verdanke dir alles in meinem Leben. Danke, dass du mich immer selbstlos unterstützt, wir so Vieles gemeinsam unternehmen und gemeinsam Spaß haben. Ich habe dich unendlich dolle lieb!

CONTENTS

ACRONYMS

ALMA	Atacama Large Millimeter/submillimeter Array
AGB	asymptotic giant branch
AGN	active galactic nucleus
AMR	age-metallicity relation
AO	adaptive optics
BCG	brightest cluster galaxy
CMB	cosmic microwave background
CMD	color magnitude diagram
ELT	Extremely Large Telescope
FoF	friends-of-friends
FSF	full spectral fitting
FWHM	full width at half maximum
GALACSI	Ground Atmospheric Layer Adaptive Corrector for Spectroscopic Imaging
GC	globular cluster
GMC	giant molecular cloud
GSMF	galaxy stellar mass function
HB	horizontal branch
HST	Hubble Space Telescope
ICM	intracluster medium
IFU	integral field unit
IMF	initial mass function
ISM	interstellar medium
IR	infrared
JWST	James Webb Space Telescope
ΛCDM	Lambda-Cold-Dark-Matter
LSF	line spread function
MDF	metallicity distribution function
MMR	mass-metallicity relation
MUSE	Multi Unit Spectroscopic Explorer
MW	Milky Way
NFW	Navarro–Frenk–White
NSC	nuclear star cluster

pPXF	penalized pixel fitting
PSF	point spread function
RGB	red giant branch
SDSS	Sloan Digital Sky Survey
SED	spectral energy distribution
SFH	star formation history
SFMS	star forming main sequence
SFR	star formation rate
SMBH	supermassive black hole
SNR	signal-to-noise ratio
sSFR	specific star formation rate
SSP	single stellar population
UCD	ultra compact dwarf
UV	ultraviolet
VLT	Very Large Telescope
WAGGS	WiFeS Atlas of Galactic Globular cluster Spectra
WiFeS	Wide Field Spectrograph
WFM	wide field mode

Part I

CONTEXT

1 PHILOSOPHY

The beauty and fascination of looking into the night sky must have been omnipresent prior to the invention of electrical light - which perhaps is the reason why astronomy is the oldest of the natural sciences. Although, up until recently (i.e. the 19th century), people would have called astronomy a natural philosophy. As I see myself as a 'lover of wisdom', I want to start this thesis with the open questions in astronomy that I *love* the most, and to which I like to contribute *wisdom* to with my research. For this purpose, I made a mindmap at the *beginning* of my PhD, to which I now look back for the first time and realize that this thesis indeed evolved into something that overall captures the ideas presented there.

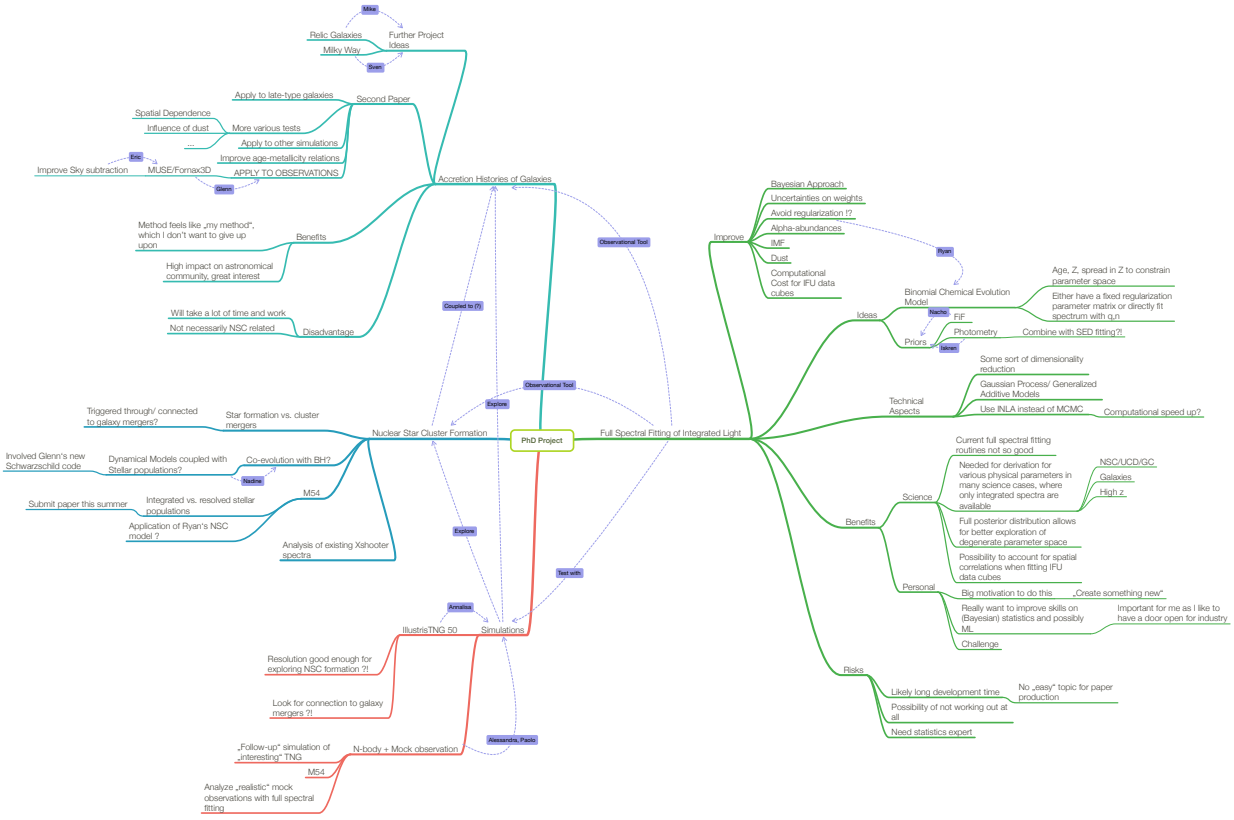

Figure 1.1. The different research projects and their connections to each other as well as potential collaborators that I thought about at the start of my PhD.

1.1 SCIENTIFIC RATIONALE

Galaxies appear in many fascinating shapes and forms, which we can study through the light of their stars. The stars can be formed either within the galaxy (*in-situ*) or be acquired via accretion of other (smaller) galaxies (*ex-situ*). The beauty of the latter mechanism is twofold: merger events are 1) able to produce global trends of the galaxy population, in the sense that increasingly bigger galaxies are build from an increasing number of smaller galaxies, and 2) are quite stochastic and therefore introduce a lot of variation resulting in a diverse galaxy population. The exact interplay of internal star formation and galaxy interactions will be the key to understand the observed properties of galaxies, and thus ultimately their formation.

Furthermore, the frequency and mass function of mergers an individual galaxy experiences throughout cosmic time are a strong prediction of the cosmology in which galaxies form and evolve. Thus, measuring these quantities from observations will be crucial to not only understand galaxy formation in itself, but also to provide a key test to our current cosmological model.

We indeed see snapshots of many galaxies in the nearby Universe that are in various stages of interacting with other galaxies. Their morphologies resemble a disturbed version of their regular appearing analogues. However, these types of observed, on-going interactions are often between equal mass galaxies and at late cosmic times, which are predicted to account for only 1% of the total merger events having ever taken place (Rodriguez-Gomez et al., 2015). We hence need to exploit more sophisticated observational approaches to uncover ancient merger events. In addition, we cannot predict from these types of observed snapshots alone what the final galaxy, the merger product, will look like. Computer simulations are therefore needed to investigate the impact of mergers in producing regular appearing galaxies.

In observations, the properties of stars, such as their ages, metallicities and kinematics, are used to determine where, when and how they formed constituting as such the assembly history of the overall galaxy. Past merger events will leave a distinct imprint in the characteristics of a galaxy's stellar content - specifically in the *distribution* of stellar population and dynamical quantities. By exploiting this fact and mapping millions of individual stars, the Gaia mission made it possible to uncover an ancient merger that the Milky Way encountered approximately 10 Gyr ago (Helmi et al., 2018; Belokurov et al., 2018). However, mapping individual stars is impossible for galaxies outside the Local Group, and will remain impossible for the majority of galaxies even with the advent of the next generation of telescopes, such as JWST and ELT (Tolstoy, 2019). Despite the Milky Way being an important benchmark with observations unmatched in detail and precision, we will not learn about the emergence of the whole galaxy population in a cosmological context from a single galaxy. We therefore need to find and test other ways to extract similarly detailed information from observations, where only the integrated stellar light is reaching us.

Current observational studies, that aim to address this for external

galaxies, mainly focus on the outskirts of galaxies, i.e. their faint stellar halos. Substructures that are visible there in the forms of streams and shells, are evidence of relatively recent accretion events of lower mass galaxies (Martínez-Delgado et al., 2010). But even if the stellar halo appears smooth, it is predicted that the majority of stars in that region are of ex-situ origin (Cooper et al., 2010). Still, due to very low surface brightness, these types of observations are time costly, and are in fact only available for either a handful of galaxies (Merritt et al., 2016; Spavone et al., 2017, 2020) or at the higher mass end (Huang et al., 2018). Furthermore, photometry of integrated light alone makes it virtually impossible to separate stars of different origins that are spatially overlapping. On the other hand, the observational product that is readily available for many thousands of galaxies *and* provides enough information about the underlying stellar populations, which has potential to disentangle their different origins, are integrated spectra.

Question 1)

How reliable are current techniques in recovering distributions of ages and metallicities from integrated spectra to understand the mass assembly of galaxies?

Additionally, it has not yet been sufficiently quantified, how big the importance and impact of merger events is in the center of galaxies. As they are the brightest part of the galaxy, the best quality observations are available there, including the aforementioned integrated spectra. Furthermore, formation scenarios of central, structural components of individual galaxies, such as bulges (Kormendy & Kennicutt, 2004) and even nuclear star clusters (Neumayer et al., 2020), include often competing pathways of in-situ and ex-situ origin. Only the newest generation of fully cosmological, hydrodynamical galaxy simulations can start to address this, as they provide the necessary resolution, large enough volume and realistically reproduced galaxy population (Pillepich et al., 2019; Nelson et al., 2019b).

Question 2)

How much is the stellar assembly in the center of galaxies influenced by the individual galaxy's merger history?

Finally, the adequate comparison of observations and simulations is essential to understand the limitations and improvements needed at *both* ends to work towards quantifying the role of merger events throughout cosmic time and in shaping the appearance of the present-day galaxy population. Specifically, claimed interpretations of observations should be verified with the known interpretation in simulations. And vice versa, the validity of simulations should be tested against observed quantities. This involves, as realistic as possible, the construc-

tion of mock observations from simulations and the application of the same inference techniques to accurately understand inevitable systematics.

Question 3)

Are the properties of stars of different origins as predicted by simulations different enough to be detected from currently available integrated spectra?

All in all, the goal of this thesis is to work towards new avenues in a) directly quantifying accretion histories of many, individual galaxies from current observations and b) unveiling the role of merger events in producing the present-day diversity of galaxies and their overall evolution. The illumination of this scientific question from the aspects of observations, simulations and modelling alike concludes the philosophy of this thesis.

1.2 OUTLINE

The thesis is outlined in five parts. The current PART I summarizes the context needed to understand the scientific rationale. Specifically, Chapter 2 provides an overall background on the current standard cosmological model, in which we think galaxies form and evolve. Chapter 3 introduces the broad subject of galaxies, especially the observational evidence we have and our current interpretations of the astrophysical processes we think are responsible for producing the observed quantities.

Summary

Text in these boxes provide a summary at the beginning of each Chapter and can be used by readers familiar with certain topics and results.

PART II is dedicated to observations to answer question 1) from the scientific rationale. Chapter 4 provides a brief methodological background on how the observed integrated light of galaxies is modelled. In Chapter 5, I test the reliability of recovering age-metallicity distributions from integrated spectra with a nearby stellar system, in which we know the detailed distribution from age and metallicity measurements of individually resolved stars.

PART III is dedicated to simulations to answer question 2) from the scientific rationale. Chapter 6 serves as a background introducing numerical galaxy simulations in general. In Chapter 7, I unveil the complexity and diversity of formation pathways of galaxy centers across the overall galaxy population in the context of the TNG50 simulation; and how the different origin of stars is imprinted in their stellar popu-

lation and dynamical properties.

PART IV combines observations and simulations to address question 3) from the scientific rationale. Chapter 8 introduces the technical background of a new observational technique that can extract a galaxy's merger history from its integrated spectrum. In Chapter 9, I demonstrate a promising first application of this method to the centers of galaxies observed with SDSS. This is accompanied by a fair comparison to predictions from the TNG50 simulation via the construction of realistic mock spectra.

PART V embeds the studies conducted throughout this thesis into the context outlined at the beginning. In Chapter 10, I first summarize the results from the three previous parts and their contribution to the field. Then, I provide future directions of follow-up studies and applications in Chapter 11. I conclude this thesis in Chapter 12.

2 COSMOLOGY

Cosmology is the study of the world[1]. To understand the existence and properties of galaxies, we have to know the world in which they came to be. Being born in different parts (both spatial and temporal) of the world can significantly shape the internal attributes of galaxies - equally leading to population-wide similarities and diversity. Thus, in this chapter I give an overview - from a modern scientist's point of view - of how we think the world (i.e. the Universe) formed. This also provides the basis for interpreting observed galaxy quantities, that I will introduce in Chapter 3.

Summary

In the standard ΛCDM cosmological model, initially small density fluctuations grow through the expansion of the Universe from which they decouple, once they enter the phase of gravitational collapse. The presence of cold dark matter allows for the right time and mass scale to produce today's observed luminous structures. Thus, in this scenario, galaxies form and grow in a hierarchical manner via the successive merging with other galaxies. Vice versa, measuring the number and masses of smaller objects which make up bigger objects observed today will present a key test of ΛCDM.

Contents

[1] I finally understand now the meaning of this word and I have much appreciation for Annalisa Pillepich always saying 'world' instead of 'universe'.

2.1 A BRIEF HISTORY LESSON

While researching for the apparently quite inevitable history lesson in theses' introductions, I come to the following realization - which is twofold: 1) the history about cosmology is quite fascinating really and 2) the standard model, which my peers and I take for granted every day, is approximately as young as me. Therefore, I retract my initial opposition of writing a history lesson at the beginning of my thesis and the interested reader shall find in what follows a quick, deep, and hopefully entertaining, dive into the history of cosmology (in which we skip the first $\sim$ 2000 years).

After the majority of humans (finally)[1] came to reason[2] and heliocentrism was widely accepted in the course of the 18th century, the concept of the Milky Way being a galaxy amongst many others was still far away. Though astronomers were not entirely oblivious to the presence of the objects we now call galaxies. After the invention of the telescope many more of these diffuse 'nebulae'[3], which you otherwise cannot see with the naked eye, were discovered. Perhaps the catalogue of Messier, first published in the 1770s, is the earliest catalogue[4] documenting 'nebulae'. Comically, he went through the trouble of constructing this catalogue[5] merely to list objects that frustrated him in his search for comets.

"We ignore the influence of dust" is perhaps one of the more iconic sentences that you will hear at some astronomical conferences. If Herschel[6], Kapteyn and Shapley had been aware of the absorption of star light through interstellar dust, they might have all agreed on the shape and size of, as well as the Sun's position within the Milky Way. Nevertheless, it was clear to them that the Milky Way was so vast it had to be the entire world. Curtis, on the other hand, was convinced that nebulae, such as Andromeda, are outside the Milky Way[7]. But who would not have been disturbed by the unimaginable distances of several hundred kiloparsecs that Curtis implied? Thus, this topic was debated greatly in 1920, and settled a few years later by Hubble, who conclusively proved, using Cepheids, that the Andromeda Nebula is a galaxy on its own (Hubble, 1929b). Hubble went on to arrange galaxies in a tuning fork pattern based on their appearance, resulting in a classification we still use today (Hubble, 1926).

By the time the existence of galaxies was finally clear, theorists were of course already done with their formula to describe the entire universe. Einstein had derived his field equations in 1917 and Friedmann had provided specific solutions in 1922. After Hubble published results in 1929 for his proportional constant that relates the recession velocity of galaxies with their distances, Einstein too became convinced of an expanding universe. Thus, Lemaître's[8] similar findings two years earlier were recognized (Lemaître, 1927), which led him to theorize a Big Bang (Lemaître, 1931).

Gamow took the consequences of a hot, dense, radiation dominated early universe and formulated a first model of primordial nucleosynthesis in 1946. Naturally, he gave the complicated equations to his PhD student Alpher for him to solve (Alpher et al., 1948). Together

1: It seems that Aristarchus of Samos ($\sim$ 300 B.C.) could have saved us from 2000 years of geocentrism. However, science is, even today and maybe more often then we like to admit, subject to beliefs of certain people until there is enough undisprovable evidence.

2: A reference to the Age of Reason or Enlightenment.

3: Nebulae during this time referred to all kinds of unresolved objects including galaxies, star clusters and star forming regions.

4: Two other important catalogues of nearby galaxies are the New General Catalogue (NGC) and its supplement the Index Catalogue (IC), all assembled by Dreyer (1888, 1895, 1910).

5: We still use his classification today. Famous examples are M 31, our nearest neighbour the Andromeda Galaxy, and M 87, the galaxy with the first directly imaged supermassive black hole.

6: Apart from mapping individual stars to deduce the structure of the Milky Way, he also catalogued thousands of nebulae in the late 18th and early 19th century (Herschel, 1786, 1789, 1802).

7: Interestingly, already in 1755, Kant reasoned for such an explanation.

8: He was also a priest by the way.

with Herman, Alpher predicted the existence of the cosmic microwave background (CMB)[9] (Alpher & Herman, 1948). However, cosmology was not fashionable at the time and the CMB - a measurable relic of the Big Bang - was forgotten.

In the 60s, the implications of a CMB were 're-discovered' by a number of astronomers around Dicke et al. (1965). Before his group could actually go about measuring it, Penzias & Wilson - naively unaware of the predicted CMB - had already found this weird background noise that they could not get rid off. This discovery favoured the Big Bang theory as a cosmological model ruling out the competing Steady State theory[10].

A last missing piece: How is structure, in the form of galaxies, created from an initially uniform field of matter as predicted by the CMB? Peebles & Yu (1970) (and many other astronomers) used linear perturbation theory to understand the size of temperature fluctuations that need to be imprinted in the CMB in order to produce masses of great structures such as galaxy clusters. The implied fluctuations are on the order of $10^{-4} - 10^{-5}$. These small values put a timing issue on the formation of observed galaxy structures, if they were to be formed purely out of baryonic matter within the age of the universe. As baryons interact with photons, gravitational collapse is slowed down, which prohibits structure formation.

In the 80s, Rubin and Ford presented rotation curves of spiral galaxies with unprecedented accuracy, which did not show a decreasing velocity as function of radius as expected from the luminous matter distribution (Rubin & Ford, 1970; Rubin et al., 1980). This led to the wide recognition[11] of galaxies having a large amount of unseen, dark mass. Given that per construction dark matter does only interact gravitationally, it is a suitable candidate to promote structure formation. The exact nature of dark matter is still unknown, however its movement is likely cold (Peebles, 1982), i.e. slow compared to the speed of light. This favours a scenario of hierarchical (bottom-up) structure formation[12], in which large structures grow out of small ones (e.g. Blumenthal et al., 1984).

In the late 90s, two teams around Riess, Schmidt and Perlmutter independently used Supernova Ia to measure distances and confirmed that the Universe is actually expanding at an accelerated rate (Riess et al., 1998; Schmidt et al., 1998; Perlmutter et al., 1999). This solved the issue of the Universe being close to the critical density to which all matter could only contribute 30% to. Although, this summoned the presence of the mysterious dark energy, which we essentially know nothing about. Nevertheless, the Lambda-Cold-Dark-Matter (ΛCDM) model is extremely successful in describing a vast variety of observational evidence and thus became the standard.

2.2 A WALK THROUGH COSMIC TIME

After the history lesson of how the current cosmological model emerged, I walk through some epochs in the cosmic history of the Universe. These are important to understand how the first atoms formed, which

9: As the plasma of the expanding Universe cooled down, neutral light elements could form. This stopped the photons from scattering off free electrons and they decoupled from the gas. These free photons redshifted to today's time constitute the CMB.

10: This theory assumed that the matter density remained constant over the expansion of the universe (Hoyle, 1948).

11: Prior to that some astronomers had already mentioned the necessity of dark matter. Zwicky (1933) was the first to apply the virial theorem to galaxy clusters to derive their mass and shaped the term 'dark matter'.

12: Initially a warm dark matter model was favoured, which produces a top-down scenario.

ultimately created the luminous structures we see today. A visual overview is given in Figure 2.1.

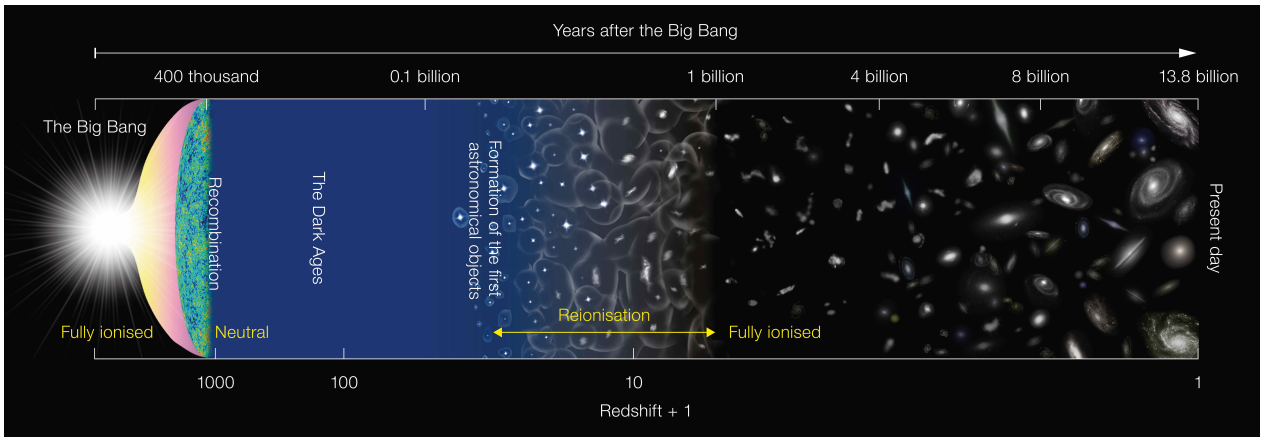

Figure 2.1. Our current understanding of the evolution of the Universe. **Credit**: NAOJ.

Big Bang: After the Big Bang, the Universe was essentially one hot, dense plasma. Within one second the temperature cooled down to 10^9 K.

Inflation: A very short exponential expansion of the Universe, whereby it grew by a factor of 10^{26} (Guth, 1981).

Primordial nucleosynthesis: The conditions were right to form atomic nuclei out of protons and neutrons[13]. The stable isotopes include: helium(-3 and -4), deuterium and lithium. No stable heavier nuclei could be created[14]. This process ended around 20 minutes after the Big Bang and left a primordial abundance of 75% hydrogen and 25% helium[15].

Photon decoupling and Recombination: Ca. 370,000 years after the Big Bang ($z = 1100$) photons decoupled from matter and began to travel freely. We see this relic radiation today, the cosmic microwave background (CMB), which has the most perfect black body spectrum ever measured with a temperature of 2.73 K. The decoupling was a consequence of recombination forming neutral hydrogen[16]. This process significantly decreased the number of free electrons, that could interact with the photons via Compton scattering. Recombination only happened efficiently by first capturing an electron in the excited state, which then decayed to the ground state.

Dark Ages: The Universe became dark in the sense that no photons with visible wavelengths existed, because they quickly redshifted due to cosmic expansion. It takes time to grow luminous structures such as galaxies and so it is suspected that the first generation of stars and galaxies formed after a few hundred million years after the Big Bang.

Reionization: Once the first stars, galaxies[17], quasars and galaxy clus-

13: It had to be cool enough for deuterium to survive photodisintegration, but still hot enough to allow significant nuclear fusion to take place.

14: Stable nuclei with mass of 5 or 8 do not exist.

15: This distribution is set by favoured production of protons and the decay of neutrons.

16: Helium was already neutral at that point due to its higher ionization energy.

17: The oldest known galaxy is at $z = 11$, which means it existed 400,000 years after the Big Bang (Oesch et al., 2016).

ters started to form, hydrogen could be ionized again. The intergalactic medium slowly became fully ionized again, but remained transparent due to its now low density. This process ended around $z = 6-7$, which is around 10^9 years after the Big Bang.

Today: Galaxies have had several gigayears of time to evolve until now. How much of that was influenced by the cosmology they live in? This is one key aspect I am interested in as a scientist.

2.3 THE STANDARD COSMOLOGICAL MODEL

I now describe the standard cosmological model in more detail to understand how structure forms, which ultimately dictates how galaxies grow through merging with others.

The ΛCDM paradigm describes a universe, which originated from a "hot, dense state" - the Big Bang - and then continuously expanded. It has, apart from "normal", baryonic matter, an unseen component, called cold dark matter. Today the cosmic energy density is governed by Λ, representing the dark energy, which accelerates the cosmic expansion.

The success of this cosmological model is largely based on the following four key observations:

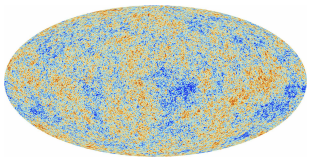

Figure 2.2. Anisotropies of the CMB measured by Planck Collaboration et al. (2014a). **Credit**: ESA and the Planck Collaboration

1. the almost perfect black body spectrum of the CMB as well as its anisotropies, as seen in Figure 2.2, measured with dedicated satellite missions (COBE: Smoot et al., 1992; Fixsen et al., 1996; WMAP: Spergel et al., 2003; Komatsu et al., 2011; Bennett et al., 2013; Planck: Planck Collaboration et al., 2014b, 2016, 2020).

2. the clustering of galaxies measured through e.g. large spectroscopic surveys (2dFGRS: Colless et al., 2001; Cole et al., 2005; SDSS: York et al., 2000; Eisenstein et al., 2005; Zehavi et al., 2011; BOSS: Anderson et al., 2012; Dawson et al., 2013).

3. the primordial abundance[18] of the light elements and their isotopes (hydrogen, helium and lithium) measured either from stars (Charbonnel & Primas, 2005), or HII regions of local gas clouds (Bania et al., 2002) or other metal-poor systems, such as dwarf galaxies (Olive & Skillman, 2004), or high redshift quasars (O'Meara et al., 2001).

4. the accelerated expansion of the universe directly measured with distances using Supernova Type Ia and the distance ladder (Riess et al., 1998; Schmidt et al., 1998; Perlmutter et al., 1999).

18: They can be worked out theoretically by knowing the photon-to-baryon ratio as measured, for example, from the CMB (Cyburt et al., 2016). For each baryon in the Universe there are roughly 6×10^{10} photons.

Feeding this model into computers and letting gravity work out the rest re-produced, at first, the large scale matter distribution (see Figure 2.3), and more recently, intrinsic properties of the galaxy population. These computer simulations are extremely valuable to the astronomical community, as they let us: a) directly compare our theoretical prediction of the Universe with observable properties of galaxies and b) trace individual galaxies back in time to uncover phenomena we cannot directly observe. I will introduce these numerical simulations in more detail in Chapter 6.

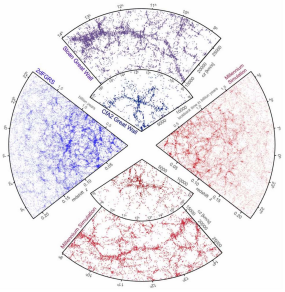

Figure 2.3. Large scale structure of the Universe seen by various redshift surveys (*blue*) and produced from cosmological simulations (*red*) (Springel et al., 2006).

2.3.1 The underlying equations

The cosmological principle states that, when viewed on a large enough scale, the Universe is isotropic[19] and homogeneous[20]. Applying this principle, yields the Friedmann-Lemaître-Robertson-Walker metric and sets the energy-stress tensor to that of a perfect fluid. These assumptions exactly solve the field equations of general relativity, which are known as the Friedmann equations:

$$\begin{aligned} H^2(t) = \left(\frac{\dot{a}}{a}\right)^2 &= \frac{8\pi G}{3}\rho + \frac{kc^2}{a} + \frac{\Lambda}{3} \\ \left(\frac{\ddot{a}}{a}\right) &= -\frac{4\pi G}{3}\left(\rho + \frac{3p}{c^2}\right) + \frac{\Lambda}{3}, \end{aligned} \tag{2.1}$$

where G is the gravitational constant and c the speed of light. The Hubble parameter H in the first equation tells us the expansion rate of the universe. The second equation describes the acceleration of said expansion. The scale factor $a(t)$ is related to the redshift by $a = \frac{1}{1+z}$, and thus $a(0) = 1$ is its present-day value. The (baryonic + dark) matter density is ρ and the pressure is p, whereas k is related to spatial curvature and Λ is the cosmological constant. The equations can be solved exactly by connecting the density and pressure via the equation of state of a perfect fluid: $p = w\rho c^2$, where w is a constant.

To make these equations more intuitive we normalize the first equation by the Hubble constant[21] $H_0 \equiv H(0)$. We also re-write in terms of the density parameter $\Omega = \frac{\rho}{\rho_c}$, which expresses the present-day density as a fraction of the critical density of the universe:

$$\rho_c = \frac{3H_0^2}{8\pi G}. \tag{2.2}$$

We obtain:

$$\left(\frac{H}{H_0}\right)^2 = \Omega_r a^{-4} + \Omega_m a^{-3} + \Omega_k a^{-2} + \Omega_\Lambda. \tag{2.3}$$

We can directly understand from this equation that radiation (Ω_r) dominated the expansion at small scale factors, i.e. early on in the Universe. At approximately $z = 3600$ it was overtaken by matter (Ω_m).

19: i.e. the same in every direction

20: i.e. the same from every location

21: If two galaxies move with the expansion of the universe, but not relative to each other, their co-moving distance d_C remains the same. It is related to the proper distance $d = a(t)d_C$. The time derivative gives the recessional velocity due to the expansion of the universe: $v = H(t)d$, which yields the Hubble-Lemaître law $cz = v = H_0 d$ at low redshifts.

From $z = 0.5$ to today, the expansion of the Universe has been dominated by dark energy (Ω_Λ). Observational data favour a flat universe, thus $\Omega_k = 0$, which means $\Omega_r + \Omega_m + \Omega_\Lambda = 1$. According to current measurements from Planck Collaboration et al. (2020), the Universe is approximately made up of 68.9% dark energy, 26.1% dark matter and 4.9% baryonic matter. The value[22] for H_0 is $67\,\mathrm{km\,s^{-1}\,Mpc^{-1}}$.

22: The value of H_0 from CMB measurements is now in serious tension with direct measurements using Supernova Ia distances (Di Valentino et al., 2021).

By solving Equation 2.3 for the time t we can estimate the age of the Universe at a given scale factor a:

$$t(a) = \frac{1}{H_0} \int_0^a \left(\Omega_r a'^{-2} + \Omega_m a'^{-1} + \Omega_\Lambda a'^2\right)^{-1/2} da' \tag{2.4}$$

The age of the Universe as of today is $t(1) = 13.8\,\mathrm{Gyr}$. When observers quantify the age of something (that will be important for later), they prefer to express it in lookback time, which is just $t_{\mathrm{lookback}} = t(1) - t(a)$.

2.3.2 Hierarchical Structure Formation

The underlying equations of the ΛCDM model described in Section 2.3.1 describe a universe, that is isotropic and homogeneous. This is true on large scale, wheres on scales $\lesssim 100\,\mathrm{Mpc}$, the Universe is highly structured, as seen by the presence of galaxies and galaxy clusters. All together, they are arranged in vast, thin filament-like structures (Zel'dovich, 1970; Geller & Huchra, 1989), often called the Cosmic Web (Gott et al., 1986; Bond et al., 1996). How do these structures form?

If the Universe were not perfectly homogeneous at the beginning, but had tiny density fluctuations, they would grow due to the expansion. Indeed, we think that these fluctuations, likely caused by quantum effects prior to inflation (Guth, 1981), are responsible for structure formation. This is also supported by the small temperature fluctuations of the order of $10^{-4} - 10^{-5}$ imprinted in the CMB (Bond & Efstathiou, 1984; Planck Collaboration et al., 2016).

2.3.2.1 *Linear Growth*

Theorists have used linear perturbation theory to understand the initial conditions of the fluctuations necessary to form the observed structure. This is done by expressing the density field as $\rho(\mathbf{x}, t) = \bar{\rho}(t)[1 + \delta(\mathbf{x}, t)]$, where δ is the perturbation field[23] and $\bar{\rho}$ the mean density. Applying this to Einstein's field equations and Fourier decomposing δ lets us understand how perturbations of different scale[24] (or mode) grow.

23: This is often assumed to be a adiabatic and distributed like a Gaussian random field.

24: The initial power spectrum of the scales is nearly linear corresponding to the Zel'dovich approximation (Zel'dovich, 1970).

Before recombination, perturbations are affected by photons diffusing from high density regions to lower ones. Due to photon pressure being dominant, this also diffused the baryons. This process, called Silk damping (Silk, 1968), erases all perturbations that would today be smaller than $\sim 10^{13}\,M_\odot$. Thus, for galaxies to form (which are $< 10^{13}\,M_\odot$), these large structures needed to fragment into smaller ones. Still, this top-down scenario was problematic, as the predicted temperature fluctuations from this scenarios are on the order of 10^{-3};

much larger than observed in the CMB (Sunyaev & Zeldovich, 1970).

Dark matter provides a solution to this dilemma, as it is not affected by Silk dampening. The perturbations in dark matter can thus grow earlier. After decoupling from the photons, the baryons can gravitationally collapse into the dark matter perturbations. If the dark matter is additionally cold, its free-streaming length is small and thus small scale structures are not damped.

2.3.2.2 *Non-linear Growth*

As soon as a perturbation has reached a certain density, the gravitational collapse of the overdensity is non-linear (e.g. White, 1976; Aarseth et al., 1979; Frenk et al., 1983). This makes it practically impossible to formulate an analytical model, unless certain assumptions are made. For example, the critical overdensity δ_C is roughly 1.68 for a spherical mass distribution (Mo et al., 2010). Since dark matter is collisionless, the collapse of spherical mass shells will oscillate around the center, i.e. expand and contract again. This happens until the system is virialized[25].

The nature of cold dark matter ensures that smaller overdensities reach this non-linear regime earlier than larger ones. These small virialized 'halos' can then subsequently merge with others and form larger structures. Gravity attracts and therefore more matter will flow towards higher density regions. This hierarchical structure formation gives rise to the Cosmic Web, with massive halos at the intersections of filaments, as well as large underdense regions, called Voids (Tifft & Gregory, 1976; Gregory & Thompson, 1978).

Dark halos can become luminous, if baryonic matter infalls into their potential wells. The subsequent gravitational collapse of baryonic matter will behave differently, as it is subjected to gas dynamics and radiation. A number of complicated physical processes arise as a consequence. Perhaps one important realization is that gas can cool by radiating away its energy during the gravitational collapse. This results in the baryons being able to collapse to much smaller scales than the dark matter. The accumulated gas can then further fragment and form stars. We then call such a luminous structure a galaxy (Rees & Ostriker, 1977; White & Rees, 1978). Due to the bottom-up scenario, small galaxies will form first and grow via merging with others.

The ΛCDM paradigm predicts exactly how many mergers a single dark matter halo experiences throughout its growth over cosmic time[26]. Therefore, measuring the mass function, i.e. how many smaller halo of a given mass constitutes a larger halo, is a strong constraint on the nature of dark matter. A warmer flavour of dark matter would predict a different mass function with fewer halos at the low mass end (see e.g. Gilman et al., 2020).

This also translates to first order to galaxies (although baryonic processes complicate this interpretation, which we will see in Chapters 3 and 6). The number and masses of galaxy mergers that built-up the galaxies that we observe today are a direct consequence of cosmology. Thus, if we could quantify the *merger history* of individual galaxies from their present day appearance, we would learn about the inter-

25: $2E_{kin} = -E_{pot}$, where E_{kin} is the kinetic and E_{pot} the potential energy.

26: This is understood through computer simulations to model the non-linear growth of structure. Although the Press-Schechter Formalism provides a statistical treatment (Press & Schechter, 1974), that was mostly used before large numerical simulations were available.

play between the influence of cosmology and internal baryonic processes on the formation and evolution of galaxies. This thesis aims to provide a foundation on how past merger events could be measured observationally.

3 GALAXIES

Galaxies are more than milky blobs. They are a gravitationally bound system of stars, gas, dust and dark matter - and they are my true passion of astronomy[1]. Their morphologies are diverse, but "not all galaxies that could exist, do exist" - as my friend Neige Frankel put it so elegantly in her thesis. But more so, they are visible traces of the underlying cosmology in which they formed. Therefore, it is crucial to understand the empirical evidence we have from observations of galaxies, as our standard cosmological model needs to be able to reproduce these. In this chapter I broadly introduce the different types of galaxies, what kinds of relations they follow and how they are structured internally. Naturally, some leading theories and explanations for the observed properties are scattered throughout this chapter.

Summary

We have many observational clues about galaxies. They reveal the multitude and complexity of physical processes involved in producing objects that span several order of magnitudes in mass. Even though the numbers of galaxies are dominated by the lowest mass systems, we preferentially observe the higher mass ones due to their greater surface brightness. The population of galaxies is bimodal separating galaxies that actively form stars and those which do not. This dichotomy is closely reflected in their visual appearance of late-type spirals and early-type ellipticals. Galaxies lie on many scaling relations that connect their spatially averaged quantities such as mass, size, star formation rate, kinematics and metallicity; often in a power law like fashion with relatively small scatter. In addition, galaxies show a diversity in internal, structural components, which are characterized by different stellar population and dynamical properties, each reflecting a galaxy's individual formation history. Many processes shape and transform galaxies throughout their lifetime: some processes are internal, like star formation and AGN feedback, and some others are external, like galaxy mergers and the surrounding environment. The better we understand the interplay and relative importance of both types of processes, the better we can understand the world that created them.

[1] Amazing galaxies imaged by Hubble Space Telescope (HST) https://esahubble.org/images/archive/category/galaxies/ and astrophotographer Mark Hanson https://www.hansonastronomy.com/astrophotos-1.

Contents

3.1 VISUAL TYPES OF GALAXIES

Humans first detected galaxy light with their eyes. Therefore, it is not surprising that galaxies were visually classified early on. Even before they were formally recognized as extragalactic objects, it was clear that some nebulae looked like a spiral (Rosse, 1850).

Also today, in the era of powerful and highly sensitive CCD[27] detectors, astronomers still follow the early classifications schemes developed by Hubble (1926) and de Vaucouleurs (1959). Even though galaxies can now be categorized through a number of – perhaps more quantitative – properties (see Section 3.2), their different demographics still robustly emerge through their visual morphologies. We therefore start this chapter by understanding the "visual types" of galaxies.

27: charged coupled device.

Broadly speaking, galaxies can be divided into two groups: early-type (ellipticals) and late-type (spirals)[28]. I also briefly talk about other types, which are lenticular, dwarf and peculiar galaxies.

28: The terms early- and late-type are historic, as Hubble thought galaxies would evolve from elliptical to spiral mythologies. Today, we think that actually the opposite is true (as a rule of thumb).

3.1.1 Late-types/Spirals

The characteristic trait of late-type galaxies are their spiral arms. They extend from the center towards the outskirts of the galaxy and are embedded in a highly flattened[29] and rotating disk. The spiral arms themselves appear bluer than the rest of the galaxy with lanes of dust throughout them. These are the sites of active star formation, where the most massive of the newly born stars ionize their surrounding gas[30]. Therefore, spiral arms are most prominent, when they are observed through blue wavelength filters. In redder filters they appear much smoother, as those wavelengths trace the main body of the underlying stellar disk. The thickness of the disk grows from blue to red wavelengths, thus the midplane is dominated by bluer, young stars.

Figure 3.1. M101, a multi-armed spiral galaxy. **Credit**: Image: European Space Agency & NASA, Acknowledgements: Project Investigators for the original Hubble data: K.D. Kuntz (GSFC), F. Bresolin (University of Hawaii), J. Trauger (JPL), J. Mould (NOAO), and Y.-H. Chu (University of Illinois, Urbana), Image processing: Davide De Martin (ESA/Hubble), CFHT image: Canada-France-Hawaii Telescope/J.-C. Cuillandre/Coelum, NOAO image: George Jacoby, Bruce Bohannan, Mark Hanna/NOAO/AURA/NSF.

The morphology of spiral arms is also diverse. Some galaxies have a grand-design structure (see Figure 3.2), which is apparent as two large, bright, point-symmetric arms; some have shorter, multi-armed spirals (see Figure 3.1); and some have flocculent spirals, which can be faint and even detached from the center of the galaxy (Elmegreen, 1990; Elmegreen et al., 2011). Flocculent spirals can be formed through local disk instabilities, that are sheared out due to the differential rotation of the disk. Grand-design spirals are thought to be a density wave (Lin & Shu, 1964) originated through a global perturbation (see Dobbs & Baba, 2014, for a review).

Figure 3.2. NGC 1300, a barred, grand-design spiral galaxy. **Credit**: NASA, ESA, and The Hubble Heritage Team (STScI/AURA).

The appearance of spiral arms is tied to the presence and characteristic of the bulge. The bulge is a central conglomeration of stars, that is much more spheroidal and therefore starkly protrudes from the disk when the galaxy is viewed edge-on. It usually appears much redder than the disk as it typically lacks young stars and large quantities of gas. Stars in the bulge also follow a more random motion compared to the orderly rotating disk stars. Although, there are bulges that are not so classical. Likewise other spiral galaxies additionally have a bar,

29: For a reference, the disk of the Milky Way, a spiral galaxy, has a characteristic scale length that is ten times larger than the scale height (e.g. Bovy & Rix, 2013).

30: called HII region.

a straight strip of stars across their centers. I will discuss both of these structures in more detail in Section 3.3.3.

The relative size of the bulge to the disk is an important diagnostic (Sandage, 1961), as it marks general trends (albeit with a large scatter): spiral galaxies with larger bulge-to-disk ratios are typically more massive (as exhibited by their higher circular velocity and central velocity dispersion see Section 3.2.3.2) and have more tightly wound spiral arms[31] (Kennicutt, 1981; Yu & Ho, 2019).

31: i.e. a lower pitch angle

3.1.2 Early-types/Ellipticals

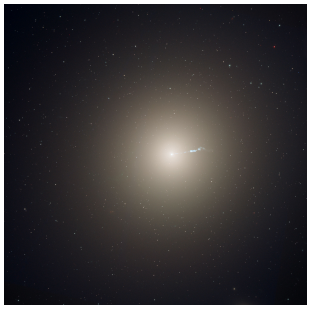

Figure 3.3. The very smooth looking M87 galaxy. **Credit**: NASA, ESA, and the Hubble Heritage Team (STScI/AURA), Acknowledgment: P. Cote (Herzberg Institute of Astrophysics) and E. Baltz (Stanford University).

Figure 3.4. The elliptical galaxy M60 with its spiral companion. **Credit**: NASA, ESA.

Early-type galaxies appear smooth and largely devoid of dust and gas as shown in Figures 3.3 and 3.4. They have an elliptical shape and a red color. The latter is typical for an old stellar populations and no active star formation. The motion of their stars is dominated by random orbits. All in all, they appear like giant bulges that are present in late-type galaxies, minus the disk of course.

The morphology of early-type galaxies varies in terms of their axis ratios and isophotal[32] shapes. Most ellipticals do not have pure elliptical isophotes, but are either slightly boxier or diskier (Bender et al., 1988). Some elltipicals appear almost spherical, however they usually have a clear minor and major axis. In general, it is difficult to assess their intrinsic shape, because the inclination at which 3D galaxies are projected onto the 2D sky is often poorly constrained. This very well implies that ellipticals could truly be triaxial in shape, i.e. have a distinct intermediate axis (Binney, 1978; Franx et al., 1989).

Indeed, it has been found that the most luminous and therefore massive ellipticals are on average more triaxial (Tremblay & Merritt, 1996), have boxier isophotes (Bender et al., 1988) and a central core (i.e. their density in the center is suppressed compared to what is expected from theoretical density profiles most commonly used to describe ellitpicals, see Ferrarese et al., 2006a; Côté et al., 2007). Fainter ellipticals are more prolate, based on their higher rotational velocity relative to their velocity dispersion (Davies et al., 1983), have diskier isophotes and a central cusp (i.e. they are more dense than what is expected from usually adopted theoretical density profiles, see Section 3.3.3 for more).

Perhaps to due their "boring" appearance, the formation of elliptical galaxies was hypothesized early on to be the result of a monolithic collapse (Eggen et al., 1962; Partridge & Peebles, 1967). In this scenario, essentially all stars form during the collapse of an initial gas cloud, which lasts around $1-2\,\mathrm{Gyr}$. This produces a lot of stars in a short period of time leaving behind a dense, spheroidal system without any gas. However, the early universe ($z > 2$) is dominated by star forming galaxies (see Section 3.2.2), thus contradicting this simple scenario. Mergers between spiral galaxies (or their high redshift equivalents), first put forward by Toomre (1977), can leave behind remnants that fit the morphology of early-type galaxies providing the more plausible formation scenario of ellipticals - also with respect to the hierarchical build-up of structure as predicted by the standard cosmological model.

32: Isophotes are lines of constant surface brightness (see Section 3.3.1).

3.1.3 More types

A brief description of some other visual types of galaxies, which are good to have in mind throughout the context of this thesis.

3.1.3.1 *Lenticulars/Sos*

Constructing a visual mean of a spiral and elliptical galaxy would perhaps yield a lenticular, or So, galaxy (Kormendy & Bender, 2012); a visual example is shown in Figure 3.5. They do not have a visible spiral structure and they are red like ellipticals (Sandage & Visvanathan, 1978), but they exhibit a stellar disk, albeit with a large bulge-to-disk ratio (Larson et al., 1980). Still, the rotational support is substantial and some also have a bar structure (Falcón-Barroso et al., 2004).

Examining their properties is crucial to understand the transition from star-forming, disk galaxies to quenched, bulge galaxies as well as the processes that could drive this transformation (i.e. the importance of mergers and environment, see Section 3.4 and Kormendy et al. 2009). Perhaps most importantly though, it is good to keep in mind that not all disk like galaxies are automatically also star forming, which will become apparent in Chapter 7.

Figure 3.5. The Sombrero galaxy (M 104, NGC 4594), an example of a lenticular galaxy. **Credit**: NASA/ESA and The Hubble Heritage Team (STScI/AURA).

3.1.3.2 *Dwarfs*

In a hierarchical structure formation scenario, the structures at the smallest scales are the most abundant in number and the building blocks for larger objects. Thus, the properties of dwarf galaxies put powerful constraints on galaxy formation within the ΛCDM paradigm (Mateo, 1998; Tolstoy et al., 2009).

A rough transition to the dwarf galaxy regime occurs around stellar masses[33] of $\sim 10^9\,M_\odot$. Due to their extremely low surface brightness (see Figure 3.6), the lowest luminosity galaxies ($\sim 10^4\,L_\odot$) can only be identified when they are companions of the Milky Way (Belokurov et al., 2007). These galaxies have extreme (dynamical) mass-to-light ratios of up to one thousand (McConnachie, 2012).

Dwarf galaxies also come in a variety of visual types (Binggeli et al., 1985), roughly following the dichotomy of their big counterparts (see Kormendy, 1985; Graham & Guzmán, 2003, for discussion on this). Although, it is rare for gas-rich, star-forming dwarf galaxies to have a spiral structure. They in fact have a more irregular shape with clumpy patches of dust and star-forming regions, as seen in Figure 3.7.

It is very likely for galaxies with stellar masses around the transition between the "normal" and dwarf regime ($\sim 10^9\,M_\odot$) to host a nuclear star cluster (see Section 3.3.3.5).

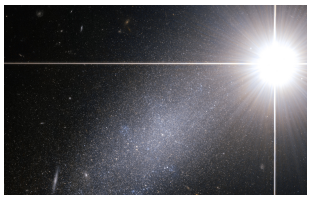

Figure 3.6. A nearby star outshining a dwarf galaxy. **Credit**: ESA/Hubble & NASA.

33: For reference the mass of the Milky Way is roughly $5 \times 10^{10}\,M_\odot$ (e.g. Bland-Hawthorn & Gerhard, 2016).

Figure 3.7. The WLM (Wolf-Lundmark-Melotte) galaxy, a little irregular dwarf galaxy at the edge of our Local Group. **Credit**: ESO, Acknowledgement: VST/Omegacam Local Group Survey.

3.1.3.3 *Peculiar*

Some galaxies look like spirals or ellipticals, but certain aspects do not fit into the classical classification. Their peculiarities were catalogued

by Arp (1966). Most of these galaxies show some morphological distortion, like a warped disk, rings or distorted spiral arms. Other galaxies are in close vicinity to and in interactions with other galaxies, like the Antennae Galaxies in Figure 3.8.

Figure 3.8. The perhaps most infamous on-going merger: the Antennae Galaxies (Arp 244). **Credit**: ESA/Hubble.

Galaxies in this catalogue provide us with a first visual evidence that galaxies indeed interact with each other and merge together to build a new, bigger galaxy (see also Figure 3.9). While on-going interactions of massive galaxies may seem obvious, it is an extremely difficult task and on-going effort to map visual traces of disrupted low mass galaxies (Martínez-Delgado et al., 2010; Duc et al., 2015; Merritt et al., 2016). Their already comparatively few stars become scattered across a large area of the sky making them often only visible after reaching $\sim 28\,\mathrm{mag\,arcsec^2}$ or more.

However, these measurements are crucial, because the number and masses of galaxies that merged to form a present-day galaxy are one of the key predictions of ΛCDM. One of the aims of this thesis is to provide first directions towards quantifying past merger events for a large number of galaxies by exploiting innovative measures.

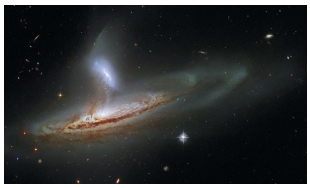

Figure 3.9. Reaching out to capture a smaller companion: Arp 282. **Credit**: ESA/Hubble & NASA, J. Dalcanton, Dark Energy Survey, DOE, FNAL/DECam, CTIO/NOIRLab/NSF/AURA, SDSS, Acknowledgement: J. Schmidt.

3.2 GALAXY POPULATION DEMOGRAPHICS

Having now great visual impressions of galaxies in mind, it is time to understand more quantitative demographics of the whole galaxy populations. Examining how galaxies are distributed in the parameter spaces of certain observable quantities (or quantities derived thereof), will let us understand two things: 1) the statistical behaviour and evolution of galaxies and 2) the principal and at the same time complex physical processes involved in forming galaxies.

For the following two sections, we can completely ignore how galaxies looks like morphologically. The last section generally requires knowledge about the structure of a galaxy (see Section 3.3.3), however the shown quantities represent an average across some spatial extent of the galaxy.

3.2.1 The galaxy luminosity/mass function

The flux density F_R of an extended[34] source on the sky (thus likely a galaxy) measured through some aperture and a photometric filter[35] R, is converted to the historically appropriate, but counterintuitive apparent magnitude m_R via:

$$m_R = -2.5 \log\left(\frac{F_R}{F_0}\right), \tag{3.1}$$

where F_0 is the flux of some reference object with zero magnitude, called the zero point.

34: i.e. larger than the point spread function (PSF)

35: The flux density through a filter with response curve $R(\lambda)$ is related to the spectral flux density f_λ (energy per area per unit wavelength) via

$$F_R = \int f_{\lambda'} R(\lambda') d\lambda'.$$

To arrive at a quantity that is related to the object's intrinsic luminosity[36] L_R, we must use the (luminosity) distance[37] d_L. The absolute magnitude of a source, normalized to a distance of 10 pc, is:

$$M_R = m_R - \mu = m_R - 5\log\left(\frac{d_L}{10\,\mathrm{pc}}\right), \tag{3.2}$$

where μ is called the distance modulus. On top of that, corrections need to be applied to account for extinction (e.g. Fitzpatrick, 1999), and, if comparisons across galaxies of different redshifts are important, for the shift of the galaxy's spectral energy distribution (SED) between the time the light was emitted and received (so called K corrections, e.g. Poggianti, 1997; Hogg et al., 2002).

Conducting such measurements for every galaxy in the sky[38], we obtain the number of galaxies of given luminosity L in some volume of the Universe, called the galaxy luminosity function (e.g. Cole et al., 2001; Blanton et al., 2003). It is well fit by a Schechter (1976) function:

$$\frac{dN}{dL} = \phi(L) = \left(\frac{\phi^\star}{L^\star}\right)\left(\frac{L}{L^\star}\right)^\alpha e^{-(L/L^\star)}, \tag{3.3}$$

where α is the slope at the low-luminosity end, $L^\star$ the characteristic luminosity, at which the profile turns over to an exponential cut off and $\phi^\star$ the overall normalization. Overall, the number density of the galaxy population is dominated by low luminosity galaxies, whereas the luminosity density is dominated by the brightest galaxies.

Magnitude measurements in at least two (better multiple) photometric bands make it possible to convert luminosities into stellar masses (e.g. Bell et al., 2003), yielding the galaxy stellar mass function (GSMF). By measuring the GSMF at different redshifts we obtain a first understanding of how the galaxy population evolves (e.g. Marchesini et al., 2009; Ilbert et al., 2013). In summary, galaxies overall grow in mass/luminosity with the most massive galaxies forming the latest as seen in Figure 3.10.

It is of tremendous importance to measure the GSMF precisely, as it presents a link between galaxy formation and (dark matter) structure formation models. Modern simulations of galaxy formation and evolution in a ΛCDM cosmology use these observations to constrain their subgrid physics models (see Chapter 6).

36: i.e. L_R expressed in solar luminosities $L_\odot$ is

$$L_R/L_{R,\odot} = 10^{0.4(M_{R,\odot}-M_R)}.$$

37: $d_L = (1+z)d_C$, for a flat universe and a negligible peculiar velocity of the galaxy.

38: As this is literally impossible, corrections for incompleteness effects due to survey footprints and magnitude limits have to be applied (Malmquist, 1922, 1925).

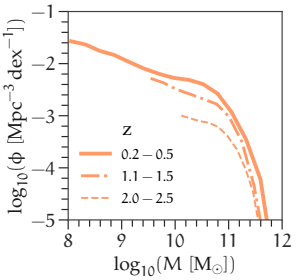

Figure 3.10. Measured galaxy stellar mass function (GSMF) in three different redshifts bins adopted from (Ilbert et al., 2013). The curves cut-off at the low-mass end due to magnitude limits.

3.2.2 The bimodality of galaxies

Taking the difference in magnitude in two different photometric filters, yields the color. This simple measure applied to galaxies reveals that they have a bimodal distribution in color (e.g. Baldry et al., 2004, 2006). Some galaxies lie in a narrow peak around red color, called "red sequence", and other are in a broader distribution centered around bluer colors, called "blue cloud". Galaxies in between those two populations are called "Green Valley" galaxies (see Salim, 2014, for a review). Slicing through this distribution by the galaxies' absolute magnitude re-

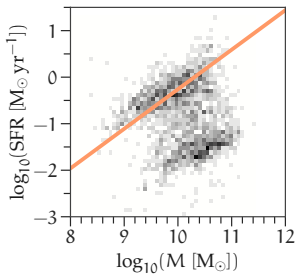

Figure 3.11. The bimodal distribution of galaxies in the SFR-$M_\star$ plane. Data is taken from Gallazzi et al. (2021) showing galaxies from SDSS for $z < 0.02$. The orange line shows the star forming main sequence.

veals that the brightest galaxies are almost exclusively red. This overabundance is gradually shifted towards bluer galaxies for increasing magnitude (or equivalently decreasing mass).

A similar observations is made when calculating the perhaps more physical quantities that relate the star formation rate (SFR)[39] and the stellar mass (Salim et al., 2007). Some galaxies, which actively form stars, form a tight sequence, called the star forming main sequence (e.g. Brinchmann et al., 2004; Speagle et al., 2014), which is seen in Figure 3.11. Other galaxies, which lie below that sequence, do not actively form stars and are thus quiescent. Galaxies can also experience a burst of star formation, which puts their star formation rate to a value larger than what is average for their given stellar mass.

The star forming main sequence itself evolves with redshift (e.g. Daddi et al., 2007; Noeske et al., 2007; Whitaker et al., 2012; Tomczak et al., 2016). It was overall higher in the young Universe due to higher gas fractions[40] and to a high gas turbulence that promoted gravitational instabilities. If a galaxy exhausted its entire cold gas reservoir and does not refuel it through some process, it will stop forming stars and move off the star forming sequence (Tacchella et al., 2016). The emergence of red, passive, quiescent galaxies roughly doubled in stellar mass since $z = 1$ (Bell et al., 2004). The most massive galaxies in the nearby Universe finished star formation $\sim 4\,\mathrm{Gyr}$[41] after the Big Bang (e.g. Thomas et al., 2010; McDermid et al., 2015). Hence, they had a particularly short, but extreme episode of star formation.

This (color) bimodality largely reflects the two (visual) types of galaxies (e.g. Holmberg, 1958; Strateva et al., 2001): early-type, elliptical galaxies are red, because they shut down star formation and hence have an old stellar population; late-type, spiral galaxies are blue, because they are actively forming stars and thus have a younger stellar population. While this is true for the majority of the galaxy population, some ellipticals do appear bluer than usual (Yi et al., 2005) indicating recent star formation (Dressler & Gunn, 1983) and consequently the presence of dust and (cold) gas (Goudfrooij et al., 1994; Morganti et al., 2006; Sarzi et al., 2006; Combes et al., 2007; Young et al., 2011; Werner et al., 2014). Likewise, some spiral galaxies are not necessarily on the star forming main sequence, the most infamous example being our nearest neighbour, the Andromeda galaxy (Barmby et al., 2006).

How can some galaxies sustain star formation for as long as the age of the Universe, whereas others completely shut down? What are the mechanisms that quench star formation? Does a once quenched galaxy remain like that or can it rejuvenate its star formation?

Over the years, astronomers discovered and discussed many processes that can be responsible for fuelling star formation and/or preventing it, some of them include: cold gas accretion from the filaments (Birnboim & Dekel, 2003; Kereš et al., 2005; Dutton et al., 2010), cooling of hot gas from the halo[42] (e.g. Shapiro & Field, 1976; Marinacci et al., 2010; Brook et al., 2012; Armillotta et al., 2016), mergers triggering star formation in pre-existing gas and/or supplying additional gas (e.g. Hernquist, 1989; Barnes & Hernquist, 1991; Mihos & Hernquist, 1994a,b, 1996; Cox et al., 2008; Di Matteo et al., 2008; Powell et al.,

39: There exist many different indicators to measure SFRs, which include SEDs modelling, gas emission lines (e.g. Hα, CO) and ultraviolet (UV) as well as infrared (IR) luminosities (see e.g. Madau & Dickinson, 2014, for a review).

40: compared to the total baryonic (stars + gas) mass.

41: This corresponds roughly to $z = 2$, when the cosmic averaged SFR density reached its peak value (Madau & Dickinson, 2014).

42: The mechanism of cooling and re-accreting gas previously expelled by supernovae is called 'galactic fountain'.

2013), gas outflows through stellar feedback (supernovae and winds) (e.g. Larson, 1974; Hopkins et al., 2012a; Hayward & Hopkins, 2017) or the active galactic nucleus (AGN) (e.g. Springel et al., 2005c; Bower et al., 2006; Martin et al., 2007; Eckert et al., 2021), gas removal through mergers (e.g. Barnes & Hernquist, 1996; Bournaud et al., 2007) or infall into a higher density environment (see Section 3.4).

It is thus a great effort to understand how galaxies exactly regulate their star formation and move through the mass-SFR diagram to achieve today's observed bimodal distribution. Perhaps, it is slightly ironic that the balance of star formation is one of the greatest uncertainties in galaxy formation and evolution despite the face that the light emitted by stars (and gas) is our predominant source of information. Therefore, it is important - and hopefully this will become clear throughout this thesis - that observational and theoretical efforts as well as the combination of both are critical to understand certain aspects of the stellar mass build-up in galaxies within a ΛCDM cosmology.

3.2.3 Scaling Relations

Certain properties of galaxies scale with some of their other properties - often spanning several orders of magnitude with a very narrow scatter. These scaling relations were found empirically and let us develop an intuition of how galaxies behave on average. More importantly, they form tight constraints on galaxy formation, as nature does not produce "random" types of galaxies. Understanding and applying the laws of physics to these scaling relations will help us understand if our standard cosmology model is able to reproduce the observations.

Often scaling relations are presented separately for early-type (commonly quenched and bulge-dominated) and late-type (commonly star-forming and disk-dominated) galaxies. The most important ones are briefly described in the following.

3.2.3.1 *The mass-size relation*

The next most fundamental parameter after the luminosity or mass of a galaxy, is its size. Galactic size or radius can be estimated in several, nuanced ways, but is typically measured as the half-light radius, which is the radius that encloses half the galaxy's total luminosity[43]. The sizes of galaxies are roughly distributed according to a log-normal function (Shen et al., 2003).

Overall, Galaxies with higher masses also have a greater spatial extent. Late-type galaxies are on average more extended and early-type galaxies more compact until this reverses for galaxies with stellar masses above $\sim 10^{11}\,M_\odot$. Therefore, late-type galaxies follow a mass-size relation with a flatter slope compared to early-type galaxies (Shen et al., 2003; van der Wel et al., 2014).

The mass-size relation also evolves with redshift (van der Wel et al., 2014; Shibuya et al., 2015) as seen in Figure 3.12. Overall, galaxies are

43: The size of the half-light radius varies for different filters due to stellar population gradients within the galaxy. Therefore, theorists use half-mass radii.

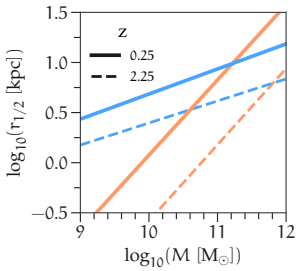

Figure 3.12. Fitted mass-size relation to data from van der Wel et al. (2014) for two redshifts. The relation is shown separately for early- and late-type galaxies (*red* and *blue* respectively). The scatter is around $0.1 - 0.2$ dex.

smaller at early cosmic times - therefore galaxies grow in mass *and* size. Comparing galaxies at fixed stellar mass across redshifts reveals that juvenile high mass galaxies $\sim 10^{11}\,M_\odot$ are considerably smaller than their low-redshift counterparts, which is only moderately the case for lower mass galaxies. This observation is particularly prominent for early-type galaxies (van der Wel et al., 2014). This suggests that there are different mechanisms that separately influence the size of equal mass late-type and early-type galaxies at different redshifts.

However, the exact interpretation of the size evolution of galaxies is complicated. Apart from the fact that it is observationally impossible to follow the evolution of individual galaxies through redshift, galaxies can transition from late-type to early-types (and vice versa ?) via merging or other quenching processes. Hence, a late-type galaxy of a given mass at early times could quench and then look like an extended early-type galaxy at later times[44].

Nevertheless, since all protogalaxies should be gas-rich, their initial size is likely set by the properties of the initial dark matter halo they form in. To first order, a galaxy's half-light radius $r_{1/2}$ is proportional to its halo's size, given by R_{vir}[45] and angular momentum λ. A halo can acquire angular momentum during its linear[46] and non-linear phases of gravitational collapse (Peebles, 1969; White, 1984), which is transferred to the infalling gas, which settles into a rotationally supported disk (Efstathiou & Jones, 1979; Fall & Efstathiou, 1980). The distribution of halo angular momenta is predicted to be log-normal with a median of ~ 0.04, which is roughly constant across halo mass and redshift (Bullock et al., 2001b; Macciò et al., 2007; Muñoz-Cuartas et al., 2011). Thus λ acts as a proportionality factor and is thought to set the scatter of the $r_{1/2} \propto R_{vir}$ relation (Kravtsov, 2013; Somerville et al., 2018). Furthermore, the presence of the disk modifies the structure of the halo causing it to contract (Eggen et al., 1962; Blumenthal et al., 1986; Gnedin et al., 2004). Thus the secondary dependence is related to halo concentration[47] (Mo et al., 1998; Somerville et al., 2008).

The emergent picture of size growth is then that late-type galaxies grow their disk from in-side out, backed up by observations of the gaseous disk being typically more extent than the stellar one (Nelson et al., 2012, 2016) and by simulations of accreting (cold) gas from the halo (e.g. Brook et al., 2012; Bird et al., 2013, and see also the next paragraph). Massive early-type galaxies significantly grow in size at late times because of dry (minor) mergers that "puff up" the outskirts (van Dokkum et al., 2008; Naab et al., 2009; van Dokkum et al., 2010; Oser et al., 2012). The formation of compact early-types can largely be explained through dissipational processes, such as gas-rich mergers (Cox et al., 2006; Naab et al., 2006) or through compaction of the gaseous disk (Zolotov et al., 2015), which trigger a burst of star formation and result in rapid quenching. This is closely connected to formation scenarios of a central bulge (see Section 3.3.3.3).

3.2.3.2 *Relations with kinematics*

The mere appearance of a late-type (a thin disk) and an early-type (a spheroid) galaxy already suggest that the motion of stars in these two

44: This is known as 'progenitor bias' (see e.g. van Dokkum & Franx, 2001).

45: The virial radius is usually defined as half the maximum expansion radius of the halo, which can be re-expressed as the radius where the density of the dark matter halo reaches a certain factor of the critical density of the Universe. This factor depends on the adopted cosmology and redshift. Another common definition is R_{200}, which uses a fixed factor of 200 times the critical density.

46: This is referred to as the Tidal Torque Theory.

47: The concentration c is defined as the ratio between the virial radius and the inner scale length of the NFW profile (Navarro et al., 1996). Lower mass halos are more concentrated at fixed redshift. At fixed halo mass, lower redshift halos are more concentrated (see e.g. Bullock et al., 2001a; Macciò et al., 2007; Muñoz-Cuartas et al., 2011).

types of galaxies are fundamentally different. Indeed, disk galaxies are dominated by ordered, rotating motion, whereas spheroidal galaxies are governed by the random motion of stars. The circular velocity[48] of spirals v_{circ} and the velocity dispersion[49] of spheroids σ is correlated with the galaxy's luminosity L, known as the Tully-Fisher (Tully & Fisher, 1977) and Faber-Jackson (Faber & Jackson, 1976) relation respectively. Additionally connecting the Faber-Jackson relation with the half-light radius[50] of ellipticals yields the Fundamental Plane (Djorgovski & Davis, 1987). The Tully-Fisher relation and the Fundamental Plane have a very small scatter of ~ 0.1 dex (Jorgensen et al., 1996; Courteau et al., 2007; Lelli et al., 2016). Hence, they provide stringent constraints on galaxy formation in our adopted cosmological framework.

Even thought these relations were discovered empirically, the observed kinematics emerge because of the underlying dynamics arising from the joint gravitational potential of baryonic and dark matter in galaxies. Therefore, applying dynamical models to kinematic measurements is one of the most important tools to understand the dark mass in galaxies (e.g. Cappellari et al., 2006).

The slopes of both these relations can be determined to first order by simple considerations. For spirals, we can assume that the circular velocity[51] is entirely governed by the gravity of the dark matter halo, which can be approximated by an isothermal sphere[52]. By using Equation 3.4, this yields the virial mass of the halo to be $M_{vir} \propto v_{circ}^3$, when setting its density (Equation 3.5) to some fraction of the Universe's critical density (Equation 2.2). And as mass follows light, we have $L \propto v_{circ}^3$. Similarly, for ellipticals, we can apply the virial theorem by setting the kinetic energy to $E_{kin} = \frac{1}{2} M \sigma^2$ and the potential energy to that of a self-gravitating sphere $E_{pot} = -\frac{3}{5}\frac{GM}{r_{1/2}}$, which yields $M_{dyn} \propto L \propto r_{1/2}\sigma^2$.

Naturally, the true slopes deviate from these assumptions (see e.g. Jorgensen et al., 1996; Courteau et al., 2007), mostly because of the conversion from mass to light. Variations in the underlying stellar populations, the concentration of the dark matter profile and non-negligible gas fractions will change the relation between the dynamical mass (all matter), the stellar mass and the stellar light (e.g. Cappellari et al., 2013a; Lelli et al., 2016). Furthermore, elliptical galaxies can have a significant amount of rotational support, which has to be taken into account by dynamical models (Emsellem et al., 2011).

3.2.3.3 *The star formation law*

Yet another power law is the Kennicutt-Schmidt relation (Schmidt, 1959; Kennicutt, 1989, 1998). It relates the globally measured star formation rate surface density with the gas[53] mass surface density. Thus, it only applies to galaxies that have measurable traces of on-going star formation.

This diagnostic is extremely valuable, as it is still very difficult to formulate the process of star formation from first principles, i.e. connecting it to physical properties of the interstellar medium, due to the numerous physical processes involved and our limited understanding

48: Typically measured from the shift in emission lines of (molecular, neutral or ionized) gas on opposite sides of the disk. As the gas has typically negligible random motions (in contrast to stars) the measured rotational velocity is equated with the circular velocity.

49: Measured from the width of absorption line spectra.

50: The half-light radius is related to the total luminosity via

$$L = 2\pi \langle I \rangle_{1/2} r_{1/2},$$

where $\langle I \rangle_{1/2}$ is the mean surface brightness within the half-light radius $r_{1/2}$.

51: The circular velocity v_{circ} is given by

$$v_{circ}^2 = \frac{GM_{vir}}{R_{vir}}, \quad (3.4)$$

where M_{vir} is virial mass of the halo and R_{vir} its radius.

52: Its density is given by

$$\rho(r) = \frac{v_{circ}^2}{4\pi G R_{vir}^2}, \quad (3.5)$$

connecting the circular velocity with the virial radius.

53: This includes molecular and neutral hydrogen. Locally within a galaxy, molecular gas is the best tracer of star formation (Bigiel et al., 2008). Neutral hydrogen (HI) is the dominant interstellar medium (ISM) component in the outskirts of disk galaxies, where star formation is low. This means that there is a critical density necessary for star formation to occur.

of them (see McKee & Ostriker, 2007, for a review).

However, we do know that stars form through the fragmentation and gravitational collapse of cold, molecular gas clouds (Larson, 1981). Hence, a gas cloud with mean density ρ_{gas} should form stars within the free-fall time $\tau_{ff} \propto \rho_{gas}^{-1/2}$ and with some star formation efficiency ϵ. This yields:

$$\dot{\rho}_\star = \epsilon \frac{\rho_{gas}}{\tau_{ff}} \propto \rho_{gas}^{1.5}, \tag{3.6}$$

which is close to the observed slope of 1.4. The star formation efficiency ϵ is found to be low ($\ll 1$), likewise for giant molecular clouds (GMCs) of the Milky Way and high redshift starburst galaxies (Krumholz et al., 2012). This means that only a small fraction of the available gas is turned into stars, hence star formation self-regulates to maintain disk stability (Toomre, 1964). The drivers for this self-regulation are likely a combination of turbulence (Krumholz & McKee, 2005) and stellar feedback (Silk, 1997).

Sometimes confusingly the star formation efficiency is also referred to as the inverse of the depletion time $\tau_{depl} = \frac{M_{gas}}{SFR}$. This term combines the effect of ϵ and the actual time it takes to use up the available amount of gas M_{gas} with a given SFR (Leroy et al., 2008). For example, the depletion time for a normal star forming galaxy is around 1 Gyr, whereas an equal mass galaxy that experiences a star burst (e.g. one dex away from the star forming main sequence) has a depletion time around 0.3 Gyr (Tacconi et al., 2018).

There is evidence that the Kennicutt-Schmidt relation does not evolve with redshift (Genzel et al., 2010; Tacconi et al., 2013). This suggests that the conditions for star formation to be able to occur do not change over time. Because SFRs in the early universe are higher, as discussed in Section 3.2.2, the amount of available molecular gas has to be consequently higher as well (Tacconi et al., 2010). Recent studies (Walter et al., 2020), that measure the cosmic molecular gas mass density until high redshifts thanks to Atacama Large Millimeter/submillimeter Array (ALMA), show that this is indeed the case. In fact, the peak of cosmic SFR and molecular gas mass density occur at roughly the same redshift ($z \approx 2$).

Lastly, the Kennicutt-Schmidt provides a critical bridge of connecting star formation, which takes place on parsec scales, with the global properties of a galaxy, which is several kiloparsec in size. This is essential for simulators to check and calibrate their star formation and feedback models in order to produce realistic galaxies (e.g. Katz, 1992; Springel, 2000).

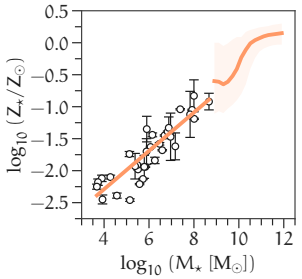

Figure 3.13. The mass-metallicity relation from Local Group dwarfs (individual data points; Kirby et al., 2013) and SDSS (Gallazzi et al., 2005).

3.2.3.4 *The mass-metallicity relation*

My favourite and most used relation is the mass-metallicity relation (Lequeux et al., 1979). It shows that higher mass galaxies are chemically more enriched on average than lower mass galaxies. This relation, shown in Figure 3.13, holds true for the metallicity measured from absorption lines of stars (Gallazzi et al., 2005) and emission lines of gas

(Tremonti et al., 2004) extending down towards the lowest mass galaxies in the Local Group (Kirby et al., 2013). Furthermore, Mannucci et al. (2010) showed that gas-phase metallicities and SFR form a fundamental plane. At fixed stellar mass, galaxies with higher metallicities have higher SFRs.

Nevertheless, gas-phase and stellar metallicities have a slightly different interpretation. The metallicity of the gas represents an instantaneous quantity, whereas the stellar metallicity refers to the amount of metals currently locked up in the photospheres of stars that originated from some previously existing gas.

Gas-phase metallicities are measured as the oxygen abundances, as it is the most abundant heavy element[54]. For stellar metallicities the iron abundance is taken as a proxy, as iron lines are easily measurable in optical absorption spectra.

Stellar abundances are given with respect to the hydrogen (H) content. The abundance ratio of a given element M is [M/H], which is measured for a given stellar object $\star$ compared to the solar abundance $\odot$ via:

$$[M/H] = \log_{10}\left(\frac{N_M}{N_H}\right)_\star - \log_{10}\left(\frac{N_M}{N_H}\right)_\odot, \tag{3.7}$$

where N_M and N_H are the number densities for iron and hydrogen respectively[55].

The mass-metallicity relation also evolves with redshift (Zahid et al., 2013); at fixed galaxy stellar mass the metallicity was lower at earlier cosmic times.

After the Big Bang, the gas was essentially metal free. The first stars[56], formed from this gas, produced heavier elements via nucleosynthesis in their interiors, which they then released back into the ISM through supernovae explosions. This enriches the ISM, from which a new generation of metal-enriched stars form. Thus, the galaxy gradually enriches in metals over time. This is called the Cosmic Baryon Cycle.

The enrichment of metals can be very intuitively understood with a simple chemical evolution model, called the closed-box model. It assumes that gas does not leave nor enter the system. The metallicity expressed as the metal mass fraction Z therefore evolves with time t as:

$$Z(t) = Z(0) - y_Z \ln[\mu(t)], \tag{3.8}$$

where y_Z is the yield, i.e. the fraction of metals returned to the ISM, and $\mu(t) = M_{gas}(t)/M_{gas}(0)$ is the instantaneous gas mass fraction. In observations, this model is used with an effective yield y_{eff} (e.g. Garnett, 2002; Lee et al., 2006), as in- and out-flows of gas make galaxies not evolve like a simple closed box (Edmunds, 1990; Dalcanton, 2007); thus typically $y_{eff} \leqslant y_Z$. Dwarf galaxies have low escape velocities and therefore low effective yields, as supernovae are able to blow out a significant amount of the galaxy's gas mass (Larson, 1974; Dekel & Silk, 1986; Agertz et al., 2020).

54: They are given in terms of $12 + \log O/H$, where O and H are the number densities N for oxygen and hydrogen respectively. This is equal to the logarithmic abundance of oxygen ϵ_O on the customary astronomical scale, where ϵ_H is set to 12 (Asplund et al., 2009).

55: Sometimes the metallicity is expressed as the logarithm of the metal mass fraction Z with respect to the solar one $Z_\odot$. The metal mass fraction is $Z = m_z/M$, where m_z is the mass in metals and M the total mass. Note that $\log_{10}(Z/Z_\odot)$ is not same as the abundance ratio definition. To convert from number densities to mass fraction one has to take into account the atomic mass A of a given isotope, i.e. $Z_M/Z_H = (N_M/N_H) \cdot (A_M/A_H)$ (Piersanti et al., 2007).

56: Also called population III stars. We have yet to observe them and also our theoretical understanding of their formation is still limited (see Bromm & Larson, 2004, for a review). However, they were likely very massive ($100 - 1000\,M_\odot$).

Furthermore, there is evidence that the mass-metallicity relation experiences a flattening for high galaxy masses, which is increasingly shifted towards lower galaxy masses for later cosmic times (Zahid et al., 2014). The saturation in metallicity is allegedly achieved when the mass of newly produced metals in massive stars equals the mass of metals that stays locked up in low-mass stars.

The prospect that lower mass galaxies are overall less efficient in enriching their ISM is great: when a high mass galaxy merges with a lower mass galaxy, their stars are chemically distinct at fixed age. Therefore, the ages and metallicities of stars in galaxies provides a possibility to disentangle their origins (Leaman et al., 2013). The work in this thesis aims to exploit this fact to understand the contribution of mergers to the mass-build of galaxies.

3.3 SPATIALLY RESOLVED PROPERTIES

We now open our eyes again and accept the fact that galaxies are not point sources. Most properties mentioned in Section 3.2.3 vary as position within the galaxy. For example, as briefly mentioned in Section 3.2.3.3, spiral galaxies are less efficient at making stars in the outskirts of their disks, as the (molecular) gas densities drop below the critical threshold for star formation to take place. The exact behaviour of this as a function of radius from the galaxy's center will probably vary from galaxy to galaxy. Thus, spatially resolved studies let us understand the individuality of galaxies at a given fixed global property or within a similar morphological class. Any successful cosmological model needs to reproduce this scatter, no matter if it is small, in addition to the mean trends.

More complicated even, galaxies are build up of certain structural components: for example spiral galaxy typically have a disk and a bulge component, as mentioned in Section 3.1.1. All of these components individually present benchmarks for galaxy formation in the ΛCDM model. They typically possess their own scaling relations correlated with either global properties of the galaxy or other (sub)components. This resulted in a wealth of mechanisms being proposed that can act upon creating, maintaining and destroying these features.

We now first want to understand how spatially revolved properties of galaxies are extracted from photometry and spectroscopy alike. I then briefly walk through the individual structural components of galaxies, their properties and debated formation scenarios.

3.3.1 Surface Photometry

The surface brightness $I(r)$ of a galaxy, i.e. the luminosity (or magnitudes) per area, is an intrinsic quantity of a galaxy, because it is independent of distance to the galaxy. Galaxies have a higher surface brightness in their centers than in their outskirts, which means that the density of stars increases towards the center.

Measuring the surface brightness as function of projected radius[57], yields a profile, which is typically well fit with the functional form introduced by Sérsic (1968):

$$I(r) = I_e \exp\left[-\beta_n\left(\left(\frac{r}{r_e}\right)^{1/n} - 1\right)\right], \tag{3.9}$$

where I_e is the surface brightness at the effective radius r_e, which encloses half of the total light, and b_n is the normalization. The Sérsic index n indicates how concentrated the profile is; higher n means more concentrated towards the center. For $n = 1$, an exponential profile is achieved, which fits well for stellar disks (Freeman, 1970). For $n = 4$, the profile becomes the one first described by de Vaucouleurs (1948), which generally fits bulges and ellipticals well. Such measurements can also be applied directly to the 2D galaxy image (see e.g. Peng et al., 2002).

Naturally, most galaxies will not be well fit by a single profile. A spiral galaxy typically has a bulge and a disk. But also elliptical galaxies can be more complex. The most massive early-type galaxies often have a diffuse outer stellar halo, which needs an additional exponential component (Seigar et al., 2007).

The literature of decomposing a galaxy's light into multiple components from photometry is vast (see the introduction of e.g. Méndez-Abreu et al., 2017), mainly because of three reasons: 1) the parameters n, R_e, I_e give us a good understanding of how the galaxy is structured (Kormendy, 1977; Salo et al., 2015), 2) photometry reaching decent surface brightness levels is now easily available for a large quantity of galaxies at varying redshfits (e.g. Simard et al., 2011; van der Wel et al., 2012), 3) subtracting a certain photometric model from the galaxy light helps to reveal more substructures (i.e. typically non-axisymmetric features; Peng et al., 2010) and allows for the analysis of other objects intrinsic to a galaxy, such as globular clusters (GCs; see e.g. Durrell et al., 2014).

Obtaining surface photometry in multiple filters adds first information about the underlying stellar populations present in galaxies (Tortora et al., 2010). Both early- and late-type galaxies show gradients in their colors (Peletier et al., 1990; Bakos et al., 2008), generally becoming bluer with increasing distance from the galaxy's center.

However, determining whether these trends are due to the age or metallicity of the stars is tricky to understand from photometry alone, because of the age-metallicity degeneracy[58] (Worthey, 1994) and reddening effects. Furthermore, structures that are decomposed from photometry, for example the bulge and the disk, do not necessarily reflect an underlying physical property, such as the amount of ordered versus random motion (Zhu et al., 2018).

57: This can be concentric circular or elliptical annuli measured through isophotes.

58: A young star is blue in color, but so is a metal-poor star. Equivalently, a red color can be achieved by old stars, but also metal-rich ones.

3.3.2 Adding Spectroscopy

Spectroscopy generally solves the two aforementioned problems: it contains kinematic information and is much better at breaking age-metallicity-reddening degeneracies. However, dispersing light into its individual wavelengths has the consequence that much longer integration times (or better instruments) are needed in order to reach a decent signal-to-noise of the stellar continuum[59]. Measuring spectra as a function of position over the galaxy's extent is therefore much more observationally challenging.

59: Emission lines are much more easily obtained, because they are much brighter.

Long-slit spectroscopy enables the simultaneous extraction of spectra along the radial direction at a given position angle. This technique has been used since the 70s to construct kinematic profiles of galaxies (e.g. Illingworth, 1977; Davies et al., 1983). They also allow to construct radial profiles of certain absorption line strengths (Worthey et al., 1994) that are sensitive to age and metallicity respectively, to understand stellar population gradients (e.g. Davies et al., 1993).

Kinematic profiles and gradients vary significantly with position angle, because galaxies are not isotropic and spherically symmetric systems. However, constructing a full 2D map of such properties is largely infeasible with long-slit spectroscopy, as a single galaxy needs to be sampled with many slit positions.

The advent of integral field unit (IFU) spectrographs (Bacon et al., 2001), which provide full spectral information at each spatial pixel, therefore revolutionized the field of extragalactic astronomy (e.g. Cid Fernandes et al., 2013). IFU surveys are now conducted for hundreds to thousands of galaxies providing us with detailed knowledge about the inner ($\sim 1-2\,R_e$) structures of galaxies (e.g. ATLAS3D: Cappellari et al., 2011a; CALIFA: Sánchez et al., 2012; MANGA: Bundy et al., 2015; SAMI: Allen et al., 2015). Powerhorses like the Multi Unit Spectroscopic Explorer (MUSE) (Bacon et al., 2014) on the Very Large Telescope (VLT) provide 30,000 spectra covering most of the optical wavelength range *per* pointing. With only a few hours of integration time MUSE provides several thousand, high-signal-to-noise ($\gtrsim 100$) spectra for the inner regions of nearby galaxies.

Spatially resolved dynamical and stellar populations properties are an important asset in understanding how galaxies form, because these quantities act as a fossil record. I briefly discuss below, what kind of stellar population and kinematic signatures we expect when looking at different regions in a galaxy, and how these are connected to a galaxy's evolution.

3.3.2.1 *Stellar Populations*

The ages and metallicities of stellar populations (see also Chapter 4) are a diagnostic of the conditions in the host galaxy at the time the stars were born. As mentioned in Section 3.2.3.4, galaxies gradually enrich in metals over time, and the efficiency with which they do so is a strong function of galaxy mass. However, even at fixed galaxy mass, stellar populations can vary quite significantly; primarily as a function

of radius (or along their major axis). To first order, galaxies are the most metal-rich and oldest in their centers. With increasing radius the stellar populations become more metal-poor and younger. This means that galaxies assemble their centers first and then gradually grow in size from inside-out[60] (e.g. González Delgado et al., 2015; Goddard et al., 2017; Zheng et al., 2017; Zibetti et al., 2020). In a sense, this resembles a local manifestation of the mass-metallicity relation (Rosales-Ortega et al., 2012; Zhuang et al., 2019). As galaxies have an increasing mass density profile towards the center, they are more efficient in turning gas into stars.

60: Some studies indicate that an outside-in scenario is more plausible for dwarf galaxies (e.g. Zhang et al., 2012; Pérez et al., 2013).

Nevertheless, depending on the galaxy type, the exact behaviour of stellar population gradients vary. Typically, metallicity gradients, measured in [M/H], and logarithmic age gradients are the flattest for the highest mass and lowest mass galaxies[61], but for very different reasons.

61: Zhuang et al. (2019) demonstrated that *linear* metallicity gradients correlate much better with morphological type.

High mass early-type galaxies had very high SFRs at early times, thus forming almost all their stellar mass within a few Gyr and enriching quickly in metals (e.g. McDermid et al., 2015). At a certain density threshold, the enrichment saturates, or is stopped by, for example, AGN feedback. This can result in flatter gradients[62] with overall old and metal-rich stellar populations (González Delgado et al., 2014).

62: Finding age gradients of a few Gyr in overall old stellar populations (> 8 Gyr) is basically impossible, as their emitted light is very similar. This results in a poor age resolution at old ages.

Low mass late-type galaxies, on the other hand, have rather flat stellar population profiles, because they are so inefficient in forming stars across their spatial extent due to their low surface brightness.

Intermediate mass galaxies, especially late-types with a bulge, have typically the steepest gradients. The inner part is dominated by the bulge, which had a short but rapid star formation, much like ellipticals. Consequently, the transition to the star forming disk is usually accompanied with a sharp decrease in metallicity and age (e.g. González Delgado et al., 2015).

There are several mechanisms that can change the shape of stellar population gradients. For example, recent star formation occurring only in the center can cause a positive age gradient in early-type galaxies, especially if light-weighted quantities are measured (e.g. Peletier et al., 2007; Kuntschner et al., 2010; Spolaor et al., 2010).

Initially steep gradients, can be flattened by dry major mergers, which is a very likely scenario for high mass ellipticals (Kobayashi, 2004; Di Matteo et al., 2009). On the contrary, dry minor mergers can steepen metallicity gradients, as the accreted low mass galaxies will have a significantly more metal poor population than the more massive host (Hilz et al., 2013). This is observed in the outskirts (stellar halos) of massive early-type galaxies (e.g. Greene et al., 2012; La Barbera et al., 2012; Greene et al., 2013, see also Section 3.3.3.1). In (star forming) disk galaxies, radial migration can cause flat age gradients in their outer parts (e.g. Minchev et al., 2013, 2014, see also Section 3.3.3.2).

Apart from ages and total metallicites, individual element abundances are also important indicators of the galaxy's formation history. They are hard to measure for external galaxies because they require: a) spectra with high spectral resolution and signal-to-noise and b) stel-

lar population models with varying element abundances, which are scarce.

The α-to-iron abundance ratio [α/Fe], which compares collectively the abundance of α-elements[63] to that of iron, is therefore the most widely used indicator. Because α-elements are predominantly formed in massive stars, which quickly explode as supernovae type II, [α/Fe] will be high in stars that were born early on in the galaxy's lifetime[64]. The overall metallicity or iron abundance, [Fe/H], increases with time, while [α/Fe] stays constant at first. The latter starts to decrease only after the onset of supernovae type Ia[65], because they predominantly enrich the ISM with iron (Tinsley, 1979). Because supernovae type Ia have a delay time of $\sim$ 1 Gyr (Mennekens et al., 2010; Ruiter et al., 2011), the simultaneous measurement of [α/Fe] and [Fe/H] acts like a chemical clock. For example, if a galaxy was extremely efficient in producing a lot of stars in a short period of time, like high mass early-types, the average star will be have high [α/Fe] (and also [Fe/H]). If star formation is more prolonged, like in the Milky Way (MW), the star forming disk will host average stars with low [α/Fe], but rich in [Fe/H]. Dwarf galaxies are more inefficient in forming stars and thus the decrease of [α/Fe] will happen at much lower values of [Fe/H] (Venn et al., 2004; de Boer et al., 2014).

Thus, measuring [α/Fe] and [Fe/H] as a function of position tells us how quickly and efficiently stellar populations formed in different parts of galaxies. This is especially important in understanding the formation of different structural components in galaxies (see Section 3.3.3). Typically, the α-abundance increases as function of radius for early-type galaxies, as metallicity decreases (e.g. Kuntschner et al., 2010; Vaughan et al., 2018; Martín-Navarro et al., 2021b). For disk galaxies, this is the case along the minor axis of the bulge and above/below the midplane of the disk (Pinna et al., 2019a,b; Martín-Navarro et al., 2021b; Martig et al., 2021), which is also accompanied with an increase of velocity dispersion compared to rotational support (see for the case of the MW Zoccali et al., 2008; Babusiaux et al., 2010; Gonzalez et al., 2011; Bovy et al., 2016). The presence of high [α/Fe] and low [Fe/H] stellar populations superimposed with the average population of a given galaxy component can indicate past accretion events (Mackereth et al., 2019).

Together, the spatial variation of ages, metallicities and α-abundances provide us with powerful constraints on the past assembly of galaxies as a whole and their structures, which I will exploit in Chapter 9 in particular.

3.3.2.2 *Kinematics and Dynamics*

Almost all galaxies, exhibit a decreasing velocity dispersion and, where present, an increasing rotational velocity with increasing radius from their center. For disk galaxies, the relative contribution of the velocity dispersion also grows with increasing height above and below the disk midplane. The different kinematic properties of stars in different regions of the galaxy are often intertwined with stellar population differences, and thus indicate different formation pathways and time

63: α-elements, like O, Ne, Mg, Si, S, Ar, Ca and Ti, are produced by the subsequent fusion of helium nuclei, i.e. the α particle.

64: Hence the exact absolute value will depend on the shape of the initial mass function (IMF), as more high mass stars produce a higher initial [α/Fe].

65: The explosion of a white dwarf that exceeds its critical mass after accreting from a companion.

scales.

Spatially resolved maps of galaxy kinematics[66], as delivered by IFU observations, re-shaped our understanding of early-type galaxies in particular (Cappellari et al., 2011b; Emsellem et al., 2011; Krajnović et al., 2011). Many do not appear as boring as their photometry might suggest. They can have kinematic peculiarities, such as decoupled cores, counter rotating disks and prolate[67] rotation; most of which are interpreted as an imprint of past interaction events with other galaxies (e.g. Balcells & Quinn, 1990; McDermid et al., 2006; Tsatsi et al., 2015; Krajnović et al., 2020).

On top of that, these IFU observations established that there are two distinct classes of early-type galaxies based on their spatially averaged angular momentum (Emsellem et al., 2007): 1) the fast rotators, which exhibit large-scale ordered rotation, much like late-types, and 2) the slow rotators, which do not exhibit large-scale ordered rotation, but can have (decoupled) small scale rotation and often display a substantial misalignment between their photometric and rotational axis. State-of-the-art cosmological simulations are able to reproduce this bimodality (Schulze et al., 2018; van de Sande et al., 2019), and thus we can investigate the distinct formation scenarios that led to these two classes of early-type galaxies. Likely, they are connected to the exact types of mergers (e.g. mass ratio, wet vs. dry, orbital configuration; see Section 6.3.1) they experienced throughout their lifetime (Bois et al., 2011).

Kinematic measurements are the basis for dynamical models, which let us understand the underlying potential that causes the observed movement of stars (see e.g. Leung et al., 2018). For example, a steep rise in the central velocity dispersion is a telltale sign of the presence of a SMBH (see Section 3.3.3.6). The application of dynamical models also inform us about the fraction of dark matter present in galaxies (e.g. Cappellari et al., 2013a), thus contributing to much needed observational measurements of the stellar-to-halo relation (see e.g. Posti et al., 2019, and Section 6.3.2 for the theoretical aspect). Even more so, they can help constrain the *shape* of the dark matter halos, which is important to understand the yet unknown nature of dark matter (Leung et al., 2021).

The most used dynamical techniques are Jeans (e.g. Cappellari, 2008, 2020) and Schwarzschild models (e.g. van den Bosch et al., 2008a; Vasiliev & Valluri, 2020). The former solves for the second velocity moment under specific assumptions about the alignment of the velocity ellipsoid, while the latter technique integrates orbit bundles to reproduce the observed kinematics. Thus, Schwarzschild models have the ability to predict the superposition of different orbits at a given (projected) position within the galaxy. This is a powerful advantage in disentangling spatially overlapping components of galaxies, which however have distinct kinematic properties, such as the disk, bulge and the stellar halo (Zhu et al., 2018).

Just recently, Schwarzschild models have been combined with stellar population measurements (Poci et al., 2019; Zhu et al., 2020), which simultaneously fit for the observed kinematics *and* spatially resolved

66: Stars are distributed in phase-space ($\mathbf{x}$, $\mathbf{v}$) according to their distribution function f. Integrating over all velocities $\mathbf{v}$ yields the velocity moments, which describe the shape of f at positions $\mathbf{x}$ as a summary statistic. For example, the zeroth velocity moment is the surface brightness, the first moment the rotational velocity, the second the velocity dispersion. Higher order moments can be interpreted as a departure from a pure Gaussian shape (e.g. van der Marel, 1994). Internal kinematics for galaxies outside the Local Group are only available along the line-of-sight. See Binney & Tremaine (2008) for an overview of galaxy dynamics.

67: That is rotation around the major axis, which is rather untypical.

stellar population properties. This makes it possible to unveil ancient merger events (see Section 3.3.3.1) and explore the age-velocity-dispersion relation[68] for external galaxies, where only integrated light measurements are available. Applying semi-analytical models to observed age-velocity-dispersion relations makes it then possible to understand the interplay between ISM turbulence and other latent heating mechanisms, caused either within the galaxy, such as scattering off of GMCs or spiral arms, or from external interactions (Leaman et al., 2017).

In summary, kinematic signatures, and dynamical models thereof, are essential predictors of a galaxy's assembly, especially in combination with observed stellar population properties. Particularly, they also act as a bridge between observation and simulations, as the latter predicts these observables given the different origins of stars within galaxies as well as the galaxy's assembly history as a whole. I will study this in Chapter 7.

68: Old stars have typically larger velocity dispersions than young ones, as they had more time to dynamically heat through various processes.

3.3.3 Individual Components

Distinct structural components of galaxies range largely in spatial extent and stellar density. Below I present a few of these components, from large to small scales, as well as observational clues we have about them[69].

Formation scenarios of all these components can be divided in general into two broader categories: an in-situ and an ex-situ formation scenario[70]. The former attributes the formation of a given component to some event that happened intrinsic to the galaxy (e.g. star formation), whereas the latter associates it with an external event (e.g. galaxy interactions). Often the formation of one component can lead to the formation of another. Their mutual influence and the evolution of the overall galaxy in a cosmological context makes it very tricky to discern the "correct" formation pathway. Likely, the combination of multiple mechanisms is at play and equally important.

69: This listing does not imply that every galaxy possesses every single one of these components.
Fun fact: the Milky Way actually does contain all the mentioned structures.

70: See also the 'morphological box' by Zwicky (1957).

3.3.3.1 *Stellar Halo*

Apart from a dark matter halo, galaxies also have a stellar one. It typically extends from 10 to $\gtrsim$ 100 kpc (Jurić et al., 2008) and is roughly spherical in shape. Due to the low number counts of stars in these regions, the Milky Way's stellar halo was first extensively studied with the help of globular clusters (GCs)[71], which are much more easily observable at large distances[72]. Their bimodality in metallicity quickly emerged with metal-rich GCs being at preferentially smaller galactrocentric distances ($\lesssim$ 10 kpc) than the most metal-poor ones (Harris, 1976). Therefore, Searle & Zinn (1978) concluded that the inner halo formed with the main stellar body of the Galaxy, while the outer halo originated from the accretion of satellite galaxies.

Simulations for galaxy formation in a ΛCDM cosmology indeed predict that stellar halos are dominated by accreted stars (Cooper et al., 2010; Pillepich et al., 2018b). Thus great observational time is invested

71: Bound, dense, roughly spherical stellar systems. See the Harris (1996, 2010) catalogue for properties of Milky Way GCs and a charming lesson about public data accessibility.

72: The GC system of a galaxy has important scaling relations with the host galaxy. Specifically, the GC system mass scales with the mass of the dark matter halo (Blakeslee et al., 1997; Spitler & Forbes, 2009; Georgiev et al., 2010; Harris et al., 2013).

into resolving the brightest stars of stellar halos in nearby galaxies (Radburn-Smith et al., 2011; Rejkuba et al., 2011; Ibata et al., 2014; Crnojević et al., 2016). A great variety is found in terms of stellar halo mass (and thus metallicity) (Iodice et al., 2016; Merritt et al., 2016; Monachesi et al., 2016; Spavone et al., 2017; Huang et al., 2018; Spavone et al., 2020) as well as the bimodal distribution of GCs in color/metallicity (Forbes et al., 1997; Peng et al., 2006; Brodie & Strader, 2006); consistent with the expected stochasticty of merger events.

Thanks to the Gaia satellite (Gaia Collaboration et al., 2018a), mapping millions of individual stars in the Milky Way, it was indisputably proven that also part of the Milky Way's inner stellar halo originated from a (major) merger (Helmi et al., 2018; Belokurov et al., 2018). New chemo-dynamical models are now being developed that can characterize the kinematic and stellar population signatures of inner stellar halos in external galaxies to uncover past merger events (Zhu et al., 2020, 2022a,b).

Thus, in the recent years stellar halos became the main focus of interest to study the accretion history of galaxies. Still, due to their faintness, observations exist only for a few galaxies. A visual example of faint substructures caused by tidal debris of past accretion events is shown in Figure 3.14. To address the frequency of mergers in galaxy formation and accordance with ΛCDM we need to extract this information for statistical samples of galaxies. The work presented in this thesis aims to work towards such a goal.

Figure 3.14. The stellar halo of NGC 474 shows spectacular features from disrupted satellite galaxies. The image was taken by the MATLAS survey (Duc et al., 2015; Duc, 2020).

3.3.3.2 *Disk*

We have already learned the following about disks: 1) they typically follow an exponential surface brightness profile (although see Pohlen & Trujillo, 2006), 2) they grow from inside out, 3) they form because the initial gas obtained angular momentum from the dark matter halo. Reconciling these these facts, however, is not at all straightforward.

Earlier simulations of disk formation showed that most angular momentum of the disk is lost to the dark matter halo making very compact disks (e.g. Navarro & White, 1994). Evidently, the hierarchical assembly within a ΛCDM cosmology favours a clumpy and turbulent disk formation as opposed to smooth gas accretion. Even if the conservation of angular momentum were perfect, resulting disks are still not exponential (Bullock et al., 2001b).

This posed a problem: there was no reason to believe that the initial angular momentum distribution of baryons should not follow the dark matter, as gravity acts equally on both (van den Bosch et al., 2001). Thus, angular momentum had to be redistributed during the formation and/or evolution of the disk. Low specific angular momentum material could be transformed into a bulge (van den Bosch, 2001, ; but then not every galaxy has a bulge), or blown out by stellar feedback (Brook et al., 2012).

Another process that diffuses angular momentum is radial migration (Sellwood & Binney, 2002), where the orbits of stars are scattered due to some non-axisymmetries such as GMCs, spiral arms or the bar. This process is thought to be secular, i.e. the galaxy needs to evolve in

near isolation. In the Milky Way, the significant scatter in metallicity of disk stars in the midplane at fixed radius has been taken as indication for such a processes (Hayden et al., 2015), which was quantified by my very smart friend Frankel et al. (2020).

To make the case of galactic disks even more complicated: they usually possess two components with varying scale height. The presence of a thin and thick disk in the Milky Way was first noted by Gilmore & Reid (1983). The thick disk is less massive and consists of stars that are older, more metal-poor and have a lower rotational to random motion support. With large spectroscopic surveys, which measure detailed abundances of individual stars, a bimodality in $[\alpha/Fe] - [Fe/H]$ plane of disk stars was also found (Bovy et al., 2012). Stars with higher α-abundance have larger scale heights.

The chemo-dynamical differences of disk stars as a function of vertical distance from the midplane, raised a number of different formation pathways for thick disks including in-situ formation (Brook et al., 2004), heating of thin disk stars (Velazquez & White, 1999; Grand et al., 2016) and external acquisition (Abadi et al., 2003). The latest IFUs measurements make it possible to also study the chemo-dynamical properties of external disk galaxies, shedding more light into their exact formation pathways (Pinna et al., 2019a,b).

3.3.3.3 *Bulge*

Almost every massive ($\gtrsim 10^{10}\,M_\odot$) late-type galaxy has a bulge (Fisher & Drory, 2011). Originally it was thought that bulges in spiral galaxies are just like small elliptical galaxies, because they share similar photometric properties (de Vaucouleurs, 1959; Sandage et al., 1970), are red in color (Balcells & Peletier, 1994) and lie on the same scaling relations, such as the Faber-Jackson relation (Whitmore et al., 1979). But then, it was increasingly noticed that not all bulges follow these trends. Bulges of spirals tend to rotate faster than early-type galaxies (e.g. Kormendy & Illingworth, 1982; Fabricius et al., 2012) and are on average fit better by Sérsic indices $n < 4$, especially for spirals with low bulge-to-disk ratios (e.g. Andredakis et al., 1995).

Thus, bulges were divided into 'classical' bulges, the ones that behave like early-types of similar mass (Kormendy et al., 2009), and 'pseudobulges', the ones that behave differently. For example, pseudobulges do not lie on the Fundamental Plane and often have Sérsic indices $n < 2$ (Fisher & Drory, 2008; Gadotti, 2009; Fisher & Drory, 2010). These low Sérsic indices mean that pseudobulges are very close to disks ($n = 1$). Indeed, pseudobulges often have signs of active star formation (Fisher, 2006), and their age correlates with the age of the disk (Peletier & Balcells, 1996; Gadotti & dos Anjos, 2001). Accompanying pseudobulges are often additional nuclear[73] morphologies, such as spirals, disks, bar and rings (see Kormendy & Kennicutt, 2004, for a full review). Again, the capabilities of IFU instruments make it now possible to discern these different structures in unprecedented details via chemo-dynamical properties (e.g. Gadotti et al., 2020; Bittner et al., 2020).

73: i.e. very central, typically on scales less than 1 kpc and distinct from the overall galactic morphology.

The stark dichotomy of bulges leads to the consensus that their for-

mation pathways must be quite different as well. Classical bulges are believed to follow similar formation mechanisms to low- to intermediate mass ellipticals, which are formed through dissipational (gas-rich) mergers (Hopkins et al., 2009a,b). The questions is then, why do some mergers produce a disk+bulge (late-type) galaxy and others just a bulge (early-type)[74]? This means that the disk must either survive the merger, perhaps because the mergers were minor enough or brought in substantial amounts of gas (Aguerri et al., 2001; Springel & Hernquist, 2005; Robertson et al., 2006; Hopkins et al., 2009d), or form after bulge formation, for example, cold gas accretion (Brooks et al., 2009; Governato et al., 2009). Other studies show that classical bulges emerge through gas-rich clumps that originally formed out in the disk through some instabilities and then in-spiraled to the center (Noguchi, 1999; Immeli et al., 2004; Elmegreen et al., 2008).

74: Let us not forget that late-type galaxies can become early-types via merging or some other processes that removes the gas (see Section 3.2.2).

In the case of pseudobulges, it is argued that they grow through secular evolution, meaning a slow, smooth process that builds up stellar mass in the center gradually (Kormendy & Kennicutt, 2004; Athanassoula, 2005). This is achieved mainly by the presence of a bars (see next Section 3.3.3.4), as they are very efficient in channeling gas to the center (e.g. Sakamoto et al., 1999). Indeed, galaxies with the conspicuous actively star forming nuclear rings or disks are often barred (see Figure 3.2).

However, what about galaxies that host pseudobulges, but do not have bars? It has been shown that bars can dissolve within a few Gyr, once, for example, a central mass concentration is build-up (e.g. Hasan & Norman, 1990; Shen & Sellwood, 2004; Bournaud et al., 2005).

Others argue that secular evolution takes too long to form a significant amount of central mass. They are in favour of a more rapid growth of pseudobulges at high redshift, where bursts of star formation occur frequently either through disk instabilities or galaxy interactions (e.g. Guedes et al., 2013; Okamoto, 2013). Likely all of these pathways contribute to bulge growth, the question is rather what the relative importance of each of those channels is (Kraljic et al., 2012).

All in all, bulges are a complicated topic and can fill entire books (Laurikainen et al., 2016). Perhaps now, with orbit-decomposition methods applied to IFU observations (Zhu et al., 2018) and to state-of-the-art cosmological simulations (Obreja et al., 2019; Du et al., 2020), we will be able to understand better bulge formation in itself and the interconnection between the different properties they possess.

3.3.3.4 *Bar*

Bars are found in around 40% of all disk galaxies (e.g. Aguerri et al., 2009; Masters et al., 2011). This fraction is found to decline significantly with redshift (see Sheth et al., 2008, for measurements up until $z \sim 1$) and their sizes vary from a few kpc to tens of kpc (Barazza et al., 2008), and correlate with galaxy stellar mass (Díaz-García et al., 2016a).

There is also a clear trend that bars are larger for galaxies with larger bulges (e.g. Laurikainen & Salo, 2002; Erwin, 2005), which is coupled with a decrease in the SFR (e.g. Cheung et al., 2013). Simulations have indeed found that bars grow later and much slower in gas-rich systems

(Athanassoula et al., 2013). These results have been interpreted as signs of secular evolution. Barred galaxies, which are less massive and star forming, are still in the process of forming their bars, whereas more massive and quiescent galaxies have finished building their bars and and grew their bulge in the process (Athanassoula, 2003).

But what are bars actually? We have seen a visual example in Figure 3.2. Dynamically speaking, bars are non-axisymmetric structure that rotates like a solid body with a certain pattern speed. This leads to certain resonances between the frequency of the bar and the frequency at which stars rotate around the galactic center (see e.g. Sellwood & Wilkinson, 1993, for bar dynamics). Resonances lead to angular momentum exchange, which give rise to a number of complicated phenomena, but generally include a slow-down of the bar (Athanassoula, 2003), in-flows of gas (Athanassoula, 1992), a vertical "buckling" instability that gives the bulge region a boxy peanut or x-shape when viewed edge-on (Raha et al., 1991).

In isolated galaxy simulations, bars are easily formed 'spontaneously' through disk instabilities (Athanassoula et al., 2013), whereas bar formation can be tied to galaxy interactions in cosmological setups (Romano-Díaz et al., 2008; Peschken & Łokas, 2019). More recently, bars produced by even the highest resolution cosmological simulations have been claimed to be too slow compared to observations, challenging the ΛCDM paradigm. Frankel et al. (2022) demonstrated that these discrepancies are likely due to inaccurate comparison between observations and simulations. Observations are subjected to selection effects (i.e. with a bias towards selecting larger, faster bars; see also Erwin, 2018), and simulations have to take into account mass-to-light conversion and other instrumental effects via the constructions of mock observations. I will follow this philosophy in Chapter 9.

3.3.3.5 *Nuclear Star Clusters*

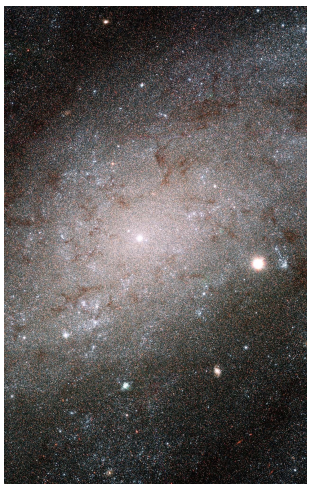

Figure 3.15. The galaxy NGC 300 has an obvious nuclear star cluster (NSC) sitting at its center. **Credit**: NASA, ESA, and The Hubble Heritage Team (AURA/STScI).

Nuclear star clusters (NSCs) are the densest stellar systems in the Universe reaching central densities of $10^6\,M_\odot/pc^3$ and more (see Neumayer et al., 2020, for a review). Photometrically they protrude as an additional Sérsic model on top of the galaxy's central surface brightness and exist in early- as well as late-type galaxies (Carollo et al., 1997; Böker et al., 2002; Côté et al., 2006). A visual example of an NSC is shown in Figure 3.15.

Essentially all galaxies with stellar masses of $10^9\,M_\odot$ host a NSC in their centers. A significant drop of the nucleation fraction for lower and higher mass galaxies than this characteristic mass is observed; the exact behavior is likely also dependent on environment (Sánchez-Janssen et al., 2019; Hoyer et al., 2021).

Just like galaxies, NSCs follow a mass-size relation. Their typical half-light radii are on scales of $1-10\,pc$ [75] (Böker et al., 2004; Côté et al., 2006). Their luminosity and mass scales with their Sérsic index as well as the host galaxy's stellar mass; lower mass NSC tend to be more flattened (Turner et al., 2012; den Brok et al., 2014; Georgiev & Böker, 2014). As the bulge mass scales with the overall stellar mass of the galaxy, so do NSCs (Balcells et al., 2003, 2007).

75: Thus, observations to reveal their inner structure are very challenging, and therefore rely on HST or adaptive optics (AO) assistance from the ground.

Furthermore, NSCs exhibit extended star formation histories (SFHs; e.g. Seth et al., 2006; Walcher et al., 2006; Rossa et al., 2006; Feldmeier-Krause et al., 2017a; Kacharov et al., 2018; Alfaro-Cuello et al., 2019), where often an older (several Gyr), redder component is more spherically distributed, while a younger (several 100 Myr), bluer component is more centrally concentrated (e.g. Seth et al., 2008; Carson et al., 2015; Feldmeier-Krause et al., 2015). This is accompanied with kinematic complexity in the form of varying rotational to random motion support (Seth et al., 2008; Feldmeier et al., 2014; Lyubenova & Tsatsi, 2019; Alfaro-Cuello et al., 2020; Pinna et al., 2021).

Yet, it is still unclear through which exact mechanism they form. The two most commonly proposed scenarios are: in-situ star formation from gas inflow (e.g. Seth et al., 2006; Bekki et al., 2006; Schinnerer et al., 2008; Aharon & Perets, 2015) and mergers of star cluster in-spiraling towards the galaxy's center (e.g. Lotz et al., 2001; Georgiev et al., 2009; Antonini et al., 2012; Gnedin et al., 2014; Arca-Sedda & Capuzzo-Dolcetta, 2014; Tsatsi et al., 2017). However, more recent studies show that likely both scenarios are contributing to NSC formation: GC in-spiral dominates at low galaxy masses, and in-situ formation at high galaxy masses, with a mix of both pathways for intermediate mass galaxies (e.g. Neumayer et al., 2011; Antonini et al., 2015; Guillard et al., 2016; Feldmeier-Krause et al., 2020; Do et al., 2020; Fahrion et al., 2021). This is based on arguments that the in-situ scenario should produce young ages and NSC metallicities similar or higher compared to the underlying host galaxy, while the GC in-spiral scenario should contribute older, more metal-poor stars to the center.

Apart from their own complex formation history, NSCs serve as tracers of other important processes in galaxy evolution. Firstly, they coexist and co-evolve with supermassive black holes (SMBHs; Wehner & Harris, 2006; Ferrarese et al., 2006b; Georgiev et al., 2016, and see next Section 3.3.3.6). This makes them an intriguing candidate, in which much needed seeds of supermassive black holes (SMBHs) could have formed (see e.g. Volonteri, 2010, for a review of the topic).

Secondly, they encode information about merger events in the stellar halo of galaxies, very similar to GC systems. If a nucleated satellite galaxy is accreted onto another galaxy, chances are high that the tightly bound nucleus survives the tidal forces[76] (e.g. Drinkwater et al., 2003; Pfeffer & Baumgardt, 2013; Seth et al., 2014). It then happily continues its life in its new host like the one in Figure 3.4.

In the Milky Way, the evidence that Omega Centauri, the most massive GC, is the nucleus of a formerly accreted galaxy is overwhelming due to its peculiar color magnitude diagram and retrograde orbit (Lee et al., 1999; Bekki & Freeman, 2003, e.g.). Furthermore, we observe the on-going disruption of the Sagittarius dwarf spheroidal galaxy (Ibata et al., 1994). At its center sits its NSC, M 54[77], which is also known for its complex stellar population composition (Siegel et al., 2007; Alfaro-Cuello et al., 2019). I will use M 54 in Chapter 5 as a laboratory for testing modelling techniques that can recover distributions in stellar population properties from integrated light alone (see Chapter 4). The robustness and reliability of such techniques has important implica-

76: These objects are then called ultra compact dwarf (UCD) galaxies, as they were observationally discovered as very luminous GCs-like objects (Hilker et al., 1999; Drinkwater et al., 2000). Note however that probably not all UCDs are stripped nuclei (Fellhauer & Kroupa, 2002).

77: Historically, M 54 was identified as a globular cluster (GC) of the Milky Way, because the faint stellar body of the Sagittarius dwarf is very hard to detect observationally.

tions for measuring past merger events in external galaxies (Boecker et al., 2020a).

3.3.3.6 *Supermassive Black Holes*

Supermassive black holes (SMBHs) sit at the center of (all ?) galaxies[78]. They are fundamentally different from the other presented galactic components. Because they are dark objects, like dark matter, we can only detect them through the influence they have on luminous matter (at least until very recently). For this we have essentially two options: 1) the SMBH is actively fed with baryonic matter, which creates all kinds of signatures across the electromagnetic spectrum, or 2) we can resolve the sphere of influence[79] in which the dynamics of (baryonic) matter is changed due to the presence of the SMBH.

Galaxies with option one are said to have an active galactic nucleus (AGN; Antonucci, 1993; Netzer, 2015); an example is shown in Figure 3.16. This class encompasses a variety of objects including quasars[80], AGN at high redshift that outshine their host galaxy and appear star-like (Schmidt, 1963), and Seyfert galaxies, AGN in low redshift galaxies with much lower energy outputs than quasars (Seyfert, 1943). The underlying mechanism in all these different objects are thought to be the same: gas is funneled to the center, which is accreted onto the black hole in a disk (Salpeter, 1964; Zel'dovich, 1964). This give rise to AGN feedback in the form of winds and jets (see also Figure 3.3), that not only influence the host galaxy, but can reach scales of Mpc (see Fabian, 2012, for a review). AGN feedback, especially in the less luminous, kinetic mode, is responsible for quenching the high mass end of the galaxy population from inside out (e.g. Silk & Rees, 1998; Springel et al., 2005c; Bower et al., 2006; Nelson et al., 2021; Eckert et al., 2021).

The best studied SMBH with option two is undoubtedly the Milky Way's (e.g. Ghez et al., 2008), as individual stars orbiting the black hole are resolvable. But even for external galaxies, dynamical models using integrated stellar light or gas as tracers are used to determine SMBH masses (see e.g. Thater et al., 2022, for the systematics involved). This has established important scaling relations between the mass of the SMBH and, for example, the mass of the bulge, the central velocity dispersion and the host galaxy's stellar mass (e.g. Häring & Rix, 2004; van den Bosch, 2016). These relations raised the question, if and how the SMBH and the center of galaxies co-evolve (see e.g. Kormendy & Ho, 2013, for a review).

It is widely accepted that SMBHs probably go through multiple phases of being dormant and active as an AGN. Furthermore, they can probably grow through two channels: gas accretion and merging with other SMBHs. It is, however, debated what the relative contribution of both of these channels is in growing the SMBH. At early epochs of the Universe, black hole growth and AGN activity is tied to galaxy mergers, which funnel gas to the center and/or bring their own black hole (Di Matteo et al., 2005; Hopkins et al., 2006, 2008). At lower redshifts ($z < 1$) the merger rate decreases, and thus a secular evolution for black hole growth is advocated by, for example, funneling gas into the center through bars (Cisternas et al., 2011).

78: The historic road of accepting SMBHs is equally as turbulent and recent as the standard cosmological model, which I highly recommend to read up on.

79: The radius of the sphere of influence (SOI) is

$$r_{SOI} = \frac{GM_\bullet}{\sigma^2},$$

where $M_\bullet$ is the mass of the SMBH and σ the central velocity dispersion.

Figure 3.16. Giant radio lobes created by the AGN of NGC 1316 (Fornax A). Credit: NRAO/AUI/NSF and J. M. Uson.

80: They are important tracers of the intergalactic medium and the reionization of the Universe. Their cosmic number density was highest around $z = 2$ (Richards et al., 2006). The most distance quasar ever detected is at $z \sim 7.5$ with a black hole mass of almost a billion solar masses, which calls for massive seeds (Bañados et al., 2018).

The relevance and mechanism of SMBH mergers is much less understood observationally. While on-going galaxy mergers with close nuclei and AGN activity are observed (Kollatschny et al., 2020), no direct SMBH merger was ever observed. This will hopefully drastically change in the next decade(s), since the discovery of gravitational waves gave us an entire new spectrum to probe (Abbott et al., 2016). Follow-up observations of the electromagnetic part already proved to be a powerful addition to understand the heavy element production in neutron star mergers (Abbott et al., 2017).

Together with star formation, the growth of SMBHs and the role of AGN feedback in quenching galaxies is perhaps one of the most challenging in galaxy formation, as these processes happen at sub-parsec scales but influence the scale of the galaxy and beyond (Springel et al., 2005a). In Chapter 7 I will touch upon the influence of SMBHs and their AGN feedback on the mass assembly of stars in the centers of galaxies.

3.4 ENVIRONMENT

Galaxies come rarely alone. The hierarchical structure formation as predicted by ΛCDM dictates that larger halos, and consequently galaxies, are build up from smaller ones. As mentioned throughout the previous sections, galaxy mergers can have various impact on the galaxy's evolution. They can trigger or end star formation causing morphological transformation and they are partially responsible for explaining scaling relations, such as the high-mass end of the mass-size relation. As the demographics of mergers have to be studied numerically, I will discuss them further in Chapter 6.

That said, mergers are not the only galaxy interaction that influence a galaxy's evolutionary pathway. The environment a galaxy lives in, i.e. if it is surrounded by many other galaxies (that are not necessarily merging with it) or not, also plays a vital role in transformation processes (see e.g. Boselli & Gavazzi, 2006, for a review). Because high density environments evoke a whole new list of physical processes, a galaxy's life can be drastically different than that of an equally sized galaxy in a low density environment. In fact, environmental processes will affect the majority of galaxies, as the structure of the Cosmic Web shows that most galaxies cluster together, whereas few live in Voids.

I therefore briefly discuss some observational clues we have about galaxy clusters as well as the mechanisms that drive galaxy transformations in such environments.

3.4.1 Galaxy Clusters

Gravitationally bound conglomerations of many galaxies are called galaxy clusters[81]. They can contain up to thousand or more galaxies. The baryonic budget is however dominated by a surrounding hot, diffuse, x-ray emitting gas, called the intracluster medium (ICM) (Cavaliere et al., 1971; Gursky et al., 1971; Rosati et al., 2002). The cluster's dark matter halo[82] naturally constitutes most of the mass, which can be reconstructed via gravitational lensing (e.g. Meneghetti et al., 2017). Their radial extent easily spans several megaparsec and the radial velocities of individual galaxies with respect to the cluster's center are on the order of 1000 km/s. This makes their two-body relaxation time[83] much larger than a Hubble time, meaning that galaxy clusters are typically dynamically young; they are just in the process of assembling (Mathiesen & Evrard, 2001). Thus many clusters are irregular in appearance and have multiple sub-groups of galaxies that are infalling and in the process of merging (Sarazin, 2002). Still a gravitational center can be identified, which often coincides with a giant elliptical galaxy surrounded by a large diffuse halo of intracluster light. This is called the central galaxy, which is, most of the time, also the brightest cluster galaxy (BCG). All other galaxies surrounding it are satellite galaxies.

The most notable nearby and earliest discovered cluster of "nebulae" is Virgo, with M 87 at its center and multiple sub-groups. Thus even before many thousands of clusters where catalogued (Abell, 1958; Abell et al., 1989), it was clear that early-type galaxies (including ellipticals and lenticulars) are predominantly found in cluster environments (Hubble & Humason, 1931; Melnick & Sargent, 1977; Dressler, 1980), as seen in Figure 3.17.

The richer the cluster, i.e. the more members it has, the typically fewer late-type galaxies are found (Oemler, 1974). More significantly even, early-types are concentrated towards the center of the cluster, whereas late-type spirals are predominantly found in the outskirts (Whitmore et al., 1993; Weinmann et al., 2006). This is accompanied by a decrease in SFR as function of clustercentric distance (Lewis et al., 2002; Goto et al., 2003).

Clusters at higher redshift show overall bluer galaxies than nearby clusters (Butcher & Oemler, 1978) often showing activity of (post) star bursts (Dressler & Gunn, 1983; Zabludoff et al., 1996; Dressler et al., 1999), but lacking significant amounts of red, ~ low-mass galaxies (De Lucia et al., 2007), especially lenticulars (Dressler et al., 1997). More recent studies show that the SFR is decreased for galaxies below $z \sim 1$ in high-density environments, while this is more dependent on galaxy mass and therefore less dependent on environment for galaxies at higher redshifts (e.g. Cooper et al., 2007; Darvish et al., 2016).

These findings suggest that especially lower to intermediate mass galaxies are transformed from the star-forming to the quiescent population by living or infalling into a high density environment. *What are the associated processes that drive this environmental quenching?*

81: These are sometimes called galaxy groups, if only a few tens of galaxies are together (or the total mass is below $\sim 10^{14}\,M_\odot$). For example, the Milky Way together with the Andromeda galaxy as well as both their satellite galaxies comprise the Local Group.

82: This does not mean that all galaxies are surrounded by one large dark matter halo. It is more thought of galaxies having their own dark matter (sub)halo that is embedded inside the cluster dark matter halo (see e.g. Kravtsov & Borgani, 2012, for a review). The latter is generally attributed to the most massive galaxy sitting at the gravitational center of the cluster.

83: The relaxation time can be approximated as

$$t_{relax} = \frac{N}{10 \ln N} t_{cross},$$

where N is the number of galaxies in a cluster and $t_{cross} = r/v$ the crossing time with typical radius r of the cluster and v the typical velocity of a galaxy within said cluster.

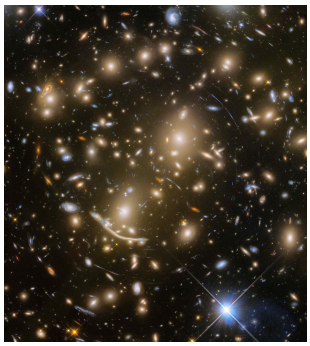

Figure 3.17. Abell 370, a galaxy cluster. **Credit**: NASA, ESA/Hubble, HST Frontier Fields

3.4.2 Transformational Processes

Due to the high relative velocities of galaxies in clusters, it is rather unlikely that the average galaxy in a cluster will merge with another. Still close encounters will have an effect on the passing galaxies, especially if they happen multiple times with the central galaxy. Disks of late-type galaxies are relatively fragile, more so if the galaxy has a low surface brightness and is more extended. This increases the tidal radius and therefore significant mass is lost during the encounter. Even if parts of the disk survive they are dynamically heated from the encounter and thus can transform to a galaxy more resembling ellipticals (Farouki & Shapiro, 1981; Moore et al., 1996, 1999).

Other processes involve the interaction of the galaxy's gaseous disk, i.e. the ISM, with the ICM. As soon as galaxies enter the cluster environment they are exposed to ram pressure (Gunn & Gott, 1972), which is a drag force exerted on the galaxy caused by its relative motion through the ICM. This causes the interstellar gas to be stripped opposite to the galaxy's velocity vector, while the stellar body remains largely undisturbed (Kenney & Koopmann, 1999). An example of such a process caught in the act is seen in Figure 3.18.

Figure 3.18. Example of a jellyfish galaxy, where ram pressure stripping is in process. The optical image is from HST overlaid with molecular gas emission measured by ALMA (Jáchym et al., 2019). The tails produce a new population of stars away from the galaxy main body. **Credit**: ALMA (ESO/-NAOJ/NRAO)

Indeed, observations find that spiral galaxies within the virial radius of the cluster are deficient in neutral hydrogen compared to field galaxies (Solanes et al., 2001). Simulations shows that ram-pressure is efficient in removing the majority of ISM, primarily gas at large galactrocentric distances (Larson et al., 1980; Abadi et al., 1999). If predominantly the hotter gas is stripped or amounts of cold gas closer to the galaxy's center is retained, the galaxy will continue to form stars until the gas is used up. This results in a gradual decrease in SFR (Balogh et al., 2000; van den Bosch et al., 2008b; Peng et al., 2015), which can, for example, explain the higher abundance of lenticular galaxies at low redshifts (Bremer et al., 2018).

While these environmental processes largely explain the cause of quenching for most galaxies, these studies show the need for other mechanisms acting at the highest galaxy mass end; because these galaxies were already quenched before infalling into the cluster. We already came across such a process capable of doing so, which is AGN feedback. Indeed, the most recent cosmological simulations with the implementation of a dual mode (kinetic + radiative) AGN feedback are able to reproduce the galaxy bimodality at the low *and* high mass end (Nelson et al., 2019b; Donnari et al., 2019, 2021a,b).

Finally, newest studies show that quenching occurring to satellites within a cluster is anisotropic with respect to their orientation to the central galaxy, which is producing AGN feedback. Satelllite galaxies along the minor axis of the central galaxy are less likely to be quenched, which is likely caused by the AGN feedback of the central carving out underdense regions in the ICM (Martín-Navarro et al., 2021a).

All in all, environmental quenching is important in explaining the red, low-mass galaxy population. This is good to keep in mind for studying the central mass assembly of galaxies in Chapter 7.

Part II

OBSERVATIONAL EFFORTS

4 GALAXY LIGHT

The light of galaxies that reaches us is comprised of a superposition of many, many stars. Thus, to understand galaxies we need to understand stars. To good approximation, stars are self-gravitating plasma spheres in hydrostatic equilibrium. Stars are born after a chain of complicated, physical processes: starting from the gravitational collapse of giant molecular gas clouds and ending with the ignition of hydrogen fusion in their interiors. Stars evolve after chains of more complicated physical events, in which their main sequence starting point and ultimate end are mostly dictated by their initial mass and chemical composition. However, apart from the Milky Way and a few other nearby ones, we cannot resolve the individual stars of galaxies. We thus need to treat light arriving from galaxies in an integrated sense, in which light contributions from different populations of stars are superimposed onto each other. I introduce how astronomers, who are interested in galaxies (like me), use the results of entire scientific fields that solely focus on providing models of (populations of) stars.

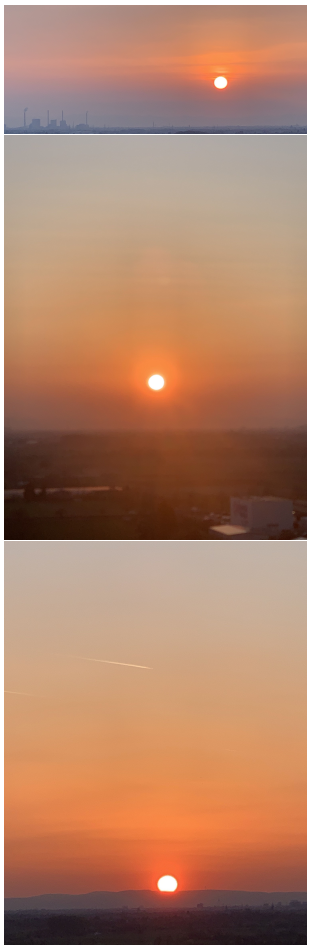

Figure 4.1. Our closest and perhaps most beautiful plasma sphere can be encountered regularly during evening strolls through the vineyards of Dossenheim. **Credit**: Alina Böcker.

Summary

The stellar light of galaxies is modelled as a superposition of many single stellar populations (SSPs), each of which have a distinct age and metallicity. The stars within a single SSP are born with masses distributed according to the initial mass function (IMF). As stars evolve, the light emitted by a SSP changes, as predicted by isochrones. Populating isochrones with spectra of stars generates SSP models. These models are used to infer, through various techniques, the star formation history and metal enrichment of galaxies, which provide important clues about how galaxies formed (see Chapter 3).

Contents

4.1 SINGLE STELLAR POPULATIONS

The implication of a "giant" star-forming gas cloud is that many stars form approximately at the same time with approximately uniform metallicity. This SSP forms the backbone of modelling any galaxy's stellar light[84] (Tinsley, 1979, 1980). The luminosity $L_\lambda(t, Z)$ per wavelength λ produced by such a population is:

$$L_{SSP,\lambda}(t, Z) = \int_{m_{min}}^{m_{max}} S_\lambda(m, t, Z)\phi(m)\, dm, \tag{4.1}$$

where S_λ is the luminosity of a single star with a given initial mass m, age t and metallicity Z and $\phi(m)$ describes how many stars where initially born in a single stellar population (SSP).

Many teams work on constructing SSP models (e.g. Bruzual & Charlot, 2003; Maraston, 2005; González Delgado et al., 2005; Le Borgne et al., 2004; Vazdekis et al., 2010, 2015, 2016; Eldridge et al., 2017; Maraston et al., 2020) and make them publicly available. I show some examples SSP models in Figure 4.2. To understand the amount of physics, considerations, assumptions and uncertainties involved in making these models I briefly walk through the three main ingredients that comprise Equation 4.1 (see also Conroy et al., 2009, 2010; Conroy & Gunn, 2010, for more details on uncertainties in stellar synthesis modelling).

84: This also includes galaxies in which individual stars are resolvable. Resolved color magnitude diagrams (CMDs) can be modelled by, for example, sampling individual stars from SSP models (e.g. Weisz et al., 2011; Gallart et al., 2019).

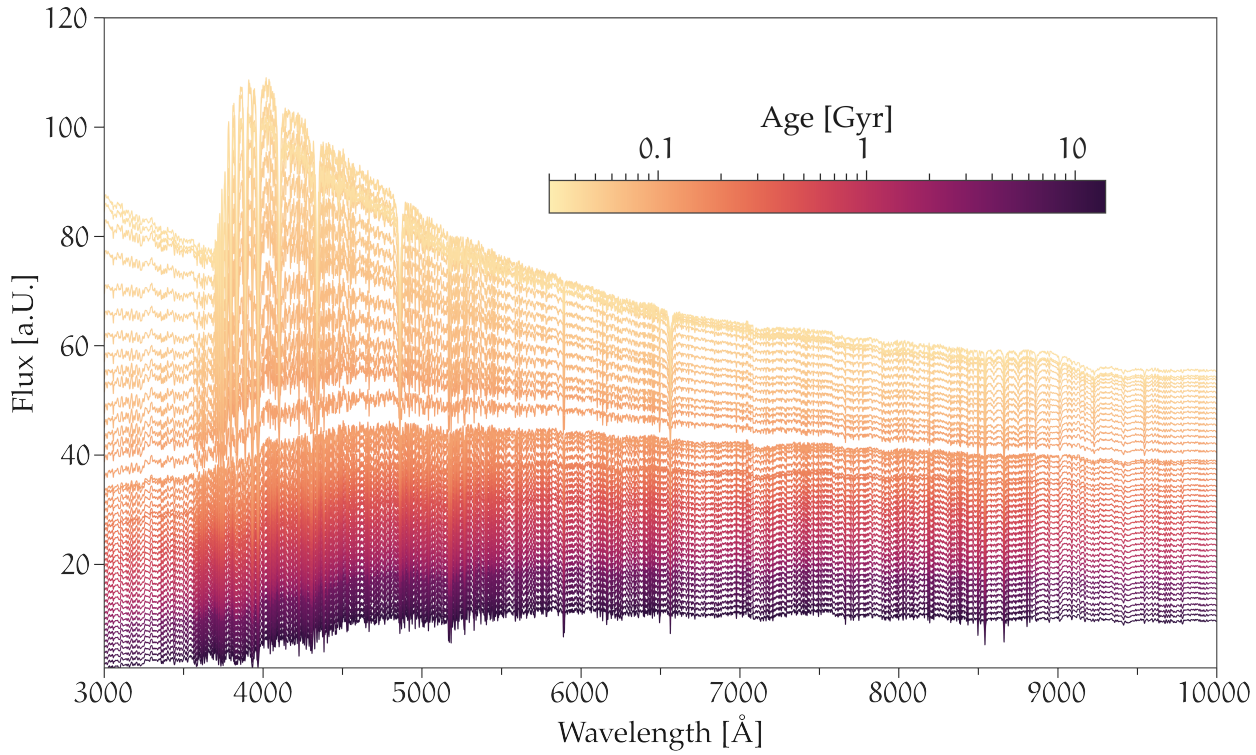

Figure 4.2. The E-MILES SSP models from (Vazdekis et al., 2016) for all available ages and solar metallicity. The biggest change in spectral shape is apparent in the first few hundred Myr, whereas old populations ($\gtrsim 8$ Gyr) emit approximately the same type and amount of light.

4.1.1 Initial Mass Function

The IMF $\phi(m)$ dictates how many stars of a given mass m form. The usual limits for the lowest and highest mass star formed are $m_{min} \simeq 0.08\,M_\odot$ and $m_{max} \simeq 100\,M_\odot$ respectively. The minimum mass is required so that hydrogen fusion takes place, while the maximum mass ensures stability against radiation pressure. Furthermore, it is practical to normalize the IMF, such that the total mass formed is one solar mass:

$$\int_{m_{min}}^{m_{max}} m\phi(m)\,dm = 1\,M_\odot \tag{4.2}$$

Observationally, the functional form of $\phi(m)$ can be determined by counting stars, which is only really possible in the Milky Way. Salpeter (1955) first found a power law[85] $\phi(m) \propto m^{-2.35}$ and subsequent studies a flattening, and perhaps even a turn-over, at the low mass end (Miller & Scalo, 1979; Scalo, 1986; Kroupa, 2001; Chabrier, 2003). Still, low mass stars are the most abundant in number, whereas the most massive stars dominate the luminosity density; similarly to the galaxy stellar mass function (GSMF).

Even though counting implies a rather simple task, multiple factors makes this effort indeed substantial. These include the non trivial conversion from observed apparent magnitudes to *initial* mass[86], accounting for stellar multiplicity, star formation history and selection effects[87] (Scalo, 1986; Kroupa et al., 1993).

Nevertheless, the shape of the IMF seems to be universal in the Milky Way (see e.g. Offner et al., 2014), however there is a debate on whether this universality is true for all galaxies (see e.g. Bastian et al., 2010). Measurements of the IMF in early-type galaxies, using either dynamical modelling (Cappellari et al., 2012) or applying SSP models to IMF sensitive absorption line features (van Dokkum & Conroy, 2010), show that the universality might not hold. Both studies find a bottom-heavy IMF, i.e. more low mass stars are present compared to the canonical form (see also Conroy & van Dokkum, 2012b, for the same conclusion from full spectral fitting methods).

There is further evidence that the IMF varies as a function of radius (e.g. Martín-Navarro et al., 2015a) advocating that the local and galaxy-wide IMF have different forms (Jeřábková et al., 2018). Furthermore, the slope of the IMF depends on metallicity (Martín-Navarro et al., 2015b, 2019), where higher metallicity regions, i.e. typically in the centers of galaxies, display a more bottom-heavy IMF. Theoretically, the fragmentation and collapse of gas clouds is indeed dependent on metallicity, as higher metallicity gas can cool more efficiently (Larson, 2005). On the other hand, some other studies (van Dokkum, 2008) suggest a top-heavy IMF at high redshifts, as the rate of star formation was higher. I show some examples for the form of the IMF in Figure 4.3.

In conclusion, the shape of IMF is not at all understood, which can impact the inferred ages and metallicities of the underlying stellar populations. However, we still think that this effect is secondary and there-

85: Often the logarithmic form is used, which has a slope of 1.35.

86: This includes accounting for extinction by dust, knowledge of the distance and stellar evolution. Good distance/parallax measurements are usually confined to the solar neighbourhood.

87: For example, the Galactic bulge and disk have different star formation histories. High mass stars are usually found in associations and young clusters. Stars in globular clusters (GCs) are affected by dynamical interactions, which can lead to the ejection of stars.

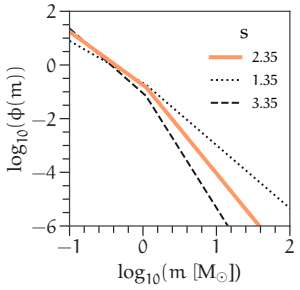

Figure 4.3. Examples of a bimodal IMF according to Vazdekis et al. (1996). The high mass slope $s = 2.35$ is the "canonical" choice (*thick orange line*). Bottom- (*dashed*) and top-heavy (*dotted*) versions are also shown.

fore often adopt the canonical form, i.e. a Salpeter high mass slope with a flattening at the low mass end.

4.1.2 Isochrones

Stars occupy certain regions in color-magnitude space depending on their current evolutionary state. Hertzsprung (1911) and Russell (1914) first systematically constructed such diagrams using the spectral classification of stars. Depending on the surface temperature[88] of the stars, different elements and molecules are in different ionization states giving rise to characteristic absorption features. Eddington (1926) first explained how these observations are linked to the stars's interiors, where energy is produced via nuclear fusion. Subsequently, the production of essentially all heavy elements could be tied to stellar evolution (Weizsäcker, 1935; Bethe, 1939; Hoyle, 1946, 1954; Burbidge et al., 1957; Hoyle & Fowler, 1960; Clayton et al., 1961; Seeger et al., 1965).

In short (see e.g. Salaris & Cassisi, 2005, for a long explanation), more massive stars evolve more quickly, because they are more efficient at nuclear fusion. They quickly move off the main sequence and explode as supernovae type II. Sun-like stars have a main sequence lifetime of around 10 Gyr[89] until they exhaust hydrogen in their cores, expand and become red giants. The lowest mass stars can have lifetimes larger than the age of the Universe.

The full traversal of a star with a given initial mass and metallicity through the Herzsprung-Russell diagram is described by stellar evolutionary tracks[90]. There are many teams working on computing these tracks, make them publicly accessible as well as update them on a regular basis (e.g. Girardi et al., 2000; Yi et al., 2001; Pietrinferni et al., 2004; Dotter et al., 2008; Bressan et al., 2012; Choi et al., 2016). They can differ quite substantially among different groups due to different ingredients and treatments of the underlying physical processes. This is a result of our limited knowledge of, for example, mass loss rates at late evolutionary stages (Miller Bertolami, 2016) and the overall effect of individual element abundances (VandenBerg et al., 2012). Observations of such stars were quite limited, because a) stars evolve quickly through their last stages and b) they were only feasible in the solar neighbourhood. Only recently, with the Gaia satellite, did astronomers obtain a new, unprecedented look at the Herzsprung-Russell diagram (Gaia Collaboration et al., 2018b).

For a population of stars, it is more useful to understand where stars with the same metallicity but different masses lie in the Herzsprung-Russell diagram at a fixed time. This is called an isochrone and it can be constructed from the stellar evolutionary tracks (Dotter, 2016). I show some examples of isochrones in Figure 4.4. At age zero all stars of a given single stellar population lie on the main sequence. As time moves on, stars will move off the main sequence starting with the most massive, i.e. hottest and most luminous stars. Consequently, a stellar population will become redder and less luminous with increasing age.

88: Or effective temperature. It is defined as the temperature of perfect black body with the same total luminosity as the measured star. Hence, the coolest stars appear red, whereas the hottest ones are blue in color.

89: so we have 5.4 Gyr more to go - phew.

90: i.e. how a star's luminosity L and effective temperature T_{eff} changes as a function of time

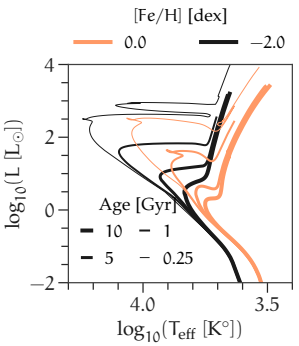

Figure 4.4. Dartmourth isochrones from Dotter et al. (2008) with varying ages and two different metallicities. All have a scaled-solar α-abundance.

This produces the main sequence turn-off point, which puts stringent constraints on the age of resolved stellar populations[91]. At fixed age, a lower metallicity will produce bluer stellar populations and isochrones, as stars are not affected by metal line blanketing (Milne, 1928; Przybylski, 1957; Sandage & Eggen, 1959). When we combine the IMF with a given isochrone, we understand how many stars of the corresponding initial mass produce how much luminosity at their current stage (and how many have already become remnants, which usually include stellar mass black holes, neutron stars and white dwarfs). Integrating over all stars yields the total luminosity of a stellar population at a given age and metallicity.

91: This is particularly useful for GCs, as all the stars approximately lie at the same distance and thus the apparent magnitude can be used.

4.1.3 Stellar Spectra

However, in reality we never truly observe the total bolometric luminosity of a system. We either record the integrated flux through some filter or its spectrum. Thus, at every point on a given isochrone we need to know the luminosity of stars as a function of wavelength $S_\lambda(m, t, Z)$. Populating the Herzsprung-Russell diagram with such stellar spectra is a tremendous task and can be done either with observations and/or theoretical calculations. Both have their (dis)advantages, which I briefly outline below.

4.1.3.1 *Empirical Libraries*

Empirical stellar spectra (e.g. Pickles, 1998; Cenarro et al., 2001; Prugniel & Soubiran, 2001; Le Borgne et al., 2003; Valdes et al., 2004; Sánchez-Blázquez et al., 2006; Yan et al., 2019; Verro et al., 2021) inherit instrumental characteristics of the spectrograph they were obtained with, which are mainly the wavelength coverage and the spectral resolution. Furthermore, the spectra have to be reduced to account for systematics created by the Earth's atmosphere and the optics system. Then, a mapping between the physical atmospheric parameters of the star, which are the luminosity L[92], effective temperature T_{eff} and metallicity Z (and possible other abundances such as [α/Fe]), and the observed quantities have to be found. This is not straightforward and many techniques exist (see e.g. Vazdekis et al., 2010; Maraston et al., 2020, for some overview). Lastly, the solar neighbourhood, in which accurate, individual stellar spectra are available, only samples a limited parameter space of these atmospheric parameters. This makes it tricky to sufficiently populate isochrones of many different ages and metallicities.

92: or surface gravity $g = \frac{GM}{r^2}$, where M and r are the mass and radius of the star respectively.

4.1.3.2 *Theoretical Libraries*

Theoretical stellar spectra (e.g. Kurucz, 1979; Lejeune et al., 1997; Westera et al., 2002; Husser et al., 2013; Coelho, 2014) essentially eliminate all the drawbacks of empirical spectra, of which I show three examples in Figure 4.5. However, replicating spectra of real stars is hard due to the complexity and manifold of physical processes involved. To model

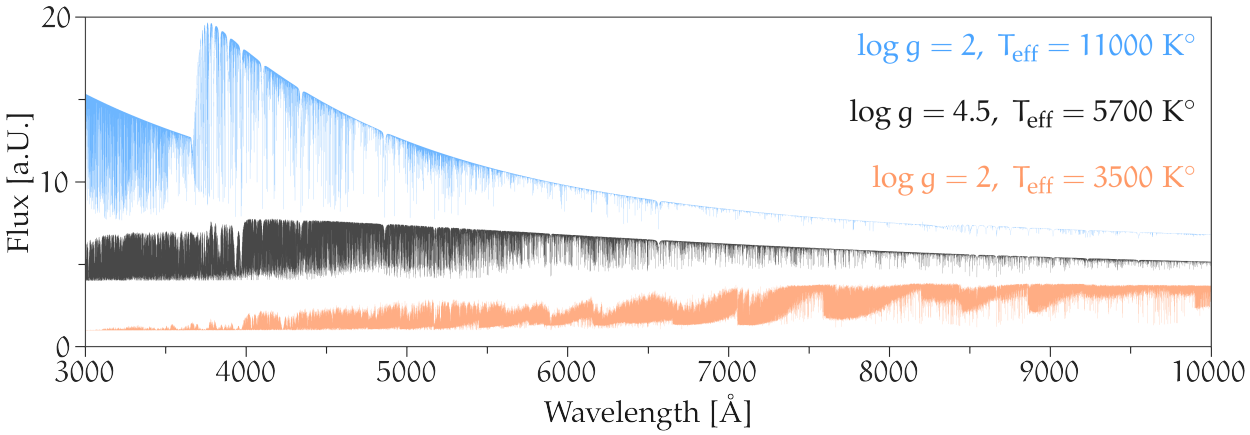

Figure 4.5. The Phoenix theoretical stellar spectra at full resolution for three combinations of the surface gravity g and effective temperature T_{eff} from Husser et al. (2013). All spectra have solar metallicity.

stellar atmospheres it is necessary to know several million atomic and molecular line transitions (e.g. Kurucz, 1970), as well as how the different energy levels are populated according to a given temperature, and ultimately how the radiation is transferred through the star (see e.g. Mihalas, 1978; Hubeny & Mihalas, 2014, for more background). Especially, when simplifying assumptions about the geometry and local thermodynamic equilibrium are dropped, this quickly also becomes a problem of computation power.

4.2 INTEGRATED LIGHT

Galaxies form many SSPs throughout their lifetime with varying SFRs and gradually enriched in metals. The latter can be modelled via the metallicity distribution function (MDF) at a given time t. Thus, the integrated spectrum of a galaxy[93] $L_{Galaxy,\lambda}$ can be expressed as:

$$L_{Galaxy,\lambda} = \int_{t_{min}}^{t_{max}} \int_{Z_{min}}^{Z_{max}} SFR(t)\, MDF(Z,t)\, L_{SSP,\lambda}(t,Z)\, dt\, dZ. \quad (4.3)$$

93: modulo extinction, various emission lines and convolution with the line-of-sight velocity distribution.

This is then solved for SFR(t) and MDF(t) taking into account other parameters, such as redshift, dust absorption, various sources[94] of emission. The upper and lower limits of t and Z depend on the underlying SSP models, as they are computed only for specific values of ages and metallicities. We will see in Chapter 9, how this can become problematic.

94: e.g. from dust, star formation or AGN activity.

In the literature, many methods exist to accomplish the task of solving Equation 4.3 encompassing varying levels of complexity (see e.g. Conroy, 2013, for a review). Overall, more importance has been given to deriving the SFH, i.e. SFR as a function of time. Determining this alone can already be highly degenerate, i.e. many different model combinations can fit the data equally well. Thus, the chemical evolution is often neglected and assumed to be constant over time for the sake of reducing the number of free parameters. In the end, the exact approach depends on the type and quality of data available.

4.2.1 Spectral Energy Distribution

The spectral energy distribution (SED) of a galaxy corresponds to many photometric measurements in different wavelength bands. Thus, to model the SED of a galaxy, Equation 4.3 is integrated over the corresponding filter response functions.

Today's large photometric surveys provide magnitudes of many galaxies in a lot of different bands, from UV to IR and beyond. The wide wavelength coverage is an advantage in constraining the influence of many different physical processes. For example, the UV is very sensitive to young stars, whereas the IR constrains the relevance of dust absorption and emission. However, this cannot resolve individual spectral lines, which makes it tricky to reliably estimate the redshift (see e.g. Salvato et al., 2019, for a review).

Perhaps one of the primary goals of these types of studies is to determine the stellar mass (i.e. the time integral of the SFR) for many galaxies at many different redshifts. The derived stellar mass can vary significantly depending on the form that is assumed to model the star formation history (SFH). Parametric models[95] are intrinsically easier, but are often a poor representation of a galaxy's true SFH (e.g. Carnall et al., 2019). Non-parametric models are the better choice naturally, but difficult to constrain due to their flexibility (e.g. Leja et al., 2019). State-of-the-art codes employ Bayesian methods to efficiently sample and constrain this multidimensional parameter space (e.g. Chevallard & Charlot, 2016; Leja et al., 2017; Carnall et al., 2018; Johnson et al., 2021).

95: These can be, for example, τ-models, in which the SFH is an exponentially declining function with an e-folding time of τ.

4.2.2 Indices

Indices of a galaxy's integrated spectrum represent the integrated flux over certain absorption line features normalized by narrow bandpasses in the neighbouring continuum[96]. The sensitivity of absorption features differs according to changes in age, metallicity, individual element abundances and the IMF of the underlying stellar populations[97]. Thus, the right combination of indices can disentangle the contribution of these effects more accurately than broad band measurements. A standardized system of indices was first introduced by Worthey et al. (1994); Worthey & Ottaviani (1997); Trager et al. (1998), which is referred to as the Lick/IDS system, and is expanded upon in numerous studies (e.g. Vazdekis et al., 1996; Trager et al., 2000a; Thomas et al., 2003; Schiavon, 2007).

Because galaxies can have a significant velocity dispersion, which changes the broadening of the absorption lines, the model indices have to be convolved accordingly. Many studies using line indices found a correlation between the velocity dispersion of the galaxy (which can act as a proxy for its dynamical mass) and its α-abundance as well as the slope of the IMF (e.g. Thomas et al., 2005; La Barbera et al., 2013; Martín-Navarro et al., 2018a, 2019).

96: This is defined as the equivalent width.

97: For example, Balmer lines and the 4000 Å break are sensitive to age (Poggianti & Barbaro, 1997), whereas TiO is sensitive to the IMF (Spiniello et al., 2014; La Barbera et al., 2016).

A drawback of indices is that they provide luminosity weighed average quantities of stellar population parameters. Even more severe, some studies use SSP-equivalent ages and metallicities, i.e. they do not consider the fact that a galaxy's spectrum consists of multiple populations. Especially the resulting ages are significantly biased towards the youngest population present in the integrated light (Trager & Somerville, 2009), because they dominate the light.

4.2.3 Full Spectral Fitting

This technique fits the whole integrated spectrum of a galaxy. Due to the large amount of available data points ($\gtrsim$ 1000), studies usually include chemical evolution (Cid Fernandes et al., 2005; Ocvirk et al., 2006b; Cappellari, 2017; Wilkinson et al., 2017) and more complex shapes of the line-of-sight velocity distribution (Cappellari & Emsellem, 2004; Ocvirk et al., 2006a). Nevertheless, the parameter space of different ages and metallicities can be of the same order, which makes it computationally expensive (even without full Bayesian approaches) as well as degenerate.

These methods are still historically young compared to SED modelling and absorption indices, as only fairly recently integrated spectra became available for large quantities of galaxies with sufficient quality and spectral resolution. Thus, their reliability in recovering full age-metallicity distributions of galaxies is not well understood, especially with regard to assumptions in the stellar population models and wavelength coverage. The next part of the thesis is devoted to address this.

RECOVERY OF AGE-METALLICITY DISTRIBUTIONS

5

The integrated spectra of galaxies encode information about their underlying stellar populations, which act as a fossil record (see Chapter 3). The true power in understanding how individual galaxies form, stems from the knowledge of the *distribution* of ages and metallicities that characterize the galaxy's stellar populations. Traditionally however, only average stellar populations quantities are derived from integrated spectra. Thus, we are missing the opportunity to extract the full formation history of thousands of galaxies for which high quality integrated spectra are available. *But how well is the method of recovering age-metallicity distributions from integrated spectra working really?* I provide an answer this question by performing several tests on a nearby system, where the age and metallicities of individual stars are known, to pave the way for future applications on large samples of galaxies.

The contents of this Chapter were published in a similar form in the Astrophysical Journal under Boecker et al. (2020b). The contributions from the authors are as follows:

Me I directed and conducted the research in this study, incorporated comparisons with additional data, made all the plots and wrote the text of the manuscript.

Mayte Alfaro-Cuello made all the results of her analysis of the individual stars available and provided comments on the draft.

Nadine Neumayer provided the original idea of this project, contributed with regular meetings about the intermediate results and status of this study and provided comments on the draft.

Ignacio Martín-Navarro discussed the contents of this paper with me regularly during his stay at MPIA and provided comments on the draft.

Ryan Leaman brought up the importance of investigating the horizontal branch stars, discussed with me the results throughout this project, gave the idea for Figure 5.10 and provided extensive comments on the draft.

Summary

Current instruments and spectral analysis programs are now able to decompose the integrated spectrum of a stellar system into *distributions* of ages and metallicities. The reliability of these methods have rarely been tested on nearby systems with resolved stellar ages and metallicities. Here we derive the age-metallicity distribution of M 54, the nucleus of the Sagittarius dwarf spheroidal galaxy, from its integrated MUSE spectrum. We find a dominant old ($8-14$ Gyr), metal-poor (-1.5 dex) and a young (1 Gyr), metal-rich (+0.25 dex) component - consistent with the complex stellar populations measured from individual stars in the same MUSE data set. There is excellent agreement between the (mass-weighted) average age and metallicity of the resolved and integrated analyses. Differences are only 3% in age and 0.2 dex metallicitiy. By co-adding individual stars to create M 54's integrated spectrum, we show that the recovered age-metallicity distribution is insensitive to the magnitude limit of the stars or the contribution of blue horizontal branch stars - even when including additional blue wavelength coverage from the WiFeS Atlas of Galactic Globular cluster Spectra (WAGGS) survey. However, we find that the brightest stars can induce the spurious recovery of an old ($>$ 8 Gyr), metal-rich (+0.25 dex) stellar population, which is otherwise not expected from our understanding of chemical enrichment in M 54. The overall derived stellar mass-to-light ratio of M 54 is $M/L_V = 1.46$ with a scatter of 0.22 across the field-of-view, which we attribute to the stochastic contribution of a young, metal-rich component. These findings provide strong evidence that complex stellar population distributions can be reliably recovered from integrated spectra of extragalactic systems.

Contents

5.1 INTRODUCTION

Analyzing ages and metallicities or other chemical abundances of any stellar systems give us insight into their assembly history. Galaxies and other stellar objects (e.g. NSCs, see Neumayer et al., 2020, for a review) are assembled by a combination of in-situ secular processes such as star formation, as well as ex-situ accretion of other systems. The varying relative contribution of these two processes will lead to complex stellar populations, thus detecting and quantifying their distribution in age and metallicity is crucial to understand how galaxies and other stellar systems assemble their stellar mass.

Deep CMDs still count as the most reliable and detailed view that we can obtain about stellar populations present in any stellar system. Spectroscopic follow-up studies of the individual stars can then also provide radial velocities and chemical abundances. Resolved CMD analysis however automatically restricts us to within the Local Group ($\lesssim 1$ Mpc), as greater distances make it impossible to resolve stars at or below the main sequence turn-off, where most of the age information lies. As an example, the most detailed studies of stellar populations in NSCs are restricted to the nearby ones in the center of the Milky Way (MW: Do et al., 2009, 2013; Feldmeier et al., 2014; Feldmeier-Krause et al., 2015, 2017a,b) and the Sagittarius dwarf spheroidal galaxy (M 54: Siegel et al., 2007; Bellazzini et al., 2008; Alfaro-Cuello et al., 2019, 2020).

Because integrated broad band colors are severely prone to age-metallicity-reddening degeneracies (e.g. Worthey, 1994; Carter et al., 2009), integrated spectra present our most detailed view of unresolved stellar systems, as different absorption lines as well as the shape of the stellar continuum respond more sensitively to age and abundance pattern changes (Sánchez-Blázquez et al., 2011). With the advancement in sensitivity, wavelength coverage and spectral resolution of spectrographs (e.g. XShooter: Vernet et al., 2011) or the new generation of integral-field units (e.g. MUSE: Bacon et al., 2014), the analysis of integrated spectra is changing from line strength analysis (e.g. Worthey, 1994; Worthey & Ottaviani, 1997; Thomas et al., 2003, 2005; Trager et al., 2000a,b) to fitting the whole observed spectrum maximizing the information present in each spectral pixel (e.g. Cid Fernandes et al., 2013; Wilkinson et al., 2015; McDermid et al., 2015; Comparat et al., 2017; Goddard et al., 2017; Chauke et al., 2018; Kacharov et al., 2018).

Even though integrated line strength analysis is still crucial in understanding certain (galaxy) features sensitive to specific spectral lines such as the IMF or individual α-element abundances (e.g. Martín-Navarro et al., 2018a, 2019), it has been shown that SSP equivalent ages and metallicities are biased towards the youngest stellar population present in the integrated light (e.g. Serra & Trager, 2007; Trager & Somerville, 2009). With full spectral fitting methods however, we are slowly moving towards uncovering the whole chemical enrichment history of a stellar system by fitting a linear combination of multiple SSP models to the observed spectrum. Yet, the techniques necessary to not only recover mean ages and metallicities, but also a *distribution* in that pa-

rameter space (e.g. Cappellari & Emsellem, 2004; Cid Fernandes et al., 2005; Ocvirk et al., 2006a,b; Cappellari, 2017; Wilkinson et al., 2017) are still under development. On top of that, additional factors influencing their performance, e.g. the wavelength coverage or spectral resolution are also not well understood yet. However, deriving age-metallicity distributions are crucial in deciphering the mass assembly of extragalactic systems (e.g. Boecker et al., 2020a).

Given these challenges, it would be beneficial to study resolved and integrated spectra of the same system to test the reliability of age-metallicity distribution recovery with full spectral fitting methods. Here, we utilize the richness of the $3.5' \times 3.5'$ MUSE (Bacon et al., 2014) data set of M 54, the nucleus in the Sagittarius dwarf spheroidal galaxy, in order to apply the full spectral fitting to its integrated spectrum aiming to recover its multiple populations and compare the results to the resolved study of the same data set (Alfaro-Cuello et al., 2019). With respect to similar comparisons between resolved and integrated SFHs (Ruiz-Lara et al., 2015, 2018), our advantage lies in the power of the MUSE instrument (see also Kuncarayakti et al., 2016): a) the two approaches are performed using the same data, which means that possible instrumental effects stay the same, b) the metallicity of each star can be directly derived from its individual spectrum, which are regarded intrinsically more reliable than photometric metallicities and thus reduce degeneracies further, when stellar ages are determined from isochrone fitting.

This Chapter is organized as follows: in Section 5.2 we present the three different IFU data sets analyzed in this work and briefly describe the analysis of the resolved stars from Alfaro-Cuello et al. (2019); in Section 5.3 we describe our analysis method of deriving age-metallicity distributions from integrated spectra; in Section 5.4 we show the results of this technique in dependence of different integrated spectra of M 54; in Section 5.5 we compare our integrated analysis method with the resolved star analysis; in Section 5.7 we discuss our results and in Section 5.8 we give our conclusions of this comparison exercise.

5.2 IFU DATA OF M 54

In this Section we briefly describe the data we use to analyze the stellar populations of M 54 from its integrated spectrum. While our comparison between resolved and integrated stellar population extraction is focused on the MUSE wide field mode (WFM) data from Alfaro-Cuello et al. (2019), we also include data from the MUSE WFM-AO science verification and the publicly available WAGGS (Usher et al., 2017) survey exploiting different instrument systematics like wavelength coverage and spectral resolution. In Figure 5.1, we show the pointings on M 54 of the three data sets as an overview.

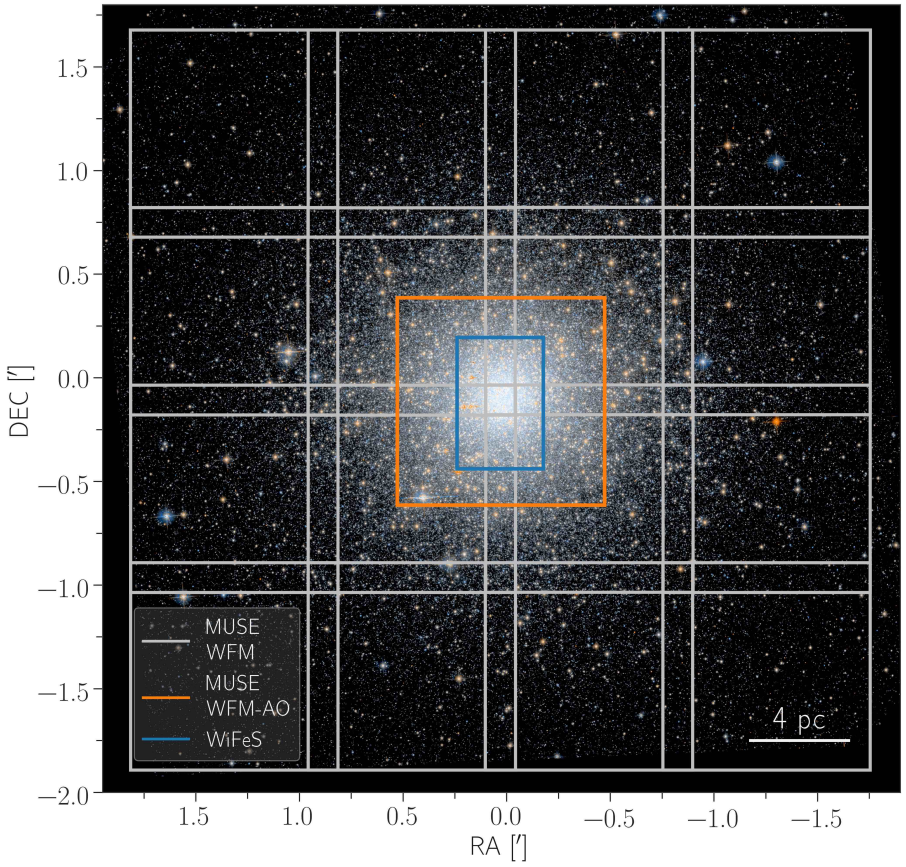

Figure 5.1. Color image from HST ACS/WFC in the F606W & F814W filters (Sarajedini et al., 2007) of M 54 overlaid with the pointings of the three integral field unit data sets used in this work: MUSE WFM (light grey), MUSE WFM-AO (orange) and WiFeS (blue).

5.2.1 MUSE WFM

Alfaro-Cuello et al. (2019) analyzed a 4×4 MUSE mosaic centered on M 54 (095.B-0585(A), PI: Lützgendorf) covering a total area of $3.5' \times 3.5'$, which corresponds to an extension of about 2.5 times the cluster's effective radius ($r_{eff} = 0.82' \hat{=} 6.78$ pc (Harris, 1996, 2010 edition) at a distance of 28.4 kpc (Siegel et al., 2011)). MUSE is an integral field spectrograph, mounted on the UT4 of the Very Large Telescope at the Paranal Observatory in Chile. It has a wavelength coverage of $4750 - 9300$ Å with 1.25 Å/pix sampling and a mean spectral resolution of ~ 3000. More information about the observing strategy and data reduction can be found in Alfaro-Cuello et al. (2019).

To derive individual ages and metallicites for the member stars of M 54 and identify multiple populations, Alfaro-Cuello et al. (2019) performed five essential steps, which are stated here in short for clarity:

1. Extract individual spectra of the resolved stars with a wavelength dependent PSF-weighting technique (PampelMuse: Kamann et al., 2013) by using a photometric reference catalogue from HST (Siegel et al., 2007). All spectra with a signal-to-noise ratio (SNR) < 10 are excluded from further analysis. This corresponds to a limiting magnitude of $I = 22$ mag, which includes stars just below the turn-off region.

2. Fit all extracted spectra with a full spectral fitting software (ULySS:

Koleva et al., 2009) and a stellar model library (ELODIE 3.2: Wu et al., 2011) to determine atmospheric parameters (T_{eff}, log g, [Fe/H]) and the radial velocities. This was done for the wavelength range of $4750 - 6800$ Å.

3. Determine member stars of the cluster by using an iterative expectation maximization technique (clumPy: Kimmig et al., 2015) based on the position and the radial velocity measurement of each star. Stars with a membership probability of $\geqslant 70\%$ are considered to belong to M 54.

4. Estimate individual stellar ages by fitting scaled-solar isochrones (from the Dartmouth Steller Evolution Database: Dotter et al., 2008) using HST photometry (F606W & F814W filters) and their spectroscopically derived iron abundances within a Bayesian framework. Horizontal branch stars were excluded from this.

5. Perform Gaussian mixture models in the derived age-metallicity parameter space to determine the most likely number of distinct stellar populations present in M 54 as well as the probability of each member star belonging to one of those populations.

5.2.2 MUSE WFM-AO

MUSE WFM is also offered with ground layer adaptive optics correction by the Ground Atmospheric Layer Adaptive Corrector for Spectroscopic Imaging (GALACSI) module aimed to double the ensquared energy in one $0.2' \times 0.2'$ spaxel as compared to natural seeing. Due to the four laser guide stars the wavelength range around the NaD lines ($5820 - 5970$ Å) is blocked. We include the analysis of MUSE WFM-AO science verification data (60.A-9181(A), PI: Alfaro-Cuello) of M 54 investigating, whether the Na notch filter has an influence on the stellar population inference. The data consists of a single, central $1' \times 1'$ pointing.

5.2.3 WAGGS survey

MUSE does not cover blue wavelengths short of 4750 Å, which is often raised as caveat (see planned BlueMUSE: Richard et al., 2019), since it is commonly understood that young stellar populations (< 1 Gyr) or certain stellar evolutionary stages, such as horizontal branch stars, dominate at these bluer wavelengths (< 4000 Å). It also misses other important spectral lines like the CaH & K lines, at 3969 Å and 3934 Å respectively, which are particularly sensitive to metallicity changes at fixed temperature. Therefore their potential contribution to the overall integrated light might not be significant enough in the MUSE wavelength range. To test this, we additionally analyze the integrated spectrum of M 54 from the WAGGS survey (Usher et al., 2017).

The goal of the survey is to provide a library of GC spectra in the Milky Way and its satellite galaxies with a higher resolution (R ~ 7000) and wider wavelength coverage (3270 – 9050 Å) than other studies to investigate their stellar populations in detail. For this purpose, they utilize Wide Field Spectrograph (WiFeS), a dual arm integral field spectrograph, on the Australian National University 2.3m telescope at the Siding Spring Observatory, which has a field of view of 38″ × 25″, hence targeting the center of the GCs. The spectrograph offers four, high resolution gratings, U7000 (3270 – 4350 Å with 0.27 Å/pix), B7000 (4170 – 5540 Å with 0.37 Å/pix), R7000 (5280 – 7020 Å with 0.44 Å/pix) and I7000 (6800 – 9050 Å with 0.57 Å/pix) in order to achieve the large wavelength coverage. For more information about the observing strategy and data reduction see Usher et al. (2017). The integrated spectra for all their observed GCs are publicly available on their website[98].

98: https://aat.anu.edu.au/surveys/waggs

As the spectra from WAGGS consist of four parts corresponding to the four gratings, we determine the new flux in the overlapping regions as the error weighted mean in order to generate one continuous spectrum. The corresponding new inverse error in that region is the mean of the inverse of the two overlapping error spectra. Then we re-sample the entire spectrum to the highest pixel dispersion of 0.57 Å/pix (using SpectRes: Carnall, 2017).

5.3 METHOD FOR ANALYZING AN INTEGRATED SPECTRUM

In this Section, we briefly describe our approach of full spectral fitting and how multiple stellar populations in age-metallicity space can be derived from an integrated spectrum. In theory, there are only two ingredients needed: a single stellar population spectral library and a fitting machinery that fits the models to the data.

5.3.1 Full spectral fitting method

We can extract stellar populations properties from an integrated spectrum by viewing the integrated light as a linear combination of many single stellar populations, each with a different, single age and metallicity[99]. Hence, the full spectral fitting algorithm finds the optimal weight for each SSP spectrum, such that their sum best represents the observed integrated spectrum. Since SSP models are normally normalized to one solar mass, the best-fit weights are mass fractions.

99: Here, we keep the IMF and heavy element abundance fixed.

Due to the vast parameter space of the SSPs (typically > 500 models) and the typical age-metallicity degeneracy, this inverse problem is usually ill-posed and ill-conditioned. In our case, ill-posed means that the solution is not necessarily unique, as many different SSP combinations can represent the data equally well. Ill-conditioned refers to the fact that fluctuations on the noise-level in the data can drastically change the solution. Regularized least-squares minimization is a common way to treat both of these issues. This technique is also implemented in the program penalized pixel fitting (pPXF) (Cappellari & Emsellem, 2004;

Cappellari, 2017), which we will use in this study. It has the advantage of being able to derive two dimensional age-metallicity distributions, which is not the case for other fitting algorithms that use similar approaches (e.g. STECKMAP: Ocvirk et al., 2006a,b).

In the context of pPXF, regularization provides a way to smoothly link the sparsely returned unregularized mass fractions in age-metallicity space until a certain criterion on the data fidelity is met. This smoothing may be well motivated in the case of galaxies, where we assume that chemical enrichment does not likely occur in a discrete manner. However, if the solution requires a more bursty star formation history, and the data quality is high enough, regularization will allow for that as well (Cappellari, 2017).

How *much* the weights become smeared out is controlled by the regularization parameter (λ), whereas the *way* they are distributed is imposed by the regularization matrix ($\mathbf{B}$), which is typically a finite difference operator. We note that we use the first finite difference ($\mathbf{B} = \mathrm{diag}(1, -1)$) throughout this work, however we made sure that the second and third order one give consistent results (see e.g. Ocvirk et al., 2006a; Huang et al., 2016a; Kacharov et al., 2018; Boecker et al., 2020a).

In any case, the essential pPXF fitting procedure is always the same, which follows the instruction in the source code of pPXF as well as Press (2007, Chapter 19.5). First, an unregularized fit is performed in order to re-scale the noise vector, such that this fit has a reduced χ^2 of unity. Then regularized fits are performed, tuning the regularization parameter such that the χ^2 of the regularized fit moves one standard deviation away, which corresponds to $\sqrt{2 \cdot \#\mathrm{pixel}}$. This sets a regularization parameter, which allows for a maximum amount of smoothness that is still regarded to be consistent with the data (see e.g. McDermid et al., 2015; Kacharov et al., 2018; Boecker et al., 2020a).

Before the first fit, we conduct the following, preparatory steps: SSP models are broadened to the wavelength-dependent line spread function (LSF) of MUSE[100], as the SSP models have slightly higher spectral resolution in the blue part of the spectrum than MUSE. In case of the WAGGS spectrum, we broaden the observed spectrum to a constant full width at half maximum (FWHM) of 2.5 Å, which is the approximate average spectral resolution of MUSE. After that the wavelength range of interest is selected and residual skylines are masked out. Solely multiplicative polynomials are used to correct for any continuum mismatch between the SSP models and the observed spectrum. Their degree is determined according to $\lfloor (\lambda_{\mathrm{max}} - \lambda_{\mathrm{min}})/200\ \text{Å} \rfloor$ ensuring that spectral features narrower than 200 Å are not influenced by the polynomial. For every fit we also include the corresponding error spectrum as determined by the data reduction process. In pPXF, all inputs have to be logarithmically re-binned in wavelength before the fitting process.

Together with the mass weights of the bestfit returned by pPXF and the predictions for the total luminosity of each SSP model in a certain photometric band, we can calculate the mass-to-light ratio (M/L) of

100: $\mathrm{FWHM}(\lambda) = 5.866 \times 10^{-8}\lambda^2 - 9.187 \times 10^{-4}\lambda + 6.040$ (from Guérou et al., 2017, Figure 4).

the stellar system. We follow Cappellari et al. (2013b, equation 2)

$$M/L_V = \frac{\sum_i w_i M_i^{\star+rem}}{\sum_i w_i L_{V,i}} \tag{5.1}$$

where, for the i-th SSP model, w are the weights returned by pPXF, $M^{\star+rem}$ is the mass in stars and dark remnants[101] and L_V the corresponding V-band luminosity.

We can also estimate the total stellar mass of the system from the integrated spectrum. For this we need to take into account the distance d to the stellar object, as well as normalization constants applied to the observed spectrum N_{obs} and the SSP models N_{SSP} prior to fitting[102]. Hence, we arrive at the following formula (see also Wilkinson et al., 2017; Kacharov et al., 2018) for the total stellar mass $M_{\star,\,tot}$:

$$M_{\star,\,tot} = \sum_i M_{SSP,i} = 4\pi d^2 \frac{N_{obs}}{N_{SSP}} \sum_i w_i M_i^{\star+rem} \tag{5.2}$$

101: The total mass of one SSP model is by construction 1 $M_\odot$. $M^{\star+rem}$ is typically $\neq 1\,M_\odot$ due to the mass loss during stellar evolution.

102: This typically means diving the spectra by the median in order to avoid numerical artifacts.

5.3.2 Single stellar population models

Due to the large age and metallicity as well as wavelength coverage (1680 – 50000 Å) we chose the SSP models from the E-MILES library (Vazdekis et al., 2016) for our main analysis of M 54's stellar populations. Using the BaSTI isochrones (Pietrinferni et al., 2004) they cover 53 age bins between 0.03 – 14.0 Gyr and 12 metallicity [M/H] bins between -2.27 and 0.4 dex. We are using the bimodal IMF with a slope of 1.3 Vazdekis et al. (1996, 2003), which is similar to a Kroupa (Kroupa, 2001) IMF.

The spectral resolution of the E-MILES models is 2.51 Å (FWHM) in the MUSE wavelength range until 8950.4 Å, after that it jumps to about 4.2 Å and then increases slowly with wavelength (see Vazdekis et al., 2016, Figure 8). This means that the LSF of MUSE is much narrower between 8950.4 – 9300 Å than the SSP models and therefore we truncate the MUSE spectrum there. Additionally, the contamination from sky residuals can be quite significant in this regime anyway. How this choice of truncation influences the age-metallicity recovery is investigated in Appendix A.3.

In Section 5.7.1 we will discuss the impact of using different SSP models for our analysis. However, it is beyond the scope of this study to provide a full comparison among different SSP libraries and their impact on the recovery of the age-metallicity distribution from integrated spectra. Thus, the reader is referred to more detailed studies of different spectral synthesis assumptions and techniques in the context of full spectral fitting (e.g. Conroy et al., 2009, 2010; Conroy & Gunn, 2010; González Delgado & Cid Fernandes, 2010; Cid Fernandes & González Delgado, 2010; Fan et al., 2016; Baldwin et al., 2018; Dahmer-Hahn et al., 2018; Ge et al., 2018, 2019).

5.4 STELLAR POPULATION RESULTS FOR DIFFERENT INTEGRATED SPECTRA OF M 54

The flux-calibration of MUSE data makes it straightforward to construct an integrated spectrum of M 54. We can either sum up the individually extracted stars or collapse the whole data cube along the spatial axes.

In this Section we will probe the recovery of M 54's multiple stellar populations depending on the details of constructing the integrated spectrum from the MUSE data and on instrumental effects like wavelength coverage and spectral resolution by analyzing the WAGGS spectrum.

We summarize in Table 5.2 the different integrated spectra of M 54 analyzed in this work.

Table 5.2. Different integrated spectra of M 54.

SET	DATA		SNR PER Å	FIGURE
A	MUSE WFM	all 16 cubes	148[a]	5.2
B	MUSE WFM	single cubes 1-16	125, 114, 119, 80, 79, 149, 141, 111, 110, 127, 148, 105, 79, 77, 94, 104[a]	5.3
C	MUSE WFM	single stars	100 (all stars), 113 (members only)[a]	5.4
D	MUSE WFM	single stars	77 (I $\leqslant$ 16 mag), 104 (I $\leqslant$ 18 mag) 114 (I $\leqslant$ 20 mag)[a]	5.5
E	MUSE WFM-AO	whole cube	134[a]	5.2
F	WAGGS	whole cube	86, 136, 366, 199[b]	5.7

[a] The SNR was estimated from the pPXF fit residuals between 5000 Å and 5500 Å. Due to the correlations in the noise and systematic effects from the data reduction, the signal-to-noise is heavily overestimated, when determined from the formal error cube. We therefore follow this more conservative approach as done in García-Benito et al. (2015); Sarzi et al. (2018).

[b] The SNR for the U,R,B,I gratings respectively was taken from Usher et al. (2017, Table 2). Although the SNR seems to be higher than from the MUSE observations, by looking at the residuals of Figure 5.7 it becomes apparent that they are of the same order.

5.4.1 Integrated spectra from the entire MUSE cube

Firstly, we construct an integrated spectrum from the full cube for each of the 16 MUSE WFM pointings (see data set B in Table 5.2). Only spaxels with a formal SNR $>$ 10 are included in the total integrated spectrum in order to avoid heavy sky residuals in the final integrated spectrum. Those are especially apparent for outer pointings. We do not exclude any possible contaminating sources and tested that the SNR cut does not affect the stellar populations recovery. We additionally combine these 16 integrated spectra into one single integrated spectrum (see data set A in Table 5.2). Note that we do not account for the overlap-

ping regions of the 16 individual pointings (see Figure 5.1). The same is done for the single MUSE WFM-AO cube (see data set C in Table 5.2).

We then feed these spectra into pPXF with the E-MILES models considering all available ages and metallicities (636 models in total). The results from the pPXF fits are shown in Figure 5.2. We can see that the residuals are on the order of 2% emphasizing the excellent data and model quality.

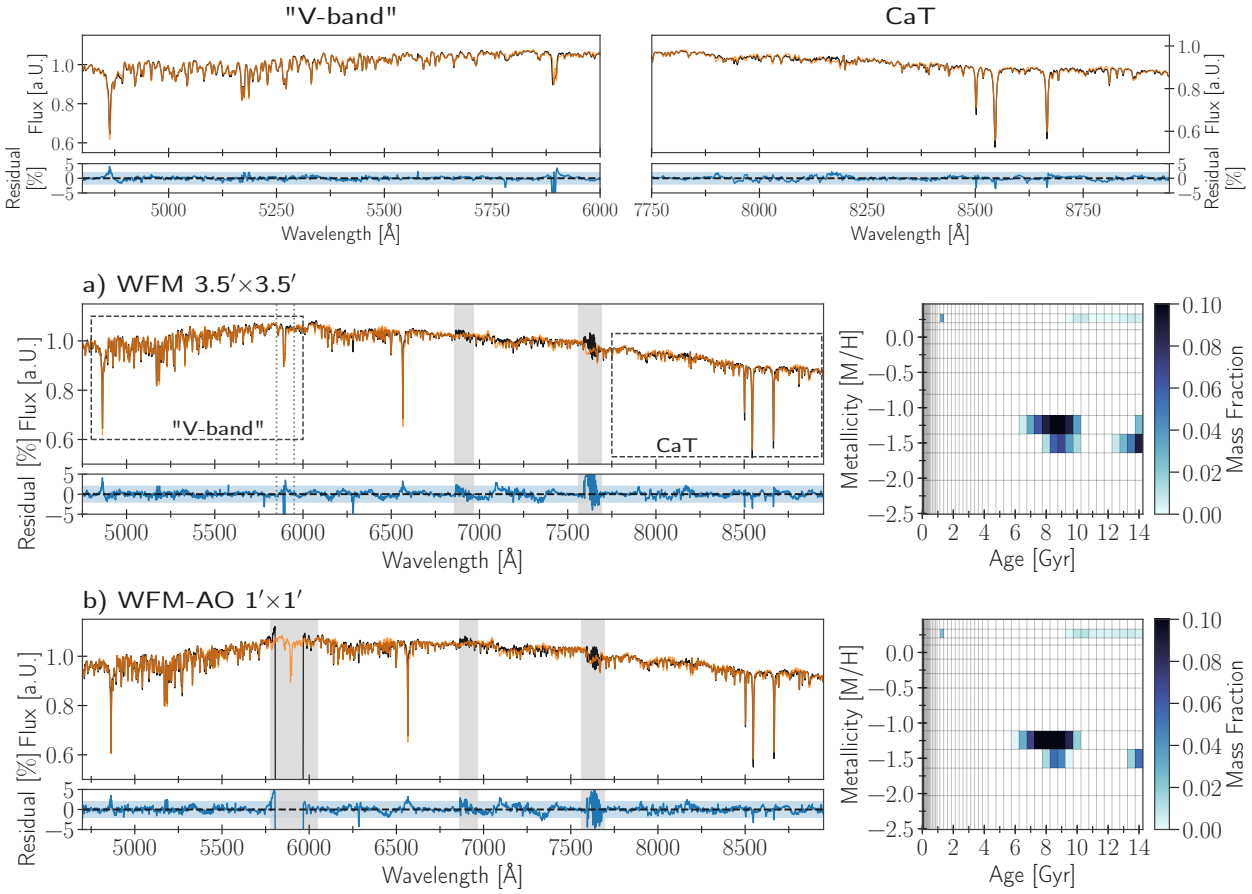

Figure 5.2. *a):* The left panel shows the pPXF fit (orange) to the integrated spectrum of M 54 (black) from the combined 3.5′ × 3.5′ MUSE WFM mosaic. The residuals are shown in blue and the corresponding band shows the 2% level. The dashed regions are highlighted as zoom-in panels around the "V-band" and calcium triplet (CaT) region. Grey shaded areas are masked out sky residuals. The grey dotted lines mark the region around the NaD line that was masked out in Alfaro-Cuello et al. (2019) due to interstellar absorption, however the age-metallicity recovery from pPXF is robust against the in- or exclusion of this region. The right panel shows the derived mass fractions in age-metallicity space that make up the bestfit from pPXF. *b):* The same as for the top panel but showing the integrated spectrum from the single pointing MUSE WFM-AO data. We see that the recovery is insensitive to the blocked region from the Na notch filter.

Both integrated spectra from the 3.5′ × 3.5′ MUSE WFM mosaic and the single WFM-AO pointing are almost identical to the eye, and the recovered mass weights in age-metallicity space show a very similar distribution. A quantitative comparison between the recovered mass weights of both data sets is shown in Figure A.1 a) in Appendix A.1.

We can identify an old, metal-poor (~ 1.5 dex) stellar population at 8 and 14 Gyr, and a young (1 Gyr) and metal-rich (+0.25 dex) contributions. We also see a smaller contribution of old, but metal-rich mass weights. These weights do not fit into our astrophysical picture

of chemical enrichment, hence their origin is further explored and discussed in Section 5.4.6.

Here, it is important to see that the lack of the sodium region in the WFM-AO data does not influence the recovery of the stellar populations properties. For the WFM data we also conducted tests of masking and not masking the NaD lines in the same region as Alfaro-Cuello et al. (2019), as this line is significantly broader than other lines in the spectrum due to interstellar absorption. Both showed consistent results meaning that pPXF is robust against such "outlier" spectral lines, at least if the wavelength range covers enough other prominent lines. The NaD lines can often be problematic as it is influenced by many different effects, such as the interstellar medium, IMF and sodium abundances.

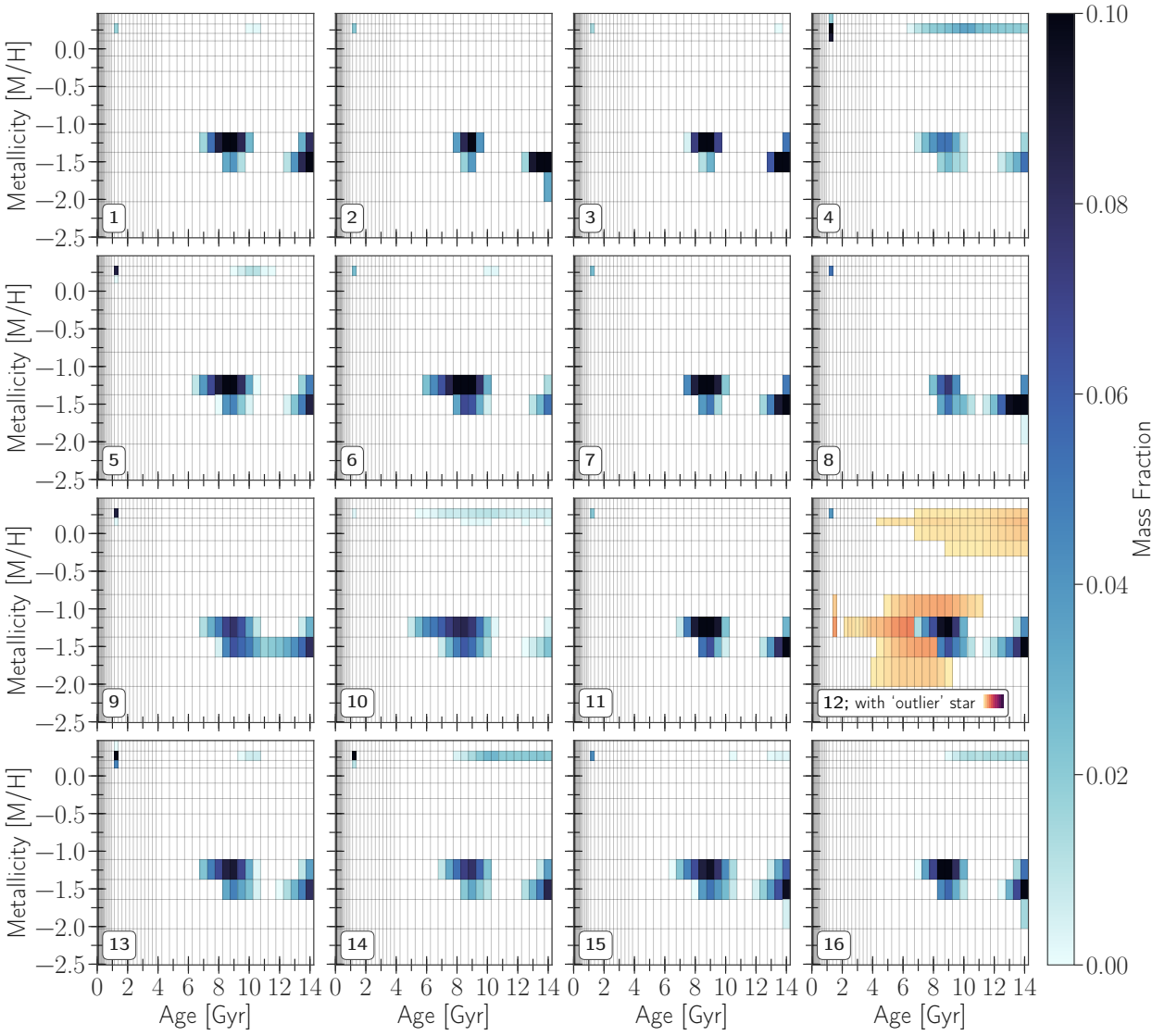

Figure 5.3. Distribution of pPXF-recovered weights in age-metallicity space for the 16 pointings from the MUSE WFM dataset of M 54 (blue color code). They are arranged in the same order as they appear on the sky in Figure 5.1. The red color code (the scale is the same as the blue color code) shows the age-metallicity distribution recovered with the extremely red supergiant star contaminating the spectrum. Note that the apparent presence of an old and metal-rich component is likely related to some of the brightest asymptotic giant branch (AGB) stars (see Figure 5.8 and Section 5.4.6).

We also show the recovered age-metallicity distribution from the analysis of the integrated spectrum for the 16 single pointings of the MUSE WFM data set in Figure 5.3. Overall, the three populations are picked up in every pointing with varying relative strength (see Figure A.1 b) for a more quantitative comparison). The only significant outlier belongs to pointing number 12 (red color code), where the integrated spectrum is heavily influenced by a red supergiant star (V = 17.15 mag & I = 13.43 mag). It can also be clearly identified in Figure 5.1, as it is extremely red. This star contributes about 4% to the total flux of the entire MUSE pointing. If we mask this star out and re-do our integrated light analysis, we obtain a consistent age-metallicity distribution (blue color code) compared to the other pointings.

5.4.2 Integrated spectra from individual stars

The individually extracted stellar spectra from Alfaro-Cuello et al. (2019, see also Section 5.2.1) of the same $3.5' \times 3.5'$ MUSE data set allow us to uniquely combine or exclude certain stars from the integrated spectrum and study the effect on the stellar population recovery. Only stellar spectra with SNR $\geqslant$ 10 are considered in this sample and they make up roughly 50% of the total flux from the $3.5' \times 3.5'$ MUSE mosaic.

First, we simply sum up the entire sample of extracted stars (7165 stars) and in a second test case we only consider those stars that were identified as member stars (6656 stars) (see data set C in Table 5.2). Identical stars that were extracted from different pointings were only accounted for once in the integrated spectrum by taking the corresponding stellar spectrum with the higher SNR. The flux of the individual stellar spectra is preserved and not normalized in any way prior to creating an integrated spectrum from them.

Results from the pPXF fit are shown in Figure 5.4. The recovered stellar populations in age-metallicity are nearly identical by eye, which is also shown in a quantitative comparison in Figure A.1 a) in Appendix A.1. Hence, pPXF seems to be robust against contaminating sources, but the stars classified as non-members only make up 8% of the total integrated light. Still, these non-member stars can have radial velocities of up to -200 km/s, whereas the systemic velocity of M 54 is around 141 km/s (see Figure 3 of Alfaro-Cuello et al., 2019), which pPXF compensates with a larger velocity dispersion. The fitted velocity dispersion for the integrated spectrum including all extracted stars is around 15 km/s, whereas for the integrated spectrum only including member stars it is 1 km/s, which is the hard coded lower limit in pPXF. The true internal velocity dispersion of M 54 is less than the spectral resolution of MUSE. Nevertheless, there is no apparent change in the recovered stellar population properties.

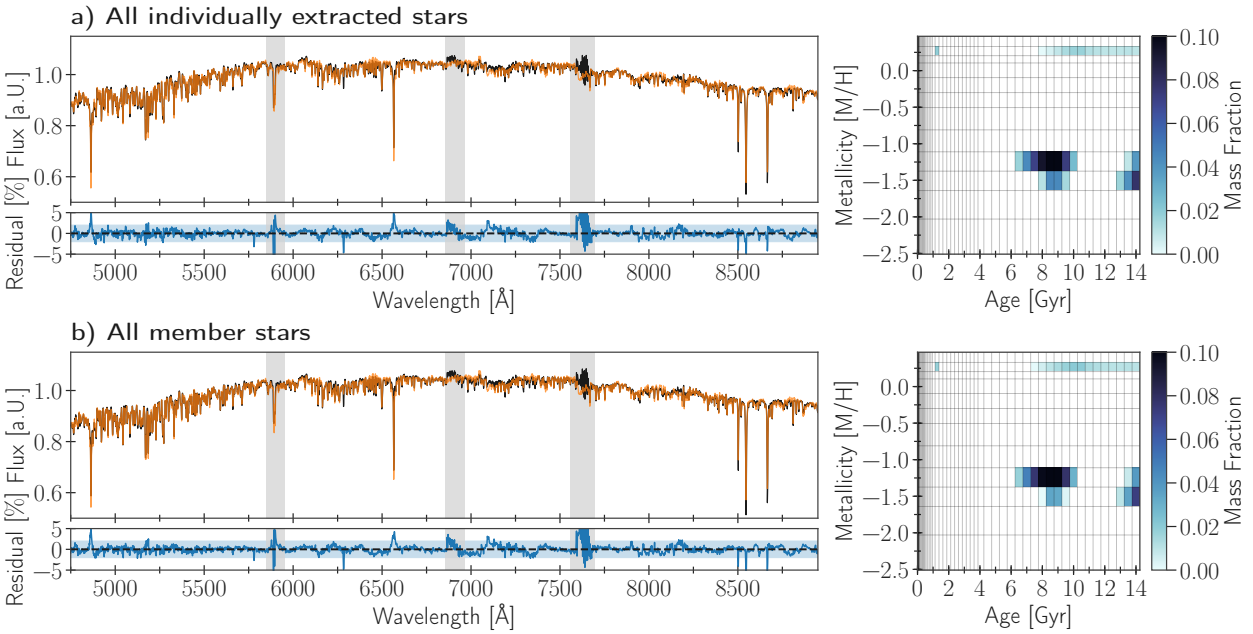

Figure 5.4. *a):* The left panel shows the pPXF fit (orange) to the integrated spectrum of M 54 (black) from all individually extracted stars (see Alfaro-Cuello et al., 2019). The residuals are shown in blue and the corresponding band shows the 2% level. Grey shaded areas are masked out regions. The right panel shows the derived mass fractions in age-metallicity space that make up the bestfit from pPXF. *b):* The same as for a) but now showing the integrated spectrum from individual stars identified as *members* of M 54. Clearly, the stellar population recovery from pPXF is robust against non-member stars.

5.4.3 Integrated spectra with limiting magnitude cutoffs

We also look at different magnitude cuts in the CMD and its effect on the recovered stellar populations parameters, as it changes the relative contribution of stars in different evolutionary stages to the total integrated light. This is particularly interesting, if we think that certain regions of the CMD, like for example the horizontal branch, can be responsible for erroneously recovered stellar population properties. Even though making magnitude cuts is inconsistent with a SSP, we expect that the difference becomes negligible at a certain magnitude.

We show in Figure 5.5 three different cases, where we include all member stars with I-band magnitudes brighter than 16, 18 and 20 mag respectively (see data set E in Table 5.2). These cuts encompass 53%, 89% and 98% of the total integrated light of all member stars.

For the first case, a), only stars brighter than the red clump are considered, for which pPXF still finds the old and intermediate-age, metal-poor population, but no longer the young, metal-rich one. This is likely due to the fact, that the fraction of young, metal-rich stars contributing to the total spectrum is lower in this particular space of the CMD. As a consequence, there are more weights in the old ($>$ 8 Gyr), metal-rich ($>$ 0.0 dex) age-metallicity regime.

For the other two cases, b) & c), the result becomes identical to Figure 5.4, where all member stars were taken into account. This can also be seen in Figure A.1 c) in Appendix A.1. In particular for case b), pPXF is able to reproduce the same results, *as if* the data had a limiting mag-

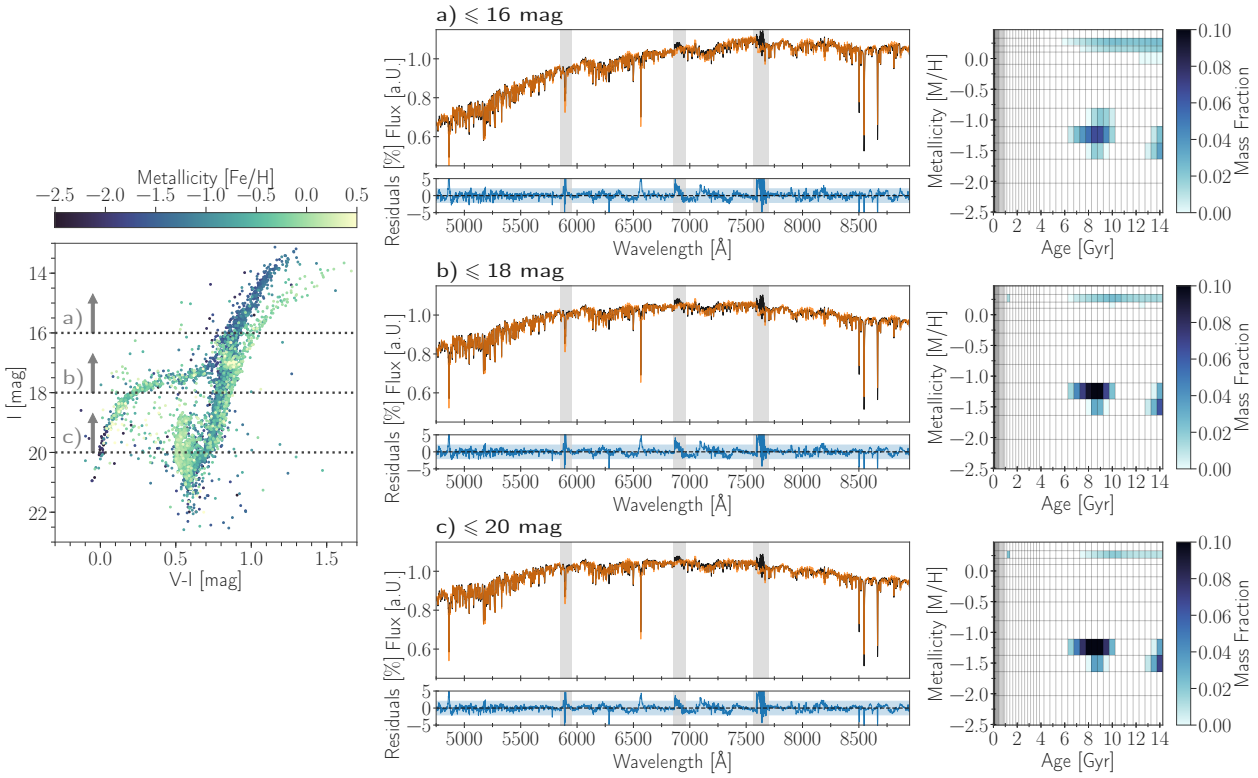

Figure 5.5. *Left*: Color-magnitude diagram of M 54 member stars color coded by metallicity from Alfaro-Cuello et al. (2019). The dotted lines show the cuts at 16 (a), 18 (b) and 20 (c) mag from which the three different integrated spectra were made. *Right, top to bottom*: The pPXF fit (orange) to the integrated spectrum of M 54 (black) from all stars above the magnitude cut is shown for the three cases a), b) and c). The residuals are shown in blue and the corresponding band shows the 2% level. Grey shaded areas are masked out regions. The corresponding derived mass fractions in age-metallicity space that make up the bestfit from pPXF are also shown. Already for I ⩽ 18 mag, the same distribution is found as if all member stars were included in the integrated spectrum.

nitude of 18 in the I-band, which is just below the red clump. This is not surprising, as the magnitude cut at 18 already includes 89% of the total integrated light coming from all member stars.

Moreover, it is reassuring to see that relatively larger contribution from the horizontal branch to the total integrated spectrum in b) does not artificially induce any additional young populations. This is investigated further in the following section.

5.4.4 A closer look at M 54's horizontal branch

M 54 has quite an extended HB with a ratio of 0.75 (Georgiev et al., 2009, a HB ratio of 1 and -1 means only blue or red HB stars respectively), which has been argued to bias age determinations by about 2 Gyr or more (e.g. Lee et al., 2000; Schiavon et al., 2004; Colucci et al., 2009; Georgiev et al., 2012) or to cause spurious young populations in integrated light analysis (e.g. Ocvirk, 2010). In particular, metal-poor globular clusters have been found to exhibit bluer horizontal branches, which have strong Balmer lines and hence can mimic young main sequence stars. Generally, HB stars are difficult to model in SSP models, as there are higher order parameters determining their morphology

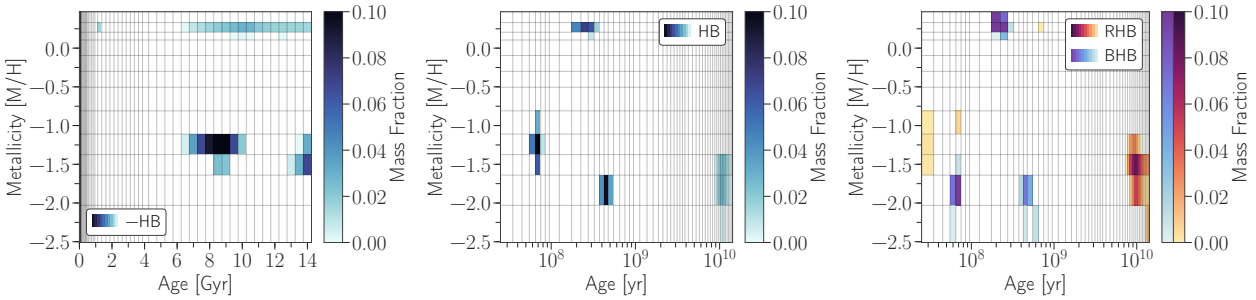

Figure 5.6. *From left to right:* pPXF recovered mass weights in age-metallicity space from fitting E-MILES models to the integrated spectrum of M 54 made from all member stars *without* the horizontal branch (HB), only HB stars, only red and blue HB stars respectively.

(e.g. Lee et al., 1994; Gratton et al., 2010).

In principle, the extended HB in M 54 could be the reason that we find the metal-poor population (~ -1.5 dex) at 8 Gyr even though we know that it is likely older than that. The advantage of our MUSE data set is that we can test this hypothesis by constructing an integrated spectrum *without* M 54's HB stars and fit it with pPXF. We exclude all stars that either have $I < 18.5$ mag and $V-I < 0.7$ mag or $I > 18.5$ mag and $V-I < 0.3$ mag.

As can be seen from Figure 5.6 the recovered stellar populations properties are identical to the fit, where all members stars were included in the integrated spectrum (see Figure A.1 c). Hence, we can conclude that the HB is not responsible for potentially shifting the metal-poor population to 8 Gyr. In Section 5.5 we give another possible explanation for this being due to the large oxygen abundances in M 54.

On the other hand, if we fit the integrated spectrum made of *only* HB stars, we indeed recover very young (< 1 Gyr), metal-poor and metal-rich alike, populations and an old (~ 10 Gyr), metal-poor population. We can even attribute the recovered old component to red ($V-I > 0.43$ mag) and the very young components to blue ($V-I < 0.43$ mag) HB stars.

Interestingly, pPXF always recovers a very small mass fraction (< 1%, which corresponds to < 10% in light) in the youngest age bin (0.03 Gyr) from fitting the E-MILES models to the MUSE integrated spectrum with *and* without HB stars alike. Hence, we cannot attribute this spurious weight in the youngest age bin to the presence of blue HB stars in the integrated spectrum as was found in Ocvirk (2010)[103].

5.4.5 Bluer wavelengths from WAGGS

The influence of hot stars, such a young stars or evolved horizontal branch stars, starts to become dominant in bluer wavelengths (< 4000 Å) than the MUSE range. To be conclusive that M 54's extended HB does *not* influence the age-metallicity distribution recovery as found in the previous section, we here analyze M 54's integrated spectrum from the WAGGS survey until 3500 Å[104] (see data set F in Table 5.2).

103: When SSP models with ages younger than 1 Gyr are excluded from the fit, this systematic vanishes, therefore it can likely be attributed to uncertainties in the SSP models at these young ages.

104: Below that wavelength the spectrum becomes noise dominated.

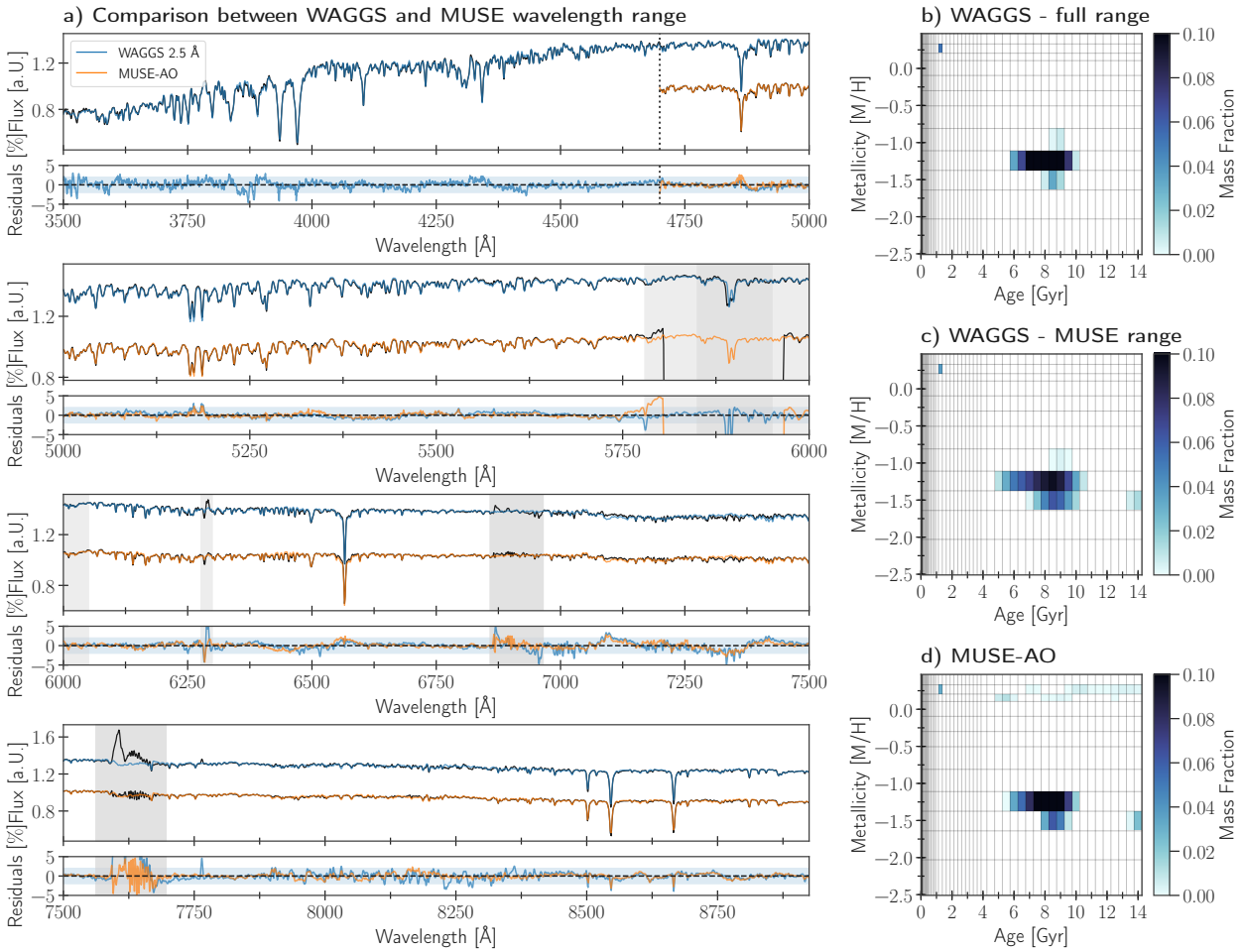

Figure 5.7. *a):* Comparison of pPXF fit to the integrated spectrum of M 54 between WAGGS (blue) and MUSE-AO (orange). The WAGGS spectrum was broadened to a FWHM of 2.5 Å, and the MUSE spectrum was made from the same field-of-view as WiFeS. The blue band shows again the 2 % level of the residuals. Both residual spectra are very similar emphasizing the high data quality. *b):* Recovered age-metallicity distribution from the full wavelength range of the broadened WAGGS spectrum. *c):* Same as b), but now only considering the MUSE wavelength range (see dotted line in top panel of a). *d):* Recovered age-metallicity distribution from the MUSE-AO spectrum with same field-of-view as WiFeS.

In Figure 5.7 a) we show the pPXF fits to the entire WAGGS spectrum and the integrated spectrum from the MUSE-AO observations. We chose the latter for the comparison as it is centered on M 54 and hence could easily be cropped to the same field-of-view as WiFeS in order to eliminate changes in the stellar population recovery induced by the differences in the spatial coverage. It is reassuring to see that both spectra acquired with completely different instruments are almost indistinguishable. The same applies to the residuals of pPXF, also when the WAGGS spectrum is fitted at native resolution (see Figure A.5 in Appendix A.4).

The recovered mass weights in age-metallicity space fitted to the whole wavelength range of WAGGS, only the wavelength covered by MUSE and to the actual MUSE-AO observations are plotted in Figure 5.7 b), c) and d) respectively (see also Figure A.1 d) in Appendix A.1 for a direct comparison). Including these bluer wavelengths does not recover any artificial young populations below 1 Gyr, therefore we con-

clude that the horizontal branch stars have no influence on the stellar population recovery from the integrated light in our analysis of M 54. Quite contrary, pPXF now puts all the mass weights at the 1 and 8 Gyr old population and the one at 14 Gyr vanishes. It reappears though, if the MUSE wavelength range is considered with the WAGGS spectrum. This could either imply that we loose the ability to recover very old ages, if we include these blue wavelengths or that the 14 Gyr population is not real/robust. However, it is more likely that this is associated with the overall difficulty to distinguish between SSP models with ages of 8 Gyr and above at fixed metallicity. Therefore, the "two" populations at 8 and 14 Gyr could also be just one. In Figure A.5 in Appendix A.4 we show M 54's integrated spectrum from WAGGS and MUSE fitted by the PEGASE-HR models, suggesting a more extended old, metal-poor population.

5.4.6 The influence of the brightest stars

The recovery of an old ($8-14$ Gyr) and metal-rich (+0.25 dex) component in all of the above age-metallicity distributions does not necessarily fit into our astrophysical understanding of chemical enrichment in the presence of the three other populations. We therefore investigated, whether this component is real. From Figure 5.4 it seems that this component might arise from a few individual pointings. To explore this further, we repeated the exercise by only considering the classified member stars of M 54. We associate each member star of M 54 to the MUSE pointing it was extracted from, create an integrated spectrum and fit it with pPXF. For pointing number 12 we again excluded the red supergiant star as before.

Overall, the three populations, the old, metal-poor ($\sim$ 1.5 dex) at 8 and 14 Gyr, and the young (1 Gyr), metal-rich (+0.25 dex), are much more clearly recovered as seen in Figure 5.8 (see also Figure A.1 e) for a more quantitative comparison). The old ($8-14$ Gyr), metal-rich (+0.25 dex) component in pointing numbers 4, 5, 13 and 14 from Figure 5.3 vanishes. Looking at those fits again, it is evident that foreground stars with large offsets in their line-of-sight velocities are disturbing the integrated spectrum and the fit when summing up the full MUSE cubes.

However, this is not the case for the central pointings (6, 7, 10 and 11) and number 16. In fact, only including M 54's member stars in the integrated spectra makes the old, metal-rich population much more prominent in the central four pointings. We speculate that this could be due to two effects, a population of high-metallicity MW foreground stars or perhaps thermally pulsing AGB stars. The former possibility was tested by running the Besançon Milky Way model (Robin et al., 2003)[105] predicting around $100-150$ MW stars still left in the M 54 member star sample. These stars have preferably old ages and solar metallicities, however the ages and metallicities of the individual M 54 member stars from Alfaro-Cuello et al. (2019) did not yield any measurements in that parameter range (see also Section 5.5).

105: https://model.obs-besancon.fr/modele_home.php

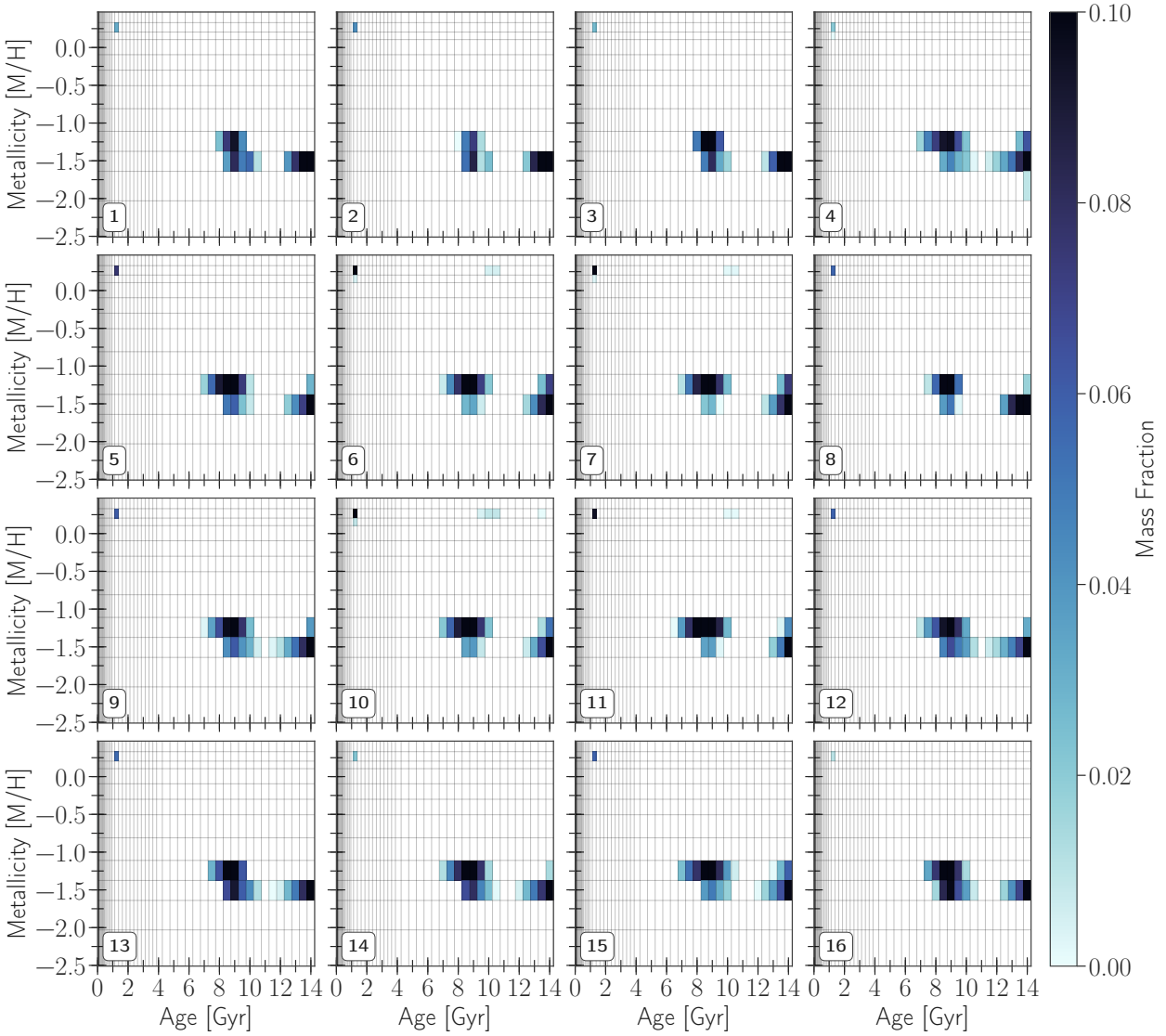

Figure 5.8. Distribution of pPXF-recovered weights in age-metallicity space for member stars of M 54 associated with the MUSE pointings they were extracted from. They are arranged in the same order as they appear on the sky in Figure 5.1. In pointings number 6, 7, 10, 11, 12 and 16 bright ($I < 14$ mag) and extremely red stars ($V - I > 1.7$ mag) are not included in the final integrated spectrum (see Section 5.4.2 & Appendix A.2).

To explore the second possibility, we looked at the color-magnitude diagram of the member stars per MUSE pointing (see Figure A.2 in Appendix A.2). Especially in the four central pointings, brighter ($I <$ 14 mag) and much redder ($V - I \gg 1.7$ mag) stars are found, that could be thermally pulsing AGB stars. These brightest stars contribute around 20% of flux to the total integrated spectrum and therefore have a non-negligible influence on the shape and spectral features of the integrated spectrum. Their red continuum shape and typical spectral features like prominent TiO bandheads can easily be mimicked by old, metal-rich stellar populations, if they are not properly accounted for in the SSP models (see e.g. Maraston, 2005; Maraston et al., 2006, for the influence of AGB stars). If they are indeed the source of an old, metal-rich component then it might also explain why the component was *not* recovered from the WAGGS data (see Section 5.4.5), as we expect that

the influence of AGB stars becomes weaker at bluer wavelengths.

Excluding these stars from the integrated spectrum of the four central pointings and repeating our analysis, we obtain the age-metallicity distributions as shown in Figure 5.8. The contribution of the old, metal-rich component decreases significantly from $20-30\%$ to $0.3-2\%$. Evidently, the old, metal-rich component is not recovered in a significant amount when considering the integrated spectrum made from the full MUSE cube in three out of the four central pointings (Figure 5.3). We attribute this to the fact that the full cubes contain enough flux from fainter, unresolved stars, such that the contribution of the brightest stars drop to around 10%.

For pointing number 16 a single star (marked by a grey circle in Figure A.2) is responsible for the recovery of the old, metal-rich component. This star also appears in pointing number 15, but its presence in the integrated spectrum of this pointing does not cause the old, metal-rich component to appear - probably because its flux contribution is only 4%, whereas in pointing number 16 it is 8%.

Counterintuitivly, the recovered age-metallicity distributions for pointings 4, 5 and 8 in Figure 5.8 do not show the old, metal-rich component even though their integrated spectra *include* stars with $I > 14$ mag that contribute around 20% to the total flux. Nevertheless, we confirm that excluding these brightest stars from the integrated spectra from Figures 5.4 b) and 5.5 b) & c), makes the old, metal-rich component completely vanish, while for Figures 5.5 a) and 5.6 the contribution significantly decreases. Instead, the relative contribution of the young, metal-rich component becomes stronger in all cases.

5.5 INTEGRATED VS. RESOLVED AGE-METALLICITY DISTRIBUTION RECOVERY

As we have seen in the previous section, the recovery of the mass distribution in age-metallicity space does not heavily depend on the exact approach used to construct the integrated spectrum of M 54 - however the contribution of the brightest stars is possibly responsible for the recovery of unphysical mass weights for this particular system (Section 5.4.6). Therefore, we restrict our comparison to the resolved stellar population analysis from Alfaro-Cuello et al. (2019) to the results from the integrated spectrum built from M 54's members *excluding* the brightest stars (see Section 5.4.6).

In Figure 5.9 a) we show the age-metallicity relation derived from the single stars binned to the same age-metallicity grid as the one we use in our integrated analysis to ease comparison. We show the stars that belong to M 54 in a red color code, where as stars that have been characterized as outliers in blue color-code, as quantified by Gaussian mixture models in Alfaro-Cuello et al. (2019). It is also important to note again that the horizontal branch stars are not included in this result.

In Figure 5.9 b) we show our result from the integrated light analysis. Now, the color code shows the absolute mass contained in each

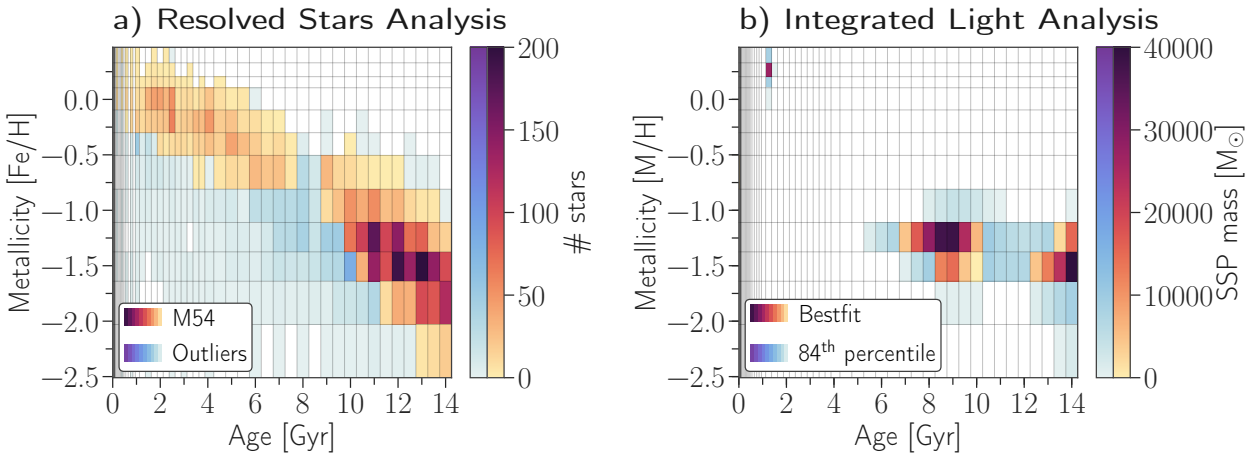

Figure 5.9. *a):* Number of resolved stars in their respective age-metallicity bin as determined in Alfaro-Cuello et al. (2019). The bins correspond to the age-metallicity grid adopted by Vazdekis et al. (2016) using the BaSTI isochrones (Pietrinferni et al., 2004). The red color code shows the stars that were characterized to M 54, whereas the blue color code shows outliers. The mean age and metallicity are 9.24 Gyr and -1.01 dex respectively. *b):* Age-metallicity distribution from fitting the full, integrated spectrum of M 54. Here, we show the result for the integrated light of individual member stars spectra *excluding* the brightest stars (see Section 5.4.6). The colorbar indicates now how much absolute stellar mass is contained in each SSP bin. The red color code shows the distribution of mass bins belonging to the bestfit solution, whereas the blue color code shows the extent of the 84th percentile mass bins derived from randomly re-sampling the residuals. The mass-weighted mean age and metallicity are 9.53 Gyr and -1.21 dex respectively.

SSP bin instead of the relative mass fraction (see equation 5.2). We show the bestfit mass bins as well as the 84th percentile from randomly re-sampling the residuals from pPXF, adding them to the bestfit spectrum and re-fitting 100 times. We chose to keep the regularization parameter fixed to the value derived for the bestfit, as opposed to use no regularization at all. This allows for studying the effect on the smoothening of individual mass bins in age-metallicity space purely due to random variation in the fitted spectrum, and not the change of the regularization parameter. We also use the variation of the derived mass fraction from the 16 nearly independent MUSE pointings to quantify how much their absolute value as opposed to their smoothening across the age-metallicity plane. The mean relative differences between the mass fractions recovered for each pointing and the total of all member stars is around 28% and 38% for age and metallicity respectively (see Figure A.1 e)). They are on the same order as the ages and metallicities measured from the individual stars from Alfaro-Cuello et al. (2019), which vary by 44% and 26% respectively across the pointings. They are likely induced by various factors such us differing SNR of the integrated spectrum or stochastic sampling of certain stars.

By focusing on the red color code of Figure 5.9, we see that the resolved star analysis shows a nicely rising chemical enrichment as a function of time. Most stars are roughly between 10 and 14 Gyr in age and -2.0 to -1.0 dex in metallicity. A more spread-out population of stars lie between 3 and 5 Gyr and around -0.25 dex in metallicity, whereas more stars seem to concentrate again at around 2 Gyr and solar metallicity.

The integrated light analysis on the other hand shows three more concentrated populations at 14 Gyr and -1.5 dex, around 8 Gyr and

-1.25 dex and at 1 Gyr and super solar metallicity respectively. The returned chemical enrichment is also less continuously rising, but shows a rather flat enrichment from 14 to 8 Gyr and then jumps to +0.25 dex in metallicity at 1 Gyr. However, the separation between the 8 and 14 Gyr is likely not real, but either induced by the general poor age resolution at old ages, or by the quite complex individual element abundances of the Sagittarius nucleus. As shown by Carretta et al. (2010b,a), stars in M 54 exhibit almost a one dex spread in oxygen abundance. This effect can bias age determinations between $5-10\%$ towards younger ages for generally old and iron-poor stars (VandenBerg et al., 2012), as the turn-off region becomes bluer for enhanced oxygen. In fact, the same phenomenon was observed in the resolved study (de Boer et al., 2015, who also recover a population around 8 Gyr from stars of the Sagittarius stream), however by applying a Gaussian age prior the authors could eliminate this problem (see Alfaro-Cuello et al., 2019, Section 3.4).

Similarly, non-solar α-abundances (especially magnesium) have a strong effect on the position of the red giant branch (RGB). It is well known that the Sagittarius stream as well as its nucleus, M 54, follow the well defined [α/Fe]-[Fe/H]-relation (see Carretta et al., 2010b; de Boer et al., 2014; Mucciarelli et al., 2017). Stars with an iron abundance around -1.5 dex are α-enhanced by about 0.4 dex, whereas stars with [Fe/H]-ratios between -1.0 and +0.0 dex have [α/Fe]-ratios between +0.2 and -0.2 dex respectively. The E-MILES models used in our integrated analysis are based on the "baseFe" SSP models, which refers to the assumption that the MILES stars have solar α-abundances (i.e. [Fe/H] = [M/H]). However, these stars actually follow the MW [α/Fe]-[Fe/H]-relation (as determined in Milone et al., 2011) and hence the solar-scaled BaSTI isochrones are inconsistent with low metallicity MILES stars. Unfortunately, this likely does not explain why the metallicity derived for the metal-poor population in the integrated analysis is consistent with the resolved study and the young population is supersolar compared to solar values from the individual M 54 stars. If α-abundances are causing the metallicities differences between the two methods, we would expect to observe the opposite trend. Furthermore, the fit residuals of the Mgb lines (see e.g. Figure 5.7) show that the magnesium abundance is actually overpredicted in the SSP models suggesting discrepancies between the adopted and actual alpha-abundance of M 54.

Furthermore, the discontinuity between the old, metal-poor and the young, metal-rich population in the integrated analysis can have a number of possible explanations. It could be that the relative contribution of stars between 2 and 8 Gyr as seen in the resolved analysis is not significant in the integrated spectrum to be picked up by pPXF. This means that the star formation rate of a certain star forming episode has to reach a specific threshold to be contributing significantly to the integrated light. It could also be that this is an issue of how regularization is applied, as it smooths the mass weights only in the horizontal and vertical direction in the age-metallicity plane, but not diagonally.

Despite the apparent differences (or similarities) between the age-

metallicity distributions of the resolved and integrated light analysis, the average quantities of both methods agree well. We quote a mean age and metallicity of 9.24 Gyr and -1.01 dex for the resolved stars and a *mass-weighted* mean age and metallicity of 9.53 Gyr and -1.21 dex for the integrated method. This corresponds to a difference of only 3% in age and 0.2 dex in metallicity, which is good precision considering the range of metallicities of almost 2 orders of magnitude. Weighting the resolved stars by their V-band luminosity yields a mean age of 9.69 Gyr and metallicity of -1.11 dex, whereas light-weighted quantities from the integrated method produce a mean age of 7.34 Gyr and metallicity of -0.99 dex.

The averages across the 16 MUSE pointings vary by about 0.43 Gyr and 0.06 dex for the resolved and by 0.82 Gyr and 0.10 dex for the integrated analysis. Statistical errors on these quantities from both Alfaro-Cuello et al. (2019) and our random re-sampling of the residuals are below a few percent. However, based on the general uncertainty of stellar population synthesis as well as the poor age resolution at old ($\gtrsim$ 8 Gyr) ages, we do not claim to recover the *true* mean age and metallicity of M 54 to better than 20%.

To summarize, the integrated light analysis of M 54 can recover a young, metal-rich and old, metal-poor stellar population even though pPXF is free to choose any, not necessarily physical, age-metallicity combination that best represents the observed integrated spectrum. The derived mean ages and metallicities are consistent with the resolved analysis despite the differences in the used SSP models and the lack of considering individual element abundances that are present in M 54.

5.6 MASS-TO-LIGHT RATIOS FROM INTEGRATED ANALYSIS

From the returned pPXF mass weights we also calculate stellar M/L ratios in the V-band (see equation 5.1) for integrated spectra made from M 54 member stars (excluding the brightest stars; see Section 5.4.6). This is done for our canonical E-MILES SSP library choice with a bimodal IMF of slope 1.3. We find a global value $M/L_V = 1.46$, however across the 16 MUSE fields we find values that vary from 1.3 to 1.8 (or with a standard deviation of 0.22 from the global M/L). These are shown in Figure 5.10 as a function of luminosity density color-coded by contribution of the young (1 Gyr), metal-rich (+0.25 dex) component. From this it appears that the four central pointings, which have the highest luminosity density, tend to have lower M/L ratios. The outer fields at lower luminosity density show a wide spread in M/L ratios. We confirm that the scatter in the derived M/L ratios originate from the varying relative contribution of the young, metal-rich mass fractions, as this directly translated to a change in the M/L ratio (see equation 5.1). This agrees with the young, metal-rich stars being more centrally concentrated as found by Alfaro-Cuello et al. (2019). There is an outlier corresponding to pointing number 4, which has a low M/L ($\approx$ 1.3) at low luminosity density ($\approx$ 20 $L_\odot/pc^2$), likely caused by the brightest star contributing around 25% to the total flux (see Figure A.2).

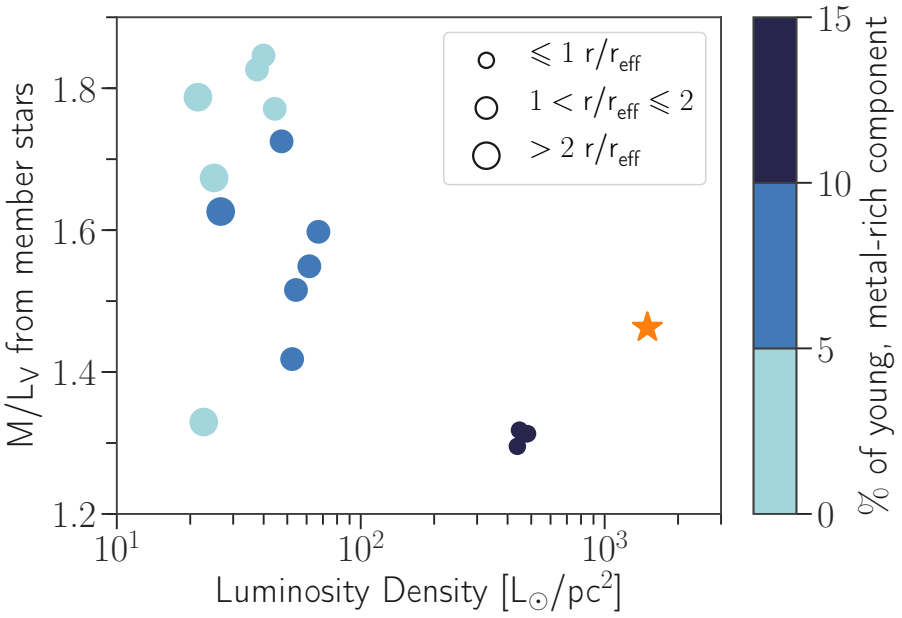

Figure 5.10. Mass-to-light ratios in the V-band derived from returned pPXF mass weights for integrated spectra made from M 54's member stars excluding the brightest stars (see Section 5.4.6) plotted against the luminosity density in each corresponding pointing. The symbol size corresponds to the distance from M 54's center, while the color-code shows the fraction of the young (1 Gyr), metal-rich (+0.25 dex) component. The orange star corresponds to the global M/L ratio obtained from an integrated spectrum made from *all* the M 54's member stars excluding the brightest stars. Estimated errors from randomly re-sampling the residuals is on the order of the symbol size.

The exclusion of the horizontal branch in the composite spectrum (see Section 5.4.4 after 5.4.6) yields a M/L ratio of 1.45, whereas the magnitude cuts (see Section 5.4.3 after 5.4.6) yield 1.53, 1.38 and 1.48 for I < 16, 18 and 20 mag respectively. Even though these changes are below our estimated statistical errors of $1-2\%$, we do not claim that they are significant, especially with respect to typical uncertainties of 6% in other studies (e.g. Cappellari et al., 2013b).

Our stellar population derived M/L$_V$ ratio agrees with measurements from Kimmig et al. (2015), who modelled M 54's velocity dispersion profile with a King profile and taking internal rotation into account. However, it is lower by about 0.5 compared to studies from Baumgardt & Hilker (2018); Dalgleish et al. (2020), who fitted N-body simulations without internal rotation to the velocity dispersion profiles. This might be an indication that it is important to include internal rotation in the dynamical modelling, as it decreases the M/L ratio measurement. There is evidence after all that M 54's young, metal-rich population exhibits a significant rotation signature (Bellazzini et al., 2008; Alfaro-Cuello et al., 2020).

5.7 Discussing comparisons of integrated and resolved studies

After thoroughly having compared the stellar population results from resolved star analysis of Alfaro-Cuello et al. (2019) and our integrated light analysis in the previous section, we have now arrived at the question, whether this comparison proves that the recovery of age-metallicity distributions from integrated spectra provides us with the

same information content as the resolved stars with regard to stellar population ages and metallicities.

Assuming now that the derived ages and metallicities of the resolved stars resemble the 'best´ knowledge we have about M 54, one might take the mismatch between the two approaches in Figure 5.9 as a failure of the integrated method. However, the importance and success of this comparison is not to be measured in how perfectly the individual bins in age and metallicity match each other, but the fact that the integrated light analysis can clearly and robustly detect that M 54 hosts *multiple* populations, which are *even* located in a similar age-metallicity space as the properties of the resolved stars. Considering that the resolved and integrated analysis techniques are also very different conceptually and in the models they use, the similarities of the recovered age-metallicity distributions are compelling.

In the following sections we will discuss in more detail, which aspects of stellar population analysis have to be considered to perform a one-to-one comparison between the resolved and integrated methods (Section 5.7.1). Furthermore, we argue that neither of those two techniques should be regarded as more reliable than the other (Section 5.7.2).

5.7.1 Is the comparison actually self-consistent?

Our comparison of integrated light versus resolved stellar population studies has the main advantage that it uses the same dataset. Nevertheless, we still need to consider two aspects related to the fitting of the stellar populations, that are both nontrivial to implement:

First, we would need to make sure to use the exact same stellar synthesis models. Only then, we would be able to estimate, if discrepancies in the derived age and metallicity properties between the two techniques are induced by the different models or the different approaches themselves. The resolved study from Alfaro-Cuello et al. (2019) uses the ELODIE 3.2 (Prugniel & Soubiran, 2001, 2004; Wu et al., 2011) stellar library to estimate the stellar parameters for $4750 - 6800$ Å and the Dartmouth (Dotter et al., 2008) isochrones in order to determine the stellar ages. On the other hand, we have used the E-MILES SSP library (Vazdekis et al., 2016) together with the BaSTI isochrones (Pietrinferni et al., 2004) to fit for ages and metallicities in the wavelength range of $4750 - 8950.4$ Å. In this wavelength regime, the E-MILES SSP models are based on three different stellar libraries: the MILES (Sánchez-Blázquez et al., 2006), the near-IR CaT (Cenarro et al., 2001) and the Indo-U.S. (Valdes et al., 2004) library (see also Vazdekis et al., 2012). With these differences basically all systematics regarding spectral and stellar synthesis as well as their respective modelling are captured. Different sets of isochrones have different assumptions about stellar evolution, in- or exclude certain evolutionary phases of stars and are computed for different age and metallicity bins. Different stellar libraries have different flux calibration, wavelength coverage and, in case of empirical ones, are biased towards metallicities in the solar neighbourhood. All

of this can influence the derived *absolute* ages and metallicities of stellar populations in *both* analysis techniques neglecting additional systematics induced by, for example, individual element abundances (Vazdekis et al., 2001; Schiavon et al., 2002) as discussed in Section 5.5.

In principle, this issue could be resolved by using the exact same models in both approaches. Where the authors of the resolved analysis have in theory the freedom to choose any combination of stellar libraries and set of isochrones, analysis of integrated light is restricted to the publicly available SSP models, which have a fixed combination of stellar library and isochrones[106]. Changing models and re-doing the integrated analysis is straightforward, but in the resolved case steps 2. – 5. in Section 5.2.1 have to be repeated, which can be quite time consuming for a decent amount of models and are out of the scope of this study.

106: However, tools like FSPS (Conroy et al., 2009; Conroy & Gunn, 2010) try to provide users a more flexible interface in calculating SSP models.

For the interested reader, we show in Appendix A.4 our integrated analysis of M 54 conducted with the PEGASE-HR SSP library (Le Borgne et al., 2004), in order to match the stellar library used in resolved method, however there the isochrones are from PADOVA (Bertelli et al., 1994). It is quite interesting to see how much the recovered age-metallicity distribution seems to depend on the adopted SSP models at first glance, while they are still recovering the same physical implications of M 54's multiple populations, all modelling uncertainties considered.

The second aspect that arises when trying to compare the two approaches is that the color code in Figure 5.9 does not represent the same physical quantity. The resolved study shows the number of stars in each age-metallicity bin, but the integrated analysis provides us with a mass (or light) fraction of an SSP corresponding to a particular age and metallicity. From the latter, we can deduce the absolute mass in each bin and consequently the total mass of M 54 relatively easily. Inferring the mass of each star can be deduced from the fitted isochrone and their magnitudes (see e.g. also Pont & Eyer, 2004; Lin et al., 2018). However, a completeness correction is necessary to account for non-detected stars below the turn-off, where most of the mass lies. Only then could the stellar mass in each age-metallicity bin for the individual star analysis be estimated. The individual star counts also influence the derived mean ages and metallicities making the comparison of their values to the integrated measurements not one-to-one let alone in a light- or mass-weighted sense.

5.7.2 Is one method more reliable than the other?

After discussing the potential ways of making the comparison between the resolved and integrated analysis of M 54 as self-consistent as possible, the question arises, whether we would gain new knowledge from this extra work. Certainly, this would put the two approaches to the ultimate test, but we would also need to assume that one approach is better or more reliable than the other. In fact, both approaches suffer from the same difficulties that are connected to the well-known degeneracies and difficulties in stellar population modelling, such as the

age-metallicity degeneracy, unknown individual element abundances and poor age resolution at old ages ($\gtrsim$ 8 Gyr).

With regard to the resolved stars from the MUSE data, their iron abundance is generally well-determined by their spectra, however the age determination from isochrone fitting is rather degenerate, as especially other element abundances shift the isochrones and can induce artificial age variations (see Section 5.5). Furthermore, fitting an isochrone through one point on the CMD is very degenerate in itself, as can be seen from the outliers in Figure 5.9 a). Some kind of measure needs to be defined in order to identify these outliers, as was done in Alfaro-Cuello et al. (2019) with the means of Gaussian mixture models.

Similarly, in the integrated analysis, SSP models at old ages ($\gtrsim$ 8 Gyr) and at fixed metallicity are more or less indistinguishable, therefore the age leverage is poor in this regime. This essentially could mean that the two old metal-poor populations in Figure 5.9 b) (one at around 8 Gyr and the other one at 14 Gyr) are the same, which is further complicated by the high oxygen abundances in M 54 as discussed in Section 5.5. Furthermore, here it is also hard to tell, which mass weights are robust and which are erroneously being generated simply due to the ill-posed nature of the inversion problem. Nevertheless, the metallicity determination seems to be more robust and hence having a handle on the metallicity distributions from integrated spectra of extragalactic objects is already a big advantage as compared to average values.

A similar argument holds when it comes to the comparison of different SSP models with the same technique. We do not know which models are intrinsically more reliable or closer to truth in nature, although a good parameter coverage across $\log g$, T_{eff} and [Fe/H] (and potentially [α/Fe]) of stellar spectra is always a limiting factor. *A* choice of a certain SSP library always has to be made, therefore absolute quantities, such as the exact position of the mass weights in age-metallicity space might not be as reliable. However, the relative trends are expected to be the same. Meaning that, if we always use the same SSP models for different stellar objects of interest, we will be able to say differentially, whether the objects have experienced different chemical enrichment histories.

In conclusion, without being prejudiced against the credibility of either of the two methods, we can reliably say that *both* results in Figure 5.9 show the following results:

1. There are *multiple* stellar populations present in M 54.
2. Overall, there is a division between an old, metal-poor ($>$ 8 Gyr and $\sim$ -1.5 dex) and a young, metal-rich ($1-2$ Gyr and $\sim$ $0.00-0.25$ dex) population.
3. The cluster is dominated by the old, metal-poor population.
4. The mean age and metallicity are in the range of $9-9.5$ Gyr and -1.0 to -1.2 dex.

Hence, the integrated analysis is capable of identifying multiple stellar populations from a single integrated spectrum. It results in a similar

star formation and enrichment history as the resolved analysis based on CMD analysis and spectral fitting of individual stars.

5.8 CONCLUSIONS

In this work we have presented the analysis of M 54's integrated spectrum from three different data sets (MUSE WFM, MUSE WFM-AO and WiFeS) with the goal to recover its multiple stellar population content via full spectral fitting (pPXF: Cappellari & Emsellem, 2004; Cappellari, 2017) of a library of SSP models (E-MILES: Vazdekis et al., 2016) to the observed spectrum. Thanks to the individually extracted stellar spectra of the $3.5' \times 3.5'$ MUSE WFM data set from Alfaro-Cuello et al. (2019), we could also investigate the influence on the stellar population recovery by excluding the contribution of certain stars to the total integrated spectrum. In light of all our tests, we draw the following conclusions in recovering age-metallicity distributions from integrated spectra:

- The derived mass fractions in age-metallicity space are robust against 1) the Na notch filter in MUSE-AO observations (Figure 5.2), 2) the inclusion of stars classified as non-members (Figure 5.4) and 3) the contribution of extended horizontal branch stars (Figure 5.6).
- The recovery of the age-metallicity distribution is not very sensitive to the limiting magnitude of the observations. Consistent results are achieved, even if the limiting magnitude were 4 times brighter than the main sequence turn-off region (Figure 5.5).
- The recovered mass fractions are consistent in their absolute position in age-metallicity space over individual pointings of the 4×4 MUSE mosaic, as long as the spectrum of an overly bright star does not dominate the integrated spectrum (Figure 5.3).
- Additional spectral coverage in the bluer wavelength ($3500 - 4000$ Å) does not change the age-metallicity distribution recovery significantly (Figure 5.7, A.5).
- Bright ($I < 14$ mag) and red ($V - I > 1.7$ mag) stars in the integrated spectrum seem to induce erroneous old (> 8 Gyr), metal-rich (+0.25 dex) populations in the recovered age-metallicity distribution (Figure 5.4). Uncertain evolutionary phases such as the thermally pulsing AGB not included in the SSP models could be an explanation for this.
- The absolute derived ages and metallicities change, as expected, with different SSP model assumptions, however differentially the trends stay the same (Figure 5.9, A.4). Hence, M 54's *multiple* stellar populations are indeed retrievable from its integrated spectrum showing an old ($8 - 14$ Gyr), metal-poor (-1.5 dex) as well as a young (1 Gyr) and metal-rich (+0.25 dex) population.

- The derived mass-weighted mean age and metallicity of 9.53 Gyr and -1.21 dex are consistent with the corresponding averages of the resolved analysis of 9.24 Gyr and -1.01 dex respectively.
- The derived stellar M/L ratios show more stochasticity in the outer regions of M 54 ($M/L_V = 1.3 - 1.8$), where the luminosity density is lower, as compared to the central region, where the value converges to around 1.46. We attribute this to the lower relative contribution of young, metal-rich mass fractions.

In this context we also compared and discussed our results with findings of the resolved stellar population analysis from same MUSE WFM data set (Alfaro-Cuello et al., 2019). From this we find that age-metallicity *distributions* can be derived from full spectral fitting of integrated spectra with comparable reliability as from resolved studies, as both approaches suffer equally from the same difficulties, uncertainties and degeneracies in stellar population synthesis modelling, especially with regard to age determinations, whereas the recovered metallicity distribution seems to be more robust. While IFU observations of resolved systems can certainly provide detailed information on a star-by-star basis, our integrated approach can provide the same information content, if the scientific goal is to disentangle multiple or complex stellar populations of stellar systems. It is also worth noting that the integrated analysis reveals this information with a single fit in several minutes as opposed to lengthy data extraction and analysis steps undertaken in the case of the resolved study (see Section 5.2.1). On top of that, our returned distributions have a physical unit attached to them (mass fractions) instead of number counts, which lets us straightforwardly calculate the stellar mass of the different populations or the system in total as well as M/L ratios. This provides us with a quick and detailed knowledge about the stellar content of an object.

In spite of the modelling differences between both methods, we find that the average age and metallicity from the integrated and resolved stars analysis agree remarkably well with each other. This is of key importance for extragalactic studies at low and high redshift, which can only access the integrated light - especially now with the advanced development of chemo-dynamical models for external galaxies (e.g. Poci et al., 2019; Zhu et al., 2020).

With the ability to study the two dimensional distribution in the age-metallicity plane of thousands of stellar objects, we can establish a connection between the properties of multiple stellar populations to their global properties like total mass, presence of super-massive black holes and environment. This means, we are now in an era (data- and modelling-wise) to constrain formation scenarios of nuclear star clusters or the stellar mass assembly of galaxies on a statistical scale with the stellar population distributions from integrated spectra.

APPENDIX A

Supplementary material for the study conducted in Chapter 5.

Contents

A.1 QUANTITATIVE COMPARISON BETWEEN RECOVERED MASS FRACTIONS

We show in Figure A.1 the results from fitting the different integrated spectra of M 54 from Section 5.4 in the form of one dimensional distributions as a function of age and metallicity respectively. This allows for a more quantitative comparison between the different fits than the two dimensional age-metallicity distributions. Evidently the recovered mass fractions show overall consistent results between the various integrated spectra that we investigated. Comparing panels b) and e) in Figure A.1 we see that the derived mass fractions across all 16 independent MUSE pointings show less variations, especially in the young (1 Gyr), metal-rich (+0.25 dex) component, when foreground stars and the brightest member stars are not included in the resulting integrated spectrum.

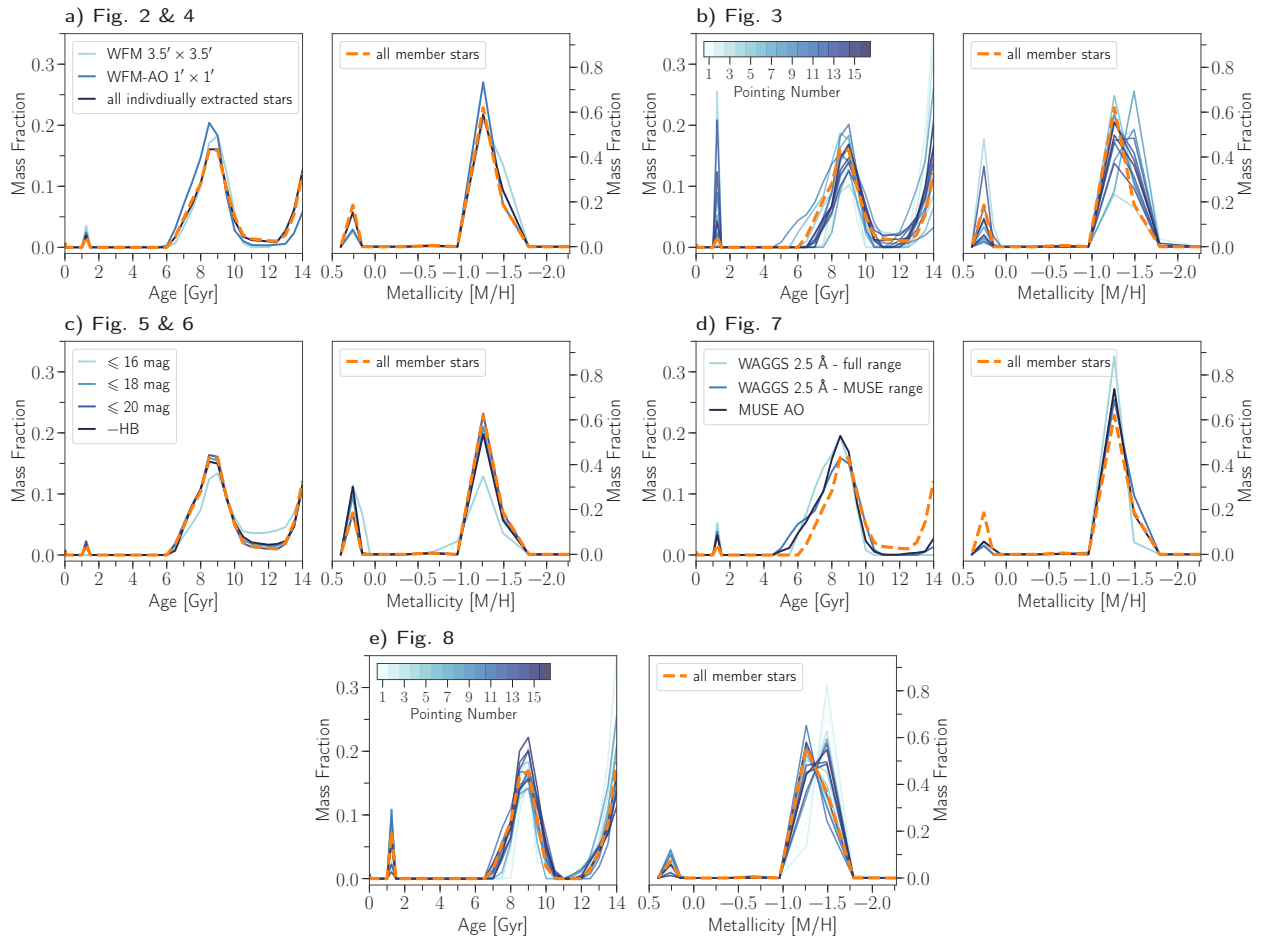

Figure A.1. *a):* One dimensional distributions of mass fractions as a function of age and metallicity respectively. They are derived from the integrated spectra presented in Figures 5.2 & 5.4. The orange dashed line shows the mass distribution for the integrated spectrum made from individual member stars. It is shown in all panels in order to ease comparison between the different results from the integrated spectra investigated in Section 5.4. *b):* The same for Figure 5.3. The color-code shows the corresponding pointing number as in Figure 5.3. *c):* The same for Figures 5.5 & 5.6. *d):* The same for Figure 5.7. *e):* The same for Figure 5.8. The orange dashed line shows now the results for all member stars without the contribution of the brightest stars as defined in Section 5.4.6.

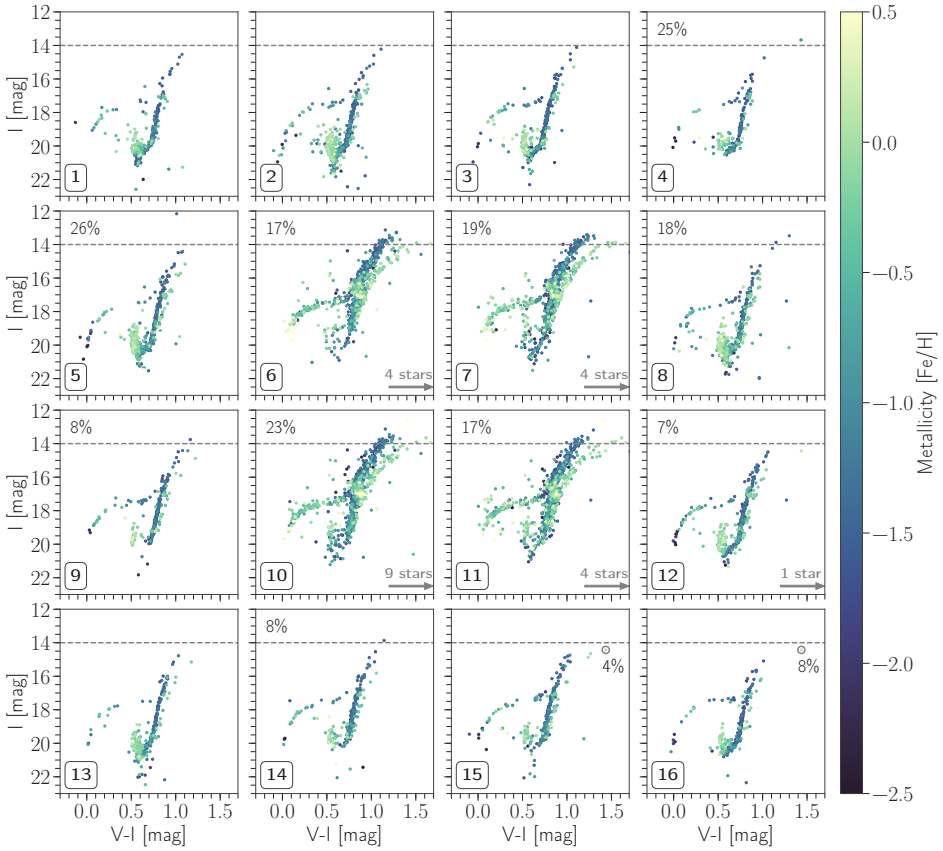

Figure A.2. Color-magnitude diagram for members stars of M 54 that where extracted from the corresponding MUSE pointing. The color code follows the measured metallicity [Fe/H] for each star from Alfaro-Cuello et al. (2019). They are arranged in the same order as they appear on the sky in Figure 5.1. The grey arrow indicates how many stars have extremely red colors ($V-I \gg 1.7$ mag) and are thus not shown. The percentage in the upper left hand corner indicates the fraction of flux of stars that are brighter than 14 mag in I and redder than 1.7 mag in $V-I$. In pointing number 15 and 16 the percentage shows the flux contribution of the same star (grey circle) to total flux of member stars in that pointing.

A.2 COLOR-MAGNITUDE DIAGRAMS OF M 54 IN THE 16 MUSE POINTINGS

Figure A.2 shows the CMDs of M 54 member stars extracted from their corresponding MUSE pointings from the $3.5' \times 3.5'$ mosaic (Alfaro-Cuello et al., 2019). Especially, the central pointings (number 6, 7, 10 and 11) have a high number of bright ($I < 14$ mag) and extremely red ($V-I \gg 1.7$ mag) stars that contribute around 20% to the total flux of the integrated spectrum made from member stars in that corresponding MUSE pointing. When these stars are excluded from the integrated spectrum, the contribution of the previously recovered old (> 8 Gyr) and metal-rich (+0.25 dex) mass fractions decreases from $20-30\%$ to under 2%. In pointing number 16 a single star with 8% flux contribution was responsible for pPXF to recover these mass weights. The same star is also present in pointing number 15, where it did not cause the old, metal-rich component to be picked up, possibly because its flux contribution is decreased to only 4%. Interestingly, other pointings (e.g. 4, 5 and 8) also have a few bright stars that contribute a significant

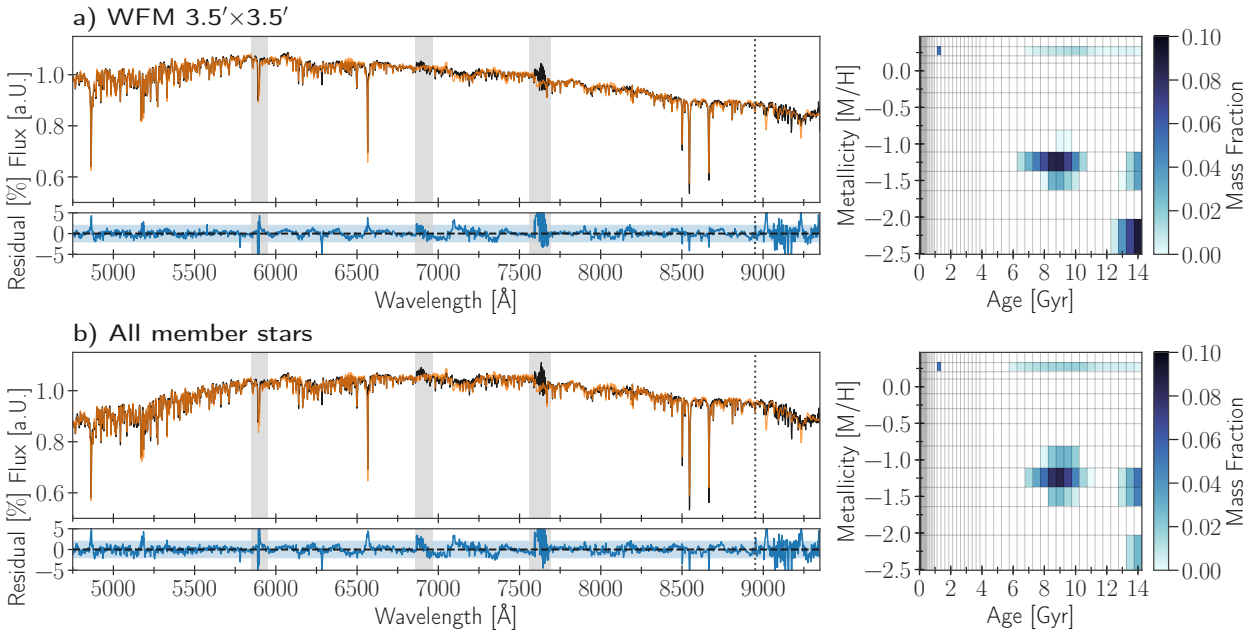

Figure A.3. *a):* The left panel shows the pPXF fit (orange) to the integrated spectrum of M 54 (black) from the combined 3.5′ × 3.5′ MUSE WFM mosaic now fitting the *entire* MUSE wavelength range. The residuals are shown in blue and the corresponding band shows the 2% level. Grey shaded areas are masked out sky residuals. The grey dotted lines shows the previous wavelength cut-off at 8950.4 Å. The right panel shows the derived mass fractions in age-metallicity space that make up the bestfit from pPXF. *b):* The same as for a) but now showing the integrated spectrum from individual member star spectra.

amount to the total flux, but did not cause any old, metal-rich component to appear in the derived age-metallicity distribution. A possible explanation might be that these stars (expect the bright star in pointing 4) do not have red continuum shapes as well as TiO absorption bands that become visible in the integrated spectrum, which could easily mimic old, metal-rich stellar populations in the SSP models.

A.3 Fitting the MUSE integrated spectrum beyond 8950.4 Å with the E-MILES library

As mentioned in Section 5.3.2 we here present the mass distribution in age-metallicity space derived from the integrated spectrum of the entire 3.5′ × 3.5′ MUSE mosaic and made from the individually extracted member stars (Alfaro-Cuello et al., 2019) fitted to the entire wavelength range of MUSE with the E-MILES models.

The results are shown in Figure A.3. We see that pPXF now recovers a third component, which is at 14 Gyr and the lowest metallicity of -2.27 dex. It is very prominent, when the integrated spectrum was made from all 16 MUSE data cubes combined. Apparently, the recovery of this component depends on the wavelength range between 8950.4 – 9300 Å, which is quite noisy, as can be seen from the residuals. Moreover, in this wavelength regime the E-MILES models have a lower resolution (FWHM ≈ 4.2 Å) than the MUSE spectrum, which makes the two Paschen lines (n = 9 and n = 10) appear very broad. Nevertheless, in the observed spectrum they do not appear nearly as deep as the

bestfit model.

Following the discussion in Section 5.5 we argue that this does not have any influence on our statements regarding the ability and reliability of recovering multiple populations from integrated spectra, as the exact absolute values of the ages and metallicites depend on the adopted SSP models. We can still make the same qualitative statement about M 54's multiple stellar populations and now the overall trend of the recovered chemical enrichment is even more consistent with a steady rise than when the wavelength rage was cut off.

To assess whether the broader spectral resolution of the E-MILES in that particular wavelength range could cause the new stellar population component, we have convolved the integrated spectrum to the lowest spectral resolution present in the E-MILES library at those wavelengths (FWHM 4.4 Å). Still the 14 Gyr old component in the lowest metallicity bin was recovered.

A.4 FITS WITH THE PEGASE-HR SSP LIBRARY

Here, we provide results of fitting the integrated spectrum of M 54 with the PEGASE-HR models (Le Borgne et al., 2004). They are based on the ELODIE 3.1 (Prugniel & Soubiran, 2001, 2004; Prugniel et al., 2007) high resolution spectra (R = 10000) and the PADOVA isochrones (Bertelli et al., 1994). The wavelength coverage is 3900 – 6800 Å, ages and metallicity span 0.001 – 20 Gyr (68 bins) and -2.3 to 0.69 dex (7 bins) respectively. The assumed IMF is Kroupa (Kroupa, 2001) and the mass of one SSP is also normalized to unity. We set the minimum age bin to 0.1 Gyr and the maximum to 14 Gyr in order to match the boundaries of the E-MILES models, however we made sure that no spurious mass weights were detected when including the full age range in PEGASE-HR models. Similarly to Kacharov et al. (2018), we also performed a pPXF fit with PEGASE-HR models that were interpolated to a finer age-metallicity grid. The models were fit to the integrated spectrum made from the individually extracted member star spectra. Both results and the comparison to the resolved study from Alfaro-Cuello et al. (2019) are shown in Figure A.4.

We again detect an old, metal-poor population with a metallicity between -1.0 and -1.5 dex and an essentially unconstrained age between 8 and 14 Gyr. Now, we can also identify an intermediate population at around 3 Gyr and between -1.0 and -0.5 dex in metallicity, which is still more metal-poor than the intermediate-age population from Alfaro-Cuello et al. (2019). We also still see the young, metal-rich population at 1 Gyr and around +0.25 dex, again more metal-rich than the one identified in the resolved analysis. Mass weights with this same super solar metallicity but older ages are again attributed to the same systematics as discussed in Section 5.5.

The result from the interpolated PEGASE-HR models shows mass weights that are in the same location in the age-metallicity space as the fiducial models, but are on average lower. The weights are hence smeared out across several more age-metallicity bins, which is not sur-

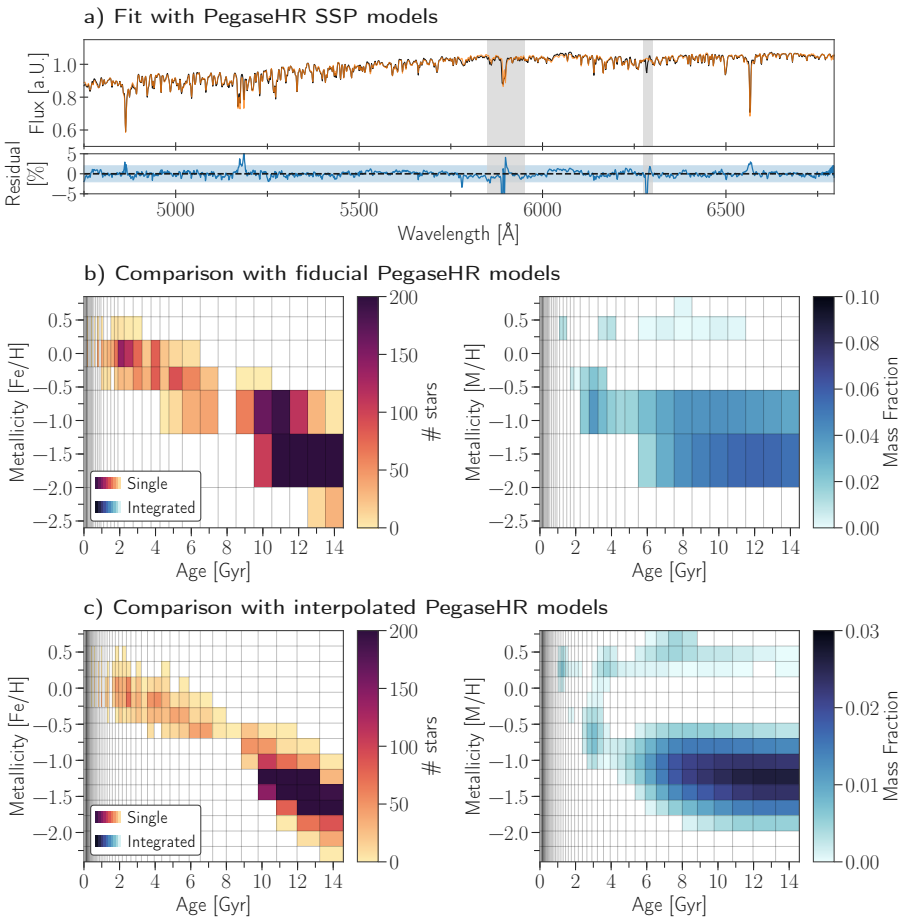

Figure A.4. *a):* pPXF fit (orange) to the integrated spectrum of M 54 (black) constructed from all individually extracted member stars (see Alfaro-Cuello et al., 2019) with the PEGASE-HR SSP models. The residuals are shown in blue and the corresponding band shows the 2% level. Grey shaded areas are masked out regions. *b):* Comparison between the resolved (left) and integrated (right) results of M 54's stellar populations. The integrated analysis has been conducted with the fiducial PEGASE-HR models. *c):* The same comparison as b), but here the PEGASE-HR models where interpolated onto a finer age-metallicity grid prior to fitting. Here, the individual mass weights returned by pPXF are on average much lower than with the fiducial model.

prising as the interpolation adds more linearly dependent models into the design matrix.

In Figure A.5 we show the results of fitting the WAGGS spectrum of M 54 with the fiducial PEGASE-HR SSP models, once for the native WAGGS spectral resolution (FWHM 0.8 Å) and once broadened to 2.5 Å to mimic the spectral resolution of MUSE. Both results are almost identical, whereas the high resolution fit retrieves much less mass weights at old age and super solar metallicity and gives more weight to the old, metal-rich (around 10 Gyr and -1.5 dex) and the young, metal-rich (around 1 Gyr and +0.25 dex) population as compared to the result from the lower resolution spectrum. We can also see some differences in the distribution of the recovered mass fractions in age-metallicity space, if we compare these to the results for the MUSE spectrum fitted with the PEGASE-HR models in Figure A.4. Nevertheless, this gives us confidence that the recovery of ages and metallicities of multiple stellar populations from integrated spectra is not severely dependent on the spectral resolution.

Even though the fit to the WAGGS spectrum with the PEGASE-HR models in Figure A.5 includes bluer wavelengths than the MUSE data, we still recover an extended old, metal-poor population, where compared to fitting the full WAGGS wavelength range with the E-MILES models in Figure 5.7, the metal-poor mass fractions at 14 Gyr vanished and instead concentrated around 8 Gyr. We argue that this difference arises

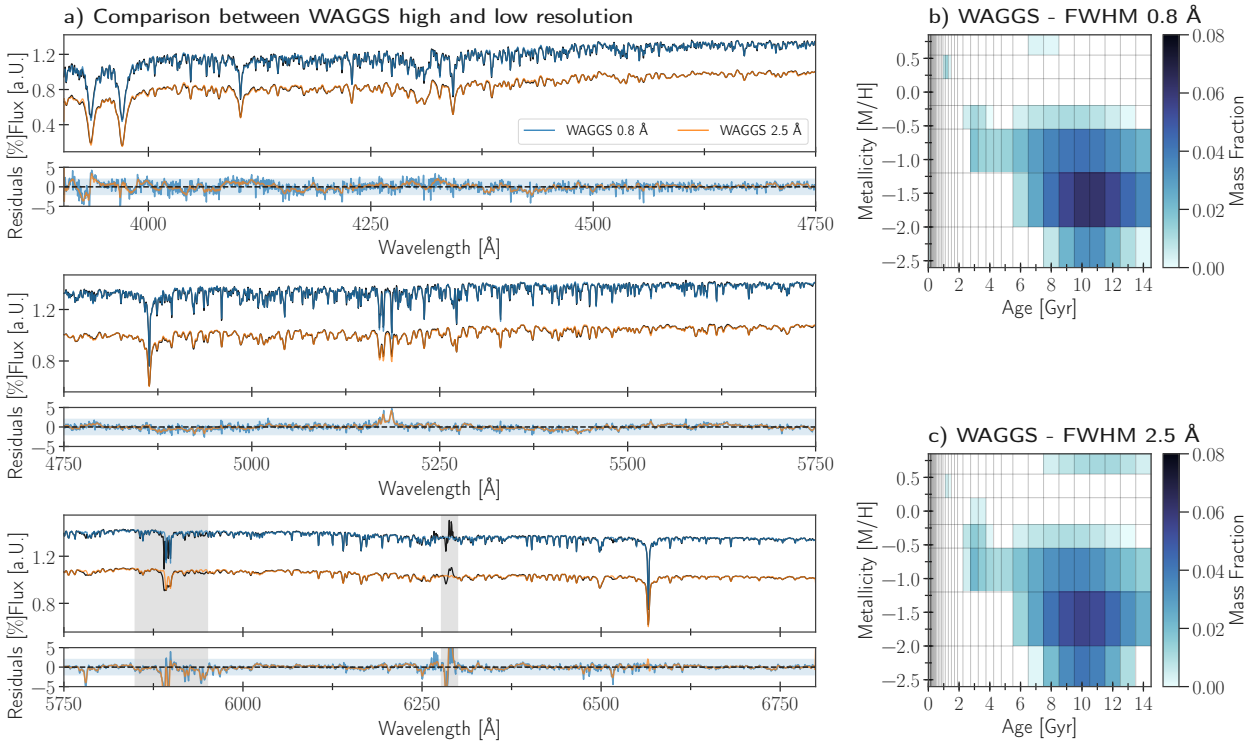

Figure A.5. *a):* pPXF fit to the integrated spectrum of M 54 from WAGGS (Usher et al., 2017) with the PEGASE-HR models. The fit to the native spectral resolution (FWHM 0.8 Å) is shown in blue, whereas the broadened one (FWHM 2.5 Å) is in orange. The residuals are on the 2% level for both resolutions. *b):* Recovered age-metallicity distribution from the high resolution spectrum. *c):* Same as b), but for the broadened spectrum with a FWHM comparable to MUSE.

because of the diverse modelling assumptions of stellar population synthesis and not because of the inclusion of bluer wavelengths.

Part III

THEORETICAL EFFORTS

COSMOLOGICAL GALAXY SIMULATIONS

6

Dynamical timescales of galaxies are very long. We only observe them at a certain evolutionary snapshot and projected on the sky nonetheless. Thus, to understand how galaxies form and evolve, we need to put our astrophysical knowledge into computers and press fast forward. *Can we reproduce properties of galaxies we observe today in the context of the standard cosmological model? What physical processes are missing? What new observational signatures can we look out for to answer missing puzzle pieces?* Numerical simulations are an inevitable asset in astrophysical research encompassing a huge investment of both the scientists developing and running the simulations as well as the computational power behind it. More so, the outputs are made publicly available so everybody can run their own simulations or analyze them for their particular interest. In this chapter, I provide some methodological background on cosmological galaxy simulations and highlight their successes in shaping our understanding of how the world formed.

Summary

Simulators use many particles to represent the matter present in galaxies to follow their evolution trough cosmic time. Depending on the exact "flavour" of matter, particles interact purely gravitationally (dark matter and stars) or not (gas), each entailing differing numerical techniques. All numerical simulations have a mass and spatial resolution limit invoking the use of so-called subgrid physics to model astrophysical processes taking place on smaller scales. The complexity quickly evolved from simulating single galaxies with a few particles, to fully cosmological hydrodynamical realizations, which form and evolve galaxies from primordial density fluctuations to today's observed, diverse galaxy population.

Contents

6.1 NUMERICAL APPROACHES

Galaxy formation combines many physical processes acting on many different scales: from quantum mechanics in the interiors of stars to general relativity describing the world. Numerical approaches thus differ depending on which flavour of 'test' particle is of interest. For example, dark matter and stars only interact gravitationally, as they are collisionless. Gas on the other hand is collisional, as it can cool and heat, and thus is also subjected to the laws of hydrodynamics. Photons are responsible for radiative transfer processes that are important for galaxy formation and for delivering all the information to us on Earth. Coupling all three processes is extremely computationally expensive, but important to understand, for example, the epoch of reionziation (e.g. Ocvirk et al., 2016; Kannan et al., 2022). Cosmological simulations that evolve galaxy formation until $z = 0$ usually assume a uniform ionizing background radiation field (e.g. Faucher-Giguère et al., 2009). I therefore only discuss numerical approaches for gravity and hydrodynamics.

6.1.1 N-body

The N-body problem describes the positions $\mathbf{x}_i$ and velocities $\mathbf{v}_i$ of N particles with masses m_i at a time t. Their new positions and velocities at a further time step are updated according to the gravitational force that acts upon them[107].

The formula for the gravitational force is simple, but numerically a nightmare, as the force acting on one particle depends on all other particles. Therefore, cleverer approaches have to be used, which only use direct force summation for the nearest neighbours and other means for long-range forces (e.g. Barnes & Hut, 1986; Hockney & Eastwood, 1988; Hernquist & Katz, 1989; Springel, 2005; Springel et al., 2021).

Still, it is impossible to follow the gravitational interaction of individual stars in (cosmological) galaxy simulations, because N is too large. Thus, we think of stellar particles or "stars" in galaxy simulations as SSPs. They present a sample of the underlying density field, and therefore gravitionally bound systems of particles, i.e. galaxies, should be resolved with a certain number of particles (perhaps $100 - 1000$) such that we can study their internal properties. Hence, the better the mass resolution the more low mass galaxies can be resolved in a cosmological volume. Consequentially, the larger the simulation volume the lower the mass resolution (see Figure 6.1).

On top of that, when the separation between two particles, i.e. point masses, becomes small, the gravitational force acted upon them diverges. To avoid that, the force is softened between two particles. Therefore, the point masses obtain a finite volume with a size equal to the softening length. Choosing the size of the softening length is usually tied to the size of the time step. Closer encounters result in larger displacements with respect to the previous time and thus require smaller

107: Perhaps the earliest N-body simulation is from Holmberg (1941), who used light bulbs as particles.

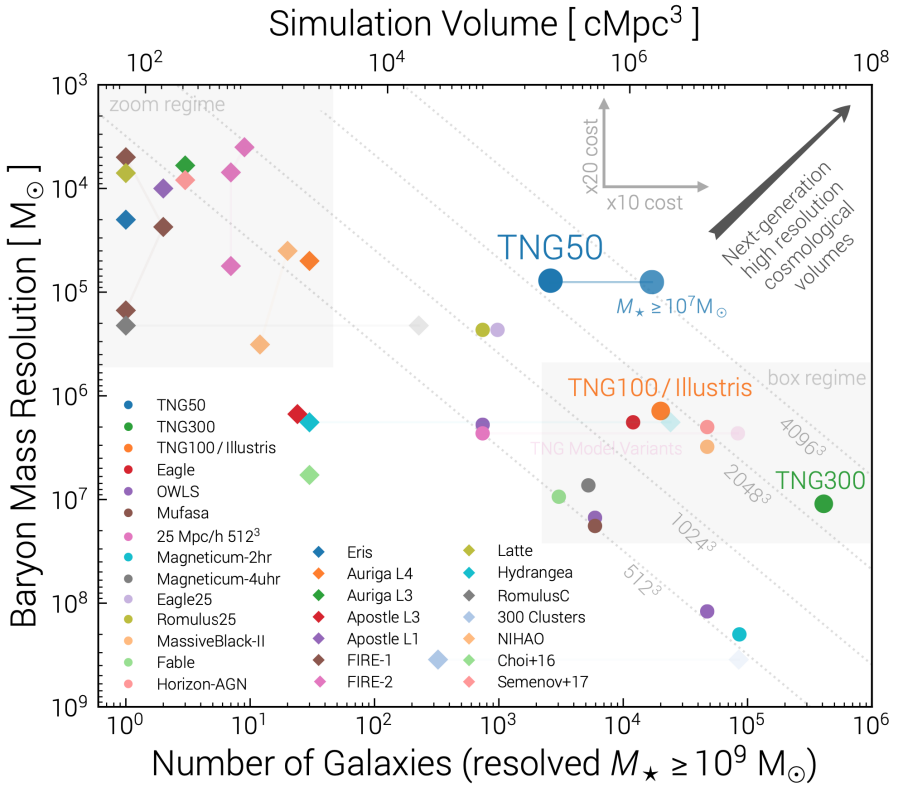

Figure 6.1. Comparison of mass resolutions in different galaxy simulations taken from Nelson et al. (2019b).

time sampling in order to be accurate (Power et al., 2003).

Together, the mass and spatial resolution set the numerical accuracy of a simulation. As a consequence, analysis performed on numerical simulations should always involve a convergence test, which compares the same properties of given objects at different resolutions.

6.1.2 Hydrodynamics

Hydrodynamical simulations in galaxy formation solve the Euler equations, i.e. the conservation of mass, momentum and energy, with self-gravity and assuming an equation of state for an ideal gas. This can be done in two ways: either the coordinates are comoving with the fluid/gas ("Lagrangian approach") or the coordinates are fixed ("Eulerian approach").

The most popular technique for the Lagrangian approach is smoothed-particle hydrodynamics (e.g Lucy, 1977; Gingold & Monaghan, 1977; Monaghan, 1992; Wadsley et al., 2004; Springel, 2010a). The fluid is represented by N particles, thus conserving mass. Their hydrodynamical properties are then calculated by summing over all neighbouring particles with a smoothing kernel of a given radius. Their time evolution can then be calculated with the same integrator used for N-body simulations. An advantage of this method is that the flow of the fluid can be directly followed, however it performs poorly when discontinuities, such as shock fronts, or hydrodynamical instabilities are present and important (e.g. Agertz et al., 2007).

Fixed grid or mesh based algorithms are better at treating these kind of phenomena (e.g. Woodward & Colella, 1984; Berger & Colella, 1989; Kravtsov et al., 1997; Teyssier, 2002). They calculate hydrodynamical quantities as an average within a given cell, and update them by taking into account the flux that passes through the cells surfaces. Because galaxy formation involves a high dynamic range, meshes or grids that adapt their size are often superior in resolution. Nevertheless, there are some problems with these techniques as well, which led Springel (2010b) to develop a hybrid approach. The generating mesh is based on a Voronoi tessellation of the domain, which moves with the fluid flow and can adaptively refine and de-refine itself. Still, with this method, the history or trajectory of a given gas element cannot be followed. However, this is important in galaxy formation, as we would like to, for example, understand the role of gas accretion. Thus, tracer particles are used to follow the gas flow (Nelson et al., 2013).

6.2 SUBGRID PHYSICS

Even though cosmological hydrodynamical simulation are now possible, the whole nature of the complex processes in a multi-phase ISM cannot be accounted for ab-initio, as it requires the resolution of very small scales (see e.g. Walch et al., 2015, for efforts to understand these processes better). Thus, star formation and the associated feedback processes, such as supernovae and winds, as well as metal enrichment are treated via subgrid physics. These subgrid recipes are based on (semi-)analytical models (see e.g. McKee & Ostriker, 1977; Springel & Hernquist, 2003; Schaye & Dalla Vecchia, 2008; Agertz et al., 2013), where stars are produced from gas once it reaches a certain density threshold, such that, for example, the Kennicutt-Schmidt law is reproduced (see Section 3.2.3.3). Similarly, the growth of SMBHs and the associated AGN feedback is implemented via subgrid models (e.g. Springel, 2005; Weinberger et al., 2017). Reviews by (Somerville & Davé, 2015; Naab & Ostriker, 2017) provide an overview of various subgrid physics employed in cosmological simulations.

Lastly, the free parameters in the subgrid models are tuned such that key, present-day observations are reproduced by the simulation. These usually include the galaxy stellar mass function (GSMF) and the SMBH-galaxy mass relation (see e.g. Schaye et al., 2015; Pillepich et al., 2018a).

6.3 GETTING LARGER AND MORE COMPLICATED

Numerical galaxy simulations started with a few hundred to thousand N-body particles (White, 1976, 1978) to simulate single galaxies. With the ever progressing capabilities of (super)computers, these simulations developed into $10^9 - 10^{12}$ N-bodies unveiling the large scale structure of the Universe. Both isolated and cosmological galaxy simulations, are important to understand the multitude of physical pro-

cesses involved in galaxy formation, which I briefly discuss in succession.

6.3.1 Idealized and isolated

Idealized simulations usually start a galaxy from some density profile (Hernquist, 1993a) and then let it evolve without a cosmological context. With this, the process, impact and remnants of galaxy mergers could finally be studied in detail (e.g. Farouki & Shapiro, 1981; Barnes, 1988; Hernquist, 1992, 1993b), primarily to answer the formation of elliptical galaxies (Toomre & Toomre, 1972). Once gas was included (e.g. Barnes & Hernquist, 1991, 1996), it emerged how 'wet' mergers produce spheroids with more rotational support in contrast to 'dry' mergers (see Chapter 3 for more references). Suites of merger simulations followed to understand the parameters responsible in shaping the final merger product[108] (e.g. Naab & Burkert, 2003; Di Matteo et al., 2005; Cox et al., 2006), which primarily depend on the following:

108: The primary galaxy during a merger is the more massive one, whereas the less massive one is the secondary.

A. The mass ratio of the two galaxies prior to merging. Usually ratios above 1:4 are considered major mergers. Minor mergers are less destructive to the main progenitor's appearance.

B. The gas fraction carried by the two galaxies ('wet', gas-rich vs. 'dry', gas-poor mergers). Gas compresses and shocks, which can trigger bursts of star formation during the merger (e.g. Mihos & Hernquist, 1994a, 1996). The applied torques can let gas flow to the galaxy's center and feed the SMBH, resulting in AGN activity (e.g. Hernquist, 1989; Springel et al., 2005a).

C. The morphologies of the two galaxies, i.e. whether they are disk or bulge dominated. Disks can be destroyed or significantly dynamically heated. Typically the consensus is that disk galaxies become ellipticals during major mergers, however the disk can also survive such events or reform later (e.g. Springel & Hernquist, 2005; Governato et al., 2009).

D. The orbital properties of the two galaxies determine if and how fast the merger happens. In case the encounter is too fast, the galaxies will just fly by each other, which nonetheless can have effects on both of them. Encounters on initially radial orbits will be more rapid, whereas more circular orbits can permit a slower in-spiral. Tidal tails are more prominent, if the intrinsic spin of secondary is retrograde with respect to the orbital spin (I highly recommend to read the thesis of Renaud, 2010).

Even though mergers are more complex and abundant in a cosmological context (e.g. Bullock & Johnston, 2005), isolated galaxy simulations are still essential, especially to understand the implementation and impact of various subgrid physics (e.g. Hopkins et al., 2013a; Smith et al., 2018; Smith, 2021; Smith et al., 2021).

6.3.2 Fully cosmological

The first fully cosmological simulations followed the evolution of dark matter to understand, if the initial density fluctuations in a ΛCDM universe as measured via the CMB could reproduce the present-day structure and clustering of galaxies (e.g. Springel et al., 2005b and see also Kuhlen et al., 2012, for a review). These simulations showed ab initio that galaxies (or more so their dark matter halos) form and grow from the non-linear gravitational collapse of Gaussian density perturbations (see Figure 6.2 and Chapter 2). This fundamental result was established as one of the successes of the ΛCDM model.

Substructures within dark matter halos, which are called subhalos and in which galaxies ultimately form, reveal that halos are self-similar (e.g. Navarro et al., 2010). This means that a halo of a given mass has the same scaled distribution of substructure than another halo of different mass. As it happens for many phenomena in astrophysics, the subhalo mass function is a power law with a slope of around -2 (Giocoli et al., 2008), predicting hundreds to thousands of subhalos within a single halo.

At last, the mass growth as well as the destruction of individual (sub)halos in these simulations can be followed through cosmic time until $z = 0$ via the construction of merger trees as visualized in Figure 6.3. A given subhalo has a main progenitor branch onto which smaller subhalo accrete. From this, we can understand when and how many mergers play a role in shaping a galaxy's evolution and present-day appearance.

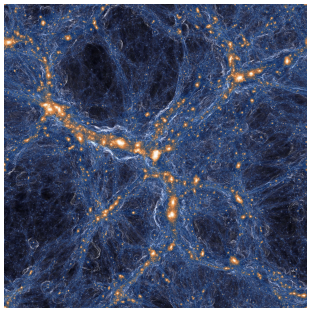

Figure 6.2. Large scale structure visualized by the dark matter density (*orange*) as well as gaseous shocks (*blue*) from the TNG100 simulation. **Credit**: TNG Simulation.

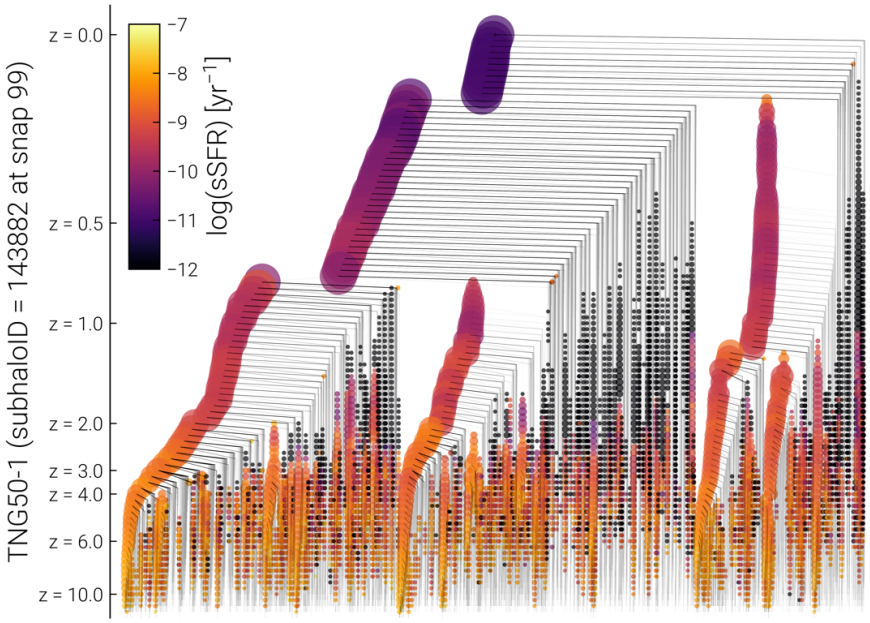

Figure 6.3. A merger tree of a galaxy with total mass of $10^{12.5}\,M_\odot$ at $z = 0$ from the TNG50 simulation. The symbol sizes scale with the total mass at each redshift. The left-most branch is the main progenitor branch, the one with the most massive history behind it. **Credit**: TNG Simulation.

Naturally, Milky Way sized halos ($\sim 10^{12}\,M_\odot$) became of particular interest, and were re-simulated with higher resolution via zoom-ins (e.g. Springel et al., 2008). How successful is ΛCDM on the scales of our own Galaxy? It quickly emerged that there seemed to be a 'problem'

(Moore et al., 1999), in which the observed number of satellite galaxies surrounding the Milky Way, was orders of magnitude smaller than predicted by ΛCDM. Thus, there seems to be a non-linear mapping between the dark and stellar mass.

Such mappings make it then possible to study the cosmic growth of stellar mass. They are constructed by, for example, matching the abundance of predicted dark matter halos to the mass function of galaxies (e.g. Moster et al., 2013). The evolution of the baryonic component of galaxies is then followed via semi-analytical models (e.g. Somerville & Primack, 1999; Guo et al., 2011). The resulting stellar-to-halo-mass relation predicts that Milky Way sized galaxies are amongst the most baryon dominated objects, whereas the lowest and highest mass galaxies are dominated by dark matter, a likely consequence of stellar and AGN feedback respectively. Still, small scale problems of ΛCDM seemed to persist (e.g. de Blok, 2010; Weinberg et al., 2015).

Only fully cosmological, hydrodynamical simulations can investigate the influence and interplay of baryons and dark matter self-consistently. However, they struggled initially to produce large and fast rotating disk galaxies as observed in the world (e.g. Navarro & Benz, 1991; Navarro & Steinmetz, 2000). This was resolved with the Eris simulation (Guedes et al., 2011), which successfully produced a close Milky Way analogue. It naturally arose from cosmological initial conditions by simultaneously evolving dark matter and baryons as well as taking into other processes such as stellar feedback.

Building on these successes, cosmological, hydrodynamical (zoom-in) simulations quickly showed that baryons have an effect on dark matter (and vice versa), which mostly alleviated the previously raised small scale problems with ΛCDM. For example, most small dark matter halos remain dark, because they cannot efficiently cool down the baryons in order for them to form stars (e.g. Sawala et al., 2016; Buck et al., 2019; Engler et al., 2021).

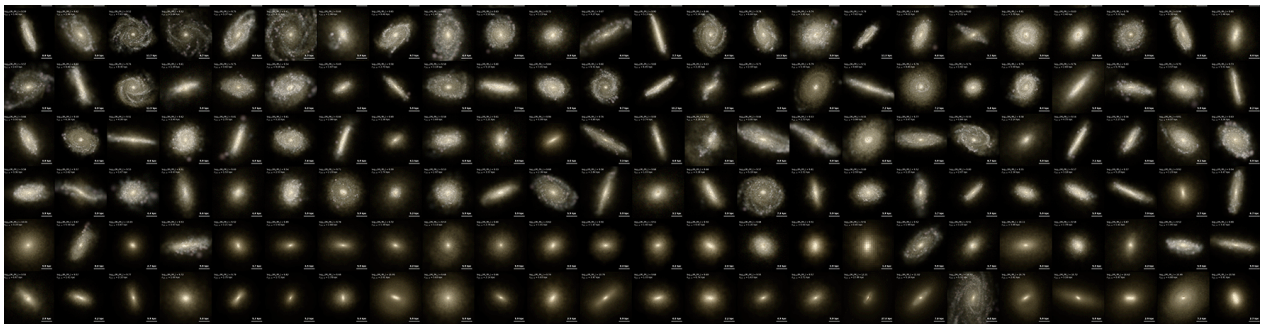

Figure 6.4. Realistic galaxies produced by the TNG50 simulation (Rodriguez-Gomez et al., 2019). **Credit**: TNG Simulation.

This provided the stepping stone for large volume cosmological, hydrodynamical simulations[109] (e.g. Genel et al., 2014; Vogelsberger et al., 2014a,b; Crain et al., 2015; Schaye et al., 2015; Weinberger et al., 2017; Pillepich et al., 2018a,b; Springel et al., 2018; Nelson et al., 2018; Naiman et al., 2018; Marinacci et al., 2018; Pillepich et al., 2019; Nelson et al., 2019b), which take into account various galaxy formation processes and reproduce key observational results of today's galaxy population: perhaps most importantly, they show the same diversity

109: Informative websites regarding these simulations are:
EAGLE: http://icc.dur.ac.uk/Eagle/
Illustris: https://www.illustris-project.org
IllustrisTNG https://www.tng-project.org

of observed galaxy morphologies, as seen in Figure 6.4. Consequently, we can use these simulations to understand the origin of stars in certain regions of galaxies as well as across their entire population. The next part of the thesis is investigating this in the context of the very central parts of galaxies.

STARS IN THE CENTERS OF TNG50 GALAXIES

7

The formation of the central parts of galaxies are thought to be dominated by in-situ processes. The new generation of cosmological, hydrodynamical simulations, like TNG50, make it now possible to test such a hypothesis across the whole galaxy population. *How much are the centers of galaxies really influenced by the hierarchical formation of structure?* As the best quality data usually originates from the bright centers of galaxies, the answer to this question will present a powerful opportunity to extract and test key predictions of ΛCDM from observations.

The contents of this Chapter are submitted to Monthly Notices of the Royal Astronomical Society, in which I am the first author. The contributions from the authors are as follows:

Me I thought about various technical and scientific aspects of this study, directed research ideas, conducted all the analysis, made all the figures and wrote the text of the manuscript.

Nadine Neumayer originally initiated the project and contributed through regular meetings, where intermediate results and plots were discussed and revised to improve the scientific message of the study, as well as provided comments on the draft.

Annalisa Pillepich contributed through the same regular meetings, provided constructive feedback to improve the scientific outcome of this study, helped with understanding certain aspects of the TNG50 simulation as well as commented on the draft.

Neige Frankel helped me define what a galaxy center really is, patiently answered all my questions regarding dynamics and provided extensive comments that specified phrasing of the text.

Ryan Leaman made me aware that a simple cut in radius was not good enough to define a galaxy's center and was persistent in me implementing a better way, which resulted in an improvement of the overall outcome of this study.

Rahul Ramesh conducted calculations for the stripping time of stellar particles in TNG50 and gave helpful comments on the draft.

Lars Hernquist provided comments on the final draft.

Summary

We investigate the origin of stars in the innermost 500 pc of galaxies spanning stellar masses of $5 \times 10^{8-12}\,M_\odot$ at $z = 0$ using the cosmological magnetohydrodynamical TNG50 simulation. Three different origins of stars comprise galactic centers: 1) in-situ (stars born in the center), 2) migrated (stars born elsewhere in the galaxy and ultimately moved to the center), 3) ex-situ (stars accreted from other galaxies). In-situ and migrated stars dominate the central stellar mass budget on average with 73% and 23% respectively. The fraction of central ex-situ stars is above 1% for galaxies $\gtrsim 10^{11}\,M_\odot$. Yet, only 9% of all galaxies exhibit no ex-situ stars in their centers and the scatter of ex-situ mass is significant ($4-6$ dex). Migrated stars predominantly originate closely from the center ($1-2$ kpc). However, if the stars migrated together in clumps, travelled distances usually span $\sim$ 10 kpc. Splitting our sample into different galaxy types reveal that 1) centrals and satellites possess similar amounts and origins of central stars and 2) star forming galaxies ($\gtrsim 10^{10}\,M_\odot$) have on average more ex-situ mass in their centers than quenched ones. We predict readily observable stellar population and dynamical properties for stars of different origins: 1) migrated stars are distinctly young (~ 2 Gyr) and rotationally supported, especially for Milky Way mass galaxies, 2) in-situ stars are most metal-rich and older than migrated stars, 3) ex-situ stars are on random motion dominated orbits and typically the oldest, most metal-poor and α-enhanced population. We demonstrate the diverse pathways of building up a galaxy's center and the close connection to the interaction history with other galaxies as anticipated in a ΛCDM universe. Our work highlights the necessity for cosmological context in formation scenarios of central galactic components and the potential to use galaxy centers as tracers of overall galaxy assembly.

Contents

7.1 INTRODUCTION

The center of a galaxy depicts its brightest and densest region. Thus observations of galaxy centers provide us with the highest data quality, which should enable us to make the most precise predictions about their formation. On the other hand, being also the deepest point of the potential well, the center witnessed the galaxy's overall stellar assembly from the earliest cosmic times onward, as understood from the inside-out formation scenario of galaxies within a ΛCDM Universe. Therefore, many transformative processes of galaxy evolution influence a galaxy's center until the present day, which need to be taken into account to uniquely interpret even the highest quality observations.

As a consequence, a variety of central stellar structures are found in galaxies. Decreasing in size from the order of one kpc to sub parsec scales, these range from bars and (pseudo)bulges (see e.g. Laurikainen et al., 2016; Kormendy & Kennicutt, 2004, for a summary), which can include other structures such as nuclear rings and disks, to nuclear star clusters (NSCs; see e.g. Neumayer et al., 2020, for a summary) and supermassive black holes (SMBHs; see e.g. Kormendy & Ho, 2013, for a summary). Some galaxies may exhibit more than one of these components or none at all. Many of these components possess scaling relations of their structural parameters, such as the Sérsic (1968) index and effective radius of bulges (e.g. Gadotti, 2009; Fisher & Drory, 2010) and the luminosity/mass-size relation of NSCs (e.g. Böker et al., 2004; Côté et al., 2006; Georgiev & Böker, 2014), as well as scaling relations with each other, such as the bulge-SMBH-mass (e.g. Häring & Rix, 2004; Sani et al., 2011; Läsker et al., 2016) and NSC-SMBH-mass relations (e.g. Ferrarese et al., 2006b; Georgiev et al., 2016), which also scale with the stellar mass of their underlying host galaxy (e.g. Scott & Graham, 2013; Reines & Volonteri, 2015; Sánchez-Janssen et al., 2019). Some of these scaling relations can differ for early-type and late-type galaxies, or depend on the bulge type or the presence of a bar (e.g. Gadotti & Kauffmann, 2009; Georgiev et al., 2016; Davis et al., 2019; Sahu et al., 2019).

As diverse as the structural properties of central components are, so are the formation scenarios trying to explain them. Broadly speaking, all of these formation scenarios can be divided into internal and external processes. For example, bulges are thought to form from merger events (e.g. Hopkins et al., 2009c, 2010), from rapid early-on star formation (e.g. Guedes et al., 2013; Okamoto, 2013), from secular evolution (e.g. Kormendy & Kennicutt, 2004; Athanassoula, 2005) or from the migration of clumps formed in the disk at high redshift (e.g. Elmegreen et al., 2009; Dekel et al., 2009); bars form through disk instabilities either in isolation (e.g. Bottema, 2003; Athanassoula et al., 2013) or in a cosmological context (e.g. Romano-Díaz et al., 2008; Kraljic et al., 2012; Peschken & Łokas, 2019); nuclear star clusters are thought to form through either star formation (e.g. Maciejewski, 2004; Aharon & Perets, 2015) or through the migration and successive merging of globular clusters in the center (e.g. Hartmann et al., 2011; Agarwal &

Milosavljević, 2011); SMBHs can grow by accreting gas and by merging with other SMBHs (e.g. Croton et al., 2006; Malbon et al., 2007; Fanidakis et al., 2011; Lapiner et al., 2021). In many cases, the formation of any one component will also influence the others. For example, once a bar is formed it can re-arrange the orbits of stars causing radial migration, or it can efficiently funnel gas to the center, which can trigger star formation in the center and also feed the SMBH. In turn, the AGN feedback caused by the SMBH will then influence the gas supply and hence truncate the formation of stars. Thus, it is important to also understand the interplay between the presence and formation of several central components.

Observationally, we can only indirectly deduce constraints on any of these formation scenarios from the stellar population and dynamical properties of a galaxy's central structure(s). For external galaxies, such necessary measurements are only possible with integral field units (IFUs) that provide spatially resolved stellar population and kinematical maps (e.g. Gadotti et al., 2020; Bittner et al., 2020). While major progress has been made in producing these maps with increasing quality, it is still difficult to disentangle stars from centrally overlapping galaxy components due to the line-of-sight integration - let alone identify stars of different origins within *a* given central component. This is possibly further complicated by the fact that stars with properties characteristic of one formation scenario might be subdominant in luminosity or mass compared to the bulk stellar population.

Even in the Milky Way, it has only become evident fairly recently that all major central components contain metal-poor subpopulations of stars that also exhibit different kinematics. For the Galactic bulge (see e.g. Barbuy et al., 2018, for a summary) there is a smooth transition from rotation to dispersion dominated kinematics for stars decreasing from (super-)solar metallicity all the way to the lowest metallicities ($[\mathrm{Fe/H}] < -2.0\,\mathrm{dex}$) (Ness et al., 2013; Zoccali et al., 2017; Arentsen et al., 2020). To a lesser extent this decrease is also seen for the nuclear stellar disk (Schultheis et al., 2021) with additional evidence of recent star formation activity ($< 1\,\mathrm{Gyr}$) on top of the overall old bulk population ($> 8\,\mathrm{Gyr}$) (Nogueras-Lara et al., 2020, 2021). The nuclear star cluster, which hosts the most metal-rich stars in the Milky Way, also has a subpopulation of sub-solar metallicity stars, which show an asymmetric spatial distribution and a higher degree of rotation (Feldmeier-Krause et al., 2020; Do et al., 2020).

Generally, signs of young, metal-rich and kinematically cold stars in these central structures such as bulges and NSCs, are associated with being formed in-situ from gas infall, while old, metal-poor and dispersion dominated systems are thought to originate from merger processes. However, stars formed in-situ at the beginning of a galaxy's lifetime are also metal-poor and might as well become dispersion dominated over time through various processes, such as resonances created by the bar. Therefore, even though observed properties of stars in the centers of galaxies act as a fossil record of their origin, we need simulations to disentangle which (combinations of) formation scenarios are able to predict those observations.

Cosmological, hydrodynamical galaxy simulations (see e.g. Somerville & Davé, 2015; Vogelsberger et al., 2020, for a summary) are ideal to study the complex formation pathways of galaxy centers as they encompass the most complete conglomeration of galaxy formation processes in a ΛCDM framework, thus capturing internal and external formation processes alike. The most recent simulations are able to produce a realistic, diverse population of galaxies (see e.g. Vogelsberger et al., 2014b; Nelson et al., 2019a, and references therein for Illustris/TNG specifically). Typically, large simulation boxes are used to study global galaxy properties across an array of different galaxies (e.g. Illustris: Genel et al., 2014; Vogelsberger et al., 2014a,b; EAGLE: Schaye et al., 2015; Crain et al., 2015; Horizon-AGN: Dubois et al., 2014, 2016; Magneticum: Hirschmann et al., 2014; Teklu et al., 2015; Bocquet et al., 2016; IllustrisTNG: Weinberger et al., 2017; Pillepich et al., 2018a; SIMBA: Davé et al., 2019), while zoom-in (re-)simulations focus on internal galaxy structures and dynamics (e.g. ERIS: Guedes et al., 2011; NIHAO: Wang et al., 2015; Latte: Wetzel et al., 2016; Auriga: Grand et al., 2017; FIRE-2: Hopkins et al., 2018; NIHAO-UHD: Buck et al., 2020). To understand the mass build-up of galaxy centers we need the advantages of both: a big enough box to probe many different assembly histories and thus galaxy demographics, and a zoom-in like resolution to focus on the center of galaxies and capture internal dynamical processes.

We therefore focus our analysis on the origin of stars in the central few hundred parsecs of galaxies in TNG50 (Pillepich et al., 2019; Nelson et al., 2019b) from the IllustrisTNG simulations. The $51.7\,\mathrm{cMpc}^3$ volume captures two $10^{14}\,\mathrm{M}_\odot$ halos and hundreds of Milky Way like galaxies, whereas the spatial resolution provides hundreds to tens of thousands stellar particles inside the central 500 pc for a four dex range in galaxy stellar mass. Importantly, TNG50 starts to capture the diversity of central components, such as low and high Sérsic index bulges in Milky Way like galaxies (Gargiulo et al., 2021), and performs well in a statistical comparison of simulated and observed bar properties (Rosas-Guevara et al., 2021; Frankel et al., 2022); both which were previously not possible with zoom-in simulations. Hence, TNG50 offers the unique opportunity to study the contribution of stars with different (internal or external) origins to the formation of the galaxy center across diverse galaxy formation pathways and demographics, while predicting the observable imprint that the different formation scenarios impose on the stars in a galaxy's center.

The goal of this study is to appeal to different scientific communities that focus on various central stellar structures of the Milky Way and external galaxies to provide an understanding where the most central stars of galaxies originate across a wide range of galaxy masses inside the TNG modelling framework. Specifically, we also study, for the first time, stars that have migrated towards the center to address formation scenarios of central structures that include the necessity for these processes such as NSC formation. Even though NSCs are not explicitly resolved in TNG50, we hope to offer new incentives for simulations (Antonini et al., 2012; Perets & Mastrobuono-Battisti, 2014; Guillard

et al., 2016) and (semi-)analytical models (Antonini, 2013; Antonini et al., 2015; Leaman & van de Ven, 2021) that are tailored towards NSC formation channels. Lastly, we aim to demonstrate that there are possibilities to use the bright centers of galaxies as a tracer of the galaxy's overall assembly history with readily available observables from current surveys such as Sloan Digital Sky Survey (SDSS) (e.g. Gallazzi et al., 2021).

This Chapter is organized as follows. In Section 7.2 we briefly describe the TNG50 simulation and the definition of properties of galaxies and stars (i.e. stellar particles) that we will analyze at $z = 0$. We also provide a detailed description and verification of selecting stars belonging to a galaxy's center and our galaxy sample selection. In Section 7.3 we present the three different possible origins for stars residing in a galaxy's center and discuss their birth locations. In Section 7.4 we show the results of the different contributions of central stars of different origins across different galaxy population demographics and their observable stellar population and dynamical properties at $z = 0$. In Section 7.5, we discuss our findings and implications from TNG50 on the central mass assembly of galaxies in a cosmological context. We also provide outlooks in the context of the formation of central galaxy components as well as the assembly of the overall host galaxy tailored towards measurements of extragalactic observations. Finally, we conclude our study in Section 7.6.

7.2 TOOLS AND METHODS

We briefly introduce the TNG50 simulation below as well as the properties of TNG50 galaxies and their stars (Section 7.2.3). We then describe in Section 7.2.4 how we define stellar particles that belong to a galaxy's center.

7.2.1 The TNG50 simulation

In this work we primarily study galaxies in TNG50 (Pillepich et al., 2019; Nelson et al., 2019b), which is the highest resolution installment of the IllustrisTNG (Illustris *The Next Generation*; Pillepich et al., 2018b; Springel et al., 2018; Nelson et al., 2018; Naiman et al., 2018; Marinacci et al., 2018) suite of cosmological, magnetohydrodynamical simulations[110]. It provides unprecedented zoom-in like resolution within a representative cosmological volume with a box of 51.7 cMpc on each side.

The simulation was performed with the Arepo code (Springel, 2010b; Pakmor et al., 2011; Pakmor & Springel, 2013; Pakmor et al., 2016), which employs a finite-volume method on a moving-mesh to solve the equations of magnetohydrodynamics coupled with a tree-particle-mesh method for self-gravity. TNG50(-1) has a mass resolution of $4.6 \times 10^5\,M_\odot$ for dark matter and $8.4 \times 10^4\,M_\odot$ for baryonic particles. The softening length is 288 cpc for collisionless particles for $z \leqslant 1$ and

110: IllustrisTNG also encompasses two larger volume runs, namely TNG100 and TNG300 with subsequently coarser resolution.

576 cpc for $z > 1$, whereas the softening length of the gas particles is adaptive depending on the local cell size of the moving mesh with a floor value of 74 cpc. TNG50 is accompanied by three additional simulation runs (-2,-3,-4) that decrease the spatial resolution each time by half. The initial conditions are set according to cosmological parameters measured by Planck Collaboration et al. (2016).

Additionally, the TNG simulations implement a list of physical subgrid models, which describe galaxy formation and evolution, such as stellar formation and feedback, chemical enrichment, galactic winds, supermassive black hole growth and feedback. Details can be found in Weinberger et al. (2017); Pillepich et al. (2018a).

Importantly, the TNG framework successfully reproduces key observational results such as the galaxy stellar mass function up until $z < 4$ (Pillepich et al., 2018b), bi-modality in galaxy color distribution (Nelson et al., 2018), the fraction of quiescent galaxies (Donnari et al., 2019, 2021b), scaling relations, such as the galaxy mass-size relation (Genel et al., 2018), the gas-phase mass-metallicity relation (Torrey et al., 2019) and certain element abundances (Naiman et al., 2018), as well as the clustering of galaxies (Springel et al., 2018) and magnetic fields of massive halos (Marinacci et al., 2018). Specifically, the resolution of TNG50 allows for the study of internal dynamics and structures of galaxies (Pillepich et al., 2019) as well as the influence of stellar and black-hole driven outflows on galaxy evolution (Nelson et al., 2019b).

Results from the TNG simulation are output in 100 snapshots ranging from $z = 20$ until today with an approximate time step of 150 Myr since $z = 4$. For each snapshot dark matter halos are identified by the friends-of-friends (FoF) algorithm (Davis et al., 1985) with a linking length of 0.2, with baryonic particles being attached to the same FoF group based on their nearest dark matter particle. Substructures within these halos, i.e. subhalos, are found through the Subfind algorithm (Springel et al., 2001), which is run on both dark matter and baryonic particles. To track the mass assembly of subhalos/galaxies through cosmic time, merger trees are constructed based on the Sublink algorithm (Rodriguez-Gomez et al., 2015). The merger trees were constructed twice, once based on dark matter and once based on baryonic matter alone.

The entire simulations' particle information for the 100 snapshots, the halo and subhalo catalogues, merger trees as well as many more additional supplementary data catalogues are made publicly available on the TNG website[111] (see also Nelson et al., 2019a, for the public data release).

111: https://www.tng-project.org

7.2.2 General note on calculations

Unless otherwise stated we employ the following definitions in our subsequent calculations and plots. To center the coordinate system on a galaxy of interest we choose the position of the most bound particle (of any type) as the galaxy's center, as given by `SubhaloPos` in the subhalo catalogue. For the systemic velocity of a galaxy we use the median

velocity of the 5% most bound stellar particles. For face-on or edge-on projections, galaxies are oriented such that the z-axis is aligned with the total angular momentum of stellar particles within twice the stellar half mass radius. To track back galaxies in time we exclusively use the merger trees based on following baryonic particles ('Sublink_gal'). Plots that display summary statistics of galaxy populations use a running median with a bin size of 0.25-0.3 dex, which is adapted, if necessary, to ensure a minimum number of ten galaxies per bin. Furthermore, all displayed quantities are in physical units and all provided `SubfindIDs` refer to galaxies at $z = 0$.

Throughout this study the terms in-situ, migrated and ex-situ always refer to stars within the central 500 pc of galaxies unless otherwise stated.

Table 7.2. Properties of galaxies and their individual stars (stellar particles) in TNG50 at $z = 0$ investigated in this study. A detailed description on the exact calculation of the properties as well as the results with respect to the centers of galaxies are found in the indicated sections.

PROPERTY	SHORT DESCRIPTION	DETAILED DESCRIPTION	RESULTS
Overall galaxy			
Mass	total stellar or dynamical (i.e. stars+gas+dark) mass	Appendix B.1.1	Section 7.4.1
Environment	central or satellite		
Star formation activity	star forming or quenched		
Morphology	(kinematically) disk or bulge dominated		
Bar-like feature	present or not, based on Fourier decomposition		
AGN feedback	above or below average AGN feedback based on the mass of the SMBH		
Physical Size	compact or extended with respect to the mass-size relation		
Individual stellar particle			
Age [Gyr]	the lookback time when the star was born	Appendix B.1.2	Section 7.4.2
Metallicity $[\log_{10} Z/Z_\odot]$	the total amount of metals		
[Mg/Fe] [dex]	the abundance of magnesium as a proxy for α-elements		
Circularity ϵ	indicates the type of orbit the star is on		

7.2.3 Galaxy characteristics and properties of their stars

Throughout this study we are interested in two sets of demographics: 1) How does the central mass assembly of galaxies change as a function of a galaxy's overall bulk properties?, 2) How do the intrinsic properties of stars in the center of galaxies differ for different origins?

To address the first question we do not only study the central 500 pc of galaxies as a function of the galaxy's total stellar (dynamical) mass, but we also divide our galaxy sample into different types of galaxies characterized at $z = 0$. To address the second question we study individual properties of stars (i.e. stellar particles) in the center of galaxies at $z = 0$. These investigated characteristics are briefly summarized in Table 7.2, whereas a detailed description on their calculations can be found in Appendix B.1.

7.2.4 Defining stars belonging to a galaxy's center

The most straightforward way to define a galaxy's center at $z = 0$ is to select all stellar particles within a 3D spherical aperture with a given radius r_{cut} around its center. This simple selection will give us knowledge about stellar particles that have an *instantaneous* radius smaller than the selected aperture. However, as we are interested in the mass assembly of the center of galaxies, we want to make sure that selected particles roughly stay inside the spherical aperture over their orbital time at $z = 0$. This ensures that we track particles that changed their orbit, should they have migrated to the center, and not particles that are just on more eccentric orbits.

To estimate, whether the particles are on such orbits confined to the center at $z = 0$, we calculate the (specific) energy E_{cut} a particle on a circular orbit with guiding radius r_{cut} would have, i.e.:

$$E_{cut} = \frac{v_{circ}(r_{cut})^2}{2} + \Phi(r_{cut}). \tag{7.1}$$

The circular velocity v_{circ} is calculated from the spherically enclosed mass (stellar, gas and dark matter particles) $v_{circ}(r) = \frac{GM(<r)}{r}$, whereas the gravitational potential energy Φ is given by the simulation and interpolated to r_{cut}. Stellar particles with total energies $E = \frac{|\mathbf{v}|^2}{2} + \Phi(\mathbf{x})$ less than E_{cut} should roughly be confined on orbits that are within the spherical volume with radius r_{cut}, whereas particles with higher energies are able to move to larger radii and hence spend less time in the center.

We additionally enforce that the angular momentum in the z-direction L_z of stellar particles in the center lies between $L_{cut} = \pm v_{circ} r_{cut}$, as we noticed that some lower mass galaxies with stellar masses $\lesssim 10^{10}\,M_\odot$ had very large L_z and hence large radii with $E < E_{cut}$, which probably stems from the fact that they are undergoing tidal stripping at present time. If particles with large orbital radii (> 2 kpc) still persisted after

this cut, we disregard them as well. These additional steps do not significantly affect the amount of central particles selected for galaxies with stellar masses $\gtrsim 10^{10}\,M_\odot$.

In general, the selection based on Equation 7.1 is a simplification as it assumes a spherical mass distribution, but it gives a good enough estimate of which particles are truly confined to the center without actually integrating their orbits; see Appendix B.2.1 for validation of this with two galaxies contained in the subbox with higher time cadence. We visualize the difference between a simple selection in radius and the one in energy using Equation 7.1 in Figure B.1.

7.2.4.1 *Choice of the central region*

The last step in selecting stellar particles belonging to a galaxy's center is to set a value for r_{cut}, with which we can in turn calculate E_{cut}.

We choose a fixed value of 500 pc[112] for r_{cut} across all galaxies to avoid running too close into the numerical softening length (see Section 7.5.4 for further elaboration on this). We explicitly do not choose to adopt a mass-dependent size, as already with a 10% scaling of the mass-size relation of TNG50 galaxies, we are at the softening length of $10^{10}\,M_\odot$ in stellar mass galaxies, while for the highest mass galaxies we approach 5 kpc, which we do not deem to be central anymore. We also refer the reader to Section 7.5.4 and Appendix B.4 for a more detailed discussion and investigation about numerical resolution effects and the choices of r_{cut}.

112: Due to the selection of stellar particles belonging to the 500 pc center based on their energies, some particles will have instantaneous radii larger than 500 pc at $z = 0$, but typically not larger than 1 kpc.

7.2.4.2 *Galaxy sample selection*

Due to the choice of a fixed central aperture of 500 pc we have to make some selection for our galaxy sample considered in this analysis.

Generally, sizes of TNG50 galaxies are numerically well converged above a stellar mass of $\sim 3 \times 10^8\,M_\odot$ (see Pillepich et al., 2019) at $z = 0$, but we employ a slightly higher lower mass cut of $5 \times 10^8\,M_\odot$ ensuring that the galaxies have a sufficient number of stellar particles for our analysis. We also only consider subhalos/galaxies that are of cosmological origin (i.e. `SubhaloFlag` is true). Any scaling relations used in this analysis such as the galaxy mass-size or the stellar-mass-black-hole-mass relation (to determine for example if galaxies lie above or below the median at fixed stellar mass) are always computed with respect to this galaxy sample.

Furthermore, for our main analysis of the centers of TNG galaxies, we enforce that the ratio of the 3D stellar half mass radius $R_{1/2}$ and the central aperture ($r_{cut} = 500$ pc) is greater than four, i.e. $R_{1/2} \geqslant 2$ kpc. Otherwise, galaxies are too compact for our selected central aperture and about half of the entire galaxy will be classified as "central". Additionally, we make sure that at least a hundred stellar particles are within the central 500 pc according to Section 7.2.4, otherwise the galaxy is disregarded.

Our galaxy sample selection yields 2531 TNG50 galaxies and their masses and sizes are visualized in Figure 7.1. The data points are color-coded by the percentage of stars inside the central 500 pc compared to

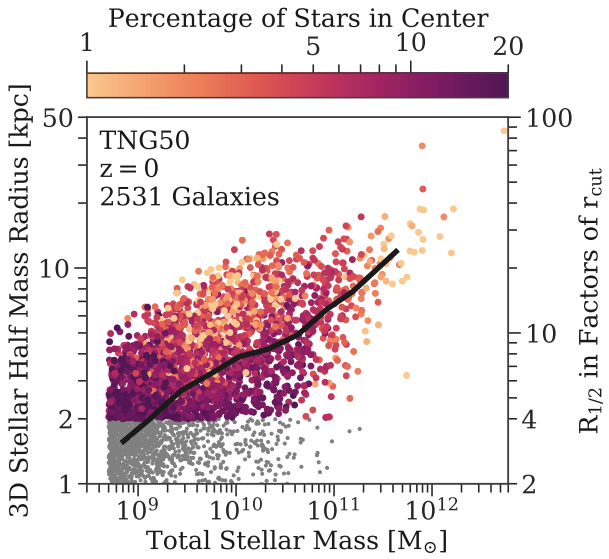

Figure 7.1. Sample selection of TNG50 galaxies at $z = 0$. Stellar mass-size relation of TNG50 galaxies at $z = 0$ considered in this analysis colored coded according to their percentage of stars in the center relative to their total number of stellar particles. We employ a lower total stellar mass cut of $5 \times 10^8\,M_\odot$ as well as a minimum 3D stellar half mass radius $R_{1/2}$ of 2 kpc (i.e., $R_{1/2}/r_{cut} \geqslant 4$ with $r_{cut} = 500$ pc). This results in a sample size of 2531 galaxies. Galaxies not considered in this analysis are displayed as grey points. The median stellar mass-size relation of all TNG50 galaxies is shown as the black line.

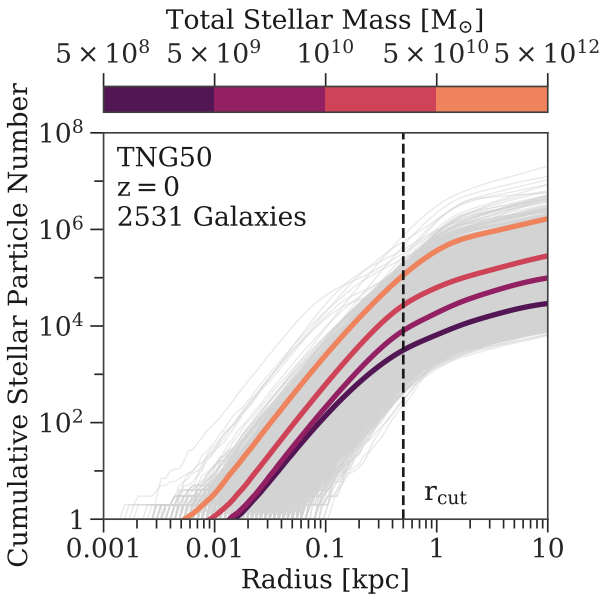

Figure 7.2. Number of stellar particles in the central 500 pc of our TNG50 galaxy sample at $z = 0$. Cumulative number of stellar particles as a function of radius per individual galaxy are shown as thin gray lines. The thick colored lines show the average per galaxy stellar mass bin as depicted by the colorbar. The dashed black line shows our adopted r_{cut} value of 500 pc. The average number of stellar particles within r_{cut} lies between 10^3 and 10^5 for the lowest and highest galaxy mass bins respectively. No individual galaxy in our sample has less than 100 stellar particles in the center.

the total amounts of stars. The color trend is neither uniform in the direction of increasing stellar mass nor size. This hints at different density profiles for galaxies across their stellar mass-size plane.

In Figure 7.2 we show the cumulative number of stellar particles as a function of their instantaneous radius at $z = 0$ for our galaxy sample. The average number of stellar particles in the center, i.e. within 500 pc, is around 10^3 for galaxy stellar masses between $5 \times 10^8\,M_\odot$ and $5 \times 10^9\,M_\odot$ and increases towards 10^5 for the highest mass bin[113]. Hence, our choice for r_{cut} ensures that we have enough stellar particles in the center to reliably study their properties. We can also observe a turnover in the stellar particle number profile at radii around $0.5 - 1$ kpc confirming that we are indeed probing the densest (central) region of TNG50 galaxies.

113: A synonymous measure can be achieved with the `StellarHsml` field, which gives an approximation for the spatial extent a single stellar particle samples from the underlying stellar density field. The spherical radius of stars within 500 pc ranges between $10 - 100$ pc for the highest to lowest mass galaxies respectively.

7.3 THE DIFFERENT ORIGINS OF STARS IN THE CENTER OF TNG50 GALAXIES

After selecting stars in the center of TNG50 galaxies at $z = 0$, we investigate their different origins. We find three general populations of stars in the central region of galaxies, which we describe in Section 7.3.1 in detail. We also present the distribution of their birth origin for stacks

in galaxy stellar mass in Section 7.3.2.

7.3.1 Definition of different origins

We define the following different origins of stars in the center of TNG50 galaxies at $z = 0$:

- *in-situ*: stars were born inside the host galaxy's center and are still found there at $z = 0$.
- *migrated*: stars were born gravitationally bound inside the host galaxy but outside its center. At $z = 0$ they reside in the host galaxy's center.
- *ex-situ*: stars were born inside other galaxies, which merged with the host and are ultimately found inside the host's center at $z = 0$.

7.3.1.1 *Born inside or outside the host galaxy*

To determine whether a star is born inside a galaxy or was brought in through merger events, we use the stellar assembly catalogue[114] produced by methods of Rodriguez-Gomez et al. (2016) for TNG50. This classifies stellar particles that formed along the main progenitor branch of a galaxy, i.e. the galaxy with the most massive history behind it, as in-situ (`InSitu` $= 1$) and otherwise as ex-situ (`InSitu` $= 0$). The ex-situ stars generally have two possible origins: they either came from galaxies that completely merged with the main galaxy, i.e. they are present in the merger tree of the host, or were stripped from galaxies that do not belong to the host's merger tree, e.g. flybys.

114: This particular catalogue has not been publicly released.

Additionally, we treat subhalos/satellites that directly merged onto the main progenitor branch of a galaxy but are flagged as not being of cosmological origin (i.e. `SubhaloFlag` $= 0$ in the subhalo catalogue) differently in this study. These subhalos are often formed within another galaxy as e.g. a fragment of the baryonic disk, contain little dark matter and hence are not thought of as galaxies (see also Nelson et al., 2019a, Section 5.2). Because the construction of the stellar assembly catalogue involves the use of merger trees, which only track stellar particles and star-forming gas cells of subhalos, these spurious galaxies are counted as of ex-situ origin. Here, we change their labelling back to in-situ (i.e. their `InSitu` flag in the stellar assembly catalogue becomes true again) for now (see Section 7.3.1.3 for the implications of this), because we only consider ex-situ particles coming from true external galaxies. We verify with Figure B.4 in Appendix B.3 that this change does not alter the overall *total* ex-situ stellar mass fraction of TNG50 galaxies significantly. We note that spurious galaxies brought to the main progenitor branch of the host galaxy through prior merging with a real galaxy are continued to be counted as ex-situ.

7.3.1.2 *Born in-situ or migrated to the center*

To address whether a stellar particle is born inside the center of the host galaxy or migrated to the center from elsewhere inside the host galaxy, we need to determine its birth radius. A stellar particle with a birth radius smaller than $r_{cut} = 500\,pc$ is then consequently born in-situ and otherwise counts as migrated[115].

115: We here apply a simple cut in the birth radius instead of calculating E_{cut} (i.e. following Section 7.2.4), as the potential is not recorded for every snapshot.

In TNG, two new fields (`BirthPos` and `BirthVel`) for their stellar particles were added. These represent the spatial position and velocity of the star-forming gas cell that parented the stellar particle at its exact time of birth (i.e. `GFM_StellarFormationTime`). In theory, this provides us with knowledge of the *exact* birth condition of a stellar particle at the original time step resolution of the simulation; and not only at the output time steps of the snapshots.

Because these quantities are provided in the reference frame of the simulation box, we need to center them on the reference frame of the galaxy of interest. This however becomes an impossible task to do to the precision needed for our analysis, as we only know the center position of subhalos at the one hundred output snapshots, but the information of its trajectory in-between is lost. We find that even interpolating the subhalos' position with a higher order spline to the exact birth times of stars can lead to centering offsets of several kpc, especially when there is a merger in process or a pericenter passage around another galaxy (see Figure B.2). As we are interested in typical scales of one kpc or less in this study, this problem is severe and will result in a strong bias towards stars being classified as migrated even though they where formed inside our selected spherical aperture.

We therefore define the birth position of stellar particles as the position they have in the snapshot they first appear in. Practically this is done by matching particles at $z = 0$ to their birth snapshot through their unique `ParticleIDs`. The caveat of this approach is that the stellar particles have already moved since their exact formation time, which can also lead to a wrong classification of migrated and in-situ stars. However, the error created by this approach is much smaller than the incorrect centering described above (see Figure B.3).

We verify this approach by looking at two subhalos that reside in the subboxes of TNG50. The subbox has 3600 snapshot outputs, which makes it possible to track the center position of galaxies across a much finer time resolution of a few Myr. The reader is referred to Appendix B.2.2 for details.

7.3.1.3 *Clumpy or smoothly migrated*

Because we have changed the `InSitu` flag from the stellar assembly catalogue for spurious galaxies, in Section 7.3.1.1, we now find two types of migrated stellar particles in the center of galaxies. Stars either travelled individually ('smoothly' migrated) or together in clumps ('clumpy' migrated) to their galaxy's center. Smoothly migrated stars are genuinely born on the main progenitor branch of the subhalo/-galaxy in question and the clumpy migrated stars originate from these spurious galaxies, i.e. stellar clumps.

Generally, these clumps are ubiquitous in TNG50 galaxies, about 36% of all galaxies considered in this work have at least one throughout their life time. In stellar or gas surface mass density maps they 'look' like massive star cluster like objects (see Figure B.7 for an example) that form within spiral arms or gaseous (disk) fragments during galaxy interactions. However, we want to be extremely cautious here, as it is unclear, if their formation is physical or due to some numerical artifact, even though measures against artificial fragmentation are in place. In fact, their sizes (i.e. 3D stellar half mass radii) lie mostly below the gravitational softening length of TNG50.

Once these clumps are formed, however, their dynamical evolution within the host galaxy is determined by gravity, which we believe is well captured in TNG50 (modulo the softening). Hence, depending on their density and the exerted tidal forces on the clumps, they are either completely disrupted or travel to the center of their host galaxy due to dynamical friction and deposit their stellar particles there. Their typical stellar masses are $\sim 10^8\,M_\odot$. We point the interested reader to Appendix B.5 for more statistics on the clumps and their properties. We provide an extensive discussion on the existence and formation of stellar clumps in simulations and observation in Section 7.5.3.

For the rest of this Chapter, we sometimes make the distinction between migrated particles coming from the 'smooth' or 'clumpy' migration, if it is explicitly stated. Otherwise, all general references to migrated properties always include both types.

7.3.2 Birth locations of the central stars

The distributions of birth radii of in-situ, migrated and ex-situ central stars are illustrated in Figure 7.3 in stacks of galaxy stellar mass.

The in-situ stars are born (by definition) in the center of the host galaxy at $z = 0$. The peak of the birth radii distribution is around $200 - 300\,\mathrm{pc}$ for galaxies larger than $10^{10}\,M_\odot$ and shifts slightly towards larger radii for the lower mass galaxy bins. We also see that higher mass galaxies birth more in-situ stars at all radii and hence are more centrally concentrated (see also Figure 7.2).

7.3.2.1 *Individually migrated stars originate close to the galaxy's center*

Most of the smoothly migrated stellar particles were also born close to the center with radii between 500 pc and 1 kpc, which is partly due to how we have defined them (i.e. purely based on their birth radius) and partly a consequence of the typical density profile of galaxies (i.e. more stars reside in the center of galaxies). For galaxies below $10^{10}\,M_\odot$ the distribution of birth radii declines exponentially reaching the highest values of about 10 kpc. The lowest mass galaxies in our sample ($\leqslant 5 \times 10^9\,M_\odot$) have 11% of smoothly migrated stars, which are born in the range of $1 - 10\,\mathrm{kpc}$, whereas this increases slightly to 17% for the next higher mass bin ($\leqslant 10^{10}\,M_\odot$).

For galaxies above $10^{10}\,M_\odot$ we observe a plateau for the distribution

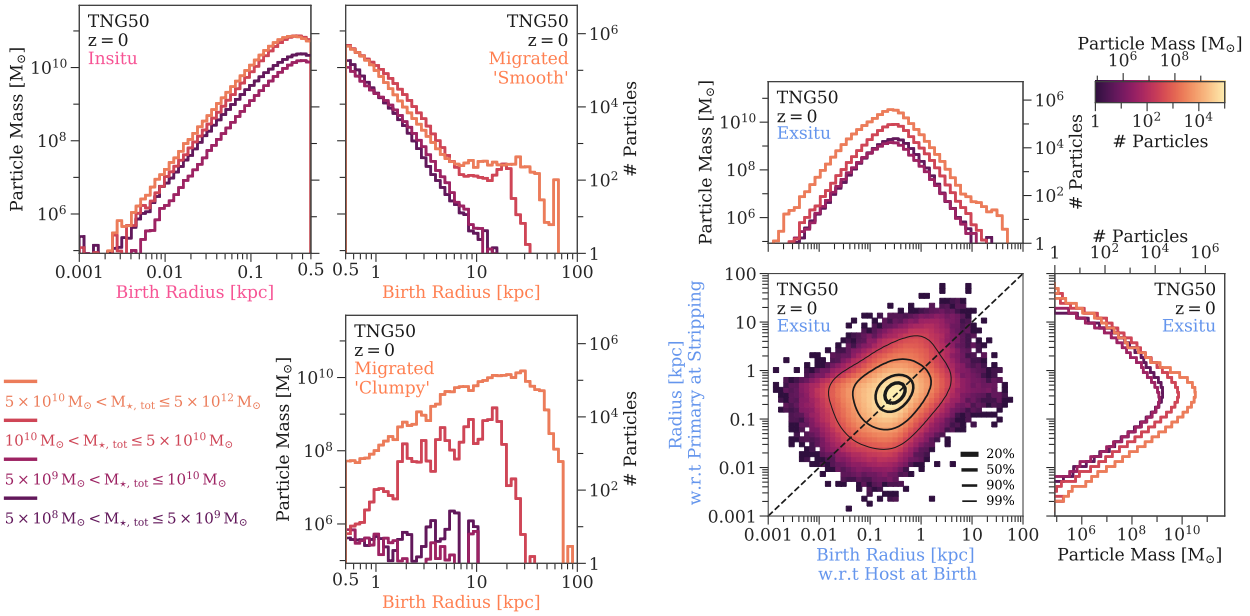

Figure 7.3. Distribution of birth radii of in-situ, migrated and ex-situ stellar populations in the central 500 pc of TNG50 galaxies at z = 0. *Left*: Histograms of birth radii of the in-situ, 'smooth' migrated and 'clumpy' migrated stars colored according to stacks of galaxy stellar mass. The left hand side of the y-axis shows stacked particle mass, whereas the right hand side shows the number of stellar particles. The migrated stars can originate from large radii (> 10 kpc) and the smoothly and clumpy migrated stars show different distributions. *Right*: 2D histogram of the birth radius with respect to the host galaxy at birth and the radius with respect to the primary galaxy (i.e. final z = 0 host) at the time of stripping for all central ex-situ stars in our galaxy sample. The contours (from thicker to thinner lines) include 20%, 50%, 90% and 99% of all ex-situ particles. The respective 1D histograms for stacks in galaxy stellar mass are also shown. Most ex-situ stars are born in the central ~ 1 kpc of their birth galaxy and stay together until they are deposited also within the central ~ 1 kpc of their z = 0 host galaxy.

of birth radii starting at ~ 10 kpc, which stops at around 30 kpc and 60 kpc for galaxies with $\leqslant 5 \times 10^9\,M_\odot$ and $> 5 \times 10^9\,M_\odot$ respectively. The migrated stars originating from these large distances likely come from gas that was stripped during a merger, but which was already attributed to be gravitationally bound to the primary galaxy according to the Subfind algorithm and hence was counted as being born in-situ to the primary host. The percentage of smoothly migrated stars with birth radii larger than 1 kpc is around 20% and 14% for the two highest stellar mass bins respectively.

7.3.2.2 *Stars migrated in clumps originate from the outskirts of galaxies*

The clumpy migrated stars show a distinctively different distribution than the smoothly migrated ones. For galaxies below $10^{10}\,M_\odot$ their contribution is negligible. For galaxies between $10^{10}\,M_\odot$ and $5 \times 10^{10}\,M_\odot$ the clumpy migrated stars are only 3% of the total migrated stars, whereas for galaxies above $5 \times 10^{10}\,M_\odot$ the contribution rises to almost 50%. Therefore, clump migration is only important for high mass galaxies, where it becomes the dominant driver for contributing migrated stars in the centers (see also Section B.5).

Furthermore, the peak of the birth radii distribution of clumpy migrated stars is above 10 kpc for the high mass galaxies. This is in agreement with the fact that the gaseous disk of galaxies is much more

extended than the stellar one (e.g. Nelson et al., 2012). Stars travelling in stellar clumps are therefore able to migrate to the center of galaxies from much farther distances compared to when they travel individually.

7.3.2.3 *Central ex-situ stars originate from the nuclei of their birth galaxies*

Regarding the ex-situ stars, we investigate two different locations: 1) their birth place with respect to their *birth* host galaxy and 2) the location they were deposited inside their $z = 0$ *host* (primary). The latter is defined as the radius the stellar particles have with respect to the primary at stripping time, i.e. the time they last switched galaxies.

We show the distribution of these two quantities also in Figure 7.3 in the same stacks of galaxy stellar mass, as well as the 2D distribution of all ex-situ stars for these two radii. About half of all ex-situ stars that reside in the center of galaxies at $z = 0$ exhibit values between 100 pc and 1 kpc for both radii respectively. This means that the ex-situ stars are also born in the center of their respective birth galaxies as well as remain in said center until they are deposited right in the center of the primary galaxy during the merger process. Hence, the central, most bound cores of galaxies are more likely to stay together during accretion events until they arrive close to the center of the primary galaxy and ultimately deposit a large quantity of stars there. This is a consequence of mergers preserving the rank order of the particles' binding energy (Barnes, 1988; Hopkins et al., 2009c).

We also find two other cases of ex-situ stars, albeit much lower in number. Firstly, TNG predicts a slight excess of ex-situ stars that are born at larger radii ($1 - 100$ kpc), but are still deposited close to the primary galaxy at stripping time, i.e. within ~ 1 kpc. These stars represent a second generation of 'migrated' stars; or likely in the case of ex-situ stars with birth radii of $\geqslant 10$ kpc, stars that were formed from stripped gas during secondary mergers, which only appear for the most massive $z = 0$ hosts. Consequently, these ex-situ stars were born at large radii in their respective host galaxies (i.e. which will become the secondary galaxy during the merger process onto the $z = 0$ host), then migrated to the center of said galaxy in order to be deposited close to the center of the primary host during accretion. We confirm this by explicitly checking that their radii are indeed central ($\lesssim 1$ kpc) with respect to the merging host galaxy one snapshot before the merger coalesces.

The second case represents ex-situ stars that were deposited at larger radii from the primary (> 1 kpc), but born within the central 1 kpc of their birth galaxy. Despite being stripped outside the center of the $z = 0$ host galaxy, these stars still were able to migrate such that they are found in the center of their respective galaxy at $z = 0$. There is a possibility that these stars were stripped earlier, i.e. before the merger coalesces, but their dynamics were still following the orbit of the galaxy undergoing the merger and hence they could arrive at the center of the final host galaxy.

7.4 THE CENTRAL IN-SITU, MIGRATED AND EX-SITU POPULATIONS ACROSS TNG50 GALAXIES

In this section we present our results of in-situ, migrated and ex-situ populations within the central ~ 500 pc of TNG50 galaxies.

We study their contributions across different galaxy properties (Section 7.4.1) and examine differences in their stellar population and dynamical properties (Section 7.4.2).

7.4.1 Galaxy population demographics

Below we depict the contribution of the central stellar mass of the different origins as an overall trend with galaxy mass (Section 7.4.1.1), in correlation to each other (Sec 7.4.1.2) and for different galaxy types (Section 7.4.1.3).

7.4.1.1 *Galaxy mass trends*

In Figure 7.4 we give an overview of the absolute and relative contribution of the ex-situ, migrated and in-situ population across galaxy masses (both stellar and dynamical) in TNG50.

For all three populations the central stellar mass increases with increasing galaxy mass with the in-situ population dominating at all galaxy masses. Whereas the relation for the in-situ and the smoothly migrated stars have the same shape, the slope for the ex-situ population is steeper. The latter also shows a larger overall scatter due to the stochasticity of merger events contributing stars to the center.

Even though the fractional mass of the ex-situ population in the center is negligible for galaxy stellar masses below 10^{11} $M_\odot$, there are only 227 (9%) galaxies in our total sample that have no central ex-situ mass. Above 10^{11} $M_\odot$ the ex-situ mass becomes of the same order as the in-situ and migrated population, which is a consequence of mergers contributing a significant amount stellar mass to build up of these galaxies. The ex-situ mass reaches about 10% of the total central stellar mass at the highest galaxy masses, albeit with a large scatter of up to 60%.

Around galaxy stellar masses of about 5×10^{10} $M_\odot$, the relation flattens for the in-situ and smoothly migrated stars, with the in-situ population reaching about 4% of the total galaxy stellar mass. Although we have low number statistics of galaxies in this regime within the TNG50 volume (there are 18 galaxies with stellar masses above 5×10^{11} $M_\odot$), it is reasonable that the in-situ mass goes down, because the ex-situ mass increases in addition to galaxies being quenched by AGN feedback. The consequential increased stochasticity[116] is also seen by the larger scatter in the in-situ and migrated population at the highest galaxy stellar masses.

The contribution of clumpy migrated stars to the overall central migrated population only starts to significantly affect galaxies with stellar

116: Another possibility for the large scatter at high galaxy stellar masses for the in-situ and migrated central stellar mass could be stars formed from accreted gas, which was brought in by gas-rich mergers. We do not quantify this further as it is beyond the scope of this study.

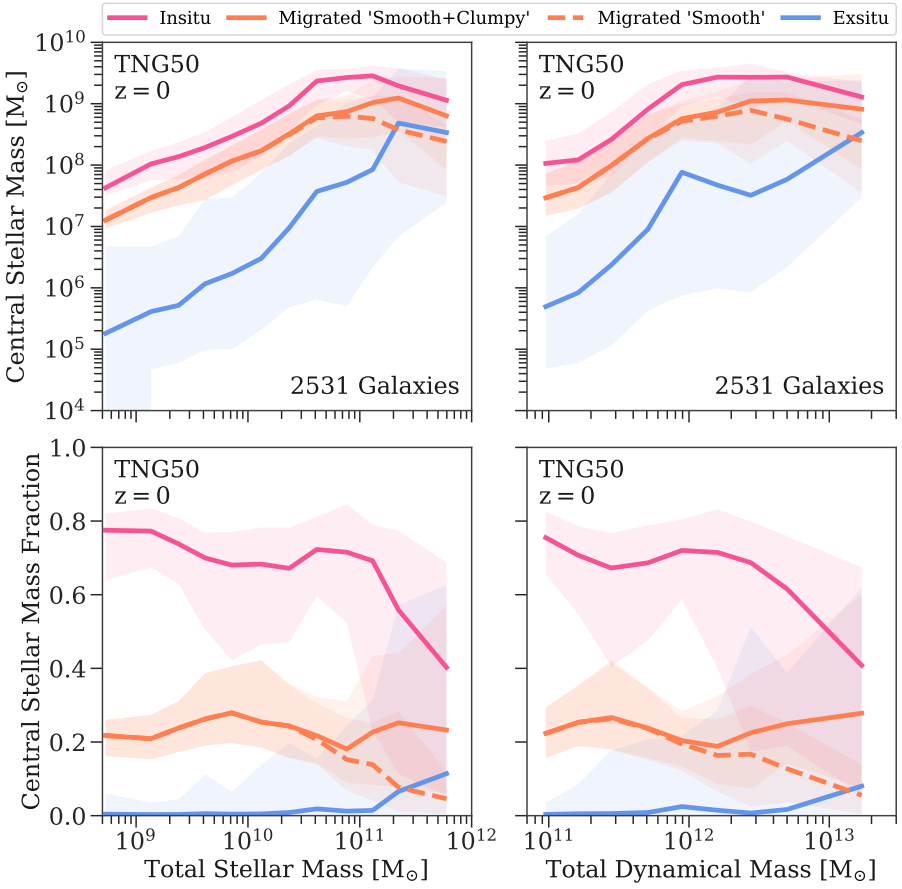

Figure 7.4. Central (500 pc) stellar mass of the in-situ, migrated and ex-situ populations of TNG50 galaxies at z = 0. Median trends of central stellar mass (*top panels*) and central stellar mass fraction (*bottom panels*) as a function of the galaxies' total stellar mass (*left*) and total dynamical mass (*right*) divided in the three origins: in-situ (*pink*), migrated (*orange*) and ex-situ (*blue*). The migrated population is shown for both 'smooth+clumpy' (*solid line*) and just 'smooth' (*dashed line*) migration (see 7.3.1.3 for details). Shaded areas show the 16th and 84th percentiles. Overall the in-situ population dominates on average across all galaxy masses with the migrated population contributing around 20% to the total central stellar mass. Only above galaxy masses of $10^{11}\,M_\odot$ the ex-situ population starts to significantly contribute to the central mass build-up.

masses higher than $5 \times 10^{10}\,M_\odot$. For galaxies higher than $2 \times 10^{11}\,M_\odot$ the clumps are responsible for roughly quadrupling the mass of migrated stars, or, in fractional terms, increasing the contribution of migrated stars to the total central mass from below 10% to slightly above 20%. Hence, the clumps are important driver to bring in stars from the outskirts of galaxies in TNG50.

Taking into account the entire migrated population ('smooth+clumpy'), we find a contribution of around 20% to the total stellar mass in the center across all TNG50 galaxies. Interestingly, the total central migrated fraction around galaxy stellar masses of $\sim 10^{10}\,M_\odot$ slightly increases, with the 84th percentile reaching almost 40%. We explicitly confirm that this is *not* due to mixing galaxies with different sizes and hence different total central stellar masses (see also Figure 7.1).

The statements made so far also apply when correlating the central stellar masses of the three populations with the total dynamical mass of TNG50 galaxies. The larger scatter in all three relations is due to the scatter in the stellar-to-halo mass relation.

7.4.1.2 *The diversity of central stellar mass at fixed galaxy mass*

In Figure 7.5 three correlations between the central ex-situ, migrated and in-situ stellar mass as 2D Gaussian kernel estimates in bins of total galaxy stellar masses are shown. The bins were specifically chosen

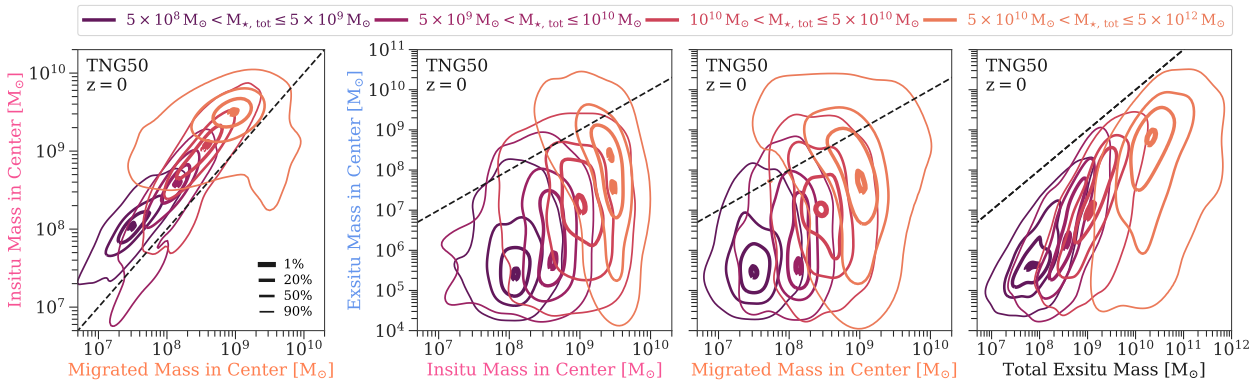

Figure 7.5. 2D distributions of the central (500 pc) in-situ, migrated, ex-situ as well as the *total* ex-situ stellar mass of TNG50 galaxies at z = 0. Gaussian kernel density estimates for different combinations of in-situ, migrated and ex-situ mass in the center as well as total ex-situ mass color-coded according to four different total stellar mass bins. The contours show different percentiles encompassing 1%, 20%, 50% and 90% of all data points (*thickest to thinnest line*). The black dashed line shows the one-to-one relation in all panels. The correlation between the central mass of the in-situ and migrated population follow the one-to-one relation closely with a fixed offset, whereas the central ex-situ population exhibits a large scatter across the other central populations.

based on the change of the average migrated fraction as a function of galaxy stellar mass and, in case of the highest mass bin, to ensure enough galaxies per bin to reliably perform the kernel density estimate.

***In-situ vs. migrated mass (Figure 7.5, first panel)*:** At all stellar masses, the mass of migrated stars correlates strongly with the in-situ stellar mass with three times as much in-situ than migrated mass. This reflects our previous statements that the shape of the median relation of the central in-situ and migrated mass versus the total stellar galaxy mass is similar.

Nevertheless, for some galaxies the migrated mass is larger than the in-situ mass in the center as seen by the 90% contours for the three highest galaxy mass bins in the range of $5 \times 10^9 - 5 \times 10^{12}\,\mathrm{M}_\odot$. Galaxies in this regime are dominated by clumpy migration. Hence, the mass contributed to the center by clumps can be significant enough to break the otherwise tight one-to-one relation of migrated and in-situ mass.

Lastly, we find for the 90% contour in the highest mass bin for galaxies above $5 \times 10^{10}\,\mathrm{M}_\odot$ that there is a larger tail of galaxies with lower in-situ and migrated mass in the center. Most galaxies situated in this space have a high ex-situ central mass fraction of 40% or higher.

***Ex-situ vs. in-situ and migrated mass (Figure 7.5, second and third panels)*:** At roughly fixed central in-situ or migrated masses there is a large variety of ex-situ mass that is deposited in the center of galaxies. The scatter of the ex-situ mass in the center increases roughly from four to six dex the from smallest to largest galaxy stellar mass bin. Compared to that the scatter in the in-situ and migrated mass direction is rather small, being roughly one dex across all galaxy stellar mass bins. However, some galaxies in mass bins below $5 \times 10^{10}\,\mathrm{M}_\odot$ have lower in-situ masses of up to one dex below the majority of the other galaxies in

their respective bins. Galaxies lying in this region have above average migrated fractions of 40% or more with some reaching extreme values of above 80%.

The spread in migrated mass compared to the in-situ mass is larger for the highest mass galaxies. This is mainly due to the increased stochasticity in the total *central* stellar mass for the 18 galaxies above $5 \times 10^{11}\,M_\odot$ in galaxy stellar mass, which almost spans one dex as opposed to only a quarter dex for galaxies between 5×10^{10} and $5 \times 10^{11}\,M_\odot$. These 18 galaxies lie between the 50% and 90% contour and have ex-situ masses spanning from 10^7 to $10^{11}\,M_\odot$. Their in-situ masses are exclusively below the 50% contour, whereas their respective migrated masses can lie towards lower or higher values.

The peak of the central ex-situ mass distributions begins to rise for galaxies above $10^{10}\,M_\odot$ in total stellar mass, going from about three dex below the one-to-one relation to one dex. This break point roughly translates to $4 \times 10^8\,M_\odot$ in central in-situ mass and $1-2 \times 10^8\,M_\odot$ in central migrated mass. The former roughly coincides with the critical mass needed for the SMBH to be in the kinetic feedback mode (e.g. Zinger et al., 2020, Figure 1). The *total* ex-situ mass also begins to rise for galaxies with total stellar masses above a few $10^{10}\,M_\odot$ (see Figure B.4).

Central ex-situ vs. total ex-situ mass (Figure 7.5, fourth panel): Lastly, we also show the correlation between the *central* ex-situ mass and the *total* ex-situ mass, i.e. all stars that were ever accreted onto the $z = 0$ host galaxy. For fixed total galaxy stellar mass the slope of the contours depict that a higher total ex-situ mass generally also implies a higher central ex-situ mass. The slope of this correlation is rather steep. While the total ex-situ mass spans approximately two dex per galaxy stellar mass bin, the ex-situ mass in the center spans four to six dex from the lowest to highest galaxy stellar masses. Consequently, it is quite stochastic which merging satellite galaxies deposit stellar mass in the center.

Furthermore, the central density contours shift closer to the one-to-one relation with increasing galaxy stellar mass. This means that more galaxies in the highest mass bin have mergers that are more effective in bringing a larger fraction of their total ex-situ mass into their center as opposed to lower mass galaxies. Nevertheless, the 90% contours for galaxy stellar masses above $5 \times 10^9\,M_\odot$ extend right up to the one-to-one relation, meaning that there some galaxies that have almost all their ex-situ mass in the central 500 pc.

7.4.1.3 *Trends for different galaxy types*

Galaxies with different present-day properties are thought to have undergone different formation pathways. Is this reflected in different contributions of in-situ, migrated and ex-situ stars building up the center of these galaxies?

In Figure 7.6 we show the running median of the central stellar mass of the three origins as a function of total galaxy stellar mass split into six different galaxy properties. The definitions of the different galaxy

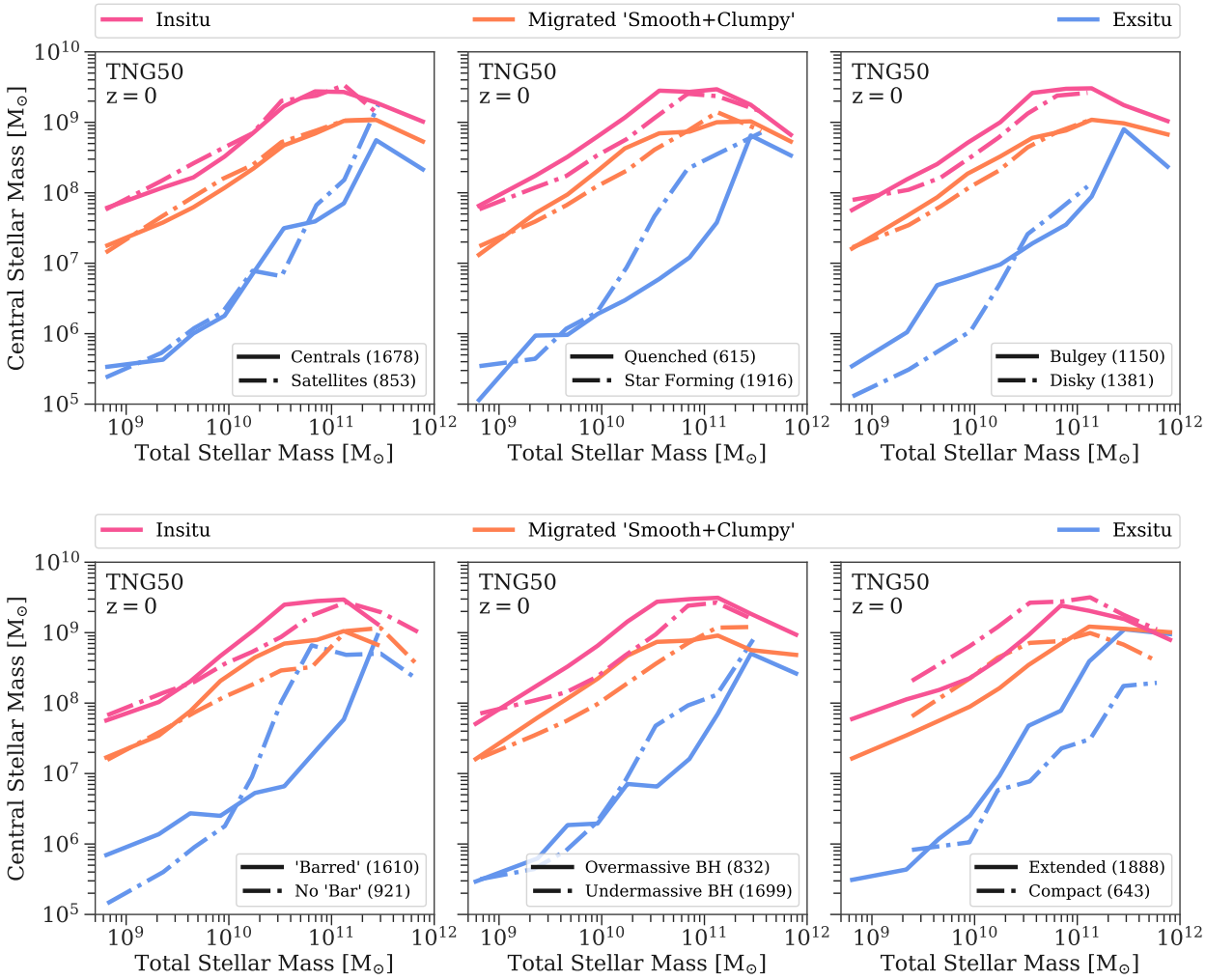

Figure 7.6. Differences in the central (500 pc) in-situ, migrated and ex-situ populations for different galaxy properties of TNG50 galaxies at z = 0. Each panel shows median trends of central stellar mass divided in the three origins: in-situ (*pink*), migrated (*orange*) and ex-situ (*blue*) as a function of the galaxies' total stellar mass. The dashed and solid lines split the TNG50 galaxy population according to different properties, which are (*form left to right*): central vs. satellite, quenched vs. star forming, bulgey vs. disky, 'barred' vs. 'non barred', overmassive vs. undermassive black holes (BH) and extended vs. compact galaxies. The bracketed numbers show the total amount of galaxies in each category.

properties are summarized in Table 7.2 and described in detail in Appendix B.1.1.

All in all, the most significant differences are seen in the central ex-situ population across various galaxy properties. This significance manifests in separation between the median relations including the scatter (which we do not show, however, in favour of clarity). Small differences for the in-situ and migrated populations are not significant with respect to the scatter around the median relations.

Centrals vs. Satellites (Figure 7.6, top left panel): On average, centrals and satellites contain the same amount of central in-situ, migrated and ex-situ mass, showing that their central 500 pc is unaffected by their environment at $z = 0$. This is sensible considering that galaxy centers likely assemble before the galaxy becomes a satellites. Additionally, most environmental effects should first take effect in the out-

skirts of galaxies. Similarly, we find no significant difference in the central mass of the three populations, when the galaxies are divided by the mass of their host halo.

Quenched vs. Star Forming (Figure 7.6, top middle panel): Quenched galaxies between 5×10^9 and $5 \times 10^{10}\,M_\odot$ have slightly higher central in-situ and migrated mass than for star forming ones. This difference primarily arises because the star forming galaxies tend to have lower central densities on average than quenched ones.

A larger difference is seen in the ex-situ. For galaxy stellar masses above $10^{10}\,M_\odot$ the average ex-situ mass starts to rise more rapidly for star forming galaxies than for quenched ones. For galaxies around $5 \times 10^{10}\,M_\odot$ this difference becomes largest, with the median central ex-situ mass of star forming galaxies being higher by more than one dex.

While this trend may seemingly be counter-intuitive for the current consensus of galaxy evolution, the difference is also true when considering the *total* ex-situ stellar mass in TNG50 (and also TNG100) as seen in Figure B.4 in Appendix B.2.2. This could be an indication that today's star forming galaxies had more or larger mass ratio mergers with galaxies with high gas content at later cosmic times (see Section 7.5.1 for a further discussion). We obtain a consistent picture when galaxies are divided according to their $g-i$ colour or total gas mass at $z = 0$.

Bulgey vs. Disky (Figure 7.6, top right panel): The in-situ and migrated central mass for disky and bulgey galaxies show a similar trend as for the star forming and quenched population. However, the trend for the central ex-situ mass is distinct. Bulgey galaxies below $10^{10}\,M_\odot$ in stellar mass have higher ex-situ masses (by roughly half a dex) in their centers than their disky counterparts. This difference disappears for galaxy stellar masses above $10^{10}\,M_\odot$.

We have checked the median relation for the *total* ex-situ mass and find that bulgey galaxies have a constant higher offset of about 0.25 dex compared to disk galaxies across the whole galaxy mass range. Hence, disky galaxies below $10^{10}\,M_\odot$ have not only lower absolute central and total ex-situ masses, but also a lower central-to-total ex-situ fraction of about 0.4% as compared to 1% for bulge dominated galaxies. Thus the relative amount of ex-situ mass that is deposited in the center might be an important driver for morphological transformation in these lower galaxy mass regimes.

For galaxies above $10^{10}\,M_\odot$ in stellar mass, the central-to-total ex-situ fraction decreases strongly as a function of galaxy stellar mass, with disk galaxies having consequently slightly higher values. This could be an indication that once a massive rational support exists in the stellar component it is hard to destroy it through mergers. Similar relations are found when adopting other definitions for disky and bulgy galaxies, such as the ratio of the kinetic energy in ordered motion compared to the total kinetic energy (see Rodriguez-Gomez et al., 2017).

Barred vs. No Bar (Figure 7.6, bottom left panel): For galaxies below $10^{10}\,M_\odot$ TNG50 predicts no difference in the central in-situ and migrated mass, however the galaxies with bar-like features have higher ex-situ masses than galaxies with no bar-like features. This trend is similar for the bulgey vs. disky galaxies. We have explicitly checked that indeed high ex-situ masses in the center of galaxies within this mass regime mainly occur in bulgey and barred galaxies, whereas bulgey and unbarred galaxies as well as disky galaxies, both barred and unbarred, have lower central ex-situ masses by approximately one dex.

For galaxies above $10^{10}\,M_\odot$ in total stellar mass, this relation for the central ex-situ mass swaps. In this regime unbarred galaxies have higher ex-situ masses in the center regardless whether they are disky or bulgey. We find that the same statements for barred and unbarred galaxies across the entire mass range are true when correlating the *total* ex-situ mass of galaxies.

Lastly, the in-situ and migrated mass in the center is higher for barred galaxies between $10^{10}\,M_\odot$ and $10^{11}\,M_\odot$. Hence, barred galaxies in this mass regime have higher central densities than unbarred galaxies in TNG50, which is consistent with observations (see Díaz-García et al., 2016b).

Over- vs. Undermassive Black Holes (Figure 7.6, bottom middle panel): We could expect that AGN feedback has an influence on the stellar mass growth in the center of galaxies. We therefore split our TNG50 sample according to whether the galaxies have an over- or undermassive black hole at $z = 0$. Identical relations are found when the galaxy population is split according to the cumulative energy injection of each feedback mode or both.

On average, galaxies between $10^{10}\,M_\odot$ and $10^{11}\,M_\odot$ in stellar mass with an undermassive black hole have a higher central ex-situ mass by about one dex than galaxies with an overmassive black hole at the same stellar masses. For galaxies with total stellar masses in the range of $5 \times 10^9 - 5 \times 10^{10}\,M_\odot$, the ones with an overmassive black hole have in-situ and migrated masses in the center that are about half a dex higher than for galaxies with an undermassive black hole. Consequently, galaxies with overmassive black holes in this mass regime have higher central densities.

We find that mainly all of these differences in the in-situ, migrated and ex-situ mass for galaxies with over- and undermassive black holes emerge because galaxies at fixed stellar mass with overmassive black holes tend to be more compact in TNG50 and vice versa. Therefore, a similar behaviour of the central stellar mass in the three populations with total galaxy stellar mass is found when the galaxy population is split into compact and extended galaxies (see below). This connection between black hole masses, central densities and sizes of galaxies at fixed galaxy stellar mass is also found in observations (Chen et al., 2020).

Extended vs. Compact (Figure 7.6, bottom right panel): Extended

galaxies tend to have on average more ex-situ mass in the center than compact galaxies at the same total stellar mass. The difference is around one dex for galaxies above $10^{10}\,M_\odot$ in stellar mass.

When we correlate with the *total* ex-situ mass, we find an opposite behaviour in TNG50. Galaxies $\lesssim 5 \times 10^{10}\,M_\odot$ and with higher total ex-situ fractions are on average more extended (see Figure B.5 in Appendix B.3).

Compact galaxies between $5 \times 10^9\,M_\odot$ and $5 \times 10^{10}\,M_\odot$ have more in-situ and migrated mass in the center, and therefore higher central densities (and black hole masses, see above). As a matter of fact, this difference is also seen for quenched vs. star forming and bulgey vs. disky galaxies, even though to a lesser extent. This stems from the fact that generally star forming galaxies tend to be more disky and hence more extended and vice versa.

7.4.2 Stellar population and dynamical properties

Are there distinguishable features in the stellar population and dynamical properties of the in-situ, migrated and ex-situ stars? The short answer is yes, especially for galaxies below $\lesssim 10^{11}\,M_\odot$, where the majority of ex-situ stars originate from lower mass satellites.

7.4.2.1 *Average age, metallicity and [Mg/Fe] of central stars*

Metallicities, ages and magnesium-to-iron abundances [Mg/Fe] of stars encode information about their birth places. Figure 7.7 illustrates average quantities of stellar populations belonging to the in-situ, migrated and ex-situ origin as a function of their galaxy's stellar mass. We also show separate relations for migrated stars that have birth radii larger than 1 kpc to exclude the majority of migrated stars that were born close to the center, which dominate the average stellar population properties (see smoothly migrated stars in Figure 7.3).

Metallicity (Figure 7.7, left panel): Stars in the central 500 pc follow a mass-metallicity relation, where galaxies at the lowest mass end ($5 \times 10^8\,M_\odot$) have on average solar metallicity and galaxies at the highest mass end ($\sim 10^{12}\,M_\odot$) have metallicities of around 0.5 dex. The total mass-metallicity relation of all the stars in the center is very close to the one for the in-situ population only, as they dominate the mass in the center of galaxies on average (see Figure 7.4).

Furthermore, the average metallicity for central stars is consistently offset by about 0.3 dex towards higher metallicities across the whole galaxy mass range compared to the mass-metallicity relation which takes into account all the stars belonging to a given galaxy. This emphasizes the self-similarity of galactic chemical enrichment.

On top of that, the scatter of the total central mass-metallicity relation is very low with around 0.1 dex, which also holds when only in-situ or only migrated stars are considered. Hence, there is little

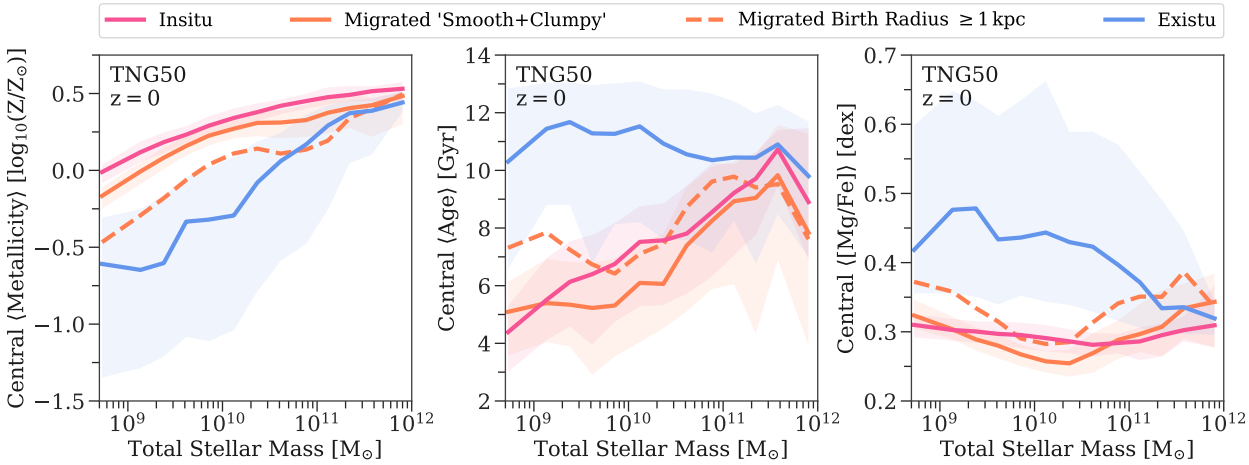

Figure 7.7. Average stellar population properties of in-situ, migrated and ex-situ stars in the central 500 pc of TNG50 galaxies at z = 0. *From left to right*: The central mass-weighted average metallicity, age and magnesium-to-iron abundance [Mg/Fe] as a function of total galaxy stellar mass for the in-situ (*pink*), migrated (*orange*) and ex-situ (*blue*) stars. The shaded bands depict the 16th and 84th percentile. The dashed orange line only shows the quantities for migrated stars that have birth radii larger than 1 kpc. Overall, the stellar population properties of in-situ and migrated stars are similar, whereas the ex-situ stars are more metal-poor, older and have higher [Mg/Fe] across the galaxy mass range.

galaxy-to-galaxy variation at fixed stellar mass regarding in-situ star formation.

The average metallicity of the in-situ population is the highest, followed by the migrated stars, which is less than a quarter dex lower across the whole galaxy mass range. This small difference is expected as most of the migrated stars are born very close to the center (0.5 – 1 kpc). When including only migrated stars with large birth radii (> 1 kpc), the difference becomes larger to about half a dex due to internal metallicity gradients present in galaxies, which is in turn caused by less efficient star formation in the galactic outskirts. Above galaxy stellar masses of $2 \times 10^{11}\,M_\odot$ the average metallicity of all migrated stars and only those with birth radii larger than 1 kpc becomes similar again. This is because migrated stars from clumps are dominating at these galaxy masses, which originate from larger distances (median distance is 30 kpc) and have high metallicities (median metallicity is 0.2 dex).

The mass-metallicity relation for the central ex-situ stars follows a steeper slope than the one for the in-situ and migrated stars, because we are showing the mass of the z = 0 host galaxy and not of the galaxy they were born in. The average metallicity of ex-situ stars is around 0.5 dex lower at the lowest galaxy masses compared to the metallicity for the in-situ stars. At the highest mass end the average metallicity of the ex-situ stars becomes close to the one for the migrated stars, which is around 0.25 dex. This steeper slope emphasizes that ex-situ stars in the center of low mass galaxies originate from galaxies of even lower mass, while most of the central ex-situ stars in high mass galaxies originate from galaxies of more similar stellar mass.

Lastly, the galaxy-to-galaxy variation at fixed galaxy stellar mass for the average metallicity of ex-situ stars is much larger compared to the in-situ and migrated population. The scatter varies from around one

dex at the low mass galaxy end to close to a quarter dex for the highest galaxy masses. This emphasizes that at lower host galaxy stellar mass, a larger variety of satellite galaxies (i.e. with different stellar masses) can deposit stars in the center of their respective $z = 0$ hosts.

Age (Figure 7.7, middle panel): The ex-situ stars have a rather constant, old age of around 10 Gyr across the whole galaxy mass range, albeit with a large scatter of around 2 Gyr. This is not surprising as most mergers happen before the redshift of one, which corresponds to a lookback time of around 8 Gyr. The flat relation for the average age of the ex-situ stars is not in conflict with their corresponding mass-metallicity relation. Because high mass galaxies are more efficient in chemical enrichment than low mass galaxies, they will consequently have higher metallicities at fixed stellar age.

The median relations for the average age for the in-situ and migrated stars are again similar to each other with the in-situ stars being slightly older by around 1 Gyr or less at fixed galaxy stellar mass. Overall, in-situ and migrated stars are younger, with average ages between 3 and 6 Gyr, in the lowest mass galaxies ($\sim 10^9\,M_\odot$), and become increasingly older with average ages of around $8-10$ Gyr at the highest mass end ($\sim 10^{12}\,M_\odot$).

The scatter of the average ages for the in-situ and migrated stars is much larger than their corresponding variations in metallicity. This could have multiple reasons, for example: different pathways in star formation histories (i.e. star formation rate as a function of time) can result in the same metallicity but different average ages, or the metallicity enrichment starts to saturate once a metallicity above solar is reached and therefore it does not matter, if star formation continues for another few Gyr.

Galaxies above $10^{11}\,M_\odot$ in stellar mass exhibit a larger scatter of the average age of their migrated population compared to their in-situ stars. This arises because migration to the center in this regime is dominated by clumps, which have a rather flat formation time distribution with the majority forming between 4 and 10 Gyr ago (see Figure B.7).

Below galaxy stellar mass of $10^{11}\,M_\odot$, the migrated stars, which were born at distances larger than 1 kpc, have a running median of averages ages that are around $1-2$ Gyr older than the total migrated population. As these stars need significantly more time to arrive in the center, their ages are consequently older.

[Mg/Fe] (Figure 7.7, right panel): In extragalactic studies magnesium is the predominant α-element present in optical spectra (see e.g. Martín-Navarro et al., 2018a, 2019, 2021b; Gallazzi et al., 2021). We therefore show the running median of the mass-weighted average magnesium-to-iron abundance as a function of galaxy stellar mass as a proxy for the total α-to-iron abundance. This abundance ratio provides to first hand information about the star formation time scale before supernovae type Ia significantly enrich the interstellar medium with iron peak elements[117].

The average central [Mg/Fe] is almost constant for the in-situ pop-

117: Influences on [α/Fe] due to IMF (initial mass function) changes are not captured in the simulation, as a Chabrier IMF (Chabrier, 2003) is assumed for every stellar particle

ulation across the whole galaxy mass range with a value of about 0.3 dex. For galaxies between $2 \times 10^9\,M_\odot$ and $6 \times 10^{10}\,M_\odot$, the migrated stars have slightly lower values. The lowest average [Mg/Fe] of around 0.25 dex is reached for galaxies around $2 \times 10^{10}\,M_\odot$. This directly maps to the increased difference of the average age between in-situ and migrated stars of around 1 Gyr in the same mass regime. Hence, in-situ stars of these galaxies form on average earlier and more rapidly as opposed to their migrated stars.

Above $6 \times 10^{10}\,M_\odot$, the average [Mg/Fe] for the migrated populations rises above the one for the in-situ stars to around 0.35 dex at the highest mass end. This cross-over is not seen in the average ages. An explanation for this could be that in the high galaxy mass regime, an increasing number of migrated stars can originate from larger distances and possibly formed from stripped gas of merging lower mass systems (see Section 7.3.2), which have larger [Mg/Fe] values due to lesser efficiency in chemical enrichment.

When only including migrated stars originating from distances farther than 1 kpc away from the center, the average [Mg/Fe] becomes larger by around 0.1 dex across all galaxy stellar masses. For galaxies below $\sim 10^{11}\,M_\odot$ the corresponding ages become older, which is thus consistent in having formed from true in-situ gas of their respective host galaxies.

The age for migrated stars with birth radii > 1 kpc in galaxies above $10^{10}\,M_\odot$ does not increase even though their [Mg/Fe] increase as well. This could indeed provide evidence for some migrated stars having formed from stripped gas for galaxies in this mass regime.

The ex-situ stars have overall higher average [Mg/Fe] values of around 0.45 dex, which decreases to around 0.35 dex for galaxies above $10^{11}\,M_\odot$ in stellar mass. This is consistent with their old ages and being formed in lower mass satellite galaxies that produced stars less efficiently than their respective $z = 0$ hosts.

The scatter in average [Mg/Fe] for the ex-situ population is significantly larger than for the in-situ and migrated population across all galaxy masses, but especially $\lesssim 10^{11}\,M_\odot$. The onset of type Ia supernovae creates probably more stochasticity in lower mass galaxies as single supernovae events can significantly enrich the interstellar medium of the entire host galaxy.

7.4.2.2 *Stacked circularity distributions*

Different birth origins also leave imprints on the stars' dynamics, which can still be visible until the present-day. We investigate such imprints by quantifying the instantaneous circularity ϵ of stars (see Zhu et al., 2022b). Circularities close to one indicate circular orbits, values around zero indicate random motion dominated orbits and negative ones show counter-rotating orbits. We then compute the normalized circularity distribution for each galaxy with a bin size of 0.1 for ϵ. Circularity distributions are than stacked together according to the galaxy's total stellar mass in bins of approximate 0.5 dex and are re-normalized.

The results for the different in-situ, migrated and ex-situ populations are displayed in Figure 7.8. The lines in Figure 7.8 trace the peak

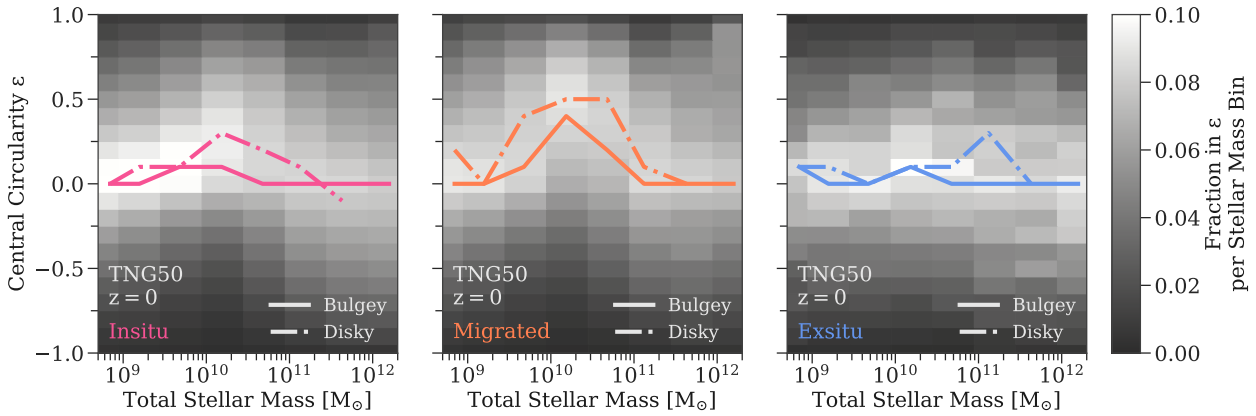

Figure 7.8. Average differences in the dynamical properties of in-situ, migrated and ex-situ stars in the central 500 pc of TNG50 galaxies at z = 0. *From left to right*: The central circularity distributions in stacks of total galaxy stellar mass for in-situ (*pink*), migrated (*orange*) and ex-situ (*blue*) stars. Per galaxy, stellar particles in the center belonging to either the in-situ, migrated or ex-situ population are binned according to their circularity ϵ and normalized to unity respectively. They are then stacked together according to the displayed galaxy stellar mass bins and then normalized again. The lines trace the circularity bin with the maximum fractional mass across galaxy stellar masses divided by bulgey (*solid*) and disky (*dashed-dotted*) galaxies respectively. Clearly the migrated population has the most rotational support for galaxies around $10^{10}\,M_\odot$ in total stellar mass, regardless of the host being disk or bulge dominated.

of the circularity distributions across galaxy stellar mass, separately for disky and bulgey galaxies.

The circularity distribution of the in-situ population is centered on random motion dominated orbits for galaxies with stellar masses smaller than $3 \times 10^9\,M_\odot$ and larger than $10^{11}\,M_\odot$. Galaxies with stellar masses in between have a circularity distribution with a peak shifted towards slightly higher circularities of around 0.25. We see that this shift is caused by galaxies that are overall disky, as the bulge dominated galaxies have a circularity peak that stays around zero. Nevertheless, the in-situ stars are in summary on warm to hot orbits even for disk dominated galaxies, which is not surprising as the velocity dispersion generally rises towards the center of galaxies.

For galaxies below $10^{10}\,M_\odot$ the stacked circularity distributions for in-situ stars have a sharper peak, whereas galaxies of higher masses have an overall broader distribution in ϵ. This could be an indication of a smaller galaxy-to-galaxy variation of the circularity distribution in the center of the smallest galaxies, regardless of whether they are disky or bulgey, as in this mass regime the absolute numbers of those two galaxy types are approximately the same in TNG50. At the high mass end on the other hand, a broader circularity distribution could indicate that in-situ stars become redistributed in their orbits due to the increased influence of mergers and contribution of ex-situ stars.

For the migrated population the circularity distribution is again centered on random motion orbits for galaxies $< 3 \times 10^9\,M_\odot$ and $> 10^{11}\,M_\odot$, although now the distribution is also overall broader for the low mass galaxies. Migrated stars in intermediate mass galaxies are on even higher circularity orbits than their corresponding in-situ stars reaching a peak of around 0.5 for galaxy stellar masses of $\sim 10^{10}\,M_\odot$. This peak is seen in disk and bulge dominated galaxies alike. Hence, migrated stars tend to have the most rotational support for galaxies

in the intermediate mass regime, which could be an indication for migration being caused by different mechanisms across the galaxy mass range in TNG50. However, migrated stars are also on average younger than the in-situ stars in these galaxies, which might be the reason why they are still more on circular orbits (see Figure 7.7). We also point out that some galaxies above $\sim 3 \times 10^{10}\,M_\odot$ have a very double peaked (i.e. one around zero and around 0.5 or higher) circularity distribution, which is washed out in Figure 7.8 due to the stacking. These stars originate from (recently) migrated clumps.

Ex-situ stars have circularities centered around zero across the entire galaxy mass range in TNG50 and also for both disk and bulge dominated galaxies. Because they originate from stochastic merger events, stars are put on average on hot, random motion dominated orbits. Nevertheless, we see a a large scatter throughout the circularity distributions for the ex-situ stars in the different galaxy stellar mass bins indicating a lot of individual galaxy-to-galaxy variation. Depending on the exact time the merger occurred and how the orbits between the host and merging satellite were configured, ex-situ stars can very well retain some rotational support and often be on counter rotating orbits.

7.4.2.3 *2D distributions of ages, metallicities and circularities*

In Figures 7.9 and 7.10 we show the 2D distributions of age and metallicity and age and circularity of the central in-situ, migrated and ex-situ stars respectively in stacks of galaxy stellar mass. For each galaxy we first compute the mass-weighted and normalized 2D histogram of the respective quantities with bin sizes of 0.5 Gyr for age, 0.25 dex for metallicity and 0.1 for circularity. We then stack those according to the total stellar mass bin of the galaxies, normalize again and then compute the Gaussian kernel density estimate. The galaxy stellar mass bins are 0.5 dex wide for galaxies between $10^{8.75}\,M_\odot$ and $10^{10.75}\,M_\odot$. We stack all galaxies with stellar masses between $10^{10.75}\,M_\odot$ and $10^{12}\,M_\odot$ together as a finer binning did not reveal any mass-dependent trends and also became stochastic due to low number statistics in this mass regime. The five galaxies with stellar masses above $10^{12}\,M_\odot$ are not included. Additionally, we show the stacked age-metallicity distributions for quenched and star forming galaxies separately to avoid averaging over too many dissimilar galaxies in this parameter space. Similarly, we divide between bulge and disk dominated galaxies for the age-circularity distributions.

With the 2D distributions we can observe a couple of new trends that are not necessarily apparent from the average stellar population properties in Figure 7.7 and the 1D circularity distributions of Figure 7.8.

Age-metallicity (Figure 7.9): For star forming galaxies (bottom row of Figure 7.9), the average distribution of the migrated stars changes very little in shape and position, apart from shifting towards higher metallicities, from the lowest mass galaxies until the $10^{10.5}\,M_\odot$ galaxy stellar mass bin. They are centered between $2-4$ Gyr. The ex-situ stars behave similarly and are centered around 12 Gyr. However, the average

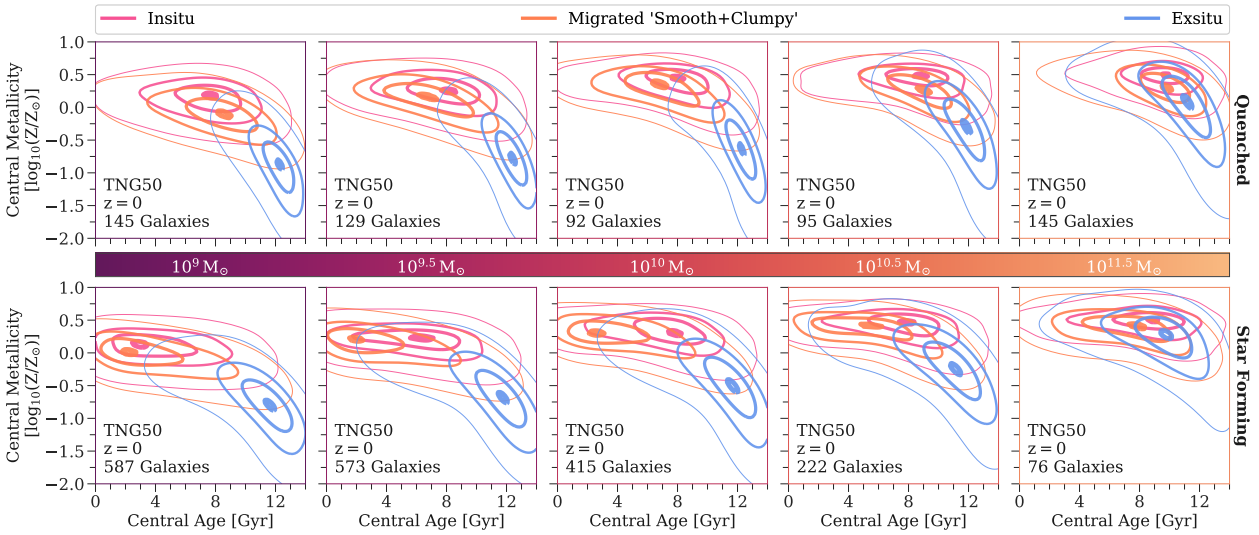

Figure 7.9. Age-metallicity distributions of central (500 pc) stars of TNG50 galaxies in stacks of stellar mass at z = 0. Gaussian kernel density estimates for in-situ *(pink)*, migrated *(orange)* and ex-situ *(blue)* stars encompassing 1%, 20%, 50% and 90% of all central stellar mass *(thickest to thinnest)* are shown in the respective galaxy stellar mass bin increasing from left to right as depicted by the colorbar. The galaxy mass bins are centered on the indicated stellar mass and are 0.5 dex wide, except for the last panel, which is approximately one dex wide. Prior to stacking the age-metallicity distribution of each galaxy is normalized. The top row shows quenched and bottom row shows star forming galaxies respectively. In each panel the number of galaxies in the corresponding stellar mass bin are indicated. The galaxy-averaged age-metallicity distribution of the three origins becomes best separated around galaxies with stellar masses of $10^{10}\,M_\odot$.

distribution of the in-situ stars shows an entirely different mass trend. While the in-situ stars are almost entirely coinciding with the migrated stars in age-metallicity space for the lowest mass bin, the peak of the in-situ distribution gradually shifts towards older ages from 2 Gyr to 8 Gyr for increasing galaxy mass. In the process the in-situ average age-metallicity distribution becomes more elongated around $10^{9.5}\,M_\odot$ in the age direction when focusing on the 20% contour.

For $10^{10}\,M_\odot$ galaxies the in-situ distribution becomes more centrally concentrated again. Furthermore, the average age-metallicity distributions of the three origins are maximally separated in this mass regime, with the migrated stars being the youngest ($1-6$ Gyr for the 20% contour), followed by the in-situ stars ($6-10$ Gyr for the 20% contour) at similar metallicity and the ex-situ stars populating the oldest ($10-13$ Gyr for the 20% contour) and most metal-poor tail. Thus, there must be a mechanism for these galaxies that halts in-situ star formation in their centers, while it continues outside of it in order to be able to produce young migrated stars. It is likely that this is connected to the (kinetic) AGN feedback implement in TNG, which quenches galaxies from inside-out (Nelson et al., 2021, see also 7.5.2 and Figure 7.11).

Starting at $10^{10.5}\,M_\odot$ the average age-metallicity distribution of the migrated stars also becomes more elongated towards older ages and above $10^{10.5}\,M_\odot$ coincides again with the one of the in-situ stars. The peak of the ex-situ distribution increases towards metallicities similar to those of the in-situ and migrated stars. For galaxies between $10^{11}\,M_\odot$ and $10^{12}\,M_\odot$ in stellar mass the average distributions for the in-situ, migrated and ex-situ stars become almost indistinguishable in

age-metallicity space.

For quenched galaxies (top row of Figure 7.9) the behaviour for the age-metallicity distributions of the in-situ and migrated stars across galaxy stellar mass is different. They are not clearly separated in any galaxy stellar mass bin as was the case for the star forming galaxies. Both the in-situ and migrated average age-metallicity distributions are more centrally concentrated than for star forming galaxies, their shapes are very similar to each other and their peaks are both at old ages (around 8 Gyr) exhibiting little galaxy mass dependence. The peak of the age-metallicity distribution for the migrated stars seem to be slightly younger for galaxies in mass bins between $10^{9.5}\,M_\odot$ and $10^{10}\,M_\odot$ and slightly older otherwise. Interestingly at both the low and high mass end, the separation in metallicity between the in-situ and migrated stars is larger for the quenched galaxies as for the star forming ones. For galaxies between $10^{11}\,M_\odot$ and $10^{12}\,M_\odot$ the three distributions are again indistinguishable.

Age-circularity (Figure 7.10): Stars with higher circularities are usually younger. The distribution for migrated stars of disky galaxies (bottom row of Figure 7.10) in the lowest galaxy stellar peaks at around 2 Gyr with high circularity values of around 0.5, whereas the distributions for the in-situ stars peaks at older ages (6 Gyr) centered on circularity values of zero. Nevertheless, the 20% contour for the in-situ stars still has a tails towards younger ages and slightly above zero circularities. In the next higher galaxy stellar mass bin the 20% contour of the distribution for the migrated stars looses its tail of older ages ($4-8$ Gyr) and zero circularities. The 20% contour for the in-situ stars in now centered on even older ages (8 Gyr). Beginning around galaxy stellar masses of $10^{10}\,M_\odot$ the 20% contour for the migrated stars elongates towards older ages spanning now $1-8$ Gyr, while roughly maintaining the high circularity. The distribution for the in-situ stars becomes broader and slightly shifts towards above zero circularities. In the $10^{10.5}\,M_\odot$ galaxy stellar mass bin the peak of the migrated stars shifts from young (2 Gyr) to old (8 Gyr) ages with just a slight decrease in circularity. Above galaxies with $10^{10.5}\,M_\odot$ in stellar mass the migrated stars switch from a rotationally supported distribution to random motion dominated one until they coincide with the age-circularity distributions of the in-situ and ex-situ stars at the highest galaxies.

The peak of the age-circularity distribution for the in-situ stars, albeit having the same young age as for the migrated stars in the lowest stellar mass bin, is near zero circularity. With increasing galaxy mass the age-circularity distribution for in-situ stars shifts towards old ages and becomes broader in the circularity direction, but stays mostly centered around zero circularity with perhaps a slight shift towards higher circularities around the $10^{10}\,M_\odot$ galaxy stellar mass bin as already observed in Figure 7.8. The age-circularity distributions for the ex-situ stars show practically no galaxy mass dependence; they are centered on random motion dominated orbits and the oldest ages.

The centers of bulge dominated galaxies (top row of Figure 7.10) above $10^{9}\,M_\odot$ have overall similar age-circularity distributions as disk dominated galaxies. However, the absolute values of the migrated dis-

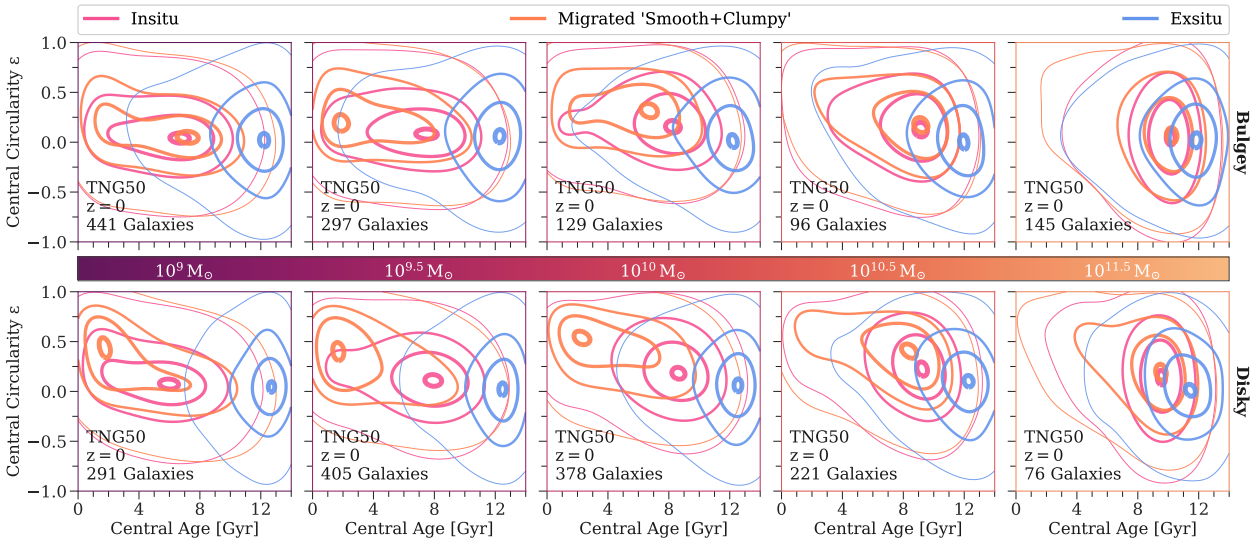

Figure 7.10. Age-circularity distributions of central (500 pc) stars of TNG50 galaxies in stacks of stellar mass at z = 0. Gaussian kernel density estimates for in-situ *(pink)*, migrated *(orange)* and ex-situ *(blue)* stars encompassing 1%, 20%, 50% and 90% of all stellar mass *(thickest to thinnest)* are shown in the respective galaxy stellar mass bin increasing from left to right as depicted by the colorbar. The galaxy mass bins are centered on the indicated stellar mass and are 0.5 dex wide, except for the last panel, which is approximately one dex wide. Prior to stacking the age-circularity distribution of each galaxy is normalized. The top row shows bulge dominated and bottom row shows disk dominated galaxies respectively. In each panel the number of galaxies in the corresponding stellar mass bin are indicated. The galaxy-averaged age-circularity distribution of the three origins becomes best separated around galaxies with stellar masses of 10^{10} M$_\odot$.

tribution do not reach the same high circularities as for the disky galaxies and its peak transitions quicker to old ages (8 Gyr) between mass bins of 9.5 and 10 dex. Below 10^{9} M$_\odot$ both the migrated and in-situ distrbition are centered on zero circularities and old ages; distinct to the disky galaxies.

For both bulge and disk dominated galaxies the average age-circularity distribution of the in-situ, migrated and ex-situ stars are well separated in mass ranges between $10^{9.5}$ M$_\odot$ and 10^{10} M$_\odot$. This dependence of increasing circularity for younger ages, especially prominent for the migrated stars, gives an indication that recently (i.e. young) migrated stars travel to the center of their host galaxies by loosing their angular momentum ("churning"; see e.g. Frankel et al., 2020, for the Milky Way disk) and then, once they have arrived in the center, become dynamically heated over time.

7.5 DISCUSSION, IMPLICATIONS AND OUTLOOKS

In this section we discuss the implications of the studied mass assembly of the central 500 pc in TNG50 galaxies on the formation scenarios of central galaxy components. We also discuss the clumps found in TNG50 as well as the robustness of our results within the TNG modelling framework. In addition, we assess how our results on the stellar population and dynamical properties can be compared to observations and used to understand the mass build-up of galaxies in general.

7.5.1 The build-up of galaxy centers in a ΛCDM cosmology

Throughout this Chapter, we have unravelled a set of relations between the properties of the stellar centers of galaxies at $z = 0$. Galaxy centers are dominated by in-situ stars (see Figure 7.4) and follow well established relations (e.g. Gallazzi et al., 2005) that correlate their increasing stellar masses with increasing average ages and metallicities (see Figure 7.7). Stars that migrated to the center are second most abundant. They follow the trends for the in-situ stars, however are often distinctively younger and on more rotation supported orbits. Ex-situ stars in the center become only significant (in mass) at high galaxy stellar masses ($> 10^{11}\,M_\odot$) (see Figure 7.4). They are amongst the oldest and most metal-poor and random motion dominated stars (see Figures 7.7 and 7.8).

While these trends are consistent with out general understanding of galaxy formation, we find others that may be more surprising. For example, there seems to be no average difference between the central mass assembly of central and satellite galaxies (see Figure 7.6). Generally, central galaxies are thought to have accreted more satellite galaxies. We have checked this relation also for the total accreted mass within TNG50 and also found no significant difference between centrals and satellites on average. Thus, perhaps TNG50 is not probing enough very high mass central galaxies around stellar masses of $10^{12}\,M_\odot$, where this trend might become apparent.

Another, rather unexpected result compared to usual assumptions, is that star forming galaxies above $10^{10}\,M_\odot$ possess on average more ex-situ mass in their centers compared to quenched ones (see Figure 7.6). Again, this difference, even though to a much less significant, remains when considering the total amount of ex-situ mass (see Figure B.4). This trend also exists for the larger box of TNG100, thus eliminating the fact for low number statistics at the higher mass end, and is in contrast to the original Illustris simulation (see Rodriguez-Gomez et al., 2016, Figure 5). We have checked the median mass growth of the central ex-situ stars for star forming and quenched galaxies alike between stellar masses of $10^{10} - 10^{11}\,M_\odot$ and found that quenched galaxies stop acquiring ex-situ mass in their centers after $z \sim 1.7$ (look-back time $\sim 10\,\mathrm{Gyr}$). Only if we split quenched galaxies further into bulgey and disky as well as barred and non barred do we see that quenched, bulgey and non barred galaxies have a similarly high ex-situ mass in their centers as their star forming counterparts. Together, this is an indication that the time of accretion and consequently the absolute amount of stellar and gas mass of the secondary galaxy (the former will be higher at later cosmic times and the latter will influence the amount of newly formed stars during the merger process) will matter in the build-up of ex-situ mass in the center of the primary and ultimately dictate what properties it has today.

On top of that, the fraction of in-situ, migrated and ex-situ stars in the center of galaxies has a significant scatter at fixed galaxy stellar mass regardless of the galaxy's bulk properties at $z = 0$ (see Figure 7.5).

Hence, median trends for different galaxy populations only reveal half of the picture, as the stochasticity of galaxy mergers and interactions in a ΛCDM cosmology leads to diverse pathways in the build-up of stellar mass in the centers of galaxies. Thus, characteristic properties of galaxies at $z = 0$ are only a limited indicator of the exact formation history of an individual galaxy. For example, there are perfectly regular spiral galaxies in TNG50 $z = 0$, of which some have experienced (multiple) major mergers and of which some had a more quiet assembly.

This diversity in the central 500 pc of TNG50 galaxies potentially reflects the variety of central galaxy components seen in observations (see Section 7.1). Even though nuclear rings, disks and star clusters are at or below the resolution limit of TNG50, the stellar population and dynamical properties that we find for central stars of different origins might be a first indication that this would also manifest in structurally distinct components. For example, the distinctly high circularities of migrated stars in $10^9 - 10^{10}\,M_\odot$ galaxies (see Figure 7.10) reflect that nuclear disk-like configurations are able to arise. Even more intriguing are their predominantly younger ages of $1 - 2$ Gyr compared to the underlying old (~ 8 Gyr) in-situ population, which is in line with observational findings of nuclear disks/rings (Bittner et al., 2020). Typically, the formation of nuclear rings in disk galaxies is associated with bars funnelling gas towards the center (see e.g. Seo et al., 2019; Tress et al., 2020; Sormani et al., 2020, for dedicated simulations). Even though we did not explicitly investigate the inflow of gas in this study, we see that the migration of stars to the center is likely connected to temporarily induced non-axisymmetries during galaxy interactions (see Section 7.5.2). Hence, this shows that mechanisms that are associated with producing distinct nuclear galaxy components are captured in TNG50. Follow-up zoom-in simulations of TNG50 galaxies would show if indeed nuclear components such as disks and rings form from these mechanisms (see Section 7.5.4).

7.5.2 Mechanisms for the formation and deposit of stars in the center of galaxies

The cosmological framework of TNG50 produces diverse properties of galaxies and their centers. Consequently, the mechanisms that are responsible for the formation and deposit of stars in the centers of galaxies also have to be diverse.

To visualize possible mechanisms for the formation and deposit of stars in the center of galaxies we walk through the central assembly history of an individual galaxy as seen in Figure 7.11. We picked this particular galaxy, which has a stellar mass of $10^{10.8}\,M_\odot$ at $z = 0$, as it shows many of the possible mechanisms that can be present in the formation of galaxy centers. This however does not mean that all galaxies show the same amount of complexity. Most galaxies will only exhibit one or two of these mechanisms with varying impact depending on their individual formation pathway. The galaxy's center at $z = 0$ consists of around 50% in-situ, 30% migrated and 20% ex-situ stars.

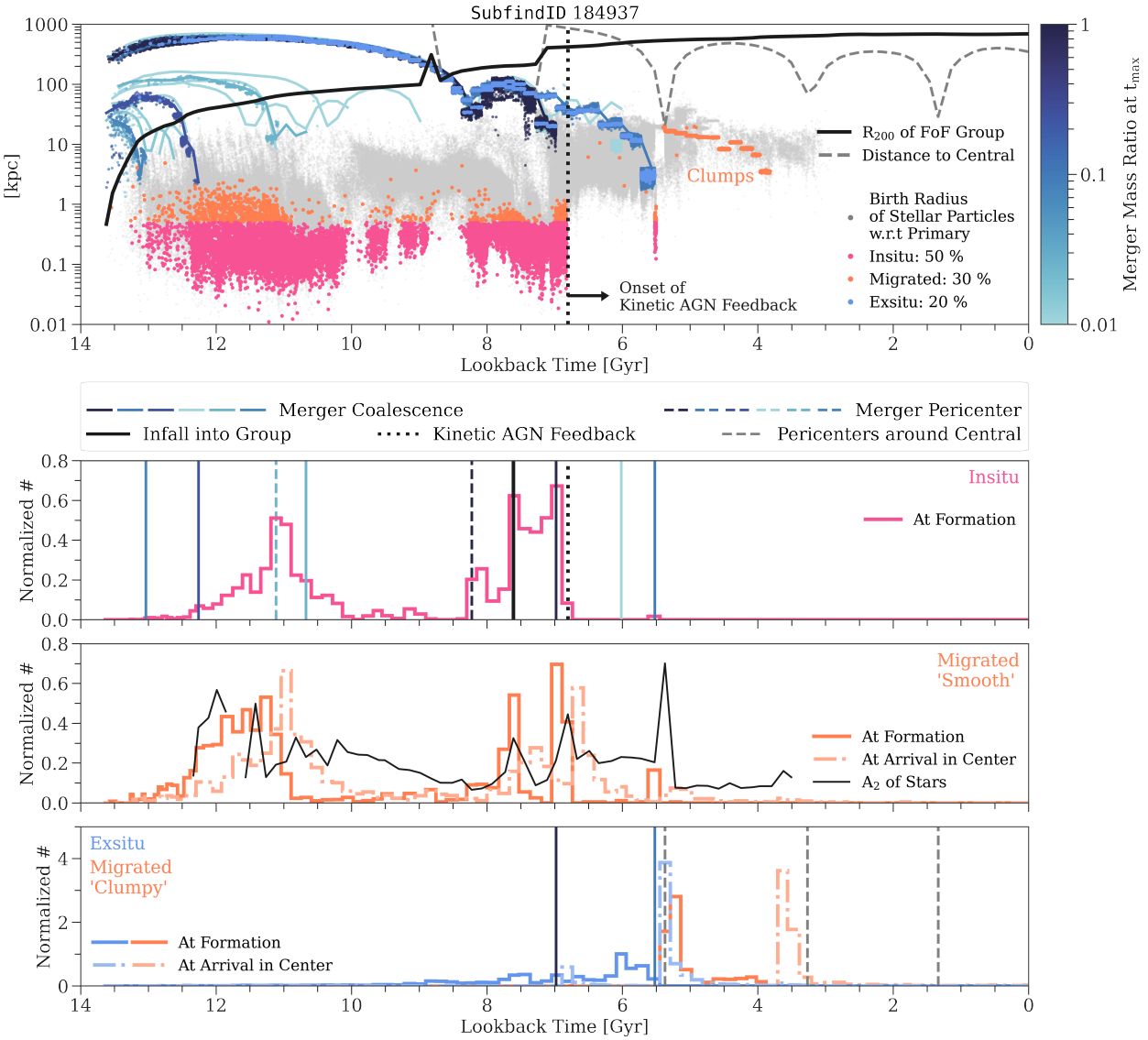

Figure 7.11. Central (500 pc) assembly history of an individual galaxy (SubfindID 184937) in TNG50 with a total stellar mass of $10^{10.8}\,M_\odot$. This galaxy encompasses many mechanisms that can shape the stellar mass build-up in the center of galaxies in a ΛCDM cosmology. *Top panel*: Points show all individual stellar particles that belong to that galaxy at $z = 0$. Their distance at the time of birth is shown with respect to their current host in the case of in-situ formed stars (*light gray*: all in-situ particles, *pink*: central in-situ stars only, *orange*: central migrated stars only). In the case of the ex-situ formed stars the distance is shown with respect to their future host galaxy at the time of birth (*color-coded according to the colorbar*: all ex-situ stars, *blue*: central ex-situ stars only). The distance to individual satellite galaxies (only with maximum stellar masses above $10^6\,M_\odot$) that will merge with the primary at some point are shown with thinner solid lines. Their coloring also follows the colorbar, which visualizes the merger mass ratio taken at the time t_{max}, when the secondary galaxy reaches maximum stellar mass. The thick black solid line shows the radius of the FoF Group the galaxy belongs to at a given lookback time (represented as R_{200}, where the group's density is 200 times the critical density of the Universe). The thick gray dashed line shows the distance between the individual galaxy and the central galaxy of the FoF group it belongs to. Approximately 7 Gyr ago the galaxy fell into another group and became a satellite galaxy. Before that it was the central of its own FoF group. The vertical black dotted line represents the time the kinetic AGN feedback starts to take effect, which quenches the center. This galaxy has 50% in-situ, 30% migrated (of which only 9% are 'smoothly' migrated and the rest comes from migrated clumps) and 20% ex-situ stars in its center. *Bottom panel*: Histograms of formation times of in-situ (*top*), formation (*solid*) and arrival (*dashed-dotted*) times at the center for 'smoothly' migrated (*middle*) as well as ex-situ and 'clumpy' migrated (*bottom*) stars. Additionally, in the panel for the in-situ stars, we mark the time of coalescence for the six most massive mergers of this galaxy with thin blue colored solid lines. According to the colorbar of the top panel, a darker blue means a higher merger mass ratio. Pericenter passages for two mergers are shown by thin dashed lines following the same colorcode. The approximate time of the galaxy falling into its $z = 0$ FoF group is shown by the thick black solid line and the onset of the kinetic AGN feedback is shown as the black dotted line. In the panel for the 'smoothly' migrated stars we also show the A_2 mode of the stars for a given lookback time (see Appendix B.1.1 for a definition). In the panel for the ex-situ and 'clumpy' migrated stars, we show the time of coalescence of the two mergers that deposited ex-situ stars in the galaxy's center (*blue solid lines*) as well as the three pericenter passages of the galaxy around its central galaxy after it became a satellite (*gray dashed lines*).

The main summary of the subsequent sections and Figure 7.11 is the following: galaxy mergers and other interactions are probably the most important driver in central stellar mass assembly, as they also strongly influence the formation of in-situ stars. Due to the diverse statistics of galaxy interactions, many of the proposed formation scenarios of central galaxy components arise naturally and in conjunction to each other, when hierarchical galaxy formation is considered. Thus, TNG50 highlights the necessity to study the central mass assembly of galaxies in a cosmological context.

7.5.2.1 *In-situ stars*

Galaxy mergers can trigger bursts of star formation as the tidal forces compress and shock gas efficiently (e.g Mihos & Hernquist, 1996; Di Matteo et al., 2007; Cox et al., 2008; Di Matteo et al., 2008), even in its nuclear region (Powell et al., 2013). While the relative enhancement of star formation rates depend on the specific configuration of the merging galaxies, e.g. merger mass ratio, gas content, orbital infall parameters, the times of intense star formation coincide with pericenter passages and coalescence.

Peaks in the formation time of central in-situ stars in Figure 7.11 coincide with times of pericenters and coalescence of mergers that this galaxy has experienced. *Thus the formation history of the central in-situ stars is directly connected with the merger history of a galaxy.* Although, it has to be further quantified, whether also the *bulk* of in-situ stars is formed during such events or if that actually happens in-between galaxy interactions. Nevertheless, it is clear that a variety of different mergers are able to produce peaks in the formation of central in-situ stars.

For example, the peak between 10 Gyr and 12 Gyr ago was induced by a very minor merger[118] with a stellar merger mass ratio of around 0.02. At these high redshifts the primary still had a high gas fraction ($\sim$ 80%) and thus the minor merger was enough to trigger a peak of star formation in the center. Evidently, the formation of in-situ stars in the center decreased between 10 Gyr and 8 Gyr ago, as the amount of available gas decreased. Thus, in order to trigger another significant peak in in-situ star formation later on, the merger between 8 Gyr and 7 Gyr had to bring in a large amount of gas. While the ratio of the stellar mass between the secondary and primary was around one (and therefore a major merger) at the time when the secondary reached its maximum stellar mass, the secondary still had around 20 times more gas than the primary.

118: We adopt the definition of Rodriguez-Gomez et al. (2016) for the calculation of merger ratios.

Furthermore, this major merger, as well as two smaller ones that coalesced around 6 Gyr ago, happened while the primary galaxy was in the process of falling into another FoF Group, i.e. transitioning from being a central galaxy of its own FoF group to being a satellite galaxy of another FoF group. This is seen by the two sharp jumps in R_{200} between 9 Gyr and 7 Gyr ago. Evidently, this process produced another peak of in-situ star formation at around 7.5 Gyr ago, which could stem from the new, higher density environment. We have also seen in other galaxies, that were able to retain enough gas in their centers after in-

falling into a group, that in-situ star formation was triggered during the pericenter passages around the central until the galaxy became quenched. In such occasions, again tidal forces are able to compress the gas efficiently.

Within TNG50, there are two main processes that can quench the in-situ star formation in the center of galaxies. The first one is the onset of the *kinetic* AGN feedback mode implemented in TNG. Often this feedback mode switches on after a merger has been completed, as is the case for our galaxy in Figure 7.11 at around 7 Gyr, shortly after the major merger coalesces. We see that only the central 1 kpc becomes quenched, while the outskirts of the galaxy continue to form stars. This is because in TNG, AGN driven quenching proceeds from inside out (see Weinberger et al., 2017; Nelson et al., 2019b, 2021, for details). After this mode is switched on only occasional gas-rich mergers or migrated clumps are able to bring in new gas to the center to cause new in-situ star formation, as seen at 5.5 Gyr in Figure 7.11. Lastly, the thermal feedback mode, which is often active prior to the kinetic mode switches on and also injects relatively more energy, is not responsible for quenching the centers of galaxies in TNG50 (Zinger et al., 2020).

The second process that will shut down star formation in the center of TNG50 galaxies is when the galaxy as a whole becomes quenched, either through environmental processes, e.g. after a few pericenters after infall into a group (as is the case for the galaxy in Figure 7.11 around 3 Gyr ago) or through AGN feedback, which is primarily important for the highest mass galaxies (see also Donnari et al., 2021a).

7.5.2.2 *Migrated stars*

The formation times of 'smoothly' migrated stars in Figure 7.11 is closely related to the formation times of the in-situ stars, which is not the case for the 'clumpy' migrated stars. This is reasonable, because the majority of 'smoothly' migrated stars are born already close to the center ($\lesssim$ 2 kpc), while the 'clumpy' migrated stars formed predominantly in the outer disk. The 'clumpy' migrated stars make up 91% of the total mass of migrated stars in the center of this galaxy.

However, the star formation in the central 2 kpc is *not* a guarantee to produce a significant amount of 'smoothly' migrated stars, as seen between lookback times of $9-11$ Gyr and also between $7-7.5$ Gyr in Figure 7.11. Thus, specific conditions must be met that transport stars from around $1-2$ kpc to the center.

Non-axisymmetric features, such as spiral arms and bars, are well known to be able to diffuse the angular momentum of stars and cause radial migration (e.g. Sellwood & Binney, 2002; Minchev & Famaey, 2010). While this effect is mainly studied in the (outer) disk of galaxies, we show here in Figure 7.11 that similar non-axisymmetries are likely responsible for the inward migration of stars to center of galaxies. We see that peaks in the A_2 mode (see Appendix B.1.1 for a definition) of the stellar mass distribution occur *before* peaks of migrated stars arriving in the galaxy center. We detect similar enhancements for the Fourier modes of the *gas* mass distribution (see also Di Matteo et al., 2007).

These temporary enhancements of non-axisymmetric features are clearly induced during galaxy interactions and the exerted torques on the gas and stars can produce these 'smoothly' migrated stars. This also indicates that it is possible for a galaxy to have experienced migration events of stars, even if the galaxy itself does not exhibit any signs of bar- or spiral-like features today.

The 'clumpy' migrated stars form after the first pericenter passage of the galaxy around its central around 5.5 Gyr ago and arrive at the center shortly before the second pericenter passage around 2 Gyr later. Similarly, we have seen qualitatively for other galaxies that clumps formed rather recently ($z < 1$) are mainly induced by fly-bys, as these are still able to destabilize the disk significantly after the predominant merger phase of the Universe is over. However, clumps are also able to form without any significant galaxy interactions and a follow-up study is needed to characterize this further as well as establish overall the credibility of the formation of the clumps (see Section 7.5.3 for a further discussion).

7.5.2.3 *Ex-situ stars*

The two mergers that are responsible for the majority of the ex-situ stars in the center of the galaxy in Figure 7.11, are the 1:1 and 1:10 merger that coalesced around 7 Gyr and 5.5 Gyr ago respectively. Both mergers brought in a comparable *total* amount of stellar mass of around $1.2 \times 10^{10}\,M_\odot$ and $8.1 \times 10^{9}\,M_\odot$ respectively. However, the major merger deposited around 10 times less stars in the central 500 pc compared to the minor merger, i.e. 0.6% and 5% of their respective total stellar mass arrived in the center. This highlights that the merger mass ratio cannot be the only parameter determining the amount of ex-situ stellar mass that is deposited in the center of galaxies. We expect that the spin-orbit coupling of the primary and secondary galaxy as well as other orbital parameters play a role in this, as the exerted tidal forces and the influence of dynamical friction differ for different configurations (see e.g. Renaud et al., 2009, for a study).

Around 67% and 93% of the ex-situ stars that arrived from the major and minor merger respectively were formed *after* both satellite galaxies entered R_{200} of the primary's FoF halo around 8.75 Gyr ago. As also all central ex-situ stars were born in the center ($\sim$ 500 pc) of their respective birth galaxies, this confirms that significant nuclear star formation is also triggered in the secondary galaxy after infall.

Most of the ex-situ stars in the center arrive there immediately after the merger coalesces. This is the case if their distance to the center of the primary was less than 500 pc at the time of stripping. Otherwise it can take up to 2 Gyr. Interestingly, the arrival of the 'clumpy' migrated stars at the center around 3.5 Gyr ago induced a second peak in the arrival of ex-situ stars from the minor merger into the center, albeit being ten times lower and hence not visible in Figure 7.11.

7.5.3 The case of stellar clumps

Disk fragmentation can occur due to gravitational instabilities in a galaxy's gas-rich and turbulent disk (Toomre, 1964; Springel, 2005; Hopkins, 2013). This fragmentation can form highly star forming clumps, which have been reproduced in several studies using hydrodynamical galaxy simulations, either isolated or fully cosmological ones (e.g. Bournaud et al., 2007; Genel et al., 2012; Bournaud et al., 2014; Mandelker et al., 2014, 2017; Buck et al., 2017). The execution of these simulations was motivated by the discovery of the clumpy morphology in the rest-frame UV light of high redshift, star forming galaxies (e.g. Elmegreen et al., 2007; Guo et al., 2015). Therefore, these simulations are tailored to focus on clump formation in massive disk galaxies $10^{10-11}\,M_\odot$ at $z \geqslant 1$.

In observations, clumps have masses between $10^7\,M_\odot$ and $10^9\,M_\odot$, as well as sizes of 1 kpc or less. Clumps in the simulations are usually identified via regions of enhanced gaseous surface mass density or from mock stellar light images. In TNG50, the identification of clumps is (so far) a passive byproduct of the Subfind algorithm, nevertheless the extracted baryonic mass distribution of the clumps peaks at $10^8\,M_\odot$ exhibiting overall high gas fractions (see Figure B.7) are in agreement with the other studies. However, all clumps in TNG50 have 3D baryonic half mass radii below 300 pc and therefore seem to be much more compact compared to observations and some simulation studies (see Figure 9 in Buck et al., 2017). The latter could be a result of the different treatments of star formation and feedback in the simulations or the clump identification, as the numerical resolution of TNG50 is largely comparable to those of the previous studies. Additionally, in TNG50 clumps seem to form continuously throughout cosmic time (see Figure B.7), which has not been investigated in other studies of clump formation.

These clumps can migrate to the center of their host galaxies due to dynamical friction, as well as merge with each other while doing so (Bournaud et al., 2007; Dekel & Krumholz, 2013; Bournaud et al., 2014; Mandelker et al., 2014; Dekel et al., 2021). The migration time to the center is found to be of the order of a few hundred Myr, which is similar for clumps in TNG50, where most of the clumps arrive at their respective galaxy's center after $1-2$ snapshots (~ 200 Myr) (see Figure B.7). This mechanism contributes to the formation of the bulge (e.g. Bournaud et al., 2007; Elmegreen et al., 2007; Dekel et al., 2009). Consequently, the properties of the clumps need to be specific, such that they survive their own internal stellar feedback and the tidal forces on their way to the center with enough stellar mass to significantly contribute to the formation of the bulge. In TNG50, the fraction of clumpy migration stars to the total stellar mass in the center is greater than 40% for about 12% of galaxies with any clumpy migrated stars in their centers (all of those galaxies have stellar masses above $10^{10.5}\,M_\odot$; see Figure B.7). Thus, the stellar mass transported by the migration of clumps is likely not very important for bulge formation for the major-

ity of high mass galaxies. Nevertheless, the clumps often retain a large amount of gas until the center, or drag gas along (see clump closest to the galaxy's center in the top right of Figure B.7), from which stars might form. We have not checked explicitly if this increases the contribution of stellar mass in the center significantly, or if such gas is lost by directly funneling into the SMBH.

In contrast to that, some simulations report clump formation, but then no migration due to almost immediate dissolution or disruption (Hopkins et al., 2012b, 2013a; Mayer et al., 2016; Oklopčić et al., 2017; Buck et al., 2017). This is likely due to the different simulation set ups, as well as the exact implementation of stellar feedback, or simply because not enough galaxy diversity is probed with isolated or zoom-in galaxy simulations. For example, in Figure B.7, we see that galaxies above $10^{10}\,M_\odot$ in stellar mass start to exhibit more than one clump on average, however significant amounts of clumps that are able to migrate to the center reside in galaxies with stellar masses around $10^{11}\,M_\odot$ and above. Hence, an investigation of clump formation and migration in a fully cosmological box is necessary to not only capture galaxies of different masses but also different galaxy assembly histories. In TNG50 mergers and other galaxy interactions, such as flybys, can trigger a significant amount of clump formation (although not exclusively; see also Di Matteo et al., 2008; Hopkins et al., 2013a; Calabrò et al., 2019, for similar reports).

Still, within TNG50 we want to exercise caution when it comes to the trustworthiness of clump formation and their exact properties. Only follow-up zoom-in simulations with higher resolution for different galaxies, as well as different treatment of star forming gas and stellar feedback (see e.g. Hopkins et al., 2013b; Smith et al., 2018; Smith, 2021; Smith et al., 2021, for the influence of highly resolved star formation and different stellar feedback schemes in galaxy simulations), will allow for a more robust quantification of clumps in TNG50. Nevertheless, the clump formation in TNG50 is unlikely to be a numerical artifact in its entirety, as the adaptive mesh refinement naturally allows for smaller cell sizes in areas of high gas density.

7.5.4 The predictive power of TNG50 at small(er) scales

While the TNG modelling framework is extremely successful in reproducing key observational results of galaxy populations, numerical resolution and the implementation of sub-grid physics are insuperable limitations of the physical model of galaxy formation. Regarding the former we demonstrate in Figure B.6 in Appendix B.4 that the total stellar mass within the central 500 pc of galaxies in TNG50 is converging (see also Pillepich et al., 2019). When splitting the central mass into the contribution of in-situ, migrated and ex-situ stars, the start of convergence is more difficult to assess due to the fixed size of r_{cut} (see Appendix B.4 for a more detailed discussion) as well as the overall influence of resolution on the amount of accreted stellar mass (which should overall increase with resolution, see also Grand et al., 2021).

Thus higher resolution runs are needed to fully determine the amount of convergence.

Higher resolution zoom-in simulations of some TNG50 galaxies - additionally with models variation of stellar feedback and a better resolved cold gas phase of the star forming gas - are certainly interesting and needed to properly evaluate the convergence of the central stellar mass, the formation of stellar clumps and observed nuclear galaxy components. Nevertheless, our study of TNG50 shows that the cosmological context plays a major role in the assembly of galaxy centers, which is unlikely to become less significant with numerical resolution and other modelling aspects. Already at the resolution of TNG50 it is *rare* to find a galaxy with *no* ex-situ stars in its central 500 pc, which is only the case for around 9% of all galaxies in our sample spanning a range between $5 \times 10^8 - 5 \times 10^{12}\,M_\odot$. This highlights that the high density, nuclear regions of galaxies can survive tidal forces and contribute to the build-up of the centers of others galaxies, and, if both galaxies are massive enough to host a black hole, to the growth ofSMBHs (see e.g. Schweizer et al., 2018; Voggel et al., 2022, for a recent observational confirmation of such a system).

Extending these trends to even smaller scales such as nuclear star cluster (NSC), which represent the densest stellar systems in the Universe, it is not impossible to think that their formation and evolution are also governed by galaxy interactions. Even though the relative fraction of ex-situ stars on tens of pc scales is likely very small for the majority of galaxies, it is clear that the in-situ star formation and the migration of stars to the center is closely connected to the formation pathway of the entire galaxy (see Figure 7.11), because galaxy interactions are able to create the conditions needed to funnel gas and stars to the center. Therefore, it is important to treat NSC formation in the context of the hierarchical build-up of galaxies in a ΛCDM cosmology (see also Brown et al., 2018) and consider the influence of galaxy interactions in (semi-)analytical models (Leaman & van de Ven, 2021).

We have explicitly checked within TNG50, if we can make predictions at smaller scales than 500 pc, by repeating our entire analysis for r_{cut} of 250 pc (approximately the softening length of TNG50) and 100 pc, as well as 1 kpc for a consistency check. In addition to TNG50-1 (the highest resolution), we repeated this for the two lower resolution realizations, which are TNG50-2 and TNG50-3 respectively. The results are shown in Figure 7.12 for galaxies between $10^{10.5}$ and $10^{11}\,M_\odot$.

With decreasing size of the center (r_{cut}) the absolute mass decreases for all three origins. However, the *fraction* of the in-situ population decreases with decreasing central size, while the migrated fraction increases; a consequence of the smaller volume that is proved. At the same time, this behaviour is also affected by the resolution, which not only sets the absolute normalization of the mass fraction, but also the spatial size at which the relative contribution of the in-situ and migrated fraction swaps. We therefore conclude, that a hypothetical higher resolution (TNG50-0) would increase (decrease) the in-situ (migrated) fraction below 250 pc due to the convergence behaviour of the absolute stellar mass at fixed aperture size. Similarly, the contribution

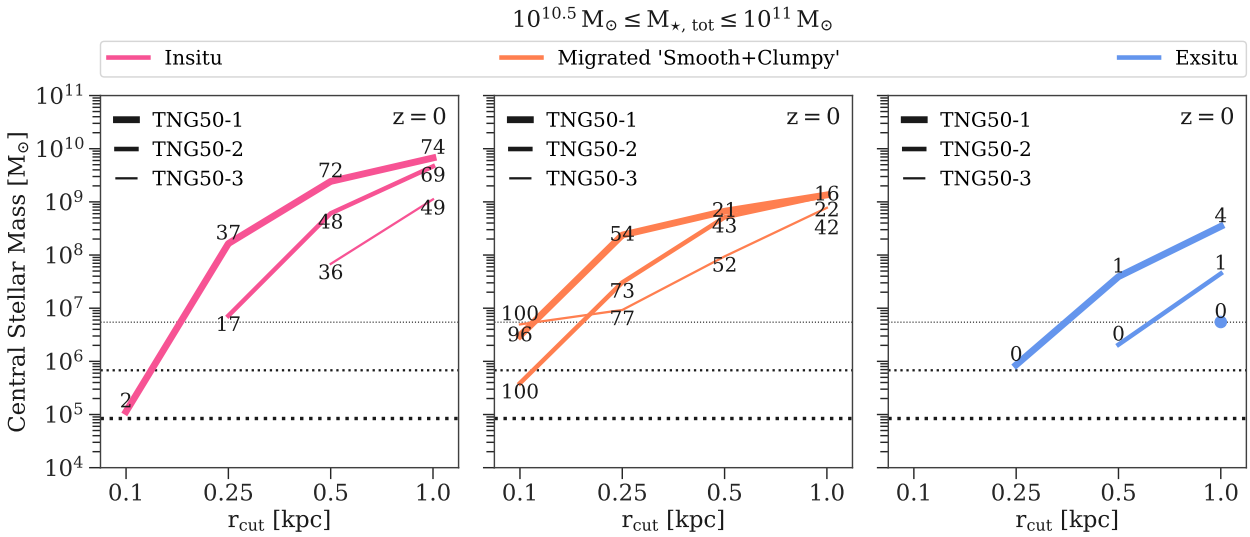

Figure 7.12. Effects of numerical resolution and aperture size on the central stellar mass for in-situ, migrated and ex-situ stars in TNG50 galaxies with $10^{10.5-11}\,M_\odot$ in stellar mass at z = 0. Lines show the median central stellar mass for in-situ (*pink*), migrated (*orange*) and ex-situ (*blue*) stars for four choices of $r_{cut} = 0.1,\ 0.25,\ 0.5$ and 1 kpc and three resolution realizations of TNG50 (thicker lines indicate better resolution). TNG50-1 is the highest resolution (flagship), followed by TNG50-2 and -3, which have 2 and 4 times lower spatial resolution. The mass resolution is 8 and 64 times lower respectively and indicated by the dotted horizontal lines. The numbers indicate the respective central stellar mass *fraction* in percent. Decreasing size of the center means decreasing stellar mass. However the fraction of migrated mass increases, while the in-situ fraction consequentially decreases. At a hypothetical higher resolution (TNG50-0) the latter effect would be lessened as more stellar mass is formed within a given aperture size. Similar trends are recovered for other galaxy masses.

of ex-situ stars will increase at a given aperture and also likely reach scales smaller than 500 pc.

This behaviour emphasizes that the contribution of all three origins will likely remain relevant on scales of 100 pc.

7.5.5 Galaxy centers as tracers of overall galaxy assembly

Unveiling the merger history of galaxies proves difficult to tackle outside our own Galaxy due to many reasons. Perhaps the most severe one is the fact that accreted material is not necessarily visually apparent in the forms of streams and shells (or any other form of irregularity), especially when the merger coalesced many Gyr ago.

Since deep photometry of galaxies (initially stacked for many galaxies) revealed the need for an additional Sérsic component to accurately fit their surface brightness profiles beyond tens of kpc (e.g. Zibetti et al., 2004; Tal & van Dokkum, 2011; D'Souza et al., 2014), the focus of quantifying accreted material has primarily been on the outskirts of galaxies, i.e. their stellar halos (e.g. Monachesi et al., 2016; Merritt et al., 2016; Spavone et al., 2017; Huang et al., 2018; Spavone et al., 2020). It is understood that the excess of light at large galactic radii should mark the transition from the in-situ to ex-situ dominated areas of a galaxy, as (significant) stellar mass can be build-up through minor merging there.

However, the new era of cosmological hydrodynamical simulations

suggest that such a transition does not necessarily exist for every galaxy, as especially high mass galaxies can be dominated by ex-situ stars at all radii (Tacchella et al., 2019; Pulsoni et al., 2021). Furthermore, Remus & Forbes (2021) showed that the transition in surface brightness profiles traced by two Sérsic fits does not correspond to the true in-situ and ex-situ dominated regions. Similarly, changes in kinematic profiles at large radii, which can, for example, be obtained with globular clusters (e.g. Arnold et al., 2014) or planetary nebulae (e.g. Pulsoni et al., 2018), do not, in general, correspond to transitions between in-situ and ex-situ dominated regions (Schulze et al., 2020; Pulsoni et al., 2021).

While detailed studies of stellar halos are certainly important and necessary, our study suggests that there lies potential in using the centers of galaxies to study their accretion history (see Figure 7.5). Not only are the centers the brightest region of a galaxy and hence deliver the highest quality data, but they are also increasingly covered in numbers by IFU surveys, which provide detailed kinematic and stellar population information (e.g. SAMI: Bryant et al., 2015, MaNGA: Bundy et al., 2015). In particular, our results in Figures 7.9 and 7.10 show that in-situ and ex-situ stars in the center are (on average) well separated in age-metallicity-circularity space for galaxies with stellar masses $\leqslant 10^{10.5}\,M_\odot$. Newly developed techniques are able to extract such *distributions* in ages and metallicity as well as circularities from IFU measurements, and already have been proven to be able to estimate the true underlying accreted stellar material much more realistically (Boecker et al., 2020a,b; Zhu et al., 2020; Davison et al., 2021; Zhu et al., 2022b).

Even though in-situ and ex-situ stars separate better in their stellar population and dynamical properties for these lower mass galaxies, the ex-situ stellar mass fraction in the central 500 pc is *on average* tenth of percent, thus picking up accreted signatures in the very centers will still be challenging even with these new techniques. However, low redshift IFU observations easily cover $1-2$ half-light radii, which extend beyond 500 pc and hence should encompass more accreted material. More follow up work will be needed to quantify the optimal extent needed from a galaxy's center to reliably pick up ex-situ fractions in observations.

On top of that, the large spread seen in the central ex-situ mass *at fixed total ex-situ mass* (see Figure 7.5) points towards significant spatial variation of ex-situ stars in the host galaxy, regardless of whether the galaxy has accreted a lot of stellar material or not. It is likely that measuring these spatial variations, will inform us about the types of mergers that have happened. Typical characteristics could be the merger ratio, for example major mergers will have the ability to deposit more of their stars in the center of galaxies, but also the gas content or orbital infall parameters. We plan to exploit this in future work.

7.5.6 Hints for (SDSS-like) observations

TNG50 predicts a diverse mass build-up of galaxy centers. What are the prospects to learn about a galaxy's central in-situ, migrated and ex-situ fraction from more "traditional" observations? For example, from SDSS DR7 (Abazajian et al., 2009), that provides single 3″ fiber spectra for centers of hundred of thousand of galaxies, *average* ages, metallicities and [α/Fe] abundances can be determined (Gallazzi et al., 2021). How much information do such measurements contain about the contribution of stellar populations of different origins to a galaxy's center?

In Figure 7.13 we show the mass-weighted average central age and metallicity for our sample of TNG50 galaxies color-coded by the mass fraction attributed to each origin (LOESS smoothed; Cappellari et al., 2013b).

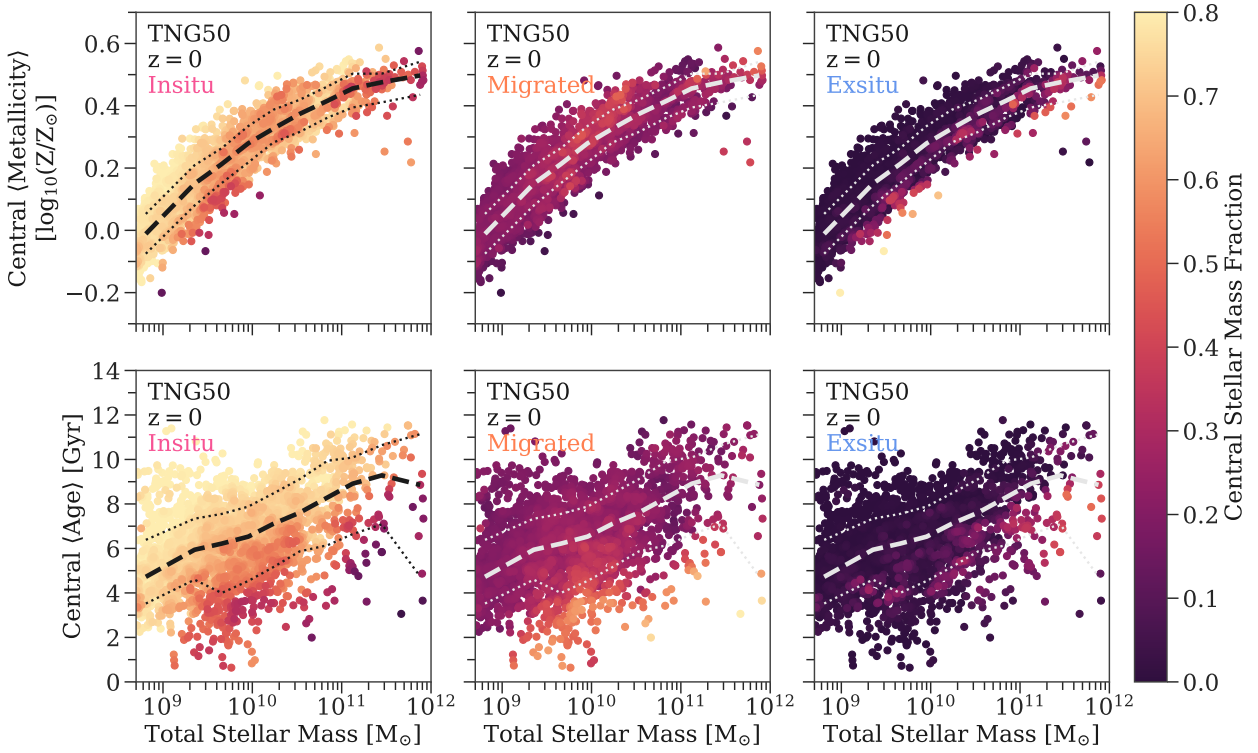

Figure 7.13. Information about the central (500 pc) fractional mass associated with in-situ, migrated and ex-situ stars contained in average age and metallicity measurements from TNG50 galaxies at z = 0. *Top row*: Mass-weighted average metallicities for *all* central stars as a function of the galaxy's total stellar mass, but color-coded in each panel *(from left to right)* according to their fraction of in-situ, migrated and ex-situ stars. The colors are LOESS (Cappellari et al., 2013b) smoothed to show the average around neighbouring galaxies. The thick dashed line shows the median relation in each panel, and the thin dotted lines show the 16th and 84th percentile respectively. *Bottom row*: The same but for the mass-weighted average age. Galaxies that are more metal-poor than the 16th percentile for their corresponding stellar mass are more likely to have high ex-situ fractions in their centers, while galaxies with high central migrated fractions are younger than the 16th percentile.

If the measured average central age and metallicity of a galaxy lies on the respective mass-age and mass-metallicity relation, the galaxy has likely a high fraction of in-situ stars in its center, except if its larger than 10^{11} $M_\odot$ in stellar mass. If the measured average metal-

licity is *below* the 16th percentile at fixed stellar mass, it is more likely that the galaxy's center is dominated by ex-situ stars. Similarly, if the galaxy has an average age below the 16th percentile, it has likely a high amount of migrated stars in its center. High mass galaxies above $10^{11}\,M_\odot$ with significant amounts of ex-situ stars in their centers, also have a slightly younger age (between the 16th percentile and the median) than the typical average galaxy in that mass regime.

Naturally, a proper mocking of observed average stellar population properties from TNG50 is needed to compare accurately to measurements from Gallazzi et al. (2021). However, Figure 7.13 seems to acknowledge that such measurements provide some leverage in determining the fraction of stars with different origins in the centers of galaxies.

With respect to comparisons to the whole SDSS galaxy sample, it would be necessary to repeat the analysis of this Chapter for different spatial apertures, The fixed 3″ diameter of the SDSS fibers will already encompass larger physical sizes than 1 kpc for galaxies with $z > 0.02$. It would be interesting to understand how the relative contribution of stars from the different origins change with greater spatial extent, especially for the ex-situ stars.

7.6 SUMMARY AND CONCLUSIONS

Galaxies growth hierarchically in a ΛCDM universe. Their centers are the regions where usually the highest quality observations are available. What information about the hierarchical growth of galaxy formation is encoded in this observationally favourable region? To answer this, we investigated the central 500 pc mass assembly of galaxies ranging from $5 \times 10^8\,M_\odot$ to $5 \times 10^{12}\,M_\odot$ with half-mass radii > 2 kpc in the TNG50 simulation.

Stars that are found at the center of TNG50 galaxies at $z = 0$ originate from one of the three possibilities: in-situ (formed inside the center), migrated (formed inside the host galaxy, but outside the center), ex-situ (brought in by mergers). Stars can migrate to the center either as as continuous distribution of individuals (smooth) or in clumps.

For each origin we characterized their radius with respect to their host galaxy at birth to understand the travelling distances for the migrated stars as well as the spatial environment of ex-situ stars at the time of birth and deposit into the $z = 0$ host.

We then investigated the amount of the central stellar mass contained in each of three origins and their relative contribution as well as their correlation to each other across the entire TNG50 galaxy mass range. Additionally, we studied differences in central in-situ, migrated and ex-situ for different galaxy types at $z = 0$.

To address whether the different origins of central stars leave a discernible imprint on their (observable) features, we characterized and correlated their ages, metallicities, [Mg/Fe] abundances as well as dynamical properties with their distributions in circularity as a function of the galaxy's total stellar mass. We summarize our most important

findings below:

- In-situ stars are on average the dominant component in stellar mass in the central 500 pc of TNG50 galaxies across the entire mass range of $5 \times 10^{8-12}\,M_\odot$. Migrated stars contribute on average 20% to the total stellar mass in the center, where below (above) $5 \times 10^{10}\,M_\odot$ in galaxy stellar mass smoothly (clumpy) migrated stars encompass their majority. The central stellar mass fraction of ex-situ stars becomes *on average* non negligible above galaxy masses of $5 \times 10^{10}\,M_\odot$ with a large scatter of up to 80%. However, it is the *exception* to find a galaxy without *any* ex-situ stellar mass in its central 500 pc, which is only the case for about 9% of galaxies in our total sample. (Figure 7.4)

- The majority of smoothly migrated stars originate close to the center (radii between 500 pc and 1 kpc), whereas $\sim$ 15% come from larger distances up until 10 kpc. Compared to that, clumpy migrated stars possess a distinctively different distribution of birth radii which peaks around $20-30$ kpc for galaxies with stellar masses greater than $5 \times 10^{10}\,M_\odot$. Most of the ex-situ stars originate in the central 1 kpc of their birth galaxies, where they remain until they are deposited inside their $z = 0$ host galaxy. (Figure 7.3)

- *At fixed galaxy stellar mass* the amount of central ex-situ stellar mass exhibits a significant scatter between $4-6$ dex, reflecting the stochasticity of the merger history of individual galaxies. In some cases, close to the *entire* total amount of ex-situ stellar material ever deposited inside the host galaxy resides within the central 500 pc. (Figure 7.5)

- In TNG at $z = 0$, star forming galaxies with stellar masses above $10^{10}\,M_\odot$ have on average *larger* ex-situ central stellar masses than their quenched counterparts. Only quenched galaxies that are additionally bulgey and have no bar signature show a rise of central ex-situ stellar mass above $10^{10}\,M_\odot$ similar to the star forming galaxies. Galaxies between $5 \times 10^{9} - 5 \times 10^{10}\,M_\odot$ with an overmassive (undermassive) SMBH in the center are more compact (extended) and show on average a higher (lower) in-situ and migrated central stellar mass. There is *no* difference in neither in-situ, migrated nor ex-situ central stellar masses for central or satellite galaxies. (Figure 7.6)

- Central ex-situ stars have on average the lowest metallicities, the oldest ages and the highest [Mg/Fe] abundances. The slope of their mass-metallicity relation is slightly steeper than that of the in-situ and migrated stars, and their mass-age relation is flat compared to the positive correlation between central age and galaxy stellar mass for the in-situ and migrated stars. Overall, the average stellar populations properties of in-situ and migrated stars are very similar, with in-situ stars being slightly more metal-rich and older. (Figure 7.7)

- The majority of central stars for galaxies with stellar masses below $10^9\,M_\odot$ and above $10^{11}\,M_\odot$ regardless of their origin are on random motion dominated orbits. For galaxies in between those stellar masses, the peak of the circularity distribution shifts by 0.5 (0.25) towards rotationally supported orbits for migrated (in-situ) stars *for both* disk and bulge dominated galaxies, whereas ex-situ stars remain random motion dominated at all galaxy masses. (Figure 7.8)
- For star forming galaxies around $10^{10}\,M_\odot$ in stellar mass, in-situ, migrated and ex-situ stars clearly separate in age-metallicity space, while the distinction becomes less clear for star forming galaxies outside that mass range and quenched galaxies in general. (Figure 7.9)
- For both disk and bulge dominated galaxies between $10^{9.5-10}\,M_\odot$ in stellar mass, in-situ, migrated and ex-situ stars clearly separate in age-circularity space. The migrated stars are the youngest with the highest amount of rotational support and the ex-situ stars are the oldest and purely random motion supported, whereas the in-situ stars are situated in between. (Figure 7.10)

Furthermore, we have demonstrated the diversity of the central 500 pc of galaxies as governed by the hierarchical mass build-up in a ΛCDM universe. Galaxy interactions are an important driver in not only contributing ex-situ stars to the center of galaxies, but also in dictating the formation of in-situ stars and the migration of stars to the center. This leads to an entanglement of different mechanisms that influence the formation history of stars in the center of galaxies. In Figure 7.11 we have qualitatively identified these mechanisms that are present in TNG50, which includes episodes of in-situ star formation and stellar migration to the center during times of pericenter passages and/or coalescence of mergers or flybys, infall into galaxy groups/clusters as well as depletion of the central gas reservoir through kinetic AGN feedback and environmental effects.

In the future, higher resolution simulations (not only spatially but also concerning star formation and stellar feedback prescriptions) will be needed to fully address the formation and migration of stellar clumps and to study the formation of nuclear galaxy structures, such as nuclear disks and star clusters, in a fully cosmological context.

Bright galaxy centers have the potential to be used in observations as tracers of the overall galaxy assembly history. TNG50 predicts distinct stellar populations and dynamical properties for the stars of different origins in the center of galaxies, which can be observed with today's IFU capabilities. Figure 7.13 demonstrates that there is even promise to deduce the fractional contribution of central in-situ, migrated and ex-situ stars from SDSS-like observations in a galaxy population averaged sense.

In summary, TNG50 is a tremendous advancement in predicting the stellar build-up of sub-kpc scales in a fully cosmological context. Its predictive power is valuable to consider new pathways in modelling formation scenarios of central stellar components as well as to push

forward novel observational techniques to unveil the formation history of galaxies.

APPENDIX B

Supplementary material for the study conducted in Chapter 7.

Contents

B.1 PROPERTIES OF TNG50 GALAXIES

Below we describe in detail the properties of TNG50 galaxies as well as their stellar particles that were mentioned in Section 7.2.3. They are either directly available from the corresponding halo/subhalo, stellar particle or supplementary data catalogues on the TNG website[119]. The classification of 'bar-like' signatures for galaxies is available upon reasonable request from the corresponding author.

119: https://www.tng-project.org/data/docs/specifications/

B.1.1 Bulk Properties

We here describe how different galaxy bulk properties are defined and measured in order to define different galaxy populations that are analyzed in Section 7.4.1. All properties refer to $z = 0$.

- *Mass*: Generally all galaxy masses are reported to be the total mass of particles of a given type (or all types in the case of dynamical mass) bound to a specific subhalo as identified by the SUBFIND algorithm.
- *Environment*: We crudely define the environment of a galaxy by distinguishing between centrals and satellites. A central galaxy is the most massive subhalo in its corresponding FoF halo, all other galaxies within the same FoF halo are satellite galaxies.
- *Star formation activity*: Whether a galaxy is actively forming stars or not is classified according to Pillepich et al. (2019) (see also Donnari et al., 2019, 2021a,b), who determined the logarithmic distance from the star forming main sequence for each galaxy ($\Delta \log_{10}$ SFR). For this, the instantaneous star formation rate (SFR) of the gas cells as well as galaxy stellar masses were calculated within twice the stellar half mass radius. Star forming and quenched galaxies have $\Delta \log_{10} \mathrm{SFR} \geqslant -0.5$ and $\Delta \log_{10} \mathrm{SFR} \leqslant -1$ respectively, whereas galaxies in the green valley are in between those two values. Unless otherwise stated we will omit the distinction of green valley galaxies and also classify them as quenched.
- *Morphology*: We quantify disk or bulge dominated galaxies based on the kinematic classification by Genel et al. (2018). For each stellar particle the circularity parameter ϵ is calculated, which gives the ratio of the particle's specific angular momentum in z-direction and its theoretical maximum angular momentum at that specific binding energy (Abadi et al., 2003; Marinacci et al., 2014). Then the mass fraction of all stellar particles with $\epsilon > 0.7$ and within ten stellar half mass radii is computed. If that fractional mass is above 0.4 we classify that galaxy as disky (see Joshi et al., 2020), otherwise the galaxy is bulge dominated.
- *Bar-like signatures*: We also provide a quick estimate of whether a galaxy has a bar-like structure in its center. For this, we calculate A_2, the ratio between the second and zeroth term of the

amplitude of the Fourier expansion, from the face-on stellar surface density of each galaxy as a function of the 2D radius in ~ 0.04 dex steps, where each bin is ensured to have at least 100 stellar particles. We then identify peaks in the A_2-radius plane with a prominence of at least 0.05. After that, the value of A_2 for the largest peak within a radius of 10 kpc is recorded. We impose this radius cut to mitigate the effect of other A_2 features that may be present at larger radii (see also Frankel et al., 2022). This is done for all snapshots between $z = 0$ (`SnapNum` 99) and $z = 4.2$ (`SnapNum` 20). Similarly to Rosas-Guevara et al. (2020)[120], we then define a bar-like structure, when the maximum A_2 value (at a given time step) is above 0.2. Bar-like structures at $z = 0$ are defined solely based on their instantaneous A_2 value at that snapshot. While this method leads to accurate identification of symmetrically elongated 'bar-like' features, we do not check if this is actually a 'proper' bar in the astrophysical sense. Nevertheless, our classification leads to a bar fraction of around 40% (50%) for disk (all) galaxies above $10^{10}\,M_\odot$ in stellar mass, which is consistent with observations (see e.g. Sheth et al., 2008; Simmons et al., 2014; Díaz-García et al., 2016a).

120: We find that our computed A_2 values are slightly lower than those measured by methods of Rosas-Guevara et al. (2020), hence we adopt their 'weak bar' threshold of 0.2, whereas their 'strong bars' have values of $A_2 \geqslant 0.3$.

- *AGN feedback*: We quantify the severity of feedback from supermassive black holes by determining whether a specific galaxy lies below or above the median scaling relation of TNG50 galaxies (e.g. similarly to Martín-Navarro et al., 2018b, for observations). Typical AGN feedback defining properties could be the black hole (BH) mass and the cumulative energy injection in the thermal and/or kinetic feedback modes (see e.g. Weinberger et al., 2017; Zinger et al., 2020, for background). Such scaling relations are always computed with respect to the total stellar mass of galaxies as well as for the total TNG50 galaxy sample above $5 \times 10^8\,M_\odot$ (see Section 7.2.4.2). Properties of black hole particles per galaxy are computed as the sum of all black holes particles associated to a given galaxy via SUBFIND.

- *Physical size*: Similarly, we define extended or compact galaxies depending on whether they are below or above the median stellar mass-size relation of TNG50 galaxies. The size is the 3D stellar half mass radius.

B.1.2 Stellar Particle Properties

Stellar particle properties at $z = 0$ that are analyzed in Section 7.4.2 are briefly described here:

- *Age*: We define the age of a stellar particle as the lookback time in Gyr calculated from the field `GFM_StellarFormationTime`, which provides the *exact* time of birth of a star in scale factors.

- *Metallicity*: We convert the mass fraction in metals Z as provided by the field `GFM_Metallicity` to $\log_{10} Z/Z_\odot$ with $Z_\odot = 0.02$. This

follows conventions adopted in observations, e.g. Gallazzi et al. (2021).

- *[Mg/Fe]*: We calculate the magnesium-to-iron abundance from the mass fraction in magnesium Z_{Mg} and iron Z_{Fe} provided by the simulation (`GFM_Metals`) via $[Mg/Fe] = \log_{10}(Z_{Mg}/Z_{Mg,\odot}) - \log_{10}(Z_{Fe}/Z_{Fe,\odot})$. The adopted solar values are $Z_{Mg,\odot} = 0.00064298$ and $Z_{Fe,\odot} = 0.001218$ respectively from Asplund et al. (2009).
- *Circularity* ϵ: We calculate the instantaneous circularity of each stellar particle following Genel et al. (2018). For this we first compute the specific angular momentum of each particle in z-direction by aligning the z-axis of the simulation box with the total angular momentum of stellar particles within twice the stellar half mass radius of a given galaxy. The theoretical maximum angular momentum each stellar particle can have at its recorded specific binding energy (i.e. $\frac{1}{2}|\mathbf{v}|^2 + \Phi$) is calculated by sliding a maximum filter across the particle list of specific angular momenta sorted by their total specific binding energy with a window size of one hundred. Stars with circularities around zero are on random motion dominated orbits, whereas values close to one indicate more circular orbits. Negative circularities depict counter rotating orbits.

B.2 Validation for analysis of TNG50 galaxy centers

We briefly validate and justify here the analysis choices we made in Sections 7.2.4 and 7.3.1 of the main text using two TNG50 galaxies as examples where applicable. Both of these galaxies are also contained within the subboxes, i.e. smaller regions of the full simulation box, which offer 3600 snapshots resulting in a time sampling of $2 - 3\,\mathrm{Myr}$. At $z = 0$, `SubfindID` 537941 is a Milky Way like galaxy, found in 'Subbox0', and `SubfindID` 35, found in 'Subbox2', is a compact $\sim 10^{10}\,M_\odot$ in stellar mass galaxy, that quenched approximately 9 Gyr ago and is now found in the most massive halo ($\sim 10^{14}\,M_\odot$) in TNG50. Both of these subhalos stay inside the subbox across their life time making it possible to compare their full histories in the higher cadence outputs to that of the hundred full box snapshot outputs.

B.2.1 Selection of central stars

We show in Figure B.1 the energy and angular momentum distribution of stars in the galaxy's centers at $z = 0$ by selecting particles based on their current radius as well as on their energies according to Equation 7.1. The selection was made with $r_{cut} = 500\,\mathrm{pc}$. We also show their peri- and apocenters which we calculated by recording their radii from all 16 subbox outputs between the last full box snapshot, i.e. $z = 0$ (`SnapNum` 99), and the one prior to that, i.e. $\approx 136\,\mathrm{Myr}$ (`SnapNum` 98) before. We

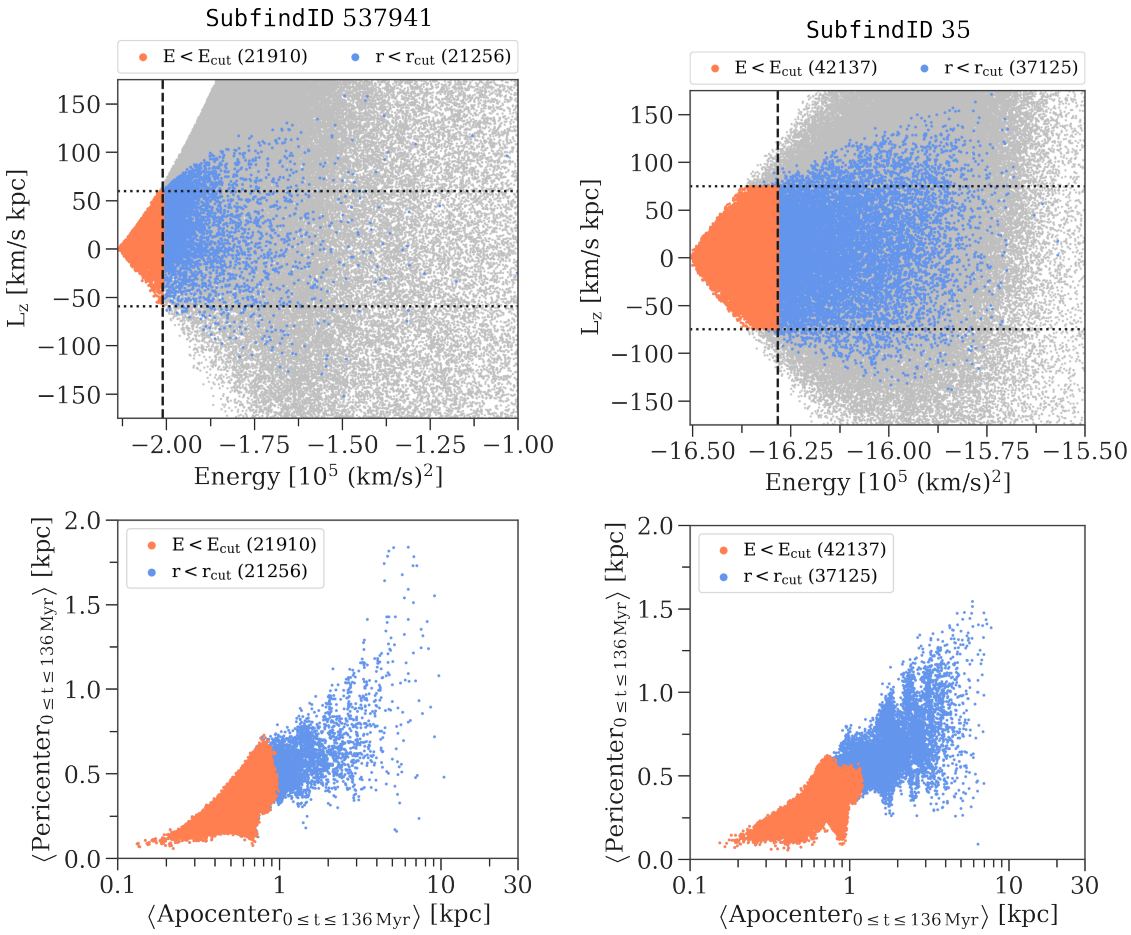

Figure B.1. Selection of stellar particles belonging to a galaxy's center, *left column* for `SubfindID` 537941 and *right column* for `SubfindID` 35. Blue points show stellar particles that have radii smaller than $r_{cut} = 500\,pc$ and orange points where selected based on their energies being smaller than E_{cut} according to Equation 7.1, also with $r_{cut} = 500\,pc$. *Top row*: Angular momentum of selected particles as a function of energy. The dashed lines emphasizes E_{cut}, whereas the two dotted lines show $L_z = \pm r_{cut} v_{circ}(r_{cut})$. Grey points show all other stellar particles belonging to the respective galaxy. *Bottom row*: Pericenter of stellar particles versus their apocenter time averaged from subbox outputs between 0 (full box snapshot 99) and 136 Myr (full box snapshot 98). Stellar particles purely selected on their radius have a wider distribution in their energies and are hence able to move much further outside our selected spherical volume of 500 pc, which is also reflected by their larger apocenters.

then found all minima and maxima and took the average respectively.

Some particles selected by their instantaneous radius at $z = 0$ have large energies and are hence able to move away from the center to much larger radii, i.e. they are not actually spending the majority of their orbital time within our selected spherical aperture. This is also reflected by their larger (up to 10 kpc) apocenters, whereas particles selected by their energy have time-averaged peri- and apocenters not larger than 1 kpc. Even though that is larger than our selected r_{cut} value, probably due to our simplifying assumptions in calculating E_{cut}, we argue that this selection gives a much cleaner selection of stars actually belonging to the center without interloping particles on much more eccentric orbits. Both selection criteria yield a comparable number of stars, with around 21000 stars for `SubfindID` 537941 (1.6% of total amount of stars) and $\sim$ 40000 stars for `SubfindID` 35 ($\sim$ 15% of total amount of stars).

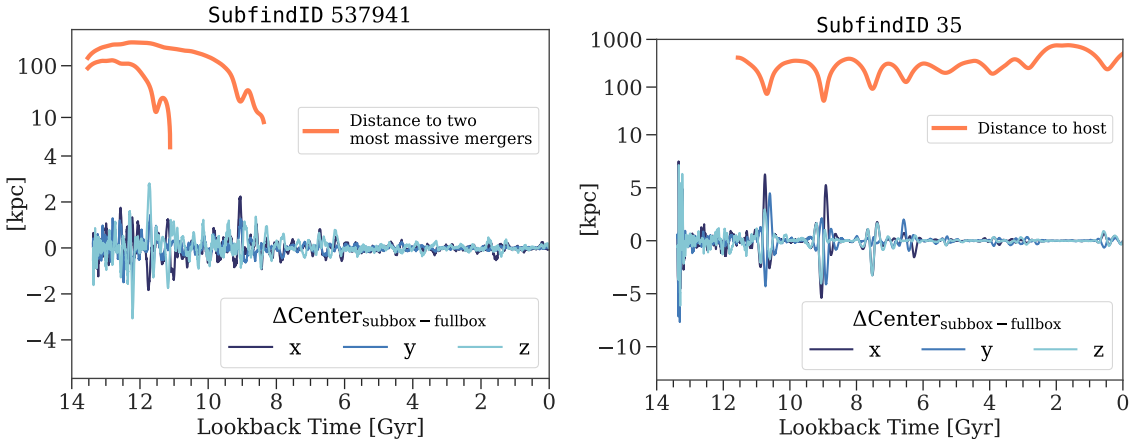

Figure B.2. Differences in galaxy centering between full box and subbox snapshots. Comparison between the interpolated (cubic spline) center position from the 100 full box snapshots (using `SubhaloPos` from the subhalo catalogue) and the center position (most bound stellar particle) from the higher cadence subbox outputs for two example galaxies (*blue shaded lines*). The *top panel* shows `SubfindID` 537941, a Milky Way like galaxy and the *bottom panel* shows `SubfindID` 35, a $\sim 10^{10}\,M_\odot$, quenched galaxy that is now a satellite of the most massive halo in TNG50. We see that the interpolated center of the galaxies starts to deviate significantly from the true center position when there are pericenter passages from satellites that merge with galaxy or when the galaxy itself is a satellite and approaches its host (*thick orange lines*).

B.2.2 Definition of birth radii of stellar particles

In Figure B.2 we show the difference between the center position of the two galaxies once taken from the high cadence subbox outputs (the most bound stellar particle)[121] and once from the `SubhaloPos` argument from the full box snapshots, which we interpolated onto the finer time sampling of the subbox outputs using a cubic spline. It is evident that deviations of around $2-5\,\mathrm{kpc}$ appear, specifically at times of pericenter passages of either satellites merging with the host (`SubfindID` 537941) or of the galaxy itself around its host (`SubfindID` 35).

These deviations of a galaxy's center position are enough to severely miss-classify migrated and in-situ stars, when their instantaneous birth positions, as provided by the simulations output (`BirthPos`), are used in conjunction with the interpolated subhalo center. For example, in Figure B.3 we show histograms of migrated and in-situ stars selected according to their instantaneous birth position using the proper center from the subbox and the interpolated one from the full box snapshots. For both galaxies the number of migrated stars doubles when the interpolated center is used compared to the correct center.

Ideally, we would like to apply our analysis to as many galaxies as possible, but as only a handful of galaxies reside inside the subboxes during their whole life time, we need an alternative measure for classifying them into migrated and in-situ stars that can be applied to the full box of TNG50. We therefore take the particle's position at the full box snapshot it first appeared in as its "birth" position and compare it to the instantaneous one with the proper centering, also shown in Figure B.3. We see that the shapes of their histograms as well as their percentages match. Of course, their classification is not identical,

121: As there is in fact no subhalo information from SUBFIND available for the subboxes, we start off with the interpolated center values from the full box snapshots and then recalculate the center in a 5 kpc box around that, recenter and recalculate the center again in a 5 kpc box around that. We verified that this gives the correct center by inspecting the galaxies by eye. We note however that this approach will not yield correct results in a general black box fashion.

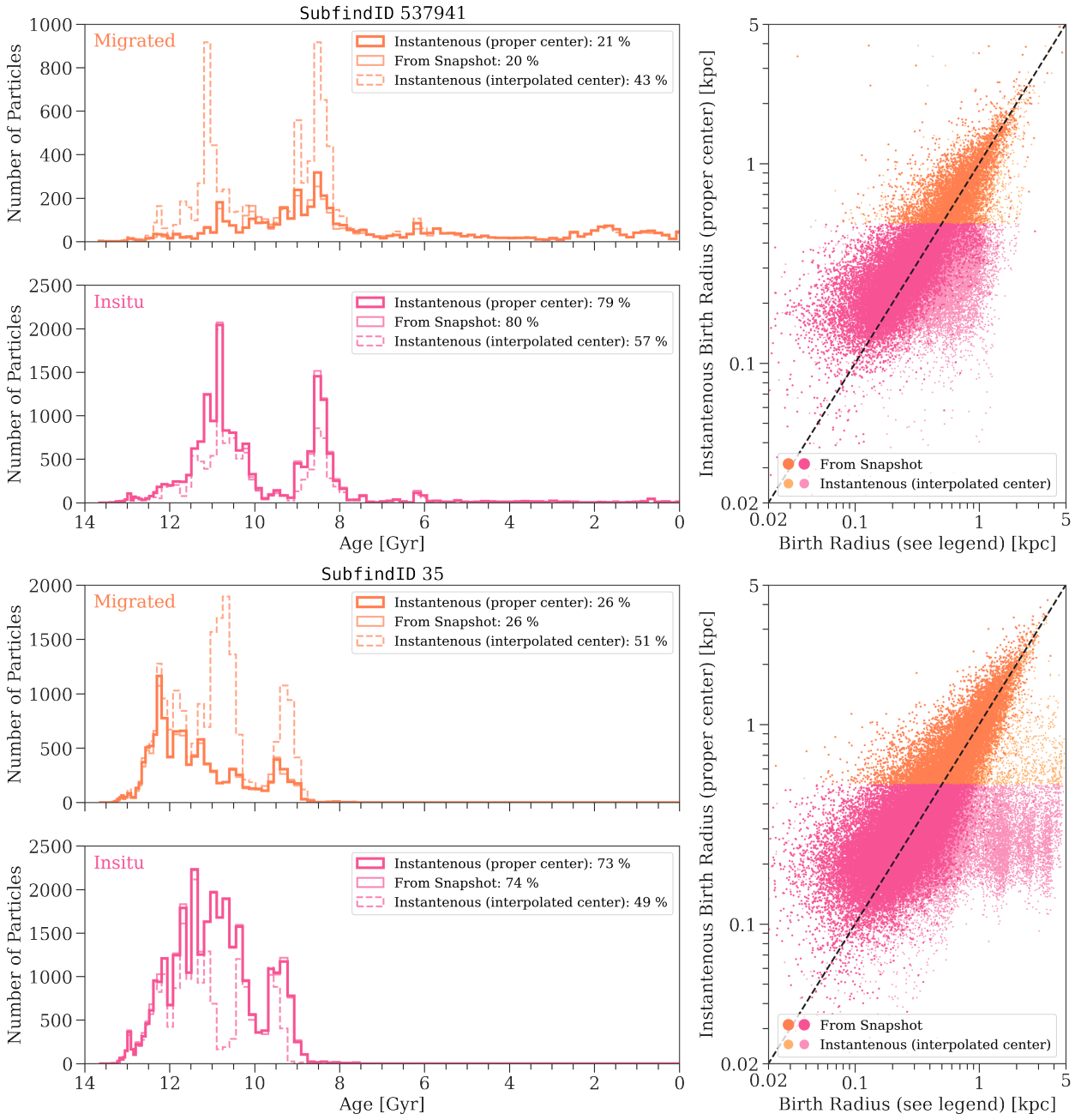

Figure B.3. Effect of erroneous galaxy centering on the classification of migrated stellar particles. *Left panels*: Histograms of particles being classified as migrated (*orange*) and in-situ (*pink*) using three different approaches: the instantaneous position at birth with the proper centering from the subbox outputs (*thick solid line*), the same but with the interpolated center (*thin dashed line*) as well as the position of particles taken from the full box snapshots they first appeared in (*thin solid line*). *Right panels*: Comparing the values of the instantaneous birth radii with the centering from the subbox outputs with the ones with the interpolated center (*fainter, smaller points*) as well as the radii from the full box snapshots in which the particles first appeared in (*bolder, bigger points*). The one-to-one relation is also shown (*black dashed lines*). The *top panel* shows `SubfindID` 537941, a Milky Way like galaxy and the *bottom panel* shows `SubfindID` 35, a $\sim 10^{10}\,M_\odot$, quenched galaxy that fell into the most massive halo of TNG50. Using the instantaneous birth position with the interpolated center leads to a wrong classification of migrated and in-situ stars, whereas using the positions from the full box snapshots at birth gives comparable results to the instantaneous birth positions with the proper centering in the actual number of particles in the two categories as well as the values of their birth radii.

as particles move between their exact formation time and the time of when the snapshot was taken, however this measure seems to be more

accurate than using the instantaneous birth positions with the interpolated center.

Finally, we compare the instantaneous birth radii using the correct center of the migrated and in-situ stars (classified with the instantaneous positions using the correct center) with birth radii calculated by the other two methods. The birth radii determined from the full box snapshots scatter around the one-to-one relation, whereas the ones with the interpolated center do not. Hence, we conclude that applying the migrated and in-situ classification based on their birth snapshot position to the whole TNG50 box seems to provide us with similar knowledge about their origin as if we would have used their instantaneous birth position.

B.3 THE TOTAL EX-SITU STELLAR MASS FRACTION OF TNG50

In Figure B.4 we show the total ex-situ stellar mass fraction as a function of total stellar mass for TNG50 galaxies. They are further divided into star forming and quenched galaxies according to their distance to the star forming main sequence at $z = 0$.

Most importantly, we see that the total ex-situ stellar mass fraction does not change worryingly, when comparing the fiducial definition of ex-situ stars according to Rodriguez-Gomez et al. (2016) as well as our definition, where we exclude stars from accreted satellites classified as clumps (i.e. `SubhaloFlag` $= 0$). Even though the clumps do not play an important role for the definition of the ex-situ fraction, they are abundant in TNG50 (see Appendix B.5). Only due to our definition, we could confirm the migration of these clumps contributing significantly to the build-up of the galaxy center for galaxies above $10^{11}\,M_\odot$ in stellar mass.

Additionally, Figure B.4 shows that star forming galaxies have a higher total ex-situ fraction on average than quenched galaxies across all stellar masses. Until galaxy stellar masses of $10^{10}\,M_\odot$ the ex-situ fraction stays roughly constant with values around 4-5% and 3% for star forming and quenched galaxies respectively. There is however a large scatter associated with the ex-situ fraction for galaxies in this mass regime. Above $10^{10}\,M_\odot$ the ex-situ fraction sharply increases with galaxy stellar mass reaching approximately 50% for galaxy between $10^{11} - 10^{12}\,M_\odot$ for TNG50. The scatter decreases accordingly. We have checked this exact relation with the lower resolution run TNG50-2 as well as TNG100 and obtained similar results.

Figure B.5 shows the mass-size relation for TNG50 galaxies colored according their relative ex-situ fraction, i.e. if they have high or low ex-situ fractions with respect to the average typical for their respective stellar mass (Merritt et al., 2020, following). Galaxies with stellar masses $\lesssim 5 \times 10^{10}\,M_\odot$ and above average ex-situ fractions are on average more extended. This median trend is not observed for the high-mass end, however compact galaxies at $10^{11}\,M_\odot$ have almost exclusively below average ex-situ fractions in agreement with other studies

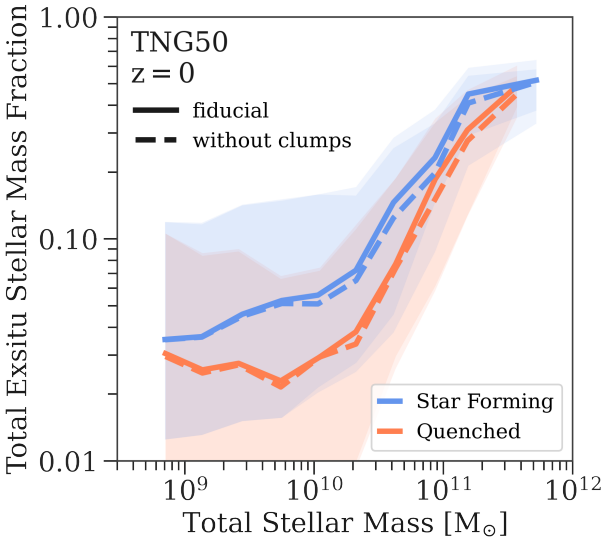

Figure B.4. Total ex-situ stellar mass fraction versus total stellar mass in TNG50 at z = 0. The solid lines show the fiducial ex-situ fraction as classified by methods in Rodriguez-Gomez et al. (2016), whereas the dashed lines show total ex-situ fractions excluding spurious (`SubhaloFlag` = 0) galaxies or "clumps" (see Section 7.3.1.2). The faint bands depict the 16th and 84th percentiles. There is no significant difference between the two classifications regarding the total ex-situ stellar mass fraction. We also divide by star-forming (*blue* lines) and quenched galaxies (*red* lines) at z = 0. The star forming galaxies have higher ex-situ fractions on average at fixed stellar mass than quenched galaxies.

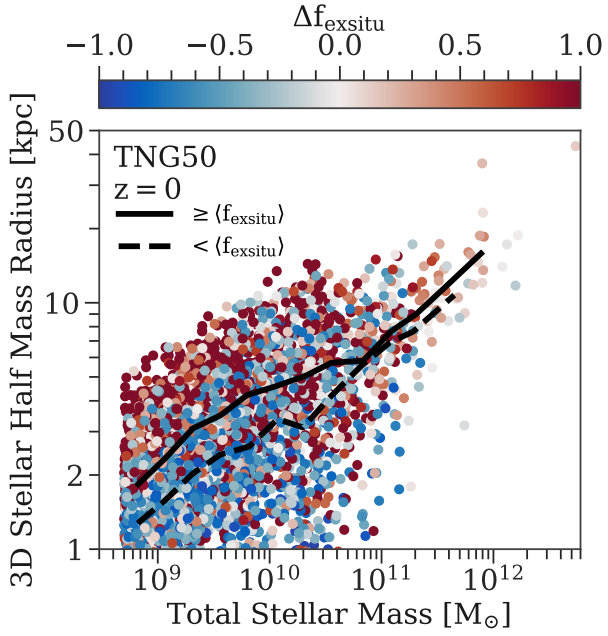

Figure B.5. Connection between the galaxy mass-size relation and total ex-situ fractions in TNG50 at z = 0. The 3D half mass radius against total stellar mass for 4344 galaxies in TNG50 ($M_{\star,tot} > 5 \times 10^8\,M_\odot$). The points are color-coded according to the relative ex-situ fraction Δf_{exsitu} indicating whether the total ex-situ fraction of a given galaxy above or below the average at fixed galaxy stellar mass. Median mass-size relations are shown separately for galaxies having above (*solid black line*) and below (*dashed black line*) average ex-situ fractions. Below $\sim 5 \times 10^{10}\,M_\odot$, galaxies with high relative ex-situ fractions are on average more extended.

(see Davison et al. 2020, for EAGLE; Merritt et al. 2020, for TNG100; Zhu et al. 2022b, for TNG50).

B.4 RESOLUTION CONVERGENCE TESTS

To test numerical convergence we perform the exact same analysis from the main text for three different resolution realizations of TNG50: TNG50-1 (flagship), TNG50-2 and TNG50-3. Throughout, the galaxy sample selection is the same as in Section 7.2.4.2 except we omit cutting galaxies with less then one hundred stellar particles in their centers.

For reference, the mass resolution of TNG50-2 and TNG50-3 is 8 and 64 times and the gravitational softening length is 2 and 4 times worse than TNG50-1 respectively. The latter translates to physical sizes of 288 pc (TNG50-1), 576 pc (TNG50-2) and 1.152 kpc (TNG50-3) for collisionless particles at z = 0.

In the top row of Figure B.6 we show the results of the central stellar mass of the in-situ, migrated and ex-situ stars as a function of total dynamical mass for all three resolutions. We see that the *total* stellar mass in the central 500 pc of TNG50 galaxies is converging at all halo

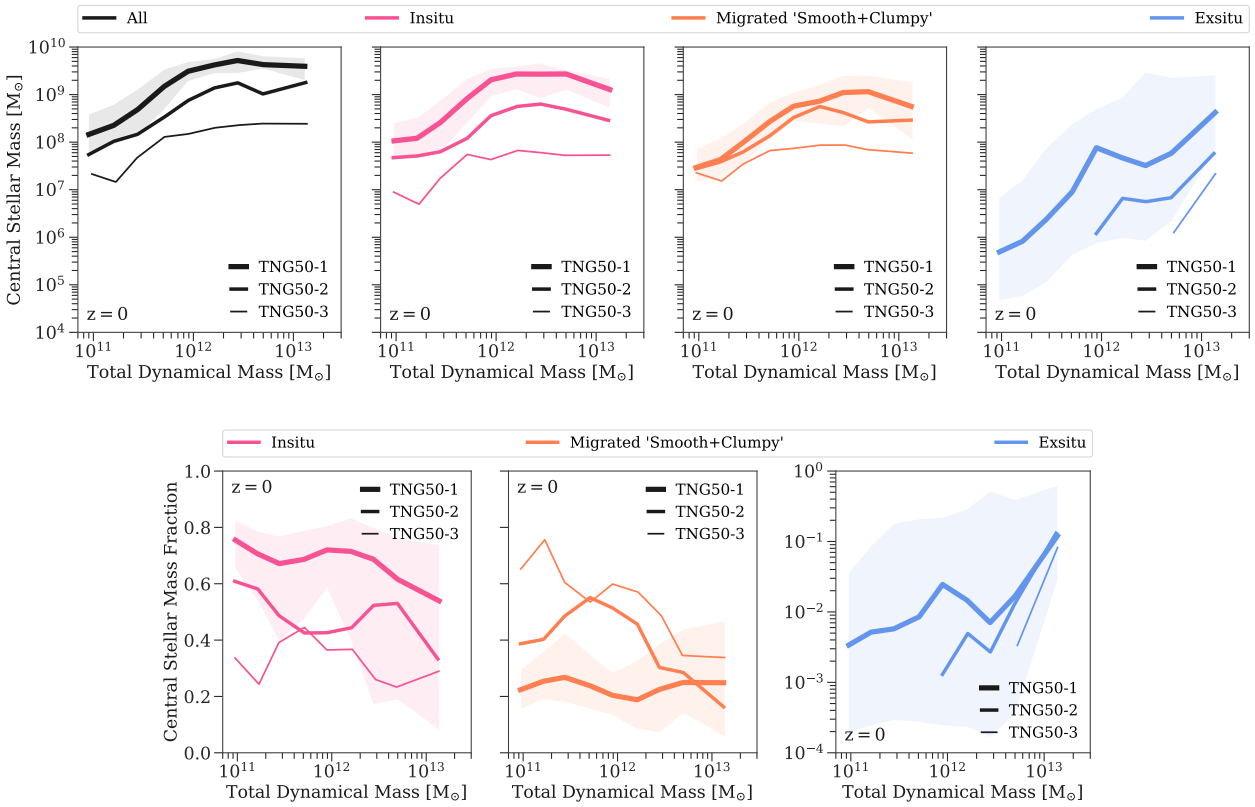

Figure B.6. Influence of the numerical resolution on the central (500 pc) in-situ, migrated and ex-situ stars of TNG50 galaxies at z = 0. *Top panel*: Median trends of the central stellar mass as a function of a galaxy's total dynamical mass for all *(all)*, in-situ *(pink)*, migrated *(orange)* and ex-situ *(blue)* stars and different numerical resolution realizations of the same cosmological volume. The thicker the line the better the numerical resolution. Shaded areas show the 16th and 84th percentiles for the highest resolution run. *Bottom panel*: Instead of the absolute stellar mass we now show the central stellar mass fraction of the in-situ, migrated and ex-situ stars. The central ex-situ mass faction is converging, whereas the behaviour is more complex for the in-situ and migrated fraction.

masses, meaning that the distance between TNG50-1 and TNG50-2 (~ 1 dex) is around 50% smaller than the distance between TNG50-2 and TNG50-3 (~ 0.5 dex). The same is true when looking at the central mass for just the in-situ stars, even though the converging of the lines becomes much less obvious. For the migrated stars it looks like the central mass is better converged for galaxies with total dynamical masses below $10^{12}\,M_\odot$. However, when comparing the central stellar mass *fraction* of in-situ and migrated stars (bottom row of Figure B.6), the convergence behaviour seems to be much more complex. For galaxies outside masses of $10^{12\pm0.5}\,M_\odot$, the central stellar mass fractions seem to be converging. Overall though, the central migrated mass becomes on average larger than the in-situ mass with decreasing resolution for all galaxy masses.

This is due to the fact that the numerical resolution also influences which stars are classified as in-situ and migrated, which is a consequence of how (spatial and mass) resolution effects star formation and feedback in the TNG model. Better resolution allows for higher gas densities *and* better spatial sampling of the gas cells, which produces galaxies with higher stellar mass *and* more compact sizes. Thus, in an absolute sense more stellar mass resides overall in the center of TNG50

galaxies for higher resolution runs, however differentially more stellar mass comes from outside the fixed 500 pc aperture for lower resolution runs (see also Section 7.5.4). Interestingly, the complexity in the central in-situ and migrated fractions seen around 10^{12} $M_\odot$ coincides with the complexity in the convergence behaviour of the mass-size relation in TNG50 (see Pillepich et al., 2019, Figure B1).

For the *absolute* stellar mass of the central ex-situ stars the start of convergence is not yet apparent, but the *fractions* is clearly converging. Again, the ex-situ mass in the center increases with increasing resolution. Additionally, the minimum galaxy mass that exhibits any ex-situ stellar mass in the center is extended towards lower mass galaxies for increasing resolution. Again, this behaviour is a consequence of the complex interplay between mass and spatial resolution. Subhalos that were either not sufficiently resolved with enough stellar particles or even remained dark at lower resolution are able to form enough stars at higher resolution. Thus, galaxies that become accreted are not only more massive in stellar mass, but also more abundant, especially at the low mass end. Thus, the ex-situ stellar mass is higher in general and also contributes at the lower galaxy masses when resolution is increased. Furthermore, lower mass galaxies become more compact, which makes them survive tidal forces more efficiently and hence they contribute more stellar material in the center their host galaxies. Even though TNG50 is a tremendous improvement in resolution for cosmological box simulations, we still need a higher resolution to fully assess the convergence behaviour of the absolute central ex-situ stellar mass (see Grand et al., 2021, for a study of the satellite galaxy population of a highly resolved Milky Way like galaxy in a cosmological context and comparison to lower resolution models).

B.5 CLUMPS IN TNG50

Here, we show some examples and properties of clumps, i.e. subhalos detected by the SUBFIND algorithm, but which were formed not through the collapse of a dark matter halo, that are present in TNG50. Instead these clumps form in the gaseous disk of galaxies or fragments of it. Particularly, we could observe qualitatively that significant clump formation predominantly occurs during galaxy interactions at $z > 1$, such as mergers or fly-bys, but it can also take place when a galaxy evolves in isolation (see also Di Matteo et al., 2008, for a similar finding).

We present a visual example of such clumps at the top of Figure B.7 for a galaxy that lives in an environment with many galaxy interactions. Clumps embedded in the stellar disk of that galaxy clearly exhibit a gaseous counterpart, whereas clumps further out and not within the disk are only seen in the stellar surface mass density (at the time of inspection). The clumps visible in both the stars and gas are clearly distributed along the spiral (or tidal) arms of that galaxy. *All* of them migrate to the center and deposit stars (and also gas) there (marked by orange arrows).

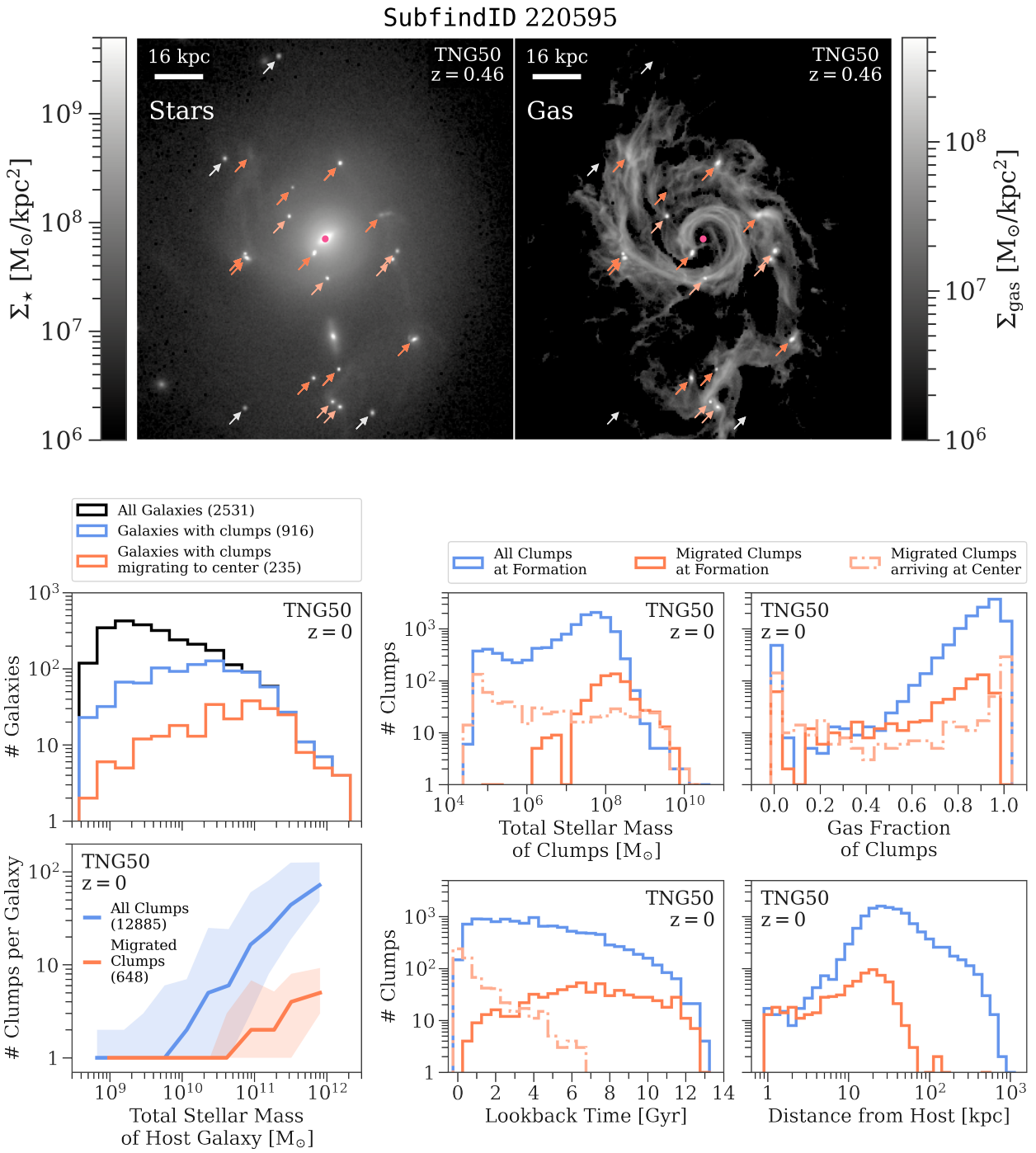

Figure B.7. Example and summary statistics of clumps in TNG50 galaxies. *Top panel*: Stellar (*left*, full projection) and gas (*right*, thin slice with $|z| \leqslant 5$ kpc) surface mass density of a TNG50 galaxy (`SubfindID 220595`) in face-on projection exhibiting clumps at $z = 0.47$. Clumps migrating to the center (pink dot) are marked with orange arrows, whereas clumps not belonging to the galaxy are marked with white arrows. Clumps with lighter orange arrows will first merge with other clumps (darker orange arrows), before arriving at the center. *Lower panel, left*: Distribution of host galaxy stellar masses (*top*) displaying clumps in general (*blue*) and clumps that migrate to the center (*orange*) *at any time*, compared to the total galaxy sample (*black*). Numbers inside the brackets display the total amount. All galaxies in our sample above $\sim 5 \times 10^{10}$ M$_\odot$ exhibit clumps at some point in their life time. The median number of clumps that ever existed per galaxy as a function of host galaxy stellar mass are also shown (*bottom*). The shaded area shows the 16th and 84th percentile. The number of clumps arriving at a galaxy's center is about a decade lower than the total amount of clumps formed. Note however that the true number of all clumps ever formed is higher due to clump-clump mergers. *Lower panel, right*: Distribution of certain clump properties (*blue solid line*: all clumps at the time of formation, *orange solid line*: clumps that migrate to the center at the time of formation, *light orange dashed-dotted line*: clumps that migrated to the center at the time of arrival at the center): *from left to right*: total stellar mass, gas fraction (ratio of gas mass to total baryonic mass), formation time (*solid lines*)/time taken to arrive at the center (*dashed line*) and distance from the host galaxy of the clumps.

In that process some of them (marked by lighter orange arrows) merge with other clumps, which we reconstructed with the merger trees.

The statistics on clumps in TNG50 shown on the bottom left hand side of Figure B.7 reveals that around 36% of all TNG50 galaxies posses clumps at any point in their lifetime of which a fourth have clumps that migrate to the center. Above $5 \times 10^{10}\,M_\odot$ in stellar mass all galaxies exhibit clumps at some point. The amount of clumps per galaxy starts to rise above one for galaxy stellar masses larger than $10^{10}\,M_\odot$. On average a Milky Way mass galaxy has five clumps, whereas the most massive galaxies in TNG50 can have up to a hundred clumps. The number of clumps that actually migrate to a galaxy's center starts to rise at higher galaxy masses at around $5 \times 10^{10}\,M_\odot$ reaching an average of about 5 migrated clumps per galaxy at the high mass end. We remind the reader that these and following numbers *do not* account for clumps that merged with other clumps, thus the true number of all clumps ever formed is actually even higher.

We also show the distribution of four properties of the clumps in TNG50 on the bottom right hand side of Figure B.7. Each property is shown for all clumps at the time of formation, for all clumps that migrated at the time of formation and for all clumps that migrated at the time they arrive at their galaxy's center.

We see that clumps are formed with a broad distribution of stellar masses with a peak at $10^8\,M_\odot$[122]. Only clumps that are formed with such stellar masses or higher are able to migrated to the center. The stellar mass that they then actually deposit at the center is a flattened out distribution all the way down to a few stellar particles. Thus clumps can suffer significant stellar mass loss while travelling to the galaxy center.

122: We caution the reader to not trust the few clumps that have stellar masses of around $10^{10}\,M_\odot$, which likely originate from switching between the host galaxy and the actual clump during the halo/subhalo finding process.

Even though there is a broader peak of clumps formed with high gas fractions ($0.6 - 1$), the gas fraction distribution of clumps that migrate to the center is significantly flatter. Thus a high gas fraction is not necessarily an indication of whether a clump is able to migrate to the center or not.

Furthermore, the clumps are formed all throughout cosmic time in TNG50, with a slight increase towards younger lookback times. The number of clumps that migrated with formation times younger than 6 Gyr ago drops compared to clumps formed at older ages. This is understandable as it takes a few Gyr for the clumps to migrate to the center. Most clumps need around 1 Gyr to do so, but there is a long tail towards higher migration times up until 6 Gyr.

The peak distance from the host galaxy, where clumps form, is around 20 kpc and flattens out towards smaller distances. Whereas the number of migrated clumps drop sharply after that distance, the distance of clumps formed overall extends all the way until several hundred kpc. Hence, clumps in TNG50 can form in the halo of galaxies, possibly in gaseous tidal tails and gas fragments during galaxy interactions. We empathize here that the clumps formed at such at such large distances are *not* part of any satellite galaxy that then merged with the host (at least according to the SUBFIND algorithm and the merger trees).

This is because we identify clumps as subhalos with `SubhaloFlag` $= 0$ that *directly* merged onto the main progenitor branch of the host galaxy. Hence, clumps that are part of satellite galaxies that are then brought in by merging with the host galaxy, are also not accounted for in our statistics.

We provide further discussion and comparison to clumps in other simulations in Section 7.5.3.

Part IV

COMBINED EFFORTS

8 MERGER HISTORIES

On-going galaxy mergers look spectacular. They exhibit almost artistic features in the forms of streams and shells caused by tidal forces. *However, what about galaxies that appear regular?* In the standard model of cosmology, almost every galaxy should have undergone such merger events. *How do we quantify such a key prediction of our cosmological model for galaxies that make these events look invisible?* We can use cosmological galaxy simulations to understand a galaxy's accretion history and the imprint they leave in other observable properties of galaxies. Exploiting this, we are able to develop new techniques that can extract this information from observations. In this Chapter I briefly walk through principles of such a method, that recovers details about a galaxy's merger history from its integrated spectrum alone.

This method was developed as part of my Master's thesis, but I made improvements and updates, as well as wrote the corresponding paper at the beginning of my PhD, which was published in Boecker et al. (2020a). In this Chapter I only show the methodological background of the technique, which is important to understand its application in Chapter 9. The contributions from the authors are as follows:

Me I implemented the code for this method, tested it with mock spectra made from simulated galaxies, extracted the merger trees, had the idea behind the definition of the most massive accretion event, made all the figures and wrote the text of the manuscript.

Ryan Leaman had the scientific idea behind this technique, developed the chemical evolution templates and gave extensive comments on the paper draft that greatly improved the manuscript.

Glenn van de Ven contributed with meetings, where discussion and scientific enthusiasm were exchanged, as well as comments on the draft.

Ted Mackereth kindly calculated the accretion origin of stellar particles in the EAGLE galaxies and provided comments on the draft.

Mark Norris provided the initial project of my Bachelor's thesis, which ultimately led to this project, discussed the results throughout this study and provided comments on the paper draft.

Robert Crain provided helpful comments on the final paper draft.

Summary

We present a new method of quantifying a galaxy's accretion history from its integrated spectrum alone. Using full spectral fitting and calibrated regularization techniques we show how we can accurately derive a galaxy's mass distribution in age-metallicity space and further separate this into stellar populations from different chemical enrichment histories. By exploiting the fact that accreted lower mass galaxies will exhibit an offset to lower metallicities at fixed age compared to the in-situ stellar population, we quantify the fraction of light that comes from past merger events, that are long since mixed in phase-space and otherwise indistinguishable. Empirical age-metallicity relations (AMRs) parameterized for different galaxy masses are used to identify the accreted stellar populations and link them back to the progenitor galaxy's stellar mass. This allows us to not only measure the host galaxy's total ex-situ mass fraction (f_{acc}), but also quantify the relative amount of accreted material deposited by satellite galaxies of different masses, i.e. the accreted satellite mass function in analogy to the subhalo mass function. Using mock spectra of present-day, early-type galaxies with total stellar mass $\sim 10^9 - 10^{12}$ $M_\odot$ from the EAGLE simulation suite we demonstrate that our method can recover the total accreted fraction to within $\approx 38\%$, the stellar mass of the most massive accreted subhalo to within $\approx 56\%$ and the slope of the accreted satellite mass function to within $\approx 17\%$ of the true values from the EAGLE merger trees. Future application of this method to observations could potentially provide us accretion histories of hundreds of individual galaxies, for which deep integrated light spectroscopy is available.

Contents

8.1 THE METHOD

The basis for observationally quantifying a galaxy's accretion history from its integrated spectrum, is to first recover the underlying age-metallicity distribution via full spectral fitting using pPXF (Cappellari & Emsellem, 2004; Cappellari, 2017). The reliability and robustness of this was tested in Chapter 5. Only with the recovery of distributions in ages and metallicities we are able to identify stellar populations of different metallicities at fixed age, which are a signs of past accretion events.

Below I explain how we can connect this information to the masses of satellite galaxies that were accreted to constitute the galaxy that we see at $z = 0$. I use a galaxy with stellar mass of $5 \times 10^{11}\,M_\odot$ from the EAGLE simulation (Crain et al., 2015; Schaye et al., 2015) as an example to explain the method and show its feasibility by comparison to the true merger tree known from the simulation. All stellar particles within a 100 kpc aperture were used to construct an integrated mock spectrum with a signal-to-noise ratio (SNR) of 100 using the MILES SSP models with the BaSTI isochrones (Vazdekis et al., 2010). The integrated mock spectrum was then fitted with pPXF.

8.1.1 Flexible mass-dependent chemical enrichment templates

Having recovered extended mass distributions in age-metallicity space from the integrated spectrum, we now need to associate the mass fractions to potential accreted galaxies. We do this by constructing flexible, mass-dependent templates in age-metallicity space, which describe how galaxies of a given mass should (on average) chemically evolve. While the detailed chemical evolution of distant high mass galaxies is not observationally constrained, here we attempt to construct a physically motivated, flexible, mass-dependent chemical framework.

To begin, we use results from Leaman et al. (2013), who derived empirical age-metallicity relations spectroscopically for local group dwarf galaxies from resolved stellar populations. To first order, leaky box chemical evolution models describe the metallicity distribution function (MDF) and age-metallicity relation (AMR) of those galaxies with only a galaxy mass-dependent variation in the effective yield $p(M_\star)$. For a given galaxy, the chemical evolution is described as:

$$Z(t) = -p(M_\star)\,\ln[\mu(t)] \tag{8.1}$$

where Z is the metallicity, t (in Gyr) is time since the Big Bang, μ the galaxy's gas fraction and $p(M_\star)$ the mass-dependent effective yield in units of solar metallicity.

The mass-dependent effective yield is empirically measured for the Local Group galaxies below $M_\star \leqslant 10^9\,M_\odot$ in Leaman et al. (2013) (see also Lee et al., 2006) and yields the observed relation of $p(M_\star) \propto M_\star^{\alpha_p}$ with $\alpha_p \simeq 0.4$. Above this mass, the observed mass-metallicity relation (MMR) is seen to flatten (e.g. Gallazzi et al., 2005), and we take this into

account by modifying the functional form of the $p(M_\star)$-relation such that a galaxy's average stellar mass will reproduce the turnover in the MMR (at $\sim 10^{10}$ $M_\odot$), while still matching the MDF of low mass galaxies:

$$\log_{10} p(M_\star) = p_0 + \log_{10}\left(1 - \exp\left[-\left(\frac{M_\star}{M_0}\right)^{\alpha_p}\right]\right), \tag{8.2}$$

here p_0 describes the value the relation asymptotes towards for high galaxies masses, M_0 is the turn-over mass and α_p is the low-mass slope. This allows us to flexibly model variations in AMRs for galaxies of arbitrary mass, while ensuring the integrated stellar population properties still match observed scaling relations (e.g. the MMR).

In order to convert the iron abundances [Fe/H], as they were derived in Leaman et al. (2013), to total metallicity [M/H], which is used in the SSP model grid, we adopt the following relation from Salaris & Cassisi (2005)

$$[M/H] = [Fe/H] + \log_{10}\left(0.694 \cdot 10^{[\alpha/Fe]} + 0.306\right). \tag{8.3}$$

We further allow each galaxy to have a mass-dependent evolution in $[\alpha/Fe]$, by utilizing the empirical $[\alpha/Fe]$-[Fe/H]-relation derived from individual stars on Local Group galaxies in de Boer et al. (2014). They found that the "knee" in the $[\alpha/Fe]$-[Fe/H] diagram ($[Fe/H]_{knee}$) occurs at higher metallicity for high mass galaxies (see also Kirby et al., 2011; Walcher et al., 2015). We adopt this mass dependence of the $[Fe/H]_{knee}$ position as well as of the slope of the low alpha sequence. We calibrate the $[\alpha/Fe]$-plateau value to have a mass dependence as well, such that the mean α-abundance versus galaxy mass trends seen in observations (Thomas et al., 2010) and EAGLE (Segers et al., 2016) are reproduced.

Lastly, we account for a mass-dependent gas fraction evolution $\mu(t)$, which can be due to gas being consumed in star formation and/or being removed through feedback processes or quenching. Higher mass galaxies ($\gtrsim 10^{10}$ $M_\star$) typically exhaust their in-situ gas much quicker than lower mass galaxies (e.g. McDermid et al., 2015; Pacifici et al., 2016a,b) and we therefore parameterize the gas fraction as:

$$\mu(t) = \frac{t - (13.5 - t_{form})}{t_{form}}, \tag{8.4}$$

where t_{form} is an epoch by which the galaxy has formed its in-situ stars. We allow a galaxy mass dependence to enter through this formation time as:

$$t_{form} = \min\left[\left(14 - \log_{10} M_\star\right)^{\alpha_t}, 13.5\right] \tag{8.5}$$

with α_t influencing how long the star formation duration will be for a given galaxy mass. This will result in AMR curves that do not evolve until $z = 0$, but reach their maximum metallicity at t_{form} for higher galaxy masses ($\gtrsim 10^{10}$ $M_\star$).

A set of these AMR templates for different galaxy masses and with

parameters $p_0 = 0.1$, $M_0 = 10^{10.5}\ M_\odot$, $\alpha_p = 0.4$ and $\alpha_t = 2.0$ is plotted in Figure 8.1 (a) as an example. Importantly however, these parameterizations enable us to flexibly vary the shape of the mass dependent chemical evolution tracks allowing for a stochastic assessment of the uncertainties in our final quantities of interest (see section 8.1.2.1).

8.1.2 Associating the spectroscopic mass fractions to accreted satellite galaxies

With the galaxy mass-dependent chemical templates described above, we are able to link the mass fractions in age-metallicity space recovered from the regularized pPXF solutions to astrophysical quantities of interest - such as the galaxy's total fraction of accreted mass as well as the distribution of merged satellite galaxies. The amount of mass in accreted satellites of a given mass can be straightforwardly computed by overlaying our mass-dependent age-metallicity relation templates onto the spectroscopically recovered mass distribution in age-metallicity space, as seen in Figure 8.1 (a). Every mass weight m_i recovered from pPXF lying *below* a certain AMR curve is treated as potentially coming from accreted satellite galaxies with chemical evolution representative of that mass or lower, i.e. $f_{acc}(\leqslant M_{sat}) = \sum_i m_i(t, [M/H] \leqslant [M/H]_{template}(t|M_{sat}))$. This procedure assumes that the age-metallicity mass fractions can be uniquely assigned to a single progenitor. In reality, there will be overlap and mixing, especially in the old, metal-poor regime. However, we partly account for this by incorporating large variations in the chemical evolution templates, thus sampling over realizations, where some galaxy masses may be contributing more or less to a particular SSP bin.

Furthermore, this method of recovering the contributions from accreted satellite galaxies of a given mass is only considered valid in a cumulative sense, as there is an astrophysical degeneracy inherent to the assignment of mass fractions of low-mass satellites. We do not know a priori, whether these recovered stellar populations with lowest [M/H] at fixed age are coming from low-mass satellites directly accreted to the host or if they were first accreted to an intermediate mass satellite, which then merged with the host.

The chemical evolution templates extend up to an AMR associated with some most massive accreted satellite galaxy, $M_{sat,\,max}$. At this mass, the method has provided an estimate of the total accreted fraction for the host galaxy, i.e. $f_{acc,\,tot} = f_{acc}(\leqslant M_{sat,\,max})$. Every mass fraction lying above the AMR template associated with $M_{sat,\,max}$ is considered *in-situ* according to our method, but naturally there will be some overlap with the ex-situ contributions, as the age and metallicity properties are very similar in that mass regime.

In Figure 8.1 we show a schematic of our method to associate the spectroscopically recovered mass fractions with accreted satellite galaxies of different masses. AMR templates corresponding to accreted galaxies of masses between 10^6 and $10^{11}\ M_\odot$ are overlaid on the spectroscopically recovered mass fractions in Figure 8.1 (a). The mass frac-

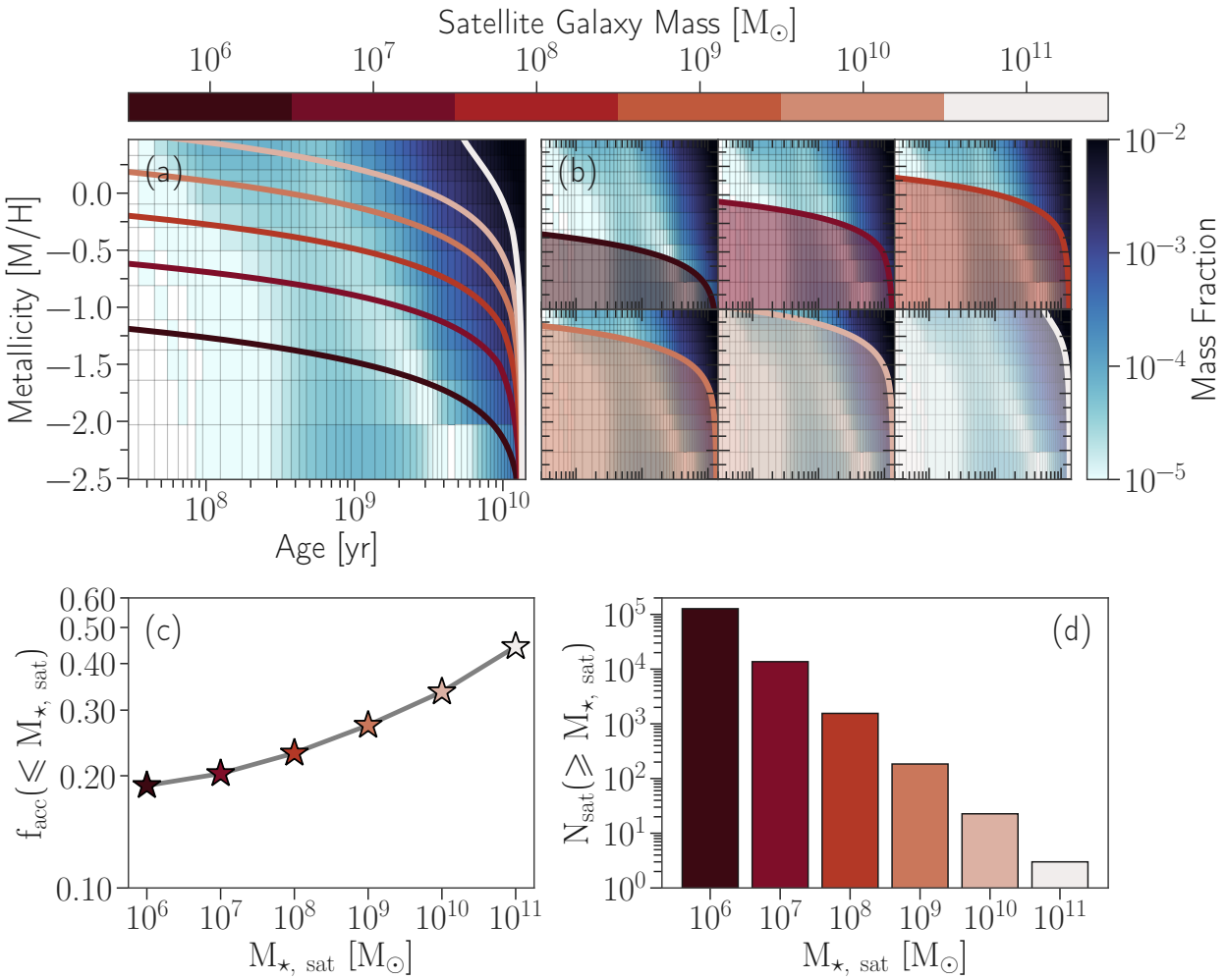

Figure 8.1. *Schematic of our method. This shows just one realization of the chemical evolution templates. (a)*: Mass-dependent age-metallicity relation templates for galaxy masses in the range of 10^6 $M_\odot$ and 10^{11} $M_\odot$ (see colorbar) overplotted onto the pPXF recovered mass fractions in age-metallicity space of a simulated galaxy from EAGLE. *(b)*: Visualization of how the accreted satellite mass function is constructed. Mass weights coinciding in the shaded regions, i.e. below each age-metallicity relation curve are summed up. This then represents the cumulative accretion fraction brought in by a satellite galaxy with a stellar mass corresponding to the associated mass-dependent age-metallicity relation. *(c)*: Resulting cumulative accretion fractions. The color of the star symbols correspond to the respective galaxy mass of the age-metallicity template from which the accretion fraction was calculated. *(d)*: An analogue to the accreted satellite mass function calculated from the accretions fractions found with our method.

tions below an AMR curve represents the contribution to the galaxy's merger history from satellite galaxies of this mass as seen in Figure 8.1 (b). The resultant cumulative accretion fractions versus the associated satellite galaxy masses are then produced by summing up the mass fractions lying in the shaded regions respectively and are plotted in Figure 8.1 (c). In Figure 8.1 (d) we show an analogue to the (unevolved) subhalo mass function, which can be calculated by dividing the recovered cumulative accreted mass by its associated satellite galaxy mass (i.e. $N_{sat}(\geqslant M_{sat}) = M_{acc}(\leqslant M_{sat})/M_{sat}$, where $M_{acc}(\leqslant M_{sat}) = f_{acc}(\leqslant M_{sat}) \cdot M_{host}$).

Figure 8.1 shows the recovered accreted mass fractions for *one* realization of the chemical evolution templates ($p_0 = 0.1$, $M_0 = 10^{10.5}$ $M_\odot$, $\alpha_p = 0.4$ and $\alpha_t = 2.0$), however in the final results (section 8.2) we

show them as the median of many realizations (see section 8.1.2.1 for more details).

8.1.2.1 *Stochastically assessing the systematic uncertainties*

As the shape of the chemical evolution templates is not well constrained by observations, especially for galaxy masses higher than found in the Local Group, we introduce flexibility and perform a Monte-Carlo (MC) simulation. We randomly draw for 1000 trials the parameters p_0, M_0, α_p (Equation 8.2) and α_t (Equation 8.4) from a uniform distribution in a range of [-0.2, 0.2], $10^{[9.5,\ 11]}$, [0.4, 0.6] and [1.7, 2.5] respectively. We also add a scatter to the sampled AMR curve, which is drawn from a Gaussian distribution with a standard deviation of $\pm$0.2 dex in order to account for the intrinsic scatter of a galaxy's metallicity at fixed stellar age (see e.g. Leaman et al., 2013). The choices of the parameter variation ranges were made such that the calculated MMR from the median of the mass-dependent AMR curves lie in the scatter of the observed MMR (Gallazzi et al., 2005; Kirby et al., 2013). Uncertainties in the derived [α/Fe]-[Fe/H]-mass relation are not accounted for, as their impact is negligible in comparison to the other parameter variations. Hence, the recovered cumulative accretion fraction as a function of satellite galaxy mass is the median of the 1000 MC trials and the uncertainty is expressed by the 16th and 84th percentiles of the trials.

8.1.2.2 *Defining the most massive accretion event*

In principle, the cumulative accretion fraction corresponding to the highest satellite galaxy mass marks the *total* accreted fraction, $f_{acc,\ tot}$, of the host galaxy. However, as we do not have any prior knowledge about the most massive satellite ever accreted by the host, $M_{sat,\ max}$, our derived curve extends arbitrarily higher than the true total accreted fraction.

In order to find this truncation of our derived *cumulative* accreted fractions at $f_{acc,\ tot}$ we define $M_{sat,\ max}$ as the mass, where the number of accreted satellite galaxies becomes unity in the spectroscopically recovered accreted satellite mass function (e.g. panel (d) of Figure 8.1 or the right panel of Figure 8.2). In return, we can truncate the cumulative accretion fractions at that point and derive the total accreted fraction of the host galaxy. Similarly, errors are computed by the intersection of the 16th and 84th percentile uncertainty of the accreted satellite mass function with unity.

This procedure works quite well even though our method can only compute a lower limit of the accreted satellite mass function, as it does not take into account any higher orders of subhalo-subhalo mergers. We found that this gives better results than using theoretical predictions of cosmological simulations, which can provide us with a statistical relation of the stellar mass of the most massive accreted satellite for a given host galaxy (see e.g. D'Souza & Bell, 2018b). In addition, it allows us to implicitly characterize $M_{sat,\ max}$ as an intrinsic measure of our method.

8.2 THE VALIDATION

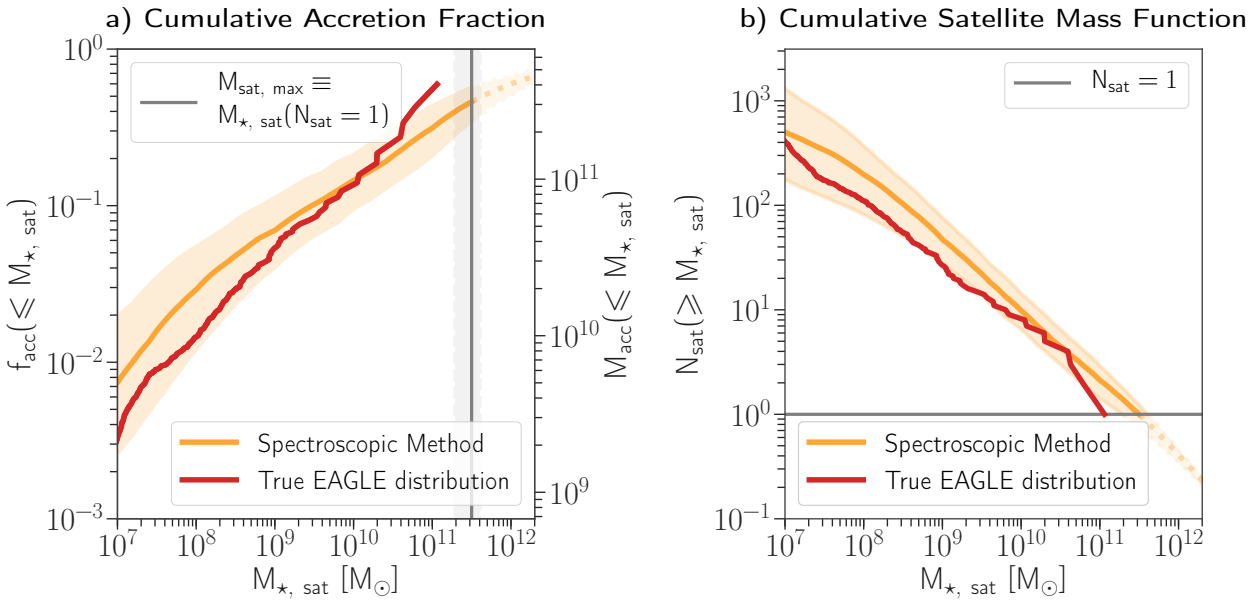

Figure 8.2. Results shown are recovered from a mock spectrum with SNR 100 and the third order difference operator as regularization matrix. *Left*: Cumulative accretion fraction (accreted mass) versus the stellar mass of the accreted satellite galaxy for a simulated galaxy from EAGLE ($M_{\star,tot} = 5 \times 10^{11}\ M_\odot$). The red line shows the true function from the simulation, while the orange line shows the function recovered from a single integrated spectrum with our method (median of the Monte-Carlo trials). The orange band marks the 16th and 84th percentile of those trials. The most massive accreted satellite ($M_{sat,\,max}$), which marks the total accreted fraction, is shown by the grey vertical line. *Right*: The cumulative number of accreted satellite galaxies versus their stellar mass for Galaxy Nr. 1. The stopping point as shown by the light grey horizontal line, where $N_{sat} = 1$, determines the most massive accreted satellite ($M_{sat,\,max}$). The approximate slope of the accreted satellite mass function is represented by the dark grey dashed-dotted line and is ~ -0.6. The true (recovered) quantities for the total accreted fraction, the mass of the most massive accreted satellite galaxy and the slope of the accreted satellite mass function are the following: $f_{acc,\,tot} = 0.42\ (0.46^{+0.11}_{-0.10})$, $\log_{10} M_{sat,\,max} = 11.06\ (11.50^{+0.12}_{-0.17})$ and $\alpha_{sat} = -0.57\ (-0.65 \pm 0.01)$.

Having optimized the recovery of extended age-metallicity distributions, and formulated a way to link these to accreted galaxies of different masses, we can proceed with an example on a massive EAGLE galaxy ($M_{\star,tot} = 5 \times 10^{11}\ M_\odot$) - one where we can independently verify the spectroscopically recovered accretion history by comparing to the known merger tree.

In the left panel of Figure 8.2 we show the derived cumulative accretion fraction as a function of accreted satellite galaxy mass as well as the uncertainties as calculated from the section above. We computed the cumulative accretion fraction with AMRs corresponding to galaxy masses between $10^{6.2}$ and $10^{12.4}\ M_\odot$ in 0.2 dex steps.

The agreement with the true accretion fractions obtained from the EAGLE merger trees is remarkable given that we obtained the "observed" quantity purely from a simulated integrated spectrum. This result suggests that the assumptions behind the mass-dependent chemical evolution templates are reasonable and provide a novel way to recover signatures of otherwise unobservable ancient merger events. However, we see that the true cumulative accretion fraction curve from the EAGLE simulations is slightly steeper than the spectroscopically re-

covered one, which is likely a result of overestimating the amount of accretion from low mass galaxies. As stated in section 8.1.2, assigning all mass fraction below a certain AMR only imposes an upper limit, as mass fraction coming from higher mass galaxies or the host overlap in the old, metal-poor regime. Disentangling this second-order effect will be the subject of our follow-up paper.

For this example galaxy, we recover a total accreted fraction of $f_{acc,\,tot} = 0.46^{+0.11}_{-0.10}$, while the true total accreted fraction from the ex-situ particle classification is 0.421. For the most massive progenitor we find a stellar mass of $\log_{10} M_{sat,\,max} = 11.50^{+0.12}_{-0.17}$ dex, whereas the actual value is 11.06 dex. The errors have been calculated by the intersections of the scatter of the MC trials of the recovered satellite mass function and where $N_{sat} = 1$.

In the right panel of Figure 8.2 we compare the true satellite mass function of the EAGLE galaxy with our estimate, which also shows excellent agreement. We measured the slope (α_{sat}) of the recovered and true satellite mass function by fitting a power law between 10^7 $M_\odot$ and $M_{sat,\,max}$ in log space. The 1σ error of the spectroscopically derived cumulative satellite mass function was taken into account during the fit. We found the values for α_{sat} to be -0.65 ± 0.01 and -0.57 respectively.

The agreement of our result with the true satellite mass function is somewhat surprising as our method is formally providing a limit to the satellite mass function, as it also cannot differentiate mergers that happened prior to a galaxy merging to the primary halo. For example, if a late time merger of high mass had its own accretion history, this would be degenerate with our solutions resulting in a flattening of the slope of the f_{acc}-M_{sat} relation and steepening of the N_{sat}-M_{sat} relation. However, we expect that this effect will be very small and well inside our uncertainties (see e.g. Jiang & van den Bosch, 2016, Figure 9).

Nevertheless, the validation of this method using the EAGLE simulations, suggests it is a powerful new way to recover the accreted satellite mass function and distribution of merger mass ratios in galaxies (see Boecker et al., 2020a, for more details).

ASSEMBLY OF GALAXY CENTERS IN SDSS & TNG50

9

I combine and exploit results of all my previous works highlighting the important synergy between observations and simulations. The TNG50 simulations show a large diversity of galaxy centers, which are strongly influenced by galaxy formation and evolution in a hierarchical ΛCDM universe (Chapter 7). The distribution of ages and metallicities of stellar populations encode this information, which we can extract with methods tested in Chapter 5 and 8. I provide a first look at results, where these methods are applied to the center of galaxies observed with SDSS, which are then compared to predictions from TNG50 with the help of realistic mock integrated spectra. *Are we moving towards observationally quantifying past merger events from statistical samples of galaxies?*

The contents of this Chapter are a paper in preparation. The contributions from collaborators are as follows:

Me I initiated this project, conducted the analysis, written the text and made all the figures.

Nadine Neumayer contributed with regular meetings, where discussion, thoughts and suggestions were shared for this project.

Annalisa Pillepich contributed with regular meetings, where discussion, thoughts and suggestions were shared for this project.

Dylan Nelson helped with understanding the construction of mock spectra and quickly provided the data that I needed to do the analysis.

Ignacio Martín-Navarro helped me with interpreting the mass-[α/Fe] relation.

Anna Gallazzi kindly provided the data from her catalogue.

Summary

We compare the central ~ 500 pc of ~ 2000 galaxies from SDSS observations and the TNG50 simulation covering a stellar mass range of $10^{9-11}\,M_\odot$ with respect to their ages, metallicities, [α/Fe] as well as accretion histories. We account for sample selection effects by matching SDSS and TNG50 galaxies in mass-size-ellipticity space. We obtain stellar population information of both samples via the same full spectral fitting method by constructing realistic SDSS-like mock integrated spectra from TNG50 with dust attenuation. We find that the recovered distribution of average ages across the probed galaxy mass range are in excellent agreement between observations and simulations. A discrepancy between SDSS and TNG50 in the average metallicities of around $0.25 - 0.5$ dex for - in particular lower mass ($\lesssim 10^{10}\,M_\odot$) and star forming - galaxies cannot easily be reconciled with purely observational effects and modelling limitations. Cross-checking the recovered and true stellar populations with TNG50, shows that the adopted full spectral fitting technique can recover distributions of ages and metallicities for individual galaxies, which allows for the detection of accreted stars, as they are more metal-poor at fixed age than the in-situ population. We demonstrate a first application of our method to SDSS observations, by extracting information about the accreted fraction and about the mass of the most massive accreted satellite galaxy from the central 500 pc alone. The promising results encourage a new possibility to understand the merger history of galaxies from their inner regions, which will make it possible to build statistical samples probing the impact of mergers on galaxy formation in a ΛCDM universe.

Contents

9.1 INTRODUCTION

Observations and simulations of galaxies in a ΛCDM cosmology are very much codependent. Observers use simulations to interpret their results, especially with respect to phenomena that are not necessarily directly observable, such as dark matter halos and merger rates. Simulators on the other hand use some observational results, such as the $z = 0$ galaxy stellar mass function or mass-size relation, to calibrate their subgrid physics models that describe processes below the resolution of state-of-the-art cosmological, hydrodynamical simulations, such as star formation and feedback.

Thus, properties that are observed or predicted by both sides provide a powerful probe in understanding agreement and disagreement between our empirical evidence and theoretical knowledge of the formation and evolution of galaxies. Such properties can be, for example, related to the underlying stellar populations, such as the color bimodality of galaxies (Torrey et al., 2014; Trayford et al., 2015; Nelson et al., 2018), or their kinematics (van de Sande et al., 2019). In particular, there seems to be a discrepancy between the mass-metallicity relation established from observations (Gallazzi et al., 2005; Kirby et al., 2013) and the one predicted by current cosmological, hydrodynamical simulations (Schaye et al., 2015; Nelson et al., 2018). Simulated galaxies seem to be more metal-rich than what is observed, especially towards lower mass galaxies ($< 10^{10}\,M_\odot$). Because the chemical enrichment of galaxies is a fundamental part of the overall galactic baryon cycle, it is essential to understand, whether this difference is due to a true failure of theoretical models or not.

To meet at an intersection of observations and simulations, we need to apply some models to either derive physical quantities from observations, or to predict observed light from simulations. Such models, the exact techniques used in applying them and observational limitations can severely affect how well observations and simulations match in some of these properties, as well as the conclusions we draw from that.

Therefore, the best way to ensure that both observations and simulations suffer from the same limitations and biases is to generate, as realistically as possible, mock observations from simulations with instrumental effects and target selection criteria matching the observational data (e.g. Torrey et al., 2015; Snyder et al., 2015; Rodriguez-Gomez et al., 2019; Nelson et al., 2018; Frankel et al., 2022). However, certain aspects of observational realism is not trivially achieved in simulations, because the star forming interstellar medium, which produces, for example, emission lines in galaxies, is only coarsely resolved in current cosmological simulations (e.g. Trayford et al., 2017; Nanni et al., 2022). To include effects of dust absorption, computationally expensive radiative transfer calculations have to be performed in postprocessing (e.g. Trayford et al., 2017; Rodriguez-Gomez et al., 2019).

Underlying to all of this are single stellar population (SSP) models, that predict the light emitted by a population of stars of a given age and metallicity born according to an initial mass function (IMF; e.g.

Leitherer et al., 1999; Bruzual & Charlot, 2003; Vazdekis et al., 2010, 2016; Conroy et al., 2009, 2010; Conroy & Gunn, 2010). However, these models are all based on slightly different ingredients concerning assumptions and input physics, and are only available for discretized values in age and metallicity, rarely taking into account variations of other elements (but see Conroy & van Dokkum, 2012a; Conroy et al., 2014; Vazdekis et al., 2015). Hence, results from observations and predictions from mock observations of simulations will differ, unless the same SSP models are adopted.

Lastly, the observational technique that is used to determine certain physical quantities about galaxies will possibly introduce additional biases due to simplifying assumptions or degeneracies between certain parameters, such as the age-metallicity degeneracy (Worthey, 1994) or mass-anisotropy degeneracy encountered in dynamical modelling (Gerhard, 1993). Luckily, state-of-the-art cosmological simulations produce realistic galaxies *and* make their data publicly available (e.g. Illustris: Vogelsberger et al., 2014a; Genel et al., 2014; EAGLE: Schaye et al., 2015; Crain et al., 2015; IllustrisTNG: Nelson et al., 2019a, and references therein), such that we can test our methods, understand limitations and consider improvements (e.g. Boecker et al., 2020a; Zhu et al., 2020).

Together with large, also publicly available, observational surveys (we focus on spectroscopy only; e.g. SDSS: York et al., 2000; MaNGA: Bundy et al., 2015; SAMI: Bryant et al., 2015), we can compare statistical samples of galaxies and understand their formation and evolution in the context of a ΛCDM universe.

In this study in particular, we focus on understanding the mass assembly of the central ($\sim 500\,\mathrm{pc}$) region of galaxies. As recently demonstrated in Boecker et al. (submitted; see Chapter 7), the centers of galaxies in the TNG50 simulation (Pillepich et al., 2019; Nelson et al., 2019b) are diverse and strongly influenced by the galaxy's individual interaction and merger history with other galaxies. Furthermore, we showed that galaxies with high fractions of accreted stars in their centers are more metal-poor than the average galaxy of similar mass. Due to these findings and their overall brightness, galaxy centers provide an ideal region to understand the contribution of mergers to a galaxy's evolution.

Building on these pure simulation results, we now investigate galaxies from SDSS under this aspect alongside with the construction of realistic mock spectra of TNG50 galaxies to ensure a fair comparison (see e.g. Wu et al., 2021, for TNG mock spectra of the LEGA-C survey). The sample of SDSS galaxies is chosen from Gallazzi et al. (2021), who measured the mean age, metallicity and $[\alpha/\mathrm{Fe}]$ from absorption indices of ~ 60000 galaxies with redshifts $0.01 < z < 0.2$. We restrict this sample to $z < 0.02$ such that the $3''$ SDSS fiber aperture approximately covers the central $500\,\mathrm{pc}$, yielding nearly 2000 galaxies.

Additionally, we derive stellar population properties via full spectral fitting (FSF) using penalized pixel fitting (pPXF; Cappellari & Emsellem, 2004; Cappellari, 2017), as this method can disentangle different stellar populations that are superimposed onto each other in the integrated

spectrum, yielding a 2D distribution of ages and metallicities (see also Wilkinson et al., 2017; Goddard et al., 2017, for a similar method). This has been tested, for example, by comparing with ages and metallicities derived from individually resolved stars (Boecker et al., 2020b; see also Ruiz-Lara et al., 2015 for a similar exercise).

Importantly, the recovery of age-metallicity distributions of individual galaxies allows for the detection of metal-poor stellar populations in the presence of metal-rich ones at fixed age. Those populations are a telltale sign of accreted stars. In Boecker et al. (2020a), we developed and tested a new observational technique that uses these age-metallicity distributions to extract information about a galaxy's accretion history, i.e. the total accreted (ex-situ) fraction and the mass of the most massive accreted galaxy. Recently, this method has been applied, for the first time, to MUSE observations of a handful of early-type galaxies (Davison et al., 2021).

Thus, the stellar population properties of this sample of SDSS galaxies, as well as the comparison to TNG50 via mock spectra, let us address three main questions:

1. How do the scaling relations of the mass-age, mass-metallicity and mass-[α/Fe] relation from SDSS compare to predictions from TNG50, when applying the same techniques to derive these quantities?

2. How do average stellar population properties of different observational methods (indices vs. FSF) compare to each other?

3. Can we probe the assembly history of galaxies with observations of their bright central regions?

This Chapter is organized as follows: in Section 9.2 we explain the sample of SDSS galaxies and the procedure to match them to TNG50 galaxies. In Section 9.3, we introduce the SSP models used throughout this study, as well as the creation of SDSS-like mock spectra from TNG50 galaxies and the method of full spectral fitting to extract stellar population properties. In Section 9.4, we present our results of average stellar population properties and their distributions derived from full spectral fitting of SDSS and TNG50 mock integrated spectra. In the process, we compare our results to those from Gallazzi et al. (2021) and explore the biases introduced by the full spectral fitting method and SSP models by comparing to the underlying known values from TNG50. In Section 9.5, we investigate the ability to observationally determine details of a galaxy's accretion history from its central region alone. We discuss our findings in Section 9.6 as well as provide outlooks to planned future investigations. We summarize our study in Section 9.7.

9.2 OBSERVATION AND SIMULATION DATA

The observed galaxies we consider here are from SDSS and simulated ones from TNG50. As their number distributions are not the same due

to inherent differences of observations and simulations, we perform a matching yielding a comparable population of galaxies. All measurements refer to a ΛCDM universe with parameters measured by Planck Collaboration et al. (2016).

9.2.1 SDSS Galaxy Sample

We use the catalogue of SDSS galaxies studied in Gallazzi et al. (2021), but restricted to $z < 0.02$. The lowest redshift is $z \approx 0.01$. This ensures that the 3″ fiber aperture of SDSS[123] covers an area with galactocentric radius of 0.32 kpc at the minimum and 0.65 kpc at the maximum redshift respectively. This yields 1916 galaxies with a median redshift of 0.0165.

123: We exclusively use SDSS legacy data taken with the SDSS spectrograph.

All associated spectra are downloaded from SDSS DR17 (Abdurro'uf et al., 2022) and have median signal-to-noise ratios (SNRs) larger than 20 per Å. The median SNR of the whole galaxy sample is 36 per Å. The wavelength range is $3800 - 9200$ Å, with a varying spectral resolution from $R \sim 1500$ at the blue end to $R \sim 2500$ at the red end of the spectrum. The wavelength step per pixel is constant in logarithmic space, such that $\Delta \log_{10} \lambda = 0.0001$.

Stellar masses are provided by Gallazzi et al. (2021) and were calculated from K+e corrected r-band Petrosian magnitudes applying mass-to-light (M/L) ratios based on $g - r$ colors from Bell et al. (2003).

Furthermore, galaxies from Gallazzi et al. (2021) are classified as centrals (most massive of a group) or satellites based on the group catalogue of Wang et al. (2014). In short, galaxies are grouped together based on the friends-of-friends (FoF; Davis et al., 1985) algorithm in both spatial distribution on the sky and redshift space. Group membership of individual galaxies is then determined by their dark matter density contrast with respect to the center of a tentative group in an iterative manner. The details of the group finding algorithm can be found in Yang et al. (2005, 2007).

Additionally, the galaxies from Gallazzi et al. (2021) are classified as star forming, quenched or green valley depending on their specific star formation rate (sSFR). The sSFRs are aperture corrected and measured by Brinchmann et al. (2004). We apply the definition of the star forming main sequence (SFMS) used in Gallazzi et al. (2021):

$$\log_{10}(\mathrm{sSFR}[M_\odot\,\mathrm{yr}^{-1}]) = -0.15 \log_{10}(M_\star[M_\odot]) - 8.46. \tag{9.1}$$

The spread of the SFMS is $\sigma_{\mathrm{SFMS}} = 0.3$ dex. The dividing line is at $2\sigma_{\mathrm{SFMS}}$ and $4\sigma_{\mathrm{SFMS}}$ below the SFMS between star forming and green valley galaxies and between green valley and quenched galaxies respectively.

We complement the catalogue by Gallazzi et al. (2021) with additional photometric measurements in the r-band. Those include the half-light radius ($R_{1/2}$), given as the radius that encompasses 50% of the Petrosian flux, and the ellipticity, i.e. $e = 1 - \frac{b}{a}$, where b and a are the minor and major axis respectively. We convert the half-light radii to physical units via the angular diameter distance calculated at the

measured redshift. The ellipticity is calculated from the mean axis ratio returned by an exponential and de Vaucouleurs (1948) profile fit. The values are taken from the `PhotObjAll` table of SDSS DR17. No measurements are available for 16 galaxies, which are thus excluded from further analysis.

Lastly, Gallazzi et al. (2021) measured the r-band luminosity weighted average age and metallicity via five absorption features from the emission line cleaned spectra. They used single stellar population (SSP) models from Bruzual & Charlot (2003)[124] and a Monte Carlo library of exponentially declining star formation historys (SFHs) with randomly superimposed bursts of star formation (see Gallazzi et al., 2005, for details). The metallicity is fixed to a single value for each SFH. On top of that, they estimate [α/Fe] based on the difference between the observed and model index ratios of the Mgb line and the mean of the Fe5270 and Fe5335 lines. This difference is then compared to models of Thomas et al. (2004), which vary [α/Fe] as a function of age and metallicity (see also Gallazzi et al., 2006).

124: These models are based on isochrones adopting a scaled-solar α-abundance. However, the used stellar spectra follow the abundance pattern of the solar neighbourhood.

9.2.2 Matching TNG50 Galaxies

We analyze simulated galaxies at $z = 0$ taken from the TNG50 simulation (Pillepich et al., 2019; Nelson et al., 2019b), which were described in detail in Chapter 7.

To compare the observed galaxy sample from SDSS with the simulated one from TNG50, we perform a matching based on three quantities: 1) the stellar mass inside the Petrosian radius (R_{petro}), 2) the half-light radius and 3) the ellipticity, all measured in the SDSS r-band.

The values for TNG50 galaxies are taken from (Rodriguez-Gomez et al., 2019), who postprocessed TNG50 galaxies above a total stellar mass of $5 \times 10^9\,M_\odot$ with the radiative transfer code SKIRT (Baes et al., 2011; Camps & Baes, 2015) including the effects of dust attenuation and scattering. They then used `statmorph` to obtain photometric measurements, from which we use the circularized Petrosian and half-light radius as well as the ellipticity. We then calculated the stellar mass inside the Petrosian radius straight from the simulations. The TNG50 galaxy sample consists of 1623 galaxies.

All TNG50 galaxies were projected along the z-axis of the simulation box for these measurements yielding randomly distributed inclinations. We continue to adopt this projection throughout this analysis, unless otherwise stated. Including the measured ellipticities in the matching procedure between SDSS and TNG50 galaxies therefore ensures to first order[125] that measured quantities in both samples are contaminated by similar line-of-sights. This mitigates the effort of projecting individual TNG50 galaxies according to measured inclinations from SDSS, which are usually poorly constrained anyway.

125: The exact behaviour depends on the intrinsic shape, which we do not know in observations.

Due to the stellar mass cut for TNG50 galaxies with available SKIRT postprocessing, the stellar masses inside the Petrosian radius of the resulting sample extends down to $2 \times 10^9\,M_\odot$. As typical stellar mass uncertainties at the low mass end are around 0.3 dex (see Gallazzi et al.,

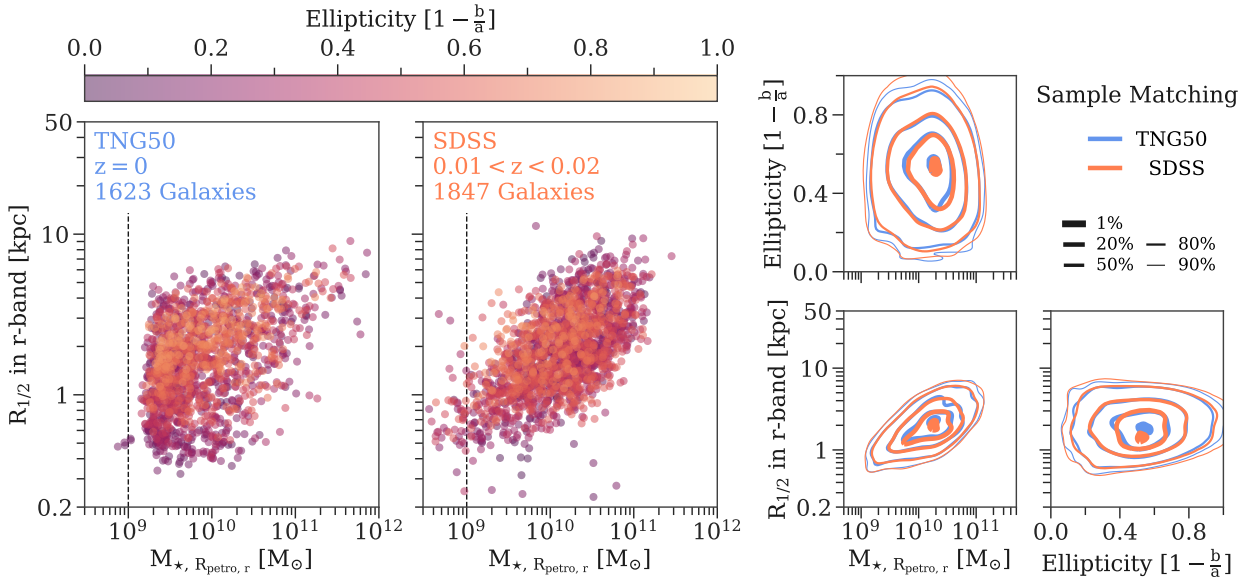

Figure 9.1. Sample Matching of SDSS and TNG50 galaxies. *Left panel*: Mass-size plane of the TNG50 and SDSS galaxy sample color-coded by their ellipticities ($\frac{b}{a}$ is the projected minor-to-major axis ratio). TNG50 quantities have been measured on mock SDSS r-band images to mimic observations; the line-of-sight was taken along the z-axis of the simulation box. The stellar mass is calculated within the Petrosian radius directly from the simulations for TNG50 galaxies. The thin dashed vertical line at 10^9 $M_\odot$ shows the lower mass cut-off that we employ for SDSS galaxies. This yields 1847 SDSS ($0.01 < z < 0.02$) and 1623 TNG50 ($z = 0$) galaxies. Due to observational limitations, SDSS misses extended, low mass galaxies, as they have a low surface brightness, and preferentially records high mass galaxies. TNG50 on the other hand, has less high mass galaxies due to the limited size of the simulation box (51.7 cMpc). *Right panel*: Corner plot of the three quantities used in the sample matching: stellar mass in the Petrosian radius, the half-light radius and the ellipticity, all measured in the SDSS r-band. The contours show Gaussian kernel density estimates for the SDSS sample (*orange*) and the matched TNG50 galaxy sample (*blue*). One SDSS galaxy is matched to one TNG50 galaxy. Now the TNG50 galaxies have the same distribution as SDSS galaxies, which makes it possible to compare the two samples to explore other quantities.

2021), we exclude SDSS galaxies with stellar masses below 10^9 $M_\odot$ prior to matching. This reduces the SDSS sample to 1847 galaxies.

We then assign one SDSS galaxy to one TNG50 galaxy based on the nearest neighbour in the 3D dimensional space of the aforementioned quantities. Because of the dynamical range of stellar masses and half-light radii, we match their logarithmic values, which results in an overall better matching. The intrinsic distribution in the mass-size plane of SDSS and TNG50 galaxies, as well as the result of the matching procedure is shown in Figure 9.1. The matched TNG50 sample has now the same distribution as the observed SDSS galaxy sample, which ensures that we compare a similar population of galaxies. This is our fiducial matched sample. Unless otherwise stated, Figures that compare TNG50 and SDSS will always consider the *matched* TNG50 sample.

As star formation and assembly histories are very individual, the fiducial matching could become problematic, if we want to compare on a galaxy-by-galaxy basis. We therefore also explore another matching procedure, for which we split the galaxy samples according to their star formation status (star forming, quenched or green valley). After splitting the observed and simulated galaxy samples according to these criteria, we again perform the matching on mass, size and ellipticity. This will be our alternative matched sample[126].

126: We also plan to split galaxies according to centrals and satellites to investigate the impact of environment.

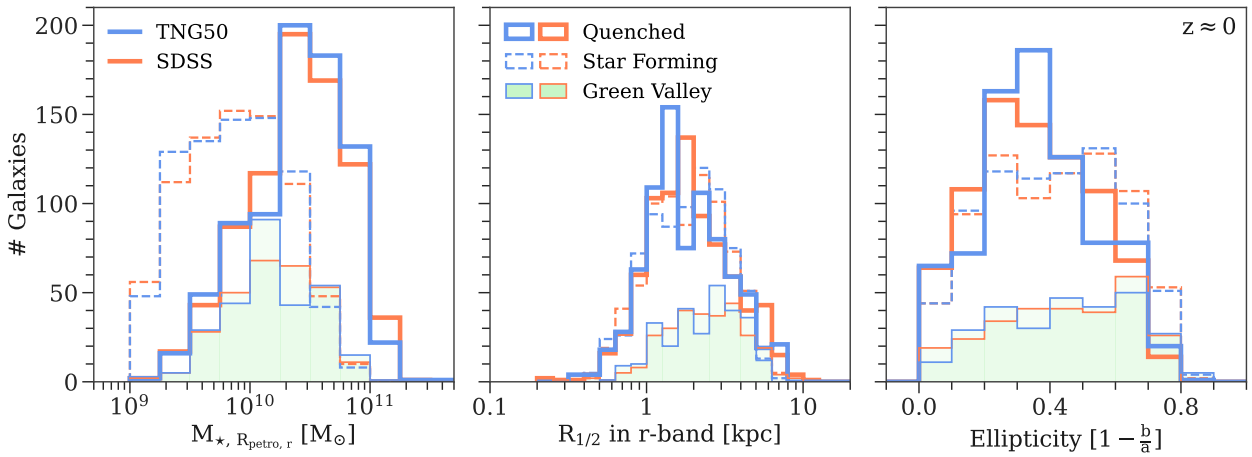

Figure 9.2. TNG50 and SDSS sample matching performed separately for star forming, quenched and green valley galaxies. *From left to right*: Distributions of the SDSS (*orange*) and matched TNG50 (*blue*) galaxies for their stellar mass inside their Petrosian radius, their half-light radius and ellipticity, all measured in the SDSS r-band. Prior to performing the matching in this three dimensional parameter space, galaxies were split according to their star formation status: star forming (*thin dashed line*), quenched (*thick solid line*) and green valley (*green filled histogram*). The distributions are matched well considering that we used separate definitions for the splitting, which are purely simulation-based quantities for TNG50 (Pillepich et al., 2019) and observational for SDSS (Gallazzi et al., 2021).

For the distinction between star forming, quenched and green valley galaxies from TNG50, we use flags provided by (Pillepich et al., 2019). Galaxies between 0.5 dex and 1 dex below the SFMS of TNG50 are in the green valley and below 1 dex they are quenched. The SFMS is measured according to instantaneous star formation rates (SFRs) and stellar masses inside twice the 3D stellar half mass radius. Thus, this definition is different from observations (see Section 9.2.1. However, we do not attempt to match directly between the measured star formation rates of SDSS and TNG50, as the latter does not resolve the low SFRs of the observed quenched galaxy population[127]. We therefore argue that splitting the galaxies according to their intrinsic definition of star formation will yield a more adequate comparison. Figure 9.2 shows the resulting distributions of mass, size and ellipticity of the TNG500 sample matched to the SDSS sample each separately performed for star forming, quenched and green valley galaxies.

127: An additional check would be to also perform a matching in color space for both galaxy samples.

9.3 TOOLS AND METHODS

One of the goals of this study is to extract stellar population information from the SDSS and matched TNG50 galaxy sample via the full spectral method described in Chapter 5. To achieve this, we need to make mock integrated spectra of the TNG50 galaxies. We therefore present below, the single stellar population (SSP) models we consider (Section 9.3.1), our procedure to create mock spectra from TNG50 (Section 9.3.2), and the full spectral fitting method (Section 9.3.3), which differs slightly depending on the observed or simulated galaxy sample. The adopted IMF is from Chabrier (2003)[128] and the metallicity of the sun is $Z_\odot = 0.02$.

128: The Chabrier IMF is used in the TNG50 simulation and also in Gallazzi et al. (2021). We thus use the same for consistency.

9.3.1 Single Stellar Population Models

We focus on the MILES[129] family of SSP models throughout this work (Vazdekis et al., 2010, 2012, 2015, 2016). As they come in a couple of different variants, which we will all use at different points in this study, we summarize them in Table 9.2. The main differences are the wavelength coverage, the adopted isochrones and the treatment of α-abundance. The MILES stellar library (Sánchez-Blázquez et al., 2006) used in creating the MILES SSP models, was extended with other stellar libraries such that the E-MILES SSP models cover the UV-IR wavelength range. Hence, the E-MILES models cover the whole wavelength range provided by SDSS data, while the MILES SSPs do not.

The two sets of isochrones used in MILES SSPs (PADOVA00: Girardi et al., 2000 and BaSTI: Pietrinferni et al., 2004, 2006) employ different physical models of the interior and evolution of stars (see also Gallart et al., 2008; Conroy & Gunn, 2010, for a comparison between the two isochrone sets). They also set the available age-metallicity grid yielding 336 models[130] in total for PADOVA00 and 636 for the BaSTI isochrones.

Because the MILES library is based on empirical stellar spectra, the stars will follow the [α/Fe]-[Fe/H] abundance pattern of the Milky Way. The "baseFe" models employ scaled-solar isochrones, i.e. [α/Fe] $= 0$, without correcting for this effect. On the other hand, the used MILES spectra in the model variants with [α/Fe] $= 0$ and 0.4 dex were corrected with theoretical stellar spectra to the corresponding α-abundance and are thus self-consistent with α-abundance of the adopted BaSTI isochrones.

We convert the (E-)MILES SSP models, which are in air wavelengths, to vacuum wavelengths, because SDSS spectra are given in vacuum[131]. We use the standard transformation given by Ciddor (1996). After that, we re-sample the SSP models to re-obtain the MILES pixel dispersion of 0.8 Å pix^{-1}. The re-sampling is done using SpectRes (Carnall, 2017). We then logarithmically re-bin the SSP models to the SDSS wavelength spacing, which is a necessary step for accurately applying and determining redshifts (see e.e.g Cappellari, 2017).

9.3.2 Creation of Mock Integrated Spectra

For the creation of mock integrated spectra of TNG50 galaxies, we focus on the E-MILES SSP models, as they cover the whole wavelength range of SDSS. Due to the mass resolution, stellar particles in TNG50 are like SSPs. And because the SSP models are normalized to $1\,M_\odot$, we can simply multiply by the particle mass to obtain the spectrum of a single particle, which is then in units of solar luminosities per units wavelength. In particular, stellar particles with a given age and metallicity are assigned an SSP model based on the closest available age-metallicity grid point in the models. The metallicity is expressed as the metal fraction Z in both the simulation *and* the SSP models[132].

For the creation of the mock spectra *only*, we subsidize the E-MILES

129: http://research.iac.es/proyecto/miles/

130: We exclude the two ages available above 14.14 Gyr.

131: We considered using the SSP models from Maraston et al. (2020), which use the MaStar stellar library (Yan et al., 2019) and thus already have the instrumental characteristics of SDSS. However, the MILES models cover a wider parameter space of age and metallicity and we therefore decided to use them instead.

132: See http://miles.iac.es/pages/ssp-models.php for corresponding values of [M/H] and Z.

Table 9.2. Properties of MILES SSP model variants used throughout this study. All models are used with a Chabrier IMF. The BaSTI isochrones refer to Pietrinferni et al. (2004, 2006) and the PADOVA00 isochrones to Girardi et al. (2000). The numbers in brackets show the number of grid points available. Note that they are not uniformly spaced. "baseFe" models follow the abundance pattern of the Milky Way, which means that [M/H] = [Fe/H] is only true for high metallicity stars. Low metallicity stars are enhanced in [α/Fe] and thus technically inconsistent with the adopted scaled-solar isochrone.

SSP MODEL	ISOCHRONE	WAVELENGTH COVERAGE [Å]	AGE GRID [Gyr]	METALLICITY GRID [M/H] [dex]	ALPHA ABUNDANCE [dex]
E-MILES	BaSTI	168 – 50000	0.03 – 14. (53)	−2.27 – +0.4 (12)	baseFe
E-MILES	PADOVA00	168 – 50000	0.063 – 14.13 (48)	−2.32 – +0.22 (7)	baseFe
MILES	BaSTI	3540 – 7410	0.03 – 14. (53)	−2.27 – +0.4 (12)	baseFe
MILES	BaSTI	3540 – 7410	0.03 – 14. (53)	−2.27 – +0.4 (12)	[α/Fe] = 0.0
MILES	BaSTI	3540 – 7410	0.03 – 14. (53)	−2.27 – +0.4 (12)	[α/Fe] = 0.4
MILES	PADOVA00	3540 – 7410	0.063 – 14.13 (48)	−2.32 – +0.22 (7)	baseFe

models with a separate set of E-MILES SSPs that extend to younger ages from 6.3 – 63 Myr (Asa'd et al., 2017), which accommodate for very young stellar particles in TNG50. These models are based on the PADOVA94 isochrones (Bertelli et al., 1994). We interpolate them in $\log_{10}$ Age – [M/H] space onto the same metallicity grid of the fiducial E-MILES models via Delaunay triangulation as well as the nearest neighbour, if they are outside the convex hull. Finally, we take the mean of two SSPs that have overlapping ages in both the young and fiducial E-MILES models (there is one overlapping age point for the PADOVA00 and four for the BaSTI isochrones).

After that, stellar particles with ages and metallicities still outside the covered age-metallicity grid of the SSP models, are assigned the closest boundary grid value.

We then select all stellar particles within a 2D galactocentric radius of 500 pc for the TNG50 galaxies described in Section 9.2.2. This is the mean area covered by the SDSS galaxies from Section 9.2.1 as well as the aperture used in Chapter 7 to study intrinsic properties of TNG50 galaxy centers, making a direct comparison more straightforward.

For each stellar particle we also model their attenuation following Nelson et al. (2018), which we re-iterate in the following.

The attenuated SSP spectrum $L_{obs,\,i}(\lambda)$ of the i-th stellar particle is given by:

$$L_{obs,\,i}(\lambda) = L_{SSP,\,i}(\lambda) \cdot e^{-\tau_\lambda^B} \cdot \frac{1 - e^{-\tau_\lambda}}{\tau_\lambda}, \tag{9.2}$$

where $L_{SSP,\,i}(\lambda)$ is the unattenuated SSP model assigned to the i-th stellar particle. Equation 9.2 incorporates two dust models.

The first is by Charlot & Fall (2000), where the wavelength depen-

dent optical depth τ_λ^B is given by :

$$\tau_\lambda^B = \left\{ \begin{array}{ll} 1.0 \cdot (\lambda/5500\,\text{Å})^{-0.7}, & t \leqslant 10\,\text{Myr} \\ 0.3 \cdot (\lambda/5500\,\text{Å})^{-0.7}, & t > 10\,\text{Myr} \end{array} \right\}. \tag{9.3}$$

This model effectively adds a stronger attenuation for young stellar particles with age t, as they are likely still surrounded by their birth gas cloud.

The second uses the internal dust model by Calzetti et al. (1994), in which ionizing gas and dust are cospatial and uniformly mixed. The total dust attenuation τ_λ is given by:

$$\tau_\lambda = \tau_\lambda^a \cdot [h_\lambda \sqrt{1-\omega_\lambda} + (1-h_\lambda)(1-\omega_\lambda)], \tag{9.4}$$

where ω_λ and h_λ are the albedo and phase function describing anisotropic dust scattering. Their fitting functions are taken directly from Calzetti et al. (1994). The optical depth for dust absorption τ_λ^a takes the neutral gas and metal content of the simulation into account and is thus viewing angle dependent (see also McKinnon et al., 2016):

$$\tau_\lambda^a = \left(\frac{A_\lambda}{A_V}\right)_\odot (1+z)^{-0.5} \left(\frac{Z_{gas}}{Z_\odot}\right)^{1.6} \left(\frac{N_H}{N_{H,0}}\right). \tag{9.5}$$

The solar neighbourhood extinction curve $\left(\frac{A_\lambda}{A_V}\right)_\odot$ is taken from Cardelli et al. (1989). We drop the redshift dependence, as it is very weak for the redshift range of the SDSS data ($0.01 < z < 0.02$). N_H is neutral hydrogen column density with a normalization of $N_{H,0} = 2.1 \times 10^{21}\,\text{cm}^{-2}$. Z_{gas} is the neutral hydrogen mass weighted gas metallicity with $Z_\odot = 0.02$. These two quantities are computed in a slightly simplified way compared to Nelson et al. (2018). In a first step, we calculate the neutral hydrogen number volume density, the neutral hydrogen mass and total metallicity of each gas cell within a square aperture of 10 kpc on each side centered on a given galaxy. We then interpolate these quantities to the coordinates of the stellar particles using Delaunay triangulation. Stellar particles within the circular 500 pc aperture are then sorted according to their z-coordinate (our line-of-sight). For each stellar particle, N_H and Z_{gas} are then obtained from the interpolated values by integrating along the line-of-sight until the stellar particle's z-position is reached. If there is no gas along the line-of-sight, the attenuation according to the first model is still applied.

Each SSP spectrum for each stellar particle is also shifted according to the relative line-of-sight velocity of the stellar particle with respect to the systemic velocity of the TNG50 galaxy. This ensures that the full line-of-sight distribution is taken into account, which does not necessarily need to be purely Gaussian.

Lastly, summing up all the individual spectra of stellar particles within the 500 pc aperture makes up the total integrated spectrum. For each of the 1623 TNG50 galaxies we record four spectra, which are the attenuated and unattenuated integrated spectra made with the E-MILES SSP models for both the BaSTI and PADOVA00 isochrones respectively. Each integrated spectrum is additionally cut-off above 8950.4 Å, even

though the SDSS range extends to slightly larger wavelengths (9200 Å). The reason for this is that the E-MILES models for the youngest ages do not extend past 8950.4 Å, which makes this wavelength range unreliable in the presence of young stellar particles.

Because we want to explore different matching criteria, as described in Section 9.2.2, we add observational realism based on the matched SDSS galaxy only before fitting the mock spectra (see Section 9.3.3). This circumvents remaking the integrated spectra from scratch for different matching criteria.

9.3.3 Full Spectral Fitting

To extract age-metallicity distributions from integrated spectra we apply pPXF (Cappellari & Emsellem, 2004; Cappellari, 2017), as tested in Chapter 5. The exact steps differ slightly depending on whether we fit an SDSS or TNG50 galaxy, which we go through in detail below. For both cases, we exclusively use multiplicative polynomials. The degree is set by $\lfloor(\lambda_{max} - \lambda_{min})/200\ \text{Å}\rfloor$. We also exclusively use the first order difference operator for the regularization matrix ($\mathbf{B} = \text{diag}(1, -1)$). As a reminder, regularization smooths out the weights applied to each age-metallicity combination of the SSP models to avoid very sparse solutions that are common in ill-conditioned, inverse problems.

9.3.3.1 *Fitting SDSS galaxies*

Each SDSS galaxy is fitted five times, which includes all four "baseFe" models from Table 9.2 to obtain age-metallicity distributions. The fifth time uses the two sets of MILES BaSTI SSPs with $[\alpha/\text{Fe}] = 0$ and 0.4 dex to simultaneously fit for age, metallicity and α-abundance. The age range of the templates is restricted to ages younger than the age of the Universe at the given redshift of a SDSS galaxy.

First, each SDSS spectrum is cut-off above 8950.4 Å to ensure that the same wavelength range as the TNG50 mock spectra is fit. This is only important when fitting with the E-MILES models. We have explicitly checked that this does not change our derived stellar population parameters, by also performing fits that cover the whole SDSS wavelength range.

Prior to fitting, each SSP model is convolved with the wavelength dependent line spread function (LSF) of the respective SDSS galaxy. If the SSP model has worse resolution at a given wavelength than the SDSS spectrum, the latter is convolved to match the LSF of the SSP. The stellar kinematics are only fit for radial velocity and velocity dispersion.

We also model gas emission lines that are present in SDSS spectra as Gaussians. The full list of used emission lines can be found in Appendix C.1. We do not derive any physical quantities from the modelled emission lines, but they have to be taken into account to accurately model the absorption spectrum of the underlying stellar populations. In particular, all Balmer lines are together in one kinematic component, and all other emission lines are in a separate component.

This allows for a better fit in case they have slightly different radial velocities and velocity dispersions. The flux of each line is allowed to vary freely, except the [OI] and [NII] doublets, which are fixed to their theoretical ratios. If the galaxy is classified as an AGN by the SDSS pipeline, we instead give pPXF two separate kinematic components *each* including *all* modelled emission lines. This makes it possible for pPXF to model narrow emission lines on top of broad ones, as common in some AGN. The redshift determined by the SDSS pipeline is given as a starting guess to all kinematic components. We also take into account the noise spectrum provided for each SDSS galaxy. The SSP templates are normalized by their total median value resulting in pPXF returning a mass fraction for each SSP model. The flux and noise spectra from SDSS are normalized to the median flux.

We then first perform a fit with pPXF *without* regularization. Then a second fit with regularization is performed. In this second fit, the best-fit total gas emission line model from the first fit is kept fixed (we pass it via the sky keyword). We also keep the stellar kinematics derived from the first fit fixed. This ensures that these quantities do not interfere with the regularization process. In particular, we chose to *not* subtract the modelled emission lines from the integrated spectrum and then fit the emission line free spectrum. This is much more error prone in case the emission lines were not accurately modelled. We also do not mask out any sky residuals or missing pixels as pPXF has enough information from the rest of the spectrum to not be majorly effected by this.

We set the regularization parameter according to the mean SNR of the SDSS spectrum, and thus depart from the manual calibration as performed in Chapter 5. We do not set the same fixed regularization parameter for each SDSS galaxy, because typically lower SNR spectra are already sufficiently smooth at lower regularization parameters than higher SNR spectra. This is because each pixel value is less constrained for low SNRs and thus the model flux has more freedom to change making the derived age-metallicity distribution overall smoother. Stellar population quantities from the regularized solution are always shown unless otherwise stated.

9.3.3.2 *Fitting TNG50 galaxies*

Before fitting the mock integrated spectra of TNG50 galaxies, we add observational realism depending on the matched SDSS galaxy. The steps are the following:

1. We shift the whole mock spectrum to the redshift of the SDSS galaxy. We use the redshift derived from pPXF and not from the SDSS pipeline.

2. We convert the luminosity at each wavelength to flux in units of $[\mathrm{ergs\,cm^2\,s^{-1}\,\AA^{-1}}]$ by taking the luminosity distance into account.

3. We convolve the mock spectrum with the LSF, which is typically different for each SDSS galaxy.

4. We then re-sample the mock spectrum to the exact wavelength grid and range of the SDSS galaxy.

5. We add realistic noise, based on the wavelength dependent SNR of each SDSS galaxy. The noise is drawn at the i-th wavelength from a random Gaussian distribution with zero mean and standard deviation of $F_{mock,i}/SNR_i$, where F_{mock} is the flux of the mock spectrum (see also Wu et al., 2021).

As we do not model gas emission lines from TNG50, we also do not include any in the pPXF fit. We pass pPXF the noise spectrum of the assigned SDSS galaxy when fitting the TNG50 mock spectra. The starting guess of the redshift is the one from the SDSS pipeline. Again, we first perform an unregularized fit and then a regularized one, where the derived stellar kinematics are kept fixed. The regularization parameter is again set to the median SNR.

Because we can check the true answer with the TNG50 mock spectra, we perform several different tests to understand biases in our full spectral fitting recovery, which are described in Section 9.4.1.3.

9.4 CENTRAL STELLAR POPULATIONS FROM SDSS AND TNG50 GALAXIES

We show the results of stellar population properties derived from full spectral fitting of SDSS galaxies and compare it to TNG50 galaxies exploring various complexities in sample matching and extraction from realistic mock observations. We also compare some results to the ones from Gallazzi et al. (2021). All shown stellar population quantities refer to the central ~ 500 pc only.

9.4.1 Mean Ages, Metallicities and [α/Fe]

Average ages, metallicites and also α-abundances form important scaling relations with galaxy stellar mass. How starkly are these trends effected by different modelling considerations in both simulations and observations?

To avoid confusion, we show our definition of average stellar population quantities that are adopted throughout this study:

$$\langle \mathrm{Age} \rangle = \frac{\sum_i w_i \mathrm{Age}_i}{\sum_i w_i} \tag{9.6}$$

$$\langle \mathrm{Metallicity} \rangle = \frac{\log_{10}[\sum_i w_i (Z_i/Z_\odot)]}{\sum_i w_i} \tag{9.7}$$

$$\langle [\alpha/\mathrm{Fe}] \rangle = \frac{\sum_i w_i [\alpha/\mathrm{Fe}]_i}{\sum_i w_i} \approx \langle [\mathrm{Mg}/\mathrm{Fe}] \rangle = \frac{\sum_i w_i [\mathrm{Mg}/\mathrm{Fe}]_i}{\sum_i w_i} \tag{9.8}$$

The summation is performed for the i-th stellar particle, in case of TNG50 intrinsic values, or the i-th weight associated with each SSP

model returned from pPXF in case of recovered values from fitting the integrated spectrum (which can be one from SDSS or and TNG50 mock). The latter are by default *mass* fractions due to our adopted normalization of the SSP models. The weight w refers to either mass or luminosity in the SDSS r-band. In case of TNG50, we use the r-band luminosities provided by the stellar particle field `GFM_StellarPhotometrics`. To convert the mass weights output from the full spectral fitting procedure into light weights, we divide by the appropriate M/L ratio provided by the (E-)MILES models. Note that the averages are calculated in *linear* space for age *and* metallicity, whereas the α-abundance average is performed in *logarithmic* space. We use [Mg/Fe] as a proxy for [α/Fe] for values from TNG50, which is also the α-element predominantly tracked in observations (see e.g. Gallazzi et al., 2006, 2021; Martín-Navarro et al., 2021b).

9.4.1.1 *Intrinsic and observational quantities from TNG50*

Mocking simulation outputs can already severely affect the shape of average trends of stellar population properties with galaxy mass. Understanding this impact is important to a) fairly assess the reliability of observational modelling techniques, b) accurately compare observational and simulation results and c) be able to project and connect these biases to studies, which are purely based on simulations (e.g. Chapter 7). The results of this section refer to the original TNG50 sample, i.e. it is not matched to the SDSS observations.

In Figure 9.3, we show the average stellar population properties from TNG50 based on three progressively more "observationally appropriate" quantities. Intrinsic quantities purely accessible from simulations are directly taken from the analysis performed in Chapter 7 (Figure 7.9) and are thus showing stellar population quantities averaged in a 3D energy-based 500 pc aperture and total stellar masses. The next progression are quantities averaged in an aperture defined by a 500 pc 2D radius and stellar masses within the Petrosian r-band radius. This aperture moves galaxies towards lower stellar masses, especially the ones with *total* stellar masses above 10^{10} $M_\odot$ (particularly visible in the average [Mg/Fe] relation). In addition, the projection contaminates the intrinsic stellar population quantities belonging to that the particular region within the galaxy with those located in other regions along the line-of-sight. On average, galaxies become slightly older, less metal-rich and more magnesium enhanced across the entire mass range. Furthermore, light instead of mass weighted averages severely affect average ages and [Mg/Fe] for galaxies below 10^{11} $M_\odot$ in total stellar mass, as the presence of younger (and thus less α-enhanced) stellar populations dominate the light. The average metallicity is largely robust against this effect.

The last progression is to construct mock spectra from TNG50 by assigning SSP models to stellar particles within the given 2D aperture. This step *alone* - without actually deriving the stellar population properties from the mock spectra via observational techniques - alters the underlying distribution, because SSP models have a limited range of available ages and metallicities[133].

133: We do not take into account α-enhanced models for the creation of mock spectra as only two [α/Fe] values are available from the MILES models.

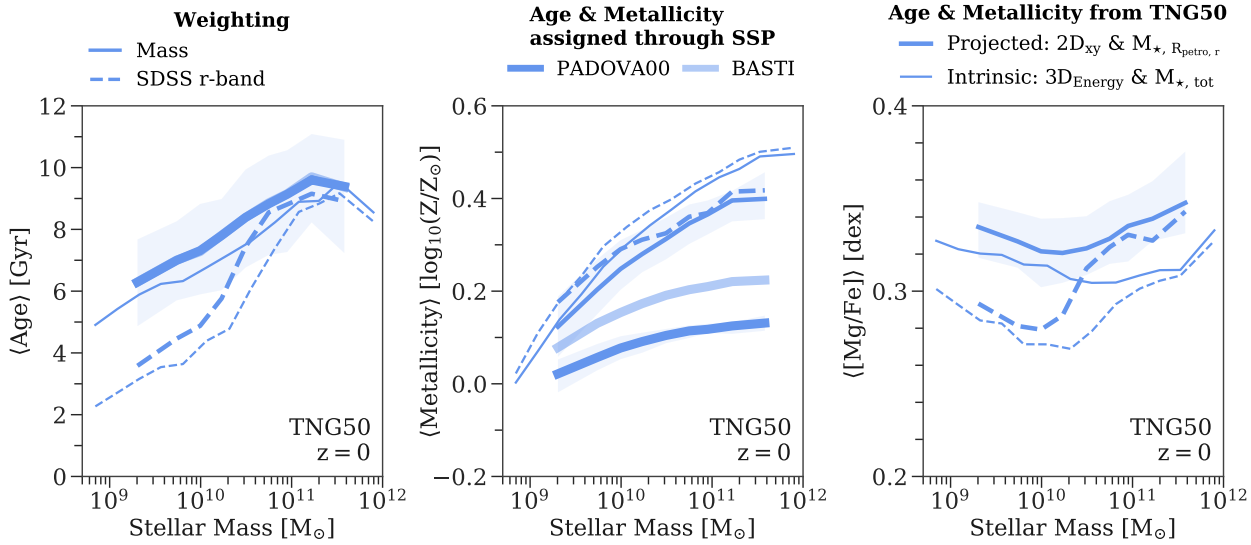

Figure 9.3. Effects of modifying intrinsic TNG50 outputs of (central, ~ 500 pc) stellar population properties during the process of constructing mock observations. *From left to right*: The median relation of average age, metallicity and magnesium-to-iron abundance [Mg/Fe] as a function of stellar mass for TNG50 galaxies at z = 0. Solid lines show mass weighted averages, whereas dashed lines show SDSS r-band weighted quantities. The thinnest lines show trends based on averages calculated from 3D energy-based 500 pc apertures as well as total stellar masses from Chapter 7. The lines with intermediate thickness show averages based on apertures defined by a 500 pc projected 2D radius and stellar masses within the Petrosian r-band radius; the 16th and 84th percentile range is also shown as the shaded area. The scatter is overall similar among the different mass weighted values. The thickest lines are average ages and metallicities after stellar particles have been assigned to the E-MILES SSP models based on the BaSTI (*light blue*) and PADOVA00 (*darker blue*) isochrones respectively. Note that in this case the age relations perfectly overlap with the intrinsic values from TNG50 measured inside the projected aperture. The mass-metallicity relation based on SSP assigned values departs from the underlying distribution of TNG50 due to the maximum metallicity available in the SSP models.

So far, none of the available SSP models reaches values above 0.4 dex, as such stars do not exist in large enough samples in the solar vicinity. However, stellar particles in TNG50 can reach metallicities one dex above solar and more. Thus, the constructed integrated mock spectrum *cannot* properly represent the intrinsic stellar population distribution output by TNG50. Therefore, comparisons between stellar population properties recovered via observational techniques from mock integrated spectra and the underlying "truth" have to be made according to this modified distribution. Figure 9.3 shows how the limited metallicity coverage of SSP models modifies the normalization *and* slope of the mass-metallicity relation of TNG50 galaxies. The relation becomes much flatter and shifts downwards by approximately 0.2 and 0.3 dex at the high mass end for BaSTI and PADOVA00 isochrones respectively. This is entirely due to the maximum available metallicity value of 0.4 and 0.22 dex in the case of BaSTI and PADOVA00 isochrones respectively.

9.4.1.2 *Matched TNG50 vs. SDSS*

We show the average stellar population scaling relations from SDSS observations, derived via full spectral fitting (FSF; see Section 9.3.3) and from spectral indices (Gallazzi et al., 2021), compared with the sample matched TNG50 galaxies in Figures 9.4 and 9.5. All average stellar population quantities are derived within the central (projected) ~ 500 pc. In

the case of TNG50, the ages, metallicites and [Mg/Fe] are the genuine simulation outputs within the given aperture to establish the "status quo" in the comparison to observations.

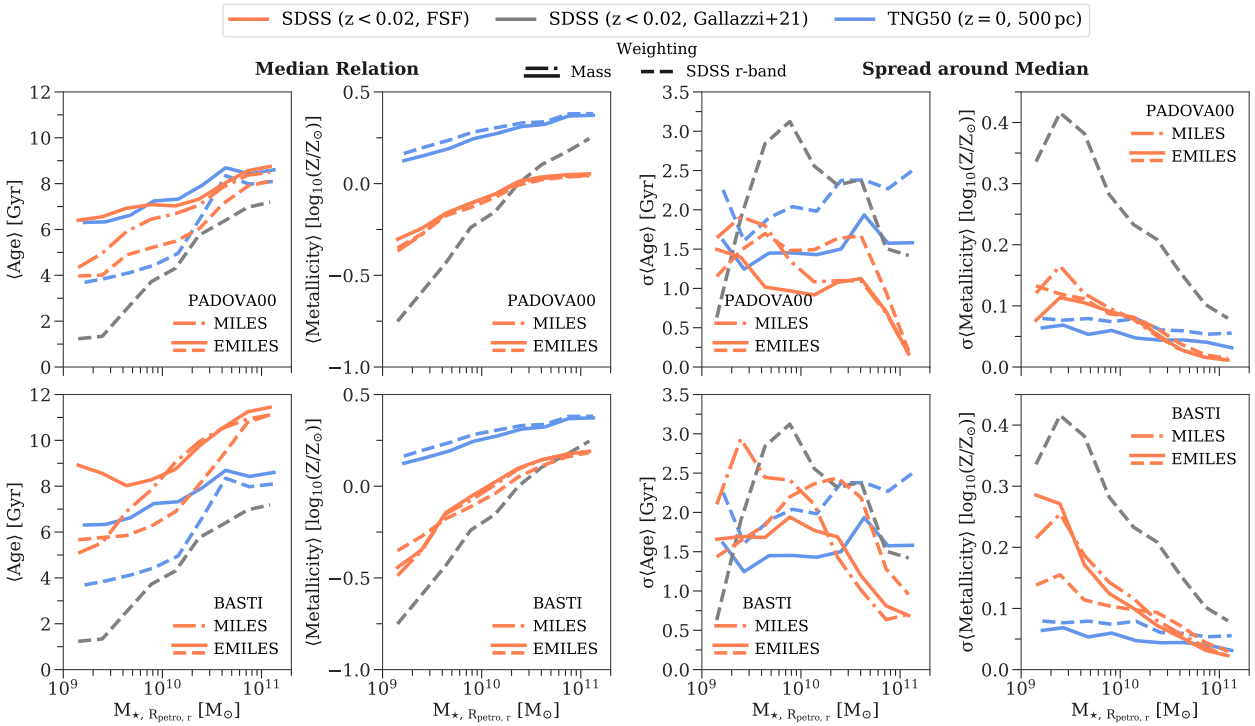

Figure 9.4. Mass-age and mass-metallicity relation for SDSS and sample matched TNG50 galaxies in the central ~ 500 pc. *Left panel*: Running median trends for average ages (*left column*) and metallicities (*right column*) as a function of galaxy mass derived from SDSS observations via full spectral fitting (FSF; *orange*) and absorption indices (Gallazzi et al., 2021, *grey*) as well as values from TNG50 galaxies (*blue*). Solid lines refer to mass-weighted averages, whereas dashed lines are weighted by the luminosity in the SDSS r-band. Additionally, stellar population quantities derived via FSF are shown for the application of "baseFe" (E-)MILES SSP models using BaSTI (*top row*) and PADOVA00 (*bottom row*) respectively. The dashed dotted orange lines show the mass-weighted averages derived from the MILES models, which only extend up to 7410 Å, whereas the solid and dashed orange lines show the mass- and light-weighted averages derived from the E-MILES models, which cover the whole SDSS wavelength range. *Right panel*: The same as the left panel, but now the spread (σ) around the median relations are shown to understand the galaxy-to-galaxy scatter in stellar population properties across the galaxy stellar mass range. The spread is calculated as the mean of the 16th and 84th percentile. Note that this does not include errors on the observed quantities.

Mass-age and mass-metallicity relation (Figure 9.4): The median trend of mass-weighted average ages derived via FSF with the E-MILES PADOVA00 SSP models agrees perfectly with values from TNG50, whereas the derived mass-metallicity has nearly a constant offset of 0.5 dex towards lower metallicities (Figure 9.4, left panel). Mass-weighted average ages measured with FSF using the E-MILES BaSTI SSP models are, on the other hand, older by around 2 Gyr compared to TNG50. They also show an upturn for galaxies with masses below $5 \times 10^9\,M_\odot$. The corresponding mass-metallicity relation has a steeper slope for the BaSTI models compared to the PADOVA00 ones, which results in an even starker discrepancy with TNG50.

The differences between measured stellar population properties for the two sets of isochrones is likely driven by two aspects. Those are: 1) the intrinsic differences of the isochrones (see Section 9.6.3) and 2) the

regularization applied during the FSF process. Even though we apply the same amount of regularization for both models, the response of the two models in the recovered average ages and metallicties is different. The effect seems to be slightly larger for the PADOVA00 models, resulting in overall lower ages as well as lower metallicities at the high mass end (see Figure C.1 in Appendix C.2).

The average ages recovered with the MILES models for both PADOVA00 and BaSTI isochrones, are younger by around 2 Gyr for galaxies below $10^{10}\,M_\odot$. The metallicities are unaffected by this. As the MILES models only extend until 7410 Å, this effect is driven by the wavelength coverage. Hence, in the presence of increasingly younger stellar populations, which dominate the blue part of the optical spectrum, the inclusion of redder wavelengths until the Calcium Triplet are important, especially, if the *mass* assembly of galaxies is of interest (Neumann et al., 2022, see also).

The light-weighted stellar population averages from FSF with the E-MILES models and TNG50 are shown, such that they are comparable in this aspect to the results from Gallazzi et al. (2021). Their values were derived with the Bruzual & Charlot (2003) SSP models, which are based on the PADOVA isochrones. Hence, differences in average ages and metallicites derived from the SDSS data for the PADOVA00 models are mainly due to the two different observational modelling techniques. Both the mass-age and mass-metallicity relation from Gallazzi et al. (2021) are steeper. While the difference in the average metallicity at the high mass end ($> 2 \times 10^{10}\,M_\odot$) can be reconciled with unregularized FSF (see Figure C.1 in Appendix C.2), the differences in age and metallicity at the low mass end could be due to multiple reasons. Because the five absorption indices used by Gallazzi et al. (2021) are in the blue part of the spectrum, the younger ages of up to 2 Gyr for galaxies below $2 \times 10^{10}\,M_\odot$ could be due to the same effect previously explained when FSF is used with the MILES models. The wavelength coverage could also explain the larger discrepancy between Gallazzi et al. (2021) and the TNG50 values at low galaxies masses (also reported by Nelson et al., 2018, section 4.1), since the light-weighted ages from TNG50 would not be affected by this. As the metallicity does not seem to be impacted by the wavelength coverage, the higher average metallicities for low mass galaxies derived from FSF as compared to Gallazzi et al. (2021) could be explained by the different treatment of chemical evolution. Gallazzi et al. (2021) used a fixed metallicity as a function of age, whereas our approach allows any combination of age and metallicity. To reconcile this effect with the observed ages, the FSF approach thus needs to recover both metal-rich and metal-poor population at fixed young ages, which is indeed the case (see Figure 9.10).

However, we also note that errors easily reach 0.2 dex metallicity for the low mass end due to typically lower signal-to-noise ratios and to age uncertainties of at least 2 Gyr at the high mass end due to overall poor age resolution at old ages (> 8 Gyr). Thus, differences of stellar population quantities in the two observational techniques as well as results from TNG50 can partially be reconciled by this (see Section 9.4.1.3).

In addition, we show the scatter of the galaxies' average stellar population properties around the median for all previously described models (Figure 9.4, right panel). The scatter in mass-weighted average age and metallicity predicted by TNG50 is rather constant as a function of galaxy mass, which is around 1.5 Gyr and 0.05 dex respectively; although there is slight decline of the scatter in metallicity towards the high mass end. This rather constant scatter is hard to reproduce in observations, as it is influenced by many different effects. The most apparent one is observational errors, which certainly inflate the scatter of observed average metallicities, especially at the low mass end. The poor age resolution at old average ages, where galaxies have high stellar masses, has the opposite affect on the scatter in age, where it is suppressed.

The scatter from the FSF approach is overall smaller compared to the Gallazzi et al. (2021) mainly because of two reasons. First, the regularization is designed to smooth out the resulting age-metallicity distribution, which especially effects the scatter in age reducing it by around 1 Gyr across the galaxy mass range (compare with the unregularized version in Figure C.1). Second, as the scatter in metallicity is only mildly influenced by the regularization, the reduced scatter of the FSF approach likely stems from the fact that the metallicity can be better constrained. This is not surprising as FSF models several thousand spectral pixels, whereas the absorption indices used by Gallazzi et al. (2021) only provide five data points.

Lastly, the shape of the scatter in the average age as a function of galaxy mass reported by Gallazzi et al. (2021), can almost be exactly reproduced by the light-weighted values from the unregularized FSF with the MILES models (see also Figure C.1). No regularization increases the overall scatter, whereas the light-weighting creates the local maximum around $5 \times 10^{10}\,M_{\odot}$ and the effect of wavelength range increases the scatter at galaxy masses of $10^{10} M_{\odot}$ to the observed maximum of around 3 Gyr. Thus, the shape of galaxy-to-galaxy variations in average stellar population properties as a function of galaxy mass are not only influenced by observational errors, but also by systematics of the adapted modelling technique.

Taking all these effects into account, it could indeed be possible to reconcile the rather constant spread in average ages and metallicities predicted by TNG50 with observations. The median relation for the average age from both observations and simulations is already in very good agreement (see also Nelson et al., 2018), while this is not yet clear for the mass-metallicity relation. We explore this further in Section 9.4.1.3 with stellar population recovery from realistic mock integrated spectra of the TNG50 galaxies.

Adding the mass-[α/Fe] relation (Figure 9.5): The use of the MILES BaSTI SSPs with $[\alpha/\mathrm{Fe}] = 0$ and 0.4 dex allows for full spectral fits that simultaneously vary the age, metallicity and α-abundance. We compare this to the median relation of $[\alpha/\mathrm{Fe}]$ values as function of galaxy mass from Gallazzi et al. (2021), as well as [Mg/Fe] from TNG50 galaxies in Figure 9.5. The trend predicted by TNG50 is flat compared to observa-

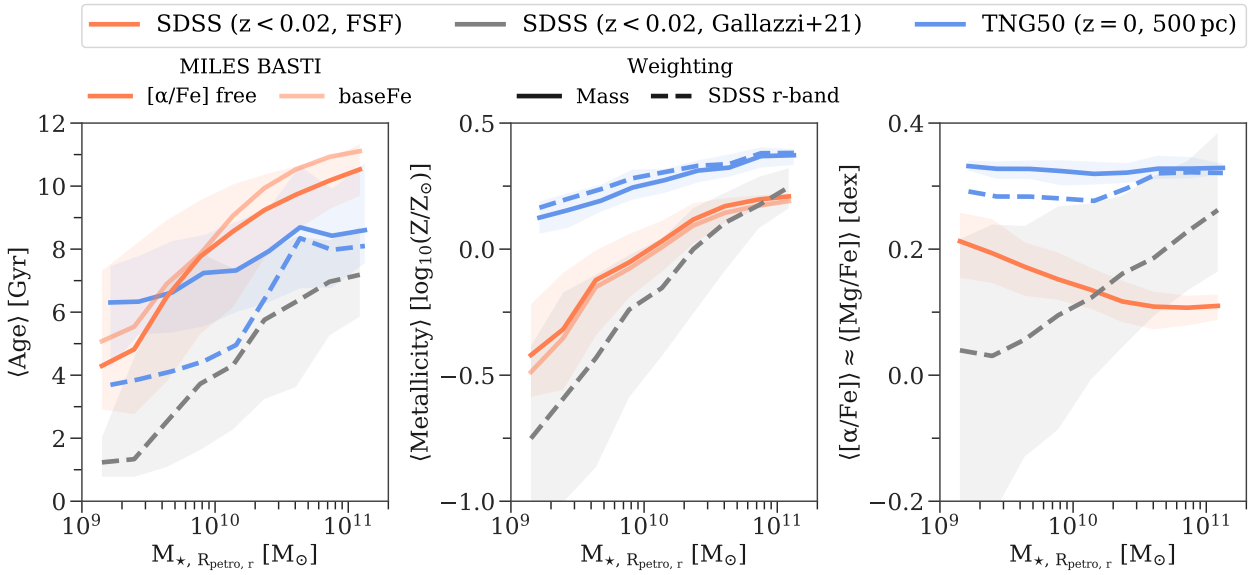

Figure 9.5. Average ages, metallicities and [α/Fe] for SDSS and sample matched TNG50 galaxies in the central ~ 500 pc. *From left to right*: Running median trends for average ages, metallicities and [α/Fe] (for SDSS) ≈ [Mg/Fe] (for TNG50) as a function of galaxy mass. Quantities derived from SDSS observations via full spectral fitting (FSF) are shown in orange and absorption indices from Gallazzi et al. (2021) are in grey. Values from TNG50 are in blue. The shaded region displays the 16th and 84th percentile range. Solid lines refer to mass-weighted averages, whereas dashed lines are weighted by the luminosity in the SDSS r-band. Stellar population quantities derived via FSF are shown for MILES BaSTI SSP models with [α/Fe] = 0 and 0.4 dex, i.e. [α/Fe] is free during the fit (*dark orange*), as well as for the "baseFe" models as a reference (*lighter orange*, same as the dashed dotted lines in Figure 9.4).

tions, with a constant value of around 0.3 dex and minimal scatter[134]. The results from (Gallazzi et al., 2021) show a continuous rise of [α/Fe] as a function of galaxy stellar mass from 0.0 dex to around 0.2 dex, albeit with a large scatter. Our FSF approach recovers the exact opposite trend, especially with respect to the unregularized solution (see Figure C.2 in Appendix C.2).

The regularizing effect of decreasing the average age at the high mass end and increasing it at the low mass end, is stronger when the variation of [α/Fe] is included in the fit. This can be seen when comparing the median age trend of Figures 9.5 & C.2 with the corresponding "baseFe" models. The average metallicity is not affected by this. As a response to the regularizing effect in age, the median trend of [α/Fe] for the regularized values reaches a plateau at 0.1 dex for galaxy masses above $10^{10} M_\odot$ compared to unregularized values, where it extends down to 0.0 dex. This is a consequence of α-enhanced isochrones being redder at fixed age and metallicity (see Vazdekis et al., 2015, Figure 1). Thus, a decrease in age (as "enforced" by the regularization at the high mass galaxy end) will result in an increase in [α/Fe]. Combining this effect with the fact that MILES models recover lower ages for galaxies below $10^{10} M_\odot$ than E-MILES models due to the wavelength coverage, we could suspect that the higher [α/Fe] values at the low mass end are a result of this age-[α/Fe] dependency. Therefore, it could be possible that full spectral fits with hypothetical E-MILES models with the BaSTI [α/Fe] variations indeed predict a flat mass-[α/Fe] relation, similar to TNG50[135]. The remaining almost purely vertical offset between TNG50 and SDSS is then similar to the mass-metallicity relation, which

134: Although we see in Figure 9.3 that there is minimal variation as a function of galaxy mass, creating a u-shape with a minimum at galaxy stellar masses of $10^{10} M_\odot$ (projected and Petrosian aperture). However, the change is on average 0.02 dex, which will be impossible to measure from extragalactic observations.

135: Some other on-going studies suggest a flatter [α/Fe] relation than currently presented in the literature (e.g. Scholz-Díaz et al., 2022).

would point towards evidence that galaxies in TNG50 overall enrich too quickly.

However, [α/Fe] values for galaxies have always been reported to be an increasing function of galaxy mass in the literature (e.g. Trager et al., 2000b; Kuntschner et al., 2001; Thomas et al., 2005; Conroy et al., 2014) and interpreted as the short star formation time scale of high mass galaxies. On the other hand, these studies do not account for complex star formation and metal enrichment histories, which could explain the differences compared with our FSF approach. It is more likely though that the variations of different α-elements probed across the SDSS and MILES wavelength range respond differently as a function of galaxy mass (e.g. Cα; see Worthey et al., 2014). This causes a different recovered behaviour of [α/Fe] from FSF, as compared to Gallazzi et al. (2021), who solely focus on magnesium lines[136] as a tracer of [α/Fe].

136: Restricting FSF to wavelength ranges only sensitive to Mg would be a way to test this [I. Martín-Navarro, priv. comm.].

9.4.1.3 *Recovery from TNG50 mock spectra*

Can we bridge the gap between stellar population properties of observations and simulations that we have seen in Section 9.4.1.2 with the application of the same FSF technique (see Section 9.3.3.2) to realistic mock integrated spectra of TNG50 galaxies (see Section 9.3.2)? How well does the FSF technique recover the mass-age and mass-metallicity relation, when we know the underlying ground truth? This section aims to answer these questions[137].

137: We plan to explore the recovery of [α/Fe] by constructing α-enhanced mock spectra is planned.

We note that the "ground truth" here refers to ages and metallicities from TNG50 as assigned through the SSP models using the BaSTI and PADOVA00 isochrones respectively, as the SSP grid boundaries alter the underlying age-metallicity distribution originally output by the TNG50 simulation (see Section 9.4.1.1). All fits are exclusively performed with the E-MILES models and all averages are mass-weighted, as we have already explored the effects of restricted wavelength coverage and light-weighted quantities in the previous section. The TNG50 galaxies are sample matched to the SDSS galaxies (see Section 9.2.2).

The effect of reddening (Figure 9.6): We show the distribution of mean ages and metallicites derived from *unregularized* FSF as a function galaxy stellar mass. The same SSP models were used in mocking *and* fitting the integrated spectra. The agreement with the true distribution from TNG50 is overall good. The scatter in the recovered average metallicities is overall larger for galaxies below $10^{10}\,M_\odot$ as originally input from TNG50, with a systematic trend to higher average metallicities. This is also accompanied with higher average ages. A plausible explanation for this could be that old and metal-rich SSP models are practically identical, especially considering shifts of mere 2 Gyr and 0.1 dex in age and metalicity respectively.

Most importantly, the recovered stellar population properties from FSF are *not* affected by reddening, which can vary drastically across TNG50 galaxies due to their gas column densities. The multiplicative polynomial, which is included during the fitting process of pPXF, acts as a flexible reddening law and thus accounts for effects that modify

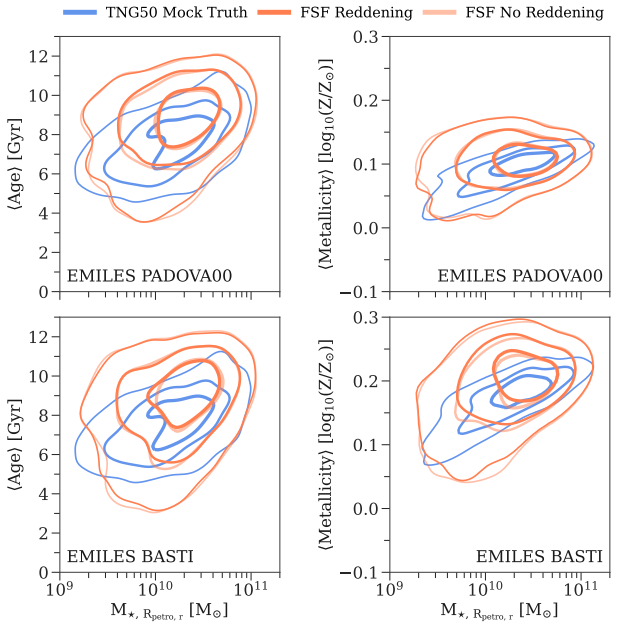

Figure 9.6. Recovery of average mass-weighted ages and metallicities from TNG50 mock spectra via unregularized full spectral fitting (FSF). Gaussian kernel density estimates of average age (*left column*) and metallicity (*right column*) as a function of galaxy stellar mass (inside the Petrosian radius measured in the SDSS r-band) known from TNG50 (*blue*) and recovered via *unregularized* FSF of reddened (*dark orange*) and unreddened (*light orange*) integrated mock spectra. The "mock truth" refers to ages and metallicites that were assigned to stellar particles via the SSP models. The contours encompass 20%, 50% and 80% of all galaxies (*from thickest to thinnest lines*). The same SSP models were used in mocking *and* fitting the integrated spectra, which are shown separately for the PADOVA00 (*top row*) and BaSTI (*bottom row*) isochrones. The derived stellar population properties from FSF are unaffected by reddening.

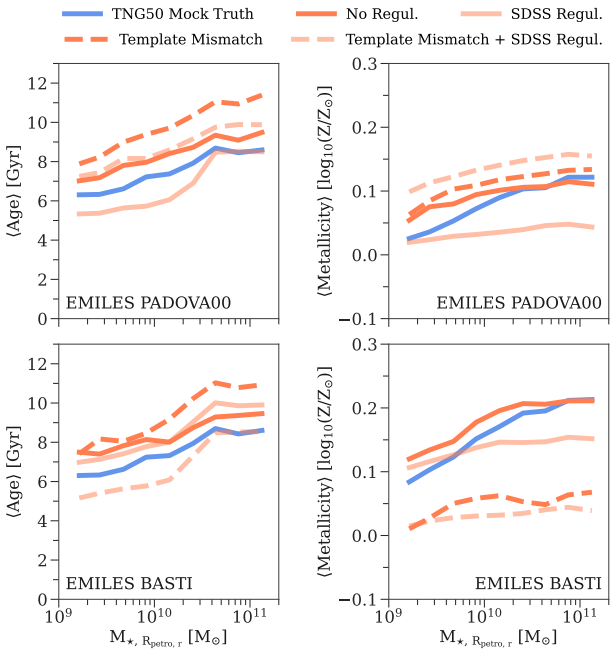

Figure 9.7. Effects of template mismatch and regularization on the recovery of the mass-age and mass-metallicity relation from full spectral fitting (FSF) of integrated mock spectra from TNG50 galaxies. Running medians of average age (*left column*) and metallicity (*right column*) as a function of galaxy stellar mass (inside the Petrosian radius measured in the SDSS r-band) known from TNG50 (*blue*) and recovered via FSF (*orange*). The integrated mock spectra were each constructed with the PADOVA00 (*top row*) and BaSTI (*bottom row*) isochrones respectively. Solid lines show the results for fits performed with the same SSP models as used in the construction of the mock spectra, whereas dashed lines used the mismatched isochrone set. All results are also shown for the unregularized (*dark orange*) and regularized (*light orange*) solution. The regularization parameter was calibrated in the same way as for SDSS galaxies. The "mock truth" refers to ages and metallicites that were assigned to stellar particles via the SSP models.

the continuum shape. We have checked that the regularized solutions are also unaffected by reddening. All subsequently shown results always use the reddened mock spectra.

Template mismatch & regularization (Figure 9.7): As shown in Section 9.4.1.2 (see also Appendix C.2), regularization affects the recovered age and metallicity relations. Overall, it reduces the scatter at fixed galaxy mass. On top of that, the normalization of the mass-age relation becomes shifted towards younger ages of around 2 Gyr and up to 3 Gyr at the high mass end. The mass-metallicity relation also shifts towards lower metallicities by approximately 0.1 dex. Even though these shifts are well within typical observational errors, it would be favourable to understand the exact effects of regularization on the recovered stellar population properties; especially, because the regularization parameter for the fits to the SDSS data was applied "ad hoc"

and based on experience in using pPXF. The "proper" calibration as advocated by the documentation of pPXF is a) infeasible for a large number of spectra and b) unphysically over-smoothed for the typical signal-to-noise regime of the SDSS spectra. As we include realistic, SDSS-like noise in the mock spectra, a perhaps wishful thinking would be to calibrate the regularization parameter against the underlying truth from TNG50.

To explore this possibility, we compare in Figure 9.7 the recovered average ages and metallicities from FSF for the unregularized and regularized solution. The regularization parameter was set exactly as for the SDSS data. Indeed, the mass-metallicity relation from the mock data experiences a similar shift by about 0.1 dex towards lower metallicities (the scatter at fixed galaxy mass is also decreased; see Figure 9.8). However, the mass-age relation only shifts by 1 Gyr towards lower ages for galaxy masses $\lesssim 5 \times 10^{10}\,\mathrm{M}_\odot$ in case of the PADOVA00 isochrones, and there is essentially no shift for the BaSTI isochrones. Consequently, the behaviour of regularization is similar but not exactly the same as for the observations, which makes a calibration to TNG50 questionable, and hence it is difficult to assess, whether the adopted regularization parameter for the SDSS data is reasonable.

A reason for the different impact of regularization on the SDSS and TNG50 spectra is partially explained by the fact that the same SSP models are used in creating and fitting the mock spectra. Thus, the fit will be better constrained (and thus less affected by regularization) by construction even in the presence of realistic noise, as the true shape of the SSP models are embedded in the integrated spectrum. This is not the case for observations, as certain aspects of stellar evolution are unknown and effects of IMF and individual element abundance variations are not taken into account.

We try to explore this effect by fitting the mock spectra with the mismatched isochrone set, i.e. if the mock spectrum was constructed with the BaSTI models, we use the PADOVA00 isochrones for the fits and vice versa. Again the unregularized and regularized solution are shown in Figure 9.7 for direct comparison. Now, the shift of the mass-age relation caused by regularization is larger for the mock spectra, especially for the mock spectra based on the BaSTI models, but fitted with the PADOVA00 isochrones. The corresponding mass-metallicity is offset by 0.1 to 0.2 dex towards lower metallicities for both the unregularized *and* regularized solution, as the PADOVA00 isochrones do not reach the high metallicties of the BaSTI models. In the case of the mock spectra constructed with the PADOVA00 models but fitted with BaSTI isochrones, the regularized case produces a shit of around 1 Gyr towards lower ages. However, now the mass-metallicity shifts towards higher metallicities, as the BaSTI models allow for this.

In conclusion, the effect of regularization is not exactly trivial and needs a better treatment in the future, which will be discussed in Section 9.6.2.

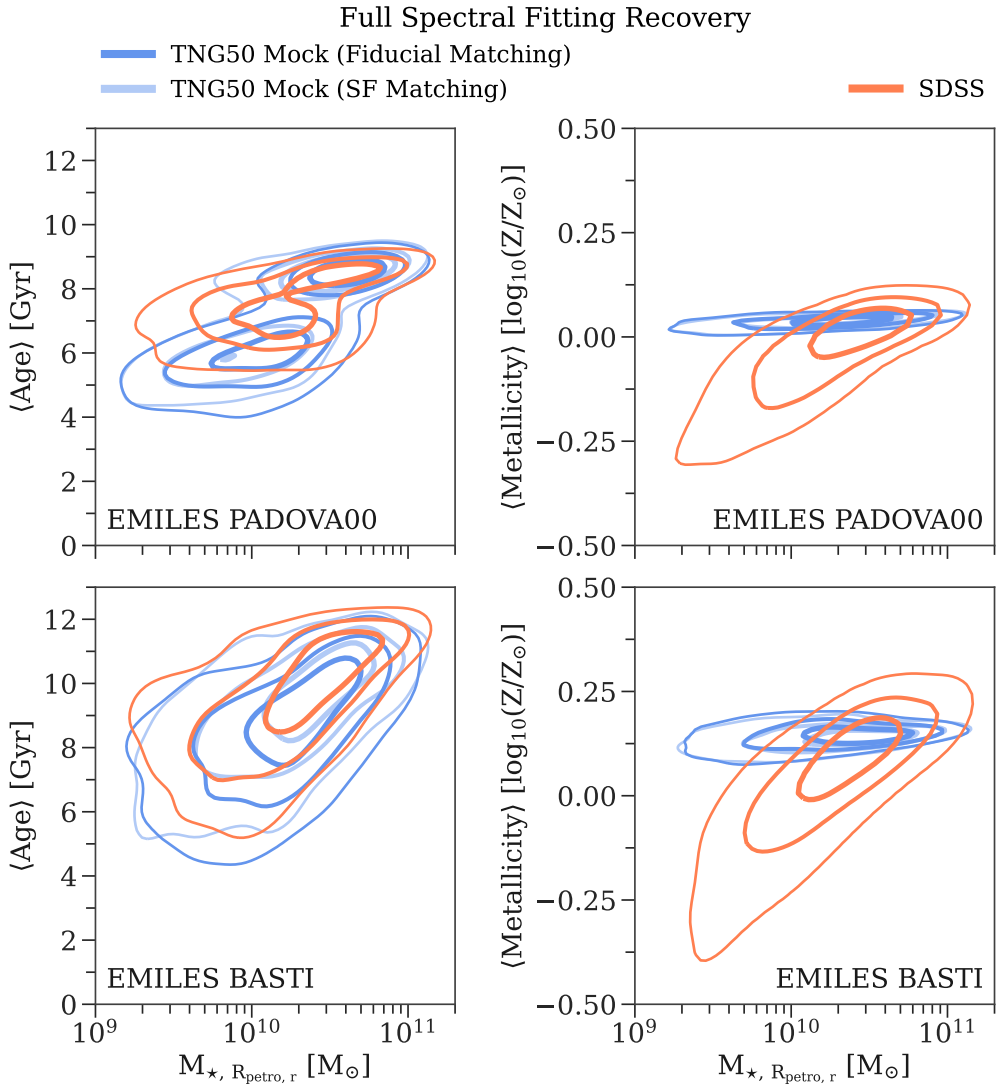

Figure 9.8. Mean (central, ~ 500 pc) ages and metallicities recovered via full spectral fitting (FSF) of integrated spectra from SDSS and TNG50 mocks. Gaussian kernel density estimates of average age (*left column*) and metallicity (*right column*) as a function of galaxy stellar mass (inside the Petrosian radius measured in the SDSS r-band) measured by applying FSF to SDSS observations (*orange*) and TNG50 mock integrated spectra (*blue*). An alternative matching procedure between TNG50 and SDSS galaxies is shown as well (*light blue*), where the galaxy samples are split according to their star formation status prior to matching. The contours encompass 20%, 50% and 80% of all galaxies (*from thickest to thinnest lines*). The same SSP models were used in mocking *and* fitting the integrated spectra of TNG50 galaxies, which are shown separately for the PADOVA00 (*top row*) and BaSTI (*bottom row*) isochrones. All shown solutions are *regularized*. The average ages are in agreement, whereas the mean metallicity observed in low mass galaxies is lower on average compared to TNG50 galaxies.

9.4.1.4 *Comparing results from SDSS and TNG50 mock spectra*

The "ultimate" comparison is displayed in Figure 9.8 showing the mean ages and metallicities derived from applying FSF to *both* SDSS observations and the mock integrated spectra of the sample matched TNG50 galaxies. Both use the same regularization "calibration" as described in Section 9.3.3.2. The distribution of mean ages across galaxy stellar mass is in excellent agreement between SDSS and TNG50. By applying our alternative matching criterion, where we split both galaxy samples according to their star formation status prior to matching

them (see Section 9.2.2), we can practically exactly mimic the derived mass-age distribution from TNG50 and SDSS using the SSP models based on the BaSTI isochrones. In case of the PADOVA00 isochrones, we do not achieve the same degree of agreement in the distribution of mean ages at the low mass galaxy end. SDSS galaxies are older compared to TNG50. However, this and the conspicuous bimodality in the mean age distribution are likely effects of the regularization. By comparing to Figure 9.6, we see that the underlying TNG50 age distribution (and the unregularized FSF solution) does not possess this bimodality. Hence, this is also likely the case for the SDSS galaxies. On top of that, this shows that the TNG50 FSF solution for the PADOVA00 isochrones is regularized too much at the low mass *with respect to* the SDSS sample (see also 9.7), while it happens to exactly match for the BaSTI isochrones. This is another indication that the degree of regularization has a different impact on observed and mock spectra, as well as the particular isochrone set that is adopted.

Despite the influence of the regularization on derived stellar population quantities, we argue that this effect alone cannot reconcile the differences between SDSS and TNG50 for the average metallicities. Especially for galaxies with masses below $10^{10}\,M_{\odot}$, the observed galaxy population has a lower average metallicity of about 0.25 dex. An even higher regularization would shift both TNG50 and SDSS results towards lower metallicites, and would produce unphysically smooth star formation histories, departing from the agreement in the mean age distributions. Nevertheless, the very flat distribution in Figure 9.8 for the mean metallicities from TNG50 is inherent to our modelling of both the mock spectra due to the SSP grid boundaries (see Figure 9.3) and the regularization in FSF recovery (see Figure 9.7). In fact, the intrinsic mean metallicities output by TNG50 (see Figure 9.4) do show a similar slope of the mass-metallicity relation compared to SDSS, but simply shifted towards higher metallicities. We discuss this further in Section 9.6.1.

9.4.2 Age-Metallicity Distributions

An important advantage of the FSF approach with pPXF compared to index measurements is that we can obtain the *distribution* of ages and metallicities from a *single* integrated spectrum (e.g. Boecker et al., 2020b). This provides us with detailed information about the overall mass assembly of a particular region of a galaxy. Perhaps the comparison of the age-metallicity distributions recovered from SDSS and TNG50 mock integrated spectra can give us some insight on the discrepancy in the mean metallicities.

9.4.2.1 *Recovery from TNG50 mock spectra*

In Figure 9.9 we show the ability of the FSF approach with pPXF in obtaining the underlying age-metallicity distribution of TNG50 galaxies that was used to create the mock spectra in the first place. Results

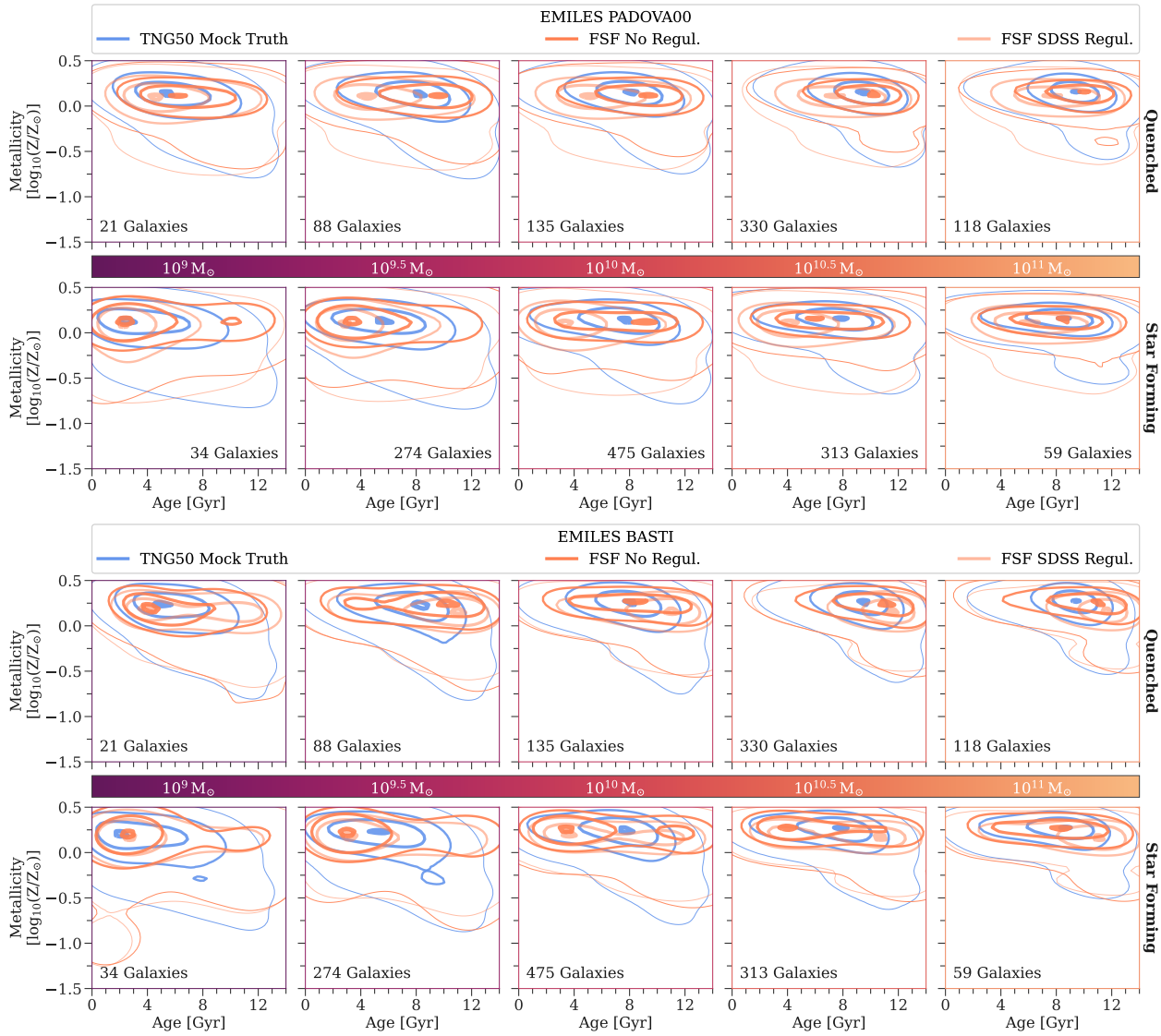

Figure 9.9. Recovery of age-metallicity distributions from the central 500 pc of TNG50 galaxies via SDSS-like mock spectra. Gaussian kernel density estimates of age-metallicity distributions encompassing 1%, 20%, 50% and 90% of all central stellar mass in stacks of galaxy stellar mass bins with a width of 0.5 dex are shown increasing from left to right as depicted by the colorbar. The panels above and below the colorbar show quenched and star forming galaxies separately. The distributions are shown for the ground truth known from TNG50 (*blue*) as well as the unregularized (*dark orange*) and regularized (*light orange*) solution that was recovered from fitting the SDSS-like mock spectra of the same TNG50 galaxies. Prior to stacking, the age-metallicity distribution of each galaxy is normalized. The "mock truth" refers to ages and metallicites that were assigned to stellar particles via the SSP models. The same SSP models were used in mocking *and* fitting the integrated spectra of TNG50 galaxies, which are shown separately for the PADOVA00 (*top row*) and BaSTI (*bottom row*) isochrones. In each panel, the number of galaxies in the corresponding stellar mass bin is indicated. Overall, the FSF approach is able to recover the underlying age-metallicity distribution reasonably well.

are shown in stacks of galaxy stellar mass in bins of 0.5 dex. Additionally, we split the *fiducial* matched TNG50 sample into star-forming and quenched (including green valley) galaxies according to (Pillepich et al., 2019).

Overall, the recovered age-metallicity distributions match well the underlying truth, especially at the low ($10^9\,M_\odot$) and high ($10^{11}\,M_\odot$) mass end respectively, where TNG50 galaxies are either young ($\lesssim 4$ Gyr) or old ($\gtrsim 8$ Gyr). In the intermediate mass range, it is harder to

recover the intermediate age distribution, especially for star-forming galaxies.

Here, the differing impact of regularization between the PADOVA00 and BaSTI isochrones becomes apparent. For example, the peak of the age distribution of star forming galaxies in the $10^{10}\,M_\odot$ bin is driven from around 8 Gyr for the unregularized solution, which is close to the ground truth, towards 4 Gyr for the regularized one in case of the PADOVA00 isochrones. On the contrary, for the BaSTI isochrones, both the unregularized and regularized solution predict the peak of the age distribution at around 4 Gyr. Above $10^{10}\,M_\odot$, regularization with the BaSTI isochrones drives the age distributions for quenched and star forming galaxies towards older ages, which has the opposite effect in case of the PADOVA00 isochrones.

The metallicity is not strongly influenced by this, at least when the metallicity is overall high. However, for star forming galaxies with stellar masses in the $10^{9.5}\,M_\odot$ bin and below, it is clear that FSF struggles to reproduce metallicities of the older stellar populations to sufficiently low values. This results in a overall flatter age-metallicity relation than originally input into the mock integrated spectra. It also looks like pPXF tries to compensate for this effect by recovering some mass weights at lower metallicities (< 0.5 dex), but instead at young ages (< 4 Gyr), as seen particularly in the lowest galaxy mass bin.

Despite these effects, the FSF approach still robustly recovers subdominant metal-poor populations at fixed old ages across the whole galaxy mass range of star forming and quenched galaxies, even if they do not reach the same low metallicities as the known truth in some cases. This is encouraging, as we know from Chapter 7 (Figure 7.9), that this is the regime, which is mostly dominated by ex-situ stars. We will exploit this fact in Section 9.5.

9.4.2.2 *Comparison to SDSS galaxies*

The results of the previous section give us confidence that age-metallicity distributions from single integrated spectra of the central ~ 500 pc mass range can be recovered reasonably well across a wide galaxy mass range. Thus, we now compare these results with the age-metallicity distributions obtained from the real SDSS observations in Figure 9.10. We only show the regularized solution for both SDSS and TNG50. The comparison between SDSS and TNG50 is done with our alternative matching procedure, where the galaxy samples are split according to their star forming status prior to matching them (see Figure 9.2). Green valley galaxies are included in the panels for quenched galaxies in Figure 9.10.

The age-metallicity distributions for quenched galaxies from SDSS and TNG50 in the $10^{10}\,M_\odot$ mass bin and above are in excellent agreement with each other for both sets of isochrones. For the $10^{10}\,M_\odot$ mass bin in particular we see that the FSF recovery of SDSS and TNG50 spectra follow the same bias, which manifests in a peak of the age distribution at 12 Gyr for the BaSTI and 4 Gyr for the PADOVA00 isochrones. As the underlying truth of TNG50 galaxies (see Figure 9.10) tells us that the peak actually lies around 8 Gyr, we could conclude that the true

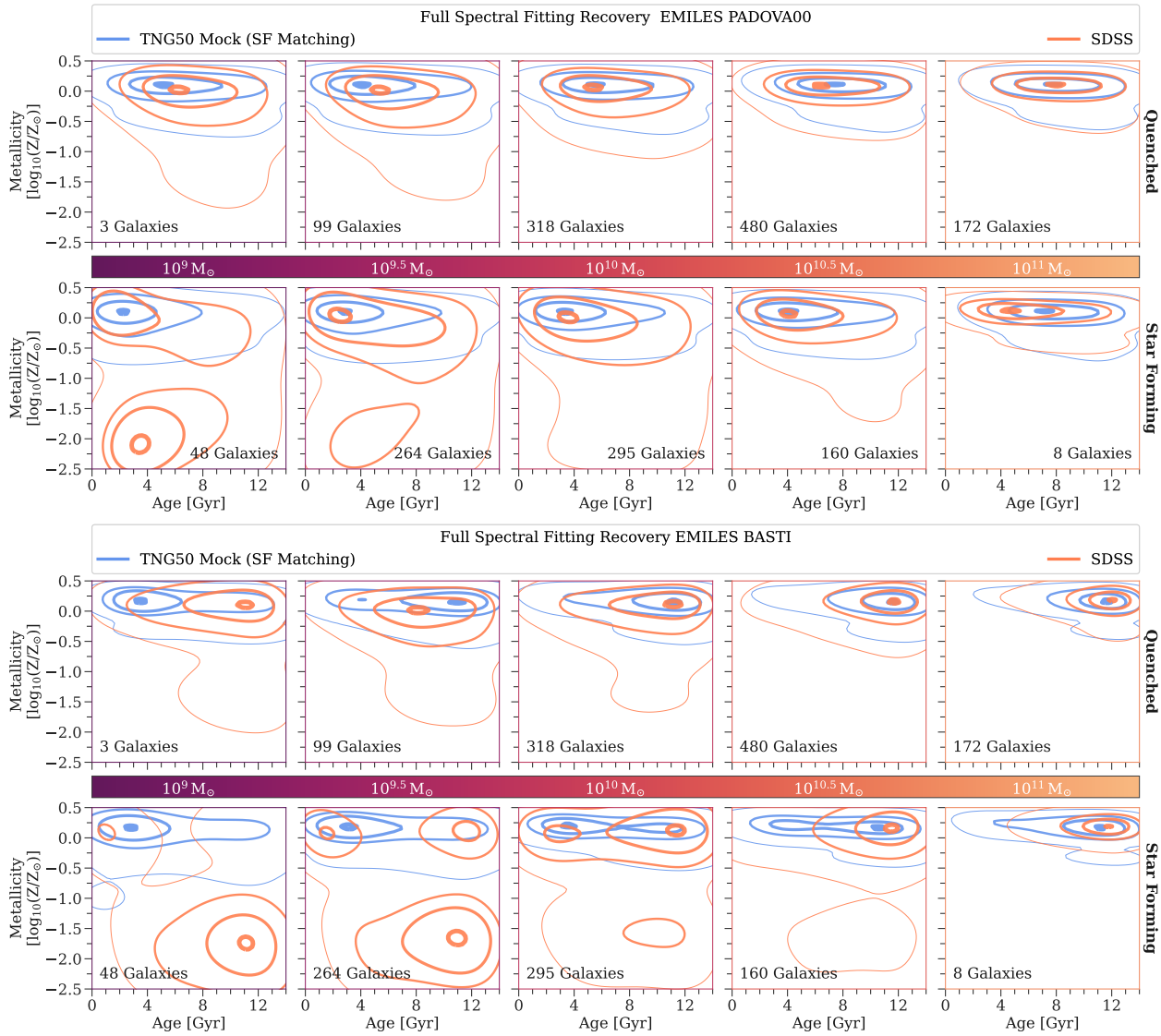

Figure 9.10. Age-metallicity distributions in the central ~ 500 pc derived via full spectral fitting (FSF) of integrated spectra from SDSS and TNG50 mocks. Gaussian kernel density estimates of age-metallicity distributions encompassing 1%, 20%, 50% and 90% of all central stellar mass in stacks of galaxy stellar mass bins with a width of 0.5 dex are shown increasing from left to right as depicted by the colorbar. The panels above and below the colorbar show quenched and star forming galaxies separately. The distributions show the *regularized* solution from FSF of TNG50 mock integrated spectra (*blue*) and SDSS observations (*orange*). The top and bottom panels show results using the PADOVA00 and BaSTI isochrones respectively. Prior to stacking, the age-metallicity distribution of each galaxy is normalized. TNG50 galaxies are matched to SDSS galaxies by splitting the galaxy samples first according to their star formation status. In each panel, the number of galaxies in the corresponding stellar mass bin is indicated.

age distribution of SDSS galaxies in that mass regime is also centered on such an intermediate age. For quenched galaxies in the 10^9 $M_\odot$ bin the distribution of SDSS galaxies deviates strongly from TNG50 for the BaSTI isochrones, while they still match well for PADOVA00 isochrones. This shows that the deviation cannot be caused by the low number statistics in that particular mass bin. Furthermore, the underlying true age distribution of TNG50 galaxies indeed peaks around 4 Gyr, which is both recovered for PADOVA00 and BaSTI isochrones (see Figure 9.9). Hence, we are indeed probing something in the SDSS spectra that causes the two isochrones to behave differently, which is not the case for the

higher mass quenched galaxies. We discuss such possibilities in Section 9.6.3.

For star forming galaxies, the picture becomes more complex, and it is now apparent that they are responsible for driving the majority of the differences in the mass-metallicity relation between SDSS and TNG50. While the age-metallicity distribution of the high mass end still matches reasonably well between SDSS and TNG50, SDSS galaxies require an increasingly more dominant metal-poor (< -1.5 dex) population for galaxies below $10^{10}\,M_\odot$. This metal-poor component is young (4 Gyr) and old (12 Gyr) for PADOVA00 and BaSTI isochrones respectively. In case of the *unregularized* solution for the PADOVA00 isochrones, we see actually that this metal-poor component is old and at more intermediate metallicities (~ -1 dex, see Figure C.3), and then becomes younger for the regularized solution. This could perhaps be an indication that it is difficult for pPXF to recover metallicities in the middle of the grid, similarly to the age distribution for galaxies $10^{10}\,M_\odot$. Another possibility could be that emission lines are interfering with the age-metallicity recovery, which we do not model with TNG50. However, this would in principle also affect the higher mass galaxies.

Generally, the two lowest mass bins of star forming SDSS galaxies are really a mix of many different star formation and chemical enrichment histories, and thus we need to look at them on a galaxy-by-galaxy basis to really understand what is causing these differences with respect to TNG50. Still, we do see most of the time that an older, metal-poor *and* younger, metal-rich component is recovered simultaneously for individual galaxies. Thus, the bimodality of the metallicity distribution in the lowest mass bins of star forming galaxies is not entirely driven by mixing completely metal-poor with completely metal-rich galaxies.

9.5 ACCRETED FRACTIONS FROM THE CENTER OF GALAXIES ?

As seen in Chapter 7 (Figure 7.9), galaxies with a high ex-situ fraction in their centers are more metal-poor than the average galaxy in a similar mass range. In Boecker et al. (2020a, and as described in Chapter 8), we have demonstrated a new observational technique that uses age-metallicity distributions determined from FSF of integrated spectra to estimate the ex-situ fraction. The previous sections showed that we can indeed recover age-metallicity distributions from SDSS observations in reasonable agreement with TNG50 galaxies, especially in the case of quenched galaxies. We now combine all these results and apply the method of Boecker et al. (2020a) to SDSS observations aiming to determine an understanding of the accretion history of galaxies from their central 500 pc. All calculations are based exclusively on the *regularized* FSF results.

9.5.1 Checking the method with TNG50

Before we attempt to extract ex-situ fractions from SDSS galaxies, we test once more our accretion history method. In Boecker et al. (2020a) we tested the method on mock spectra made from EAGLE simulated galaxies. However, the set-up of the integrated mock spectra was much more idealized: a) the signal-to-noise ratio was 100, which is much higher than for our SDSS galaxy sample and b) the constructed spectra included all stellar particles in a 100 kpc aperture, which is impossible to achieve with real observations. Furthermore, the explored sample size was very small ($\sim$ 10), while here extend it to almost 2000 galaxies, and therefore including a greater variety of individual merger histories.

The 500 pc aperture that we are now probing with this work complicates the determination of the most massive accreted satellite galaxy, which we do not know a priori. In Boecker et al. (2020a), we established this stopping point, when the mass of the recovered age-metallicity distribution calculated underneath a given AMR exceeds the satellite galaxy mass to which the AMR belongs to, i.e.:

$$f_{\mathrm{exsitu}} \cdot M_{\star,\,\mathrm{tot}} \stackrel{!}{=} M_{\star,\,\mathrm{sat}}, \tag{9.9}$$

where f_{exsitu} is the ex-situ fraction, $M_{\star,\,\mathrm{tot}}$ the total stellar mass of the host galaxy and $M_{\star,\,\mathrm{sat}}$ the total stellar mass of the accreted satellite galaxy. This is reasonable, when we are probing the majority of the total galaxy's stellar mass. In case of the central 500 pc aperture, we do not know how much of the total mass of a given accreted satellite galaxy is actually contributing to the center that we are probing with the integrated spectrum. For now, we crudely approximate the mass of the most massive accreted satellite galaxy deposited in the central 500 pc compared to its total mass to be the same ratio as of the host galaxy's stellar mass inside the 500 pc to its total stellar mass. This yields again the exact same stopping point criterion used in Equation 9.9. If this criterion calculates the mass of the most massive accreted satellite ($M_{\star,\,\mathrm{max\,sat}}$) to be larger than half the host's total stellar mass, we enforce an earlier stopping point by substituting $M_{\star,\,\mathrm{tot}}$ with the stellar mass inside the 500 pc center[138]. By comparing to the underlying truth known from TNG50, we found that this method generally provides better estimates (or to be more precise upper limits) of the *total* ex-situ fraction, and not just the central one. This is still probably a consequence of how we define the stopping point, which needs to be investigated further.

For now we proceed and compare in Figure 9.11 the total ex-situ fraction and the stellar mass of the most massive accreted satellite galaxy inferred with our method from TNG50 mock spectra to the known truth. The true mass of the most massive accreted satellite galaxy that contributes stars to the central 500 pc of the $z = 0$ host, was calculated at the time, when the satellite reached its maximum stellar mass (see Rodriguez-Gomez et al., 2016). Results show TNG50 galaxies that were

138: The estimate of the central stellar mass in the SDSS fiber is calculated from our FSF results via Equation 5.2. The distance is calculated via the luminosity distance for the redshift of a given SDSS galaxy.

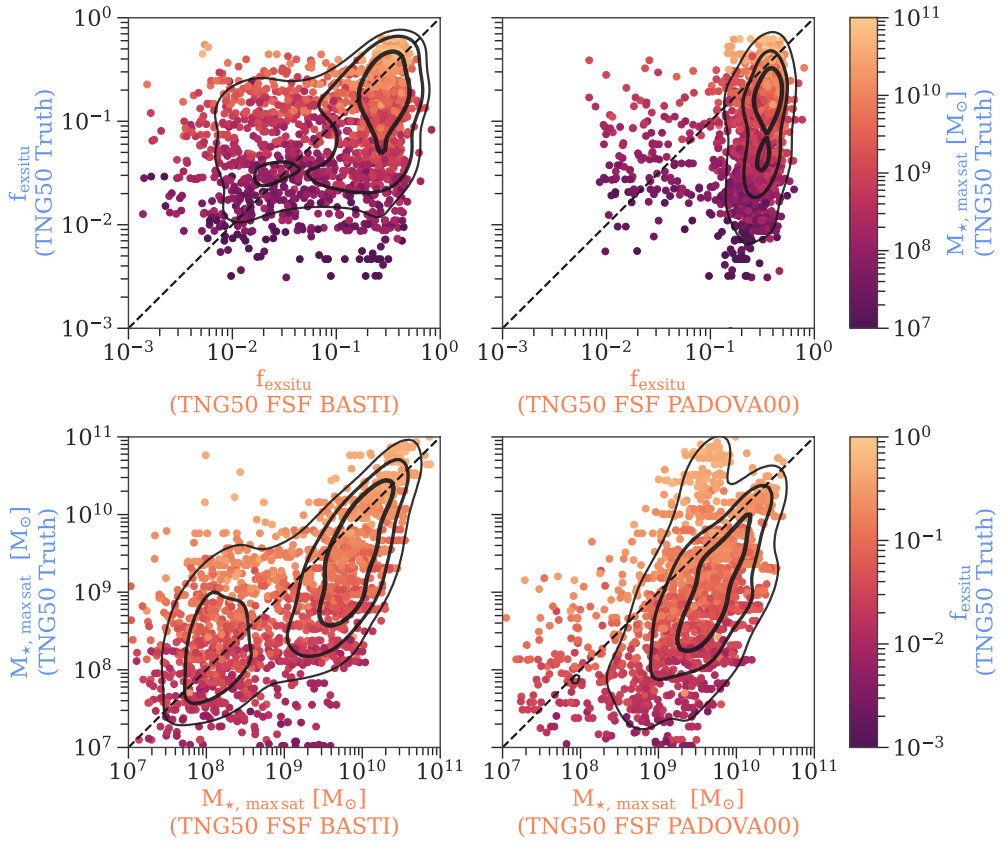

Figure 9.11. Information about the accretion history of TNG50 galaxies extracted from the central 500 pc. *Top row*: Comparison between the total ex-situ fraction (f_{exsitu}) known from TNG50 (*on the vertical axis in blue*) and the recovered values from full spectral fitting (FSF; *on the horizontal axis in orange*) SDSS-like mock spectra with the BaSTI (*left*) and PADVOVA00 (*right*) isochrones respectively. The points are color-coded according to the stellar mass of the most massive accreted satellite galaxy ($M_{\star,\,max\,sat}$) that contributes stars to the central 500 pc and is known from TNG50. The dashed line indicates the one-to-one relation. Contours show Gaussian kernel density estimates encompassing 20%, 50% and 80% of all data points (*from thickest to thinnest solid lines*). *Bottom row*: The same but now for the recovery of the mass of the most massive accreted satellite galaxy. The points are color-coded by the ex-situ fraction known from TNG50. Statistical variations per data point are on the order of $0.25 - 0.5$ dex for both derived quantities. Overall, the ex-situ fractions are overestimated for the majority of galaxies, reflected in a too high $M_{\star,\,max\,sat}$, especially towards the low mass end.

matched to the SDSS sample via our alternative matching procedure, where the samples are split according to their state of star formation.

Evidently, the ex-situ fraction inferred with our method is overestimated for the majority of galaxies, whereas the mass of the most massive accreted galaxy seems to be closer to the one-to-one relation. Still there is a clear trend that $M_{\star,\,max\,sat}$ is overestimated, especially for masses $\lesssim 5 \times 10^9\,M_\odot$. The Monte Carlo simulation of our AMR templates yields variations of roughly $0.25 - 0.5$ dex for both derived quantities.

The recovery using the BaSTI isochrone performs overall better as it is able to correctly estimate some low mass accretion events ($M_{\star,\,max\,sat} < 10^9\,M_\odot$). Results with the PADOVA00 isochrones mostly fail to do so, and they underestimate $M_{\star,\,max\,sat}$ for the highest mass end. A reason for the latter is likely that the mock spectra constructed and fitted with the PADOVA00 isochrones limit the highest metallicity, which is achievable with the SSP models, even more severely than the BaSTI isochrones.

As accreted galaxies at the high mass end are of nearly the same metallicity as the host (see also Figure 7.9), the PADOVA00 isochrones wash out these little differences even more. Thus, the mock spectrum and also our accretion history method looses the information and leverage to separate these high mass merger events.

The overall overestimation of the ex-situ fraction for $M_{\star,\,\mathrm{max\,sat}} \lesssim 5 \times 10^9\,M_\odot$ for both isochrones, likely stems from the fact that our AMRs are based on measurements of Local Group galaxies and are calibrated to reproduce the observed mass-metallicity relation (Gallazzi et al., 2005; Kirby et al., 2013). However, because TNG50 galaxies with galaxy stellar masses of $\lesssim 10^{10}\,M_\odot$ are more metal-rich than observed galaxies (see Figure 9.8 and also Nelson et al., 2018, Figure 2), the stopping point of our method will automatically be associated to a higher mass accreted satellite galaxy (as they are more metal-rich). We tried to accommodate for this effect by re-calibrating our AMRs to TNG50 galaxies, however we found that it is not trivial to achieve a better agreement for lower $M_{\star,\,\mathrm{max\,sat}}$, while preserving the already good agreement at the very high mass end. We need to investigate this further, but for now we keep the original calibration of Boecker et al. (2020a), which will also make the comparison with SDSS observations in the subsequent section more straightforward.

9.5.2 Application to SDSS

We extract the the ex-situ fraction and mass of the most massive accreted satellite galaxy from the FSF results of our SDSS sample with the exact same procedure applied to the TNG50 mock spectra. However, we restrict our sample to quenched and green valley galaxies (i.e. just referred to as quenched galaxies as in Figure 9.10). The reason for this is that the young metal-poor components seen in SDSS galaxies, especially at the low mass end, would be counted as of ex-situ origin in our method. Our method is not yet able to account for possible metal-poor in-situ components that could be caused by, for example, line-of-sight overlap with the more metal-poor outer disk. Furthermore, it is not yet clear what causes the discrepancy between SDSS and TNG50 in this regime as well as the disagreement in the age of the metal-poor population between the two isochrone sets. We discuss all of this in more detail in Section 9.6.

Figure 9.12 shows our results including the genuine ex-situ fractions predicted by TNG50. Perhaps reassuringly, we see that the SDSS galaxies produce very similar trends as their TNG50 counterparts for the BaSTI and PADOVA00 isochrones respectively. In particular for the BaSTI isochrones, the variation of the extracted ex-situ fractions at fixed stellar mass is now larger for SDSS galaxies as compared to TNG50, which we attribute to the calibration of our AMR templates, as previously discussed. However, this is not seen for the PADOVA00 isochrones, which yield an equally narrow range of accreted fractions as the TNG50 mocks. This could be related to the available ages for PADOVA00 isochrones, which result in a coarser age sampling at old ages compared to the

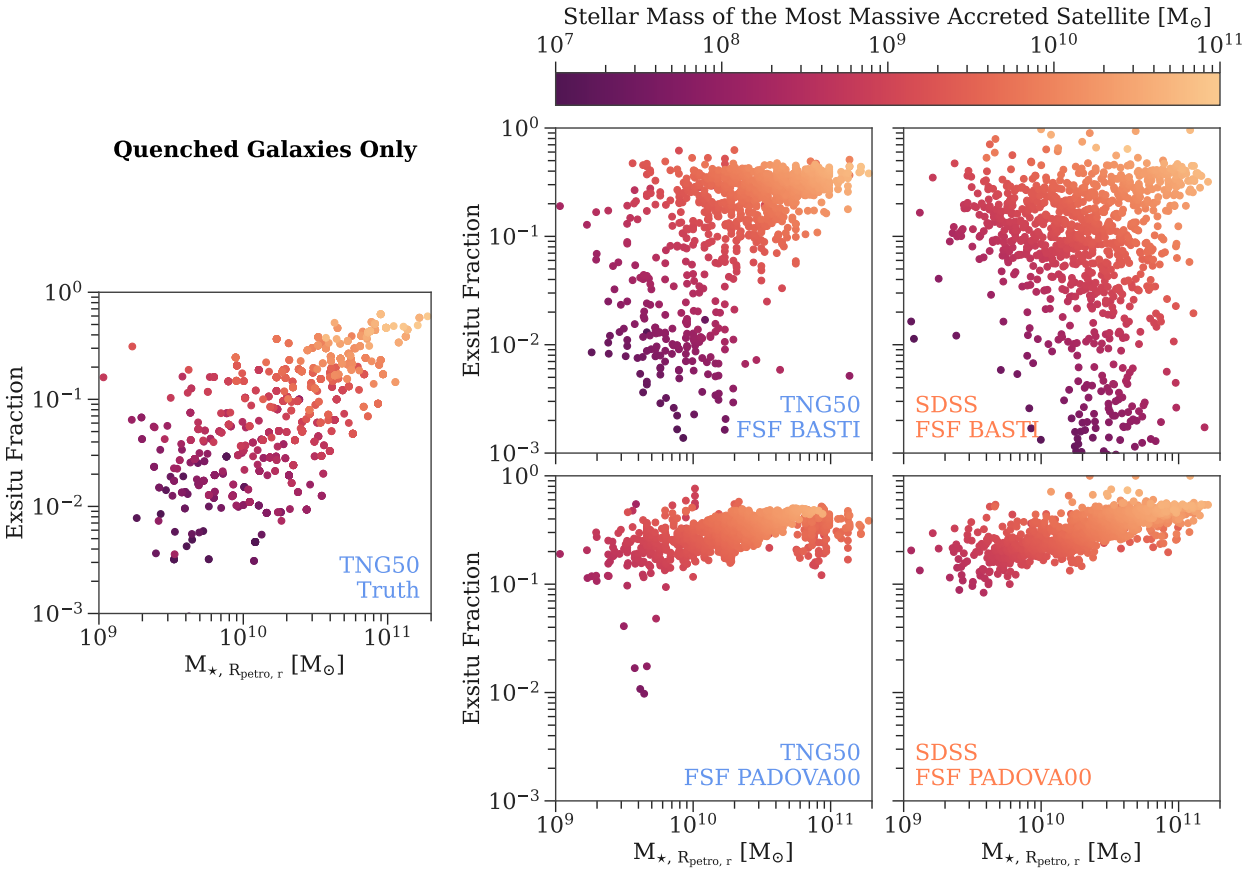

Figure 9.12. Comparison of ex-situ fractions and masses of the most massive accreted satellite galaxy extracted from full spectral fitting (FSF) in the central 500 pc between SDSS and TNG50 quenched galaxies. *Left panel*: Ex-situ fractions as a function of galaxy stellar mass (inside the Petrosian r-band radius) of TNG50 galaxies at $z = 0$ color-coded by the stellar mass of the most massive accreted satellite galaxy. These are the genuine quantities predicted by TNG50. *Right panel*: Comparison between the same quantities, but now shown for the derivation from integrated spectra of TNG50 mocks (*left column*) and SDSS observations (*right column*) fitting with BaSTI (*top row*) and PADOVA00 (*bottom row*) isochrones respectively. *Both* the ex-situ fraction and the mass of the most massive accreted satellite galaxy are quantified from the FSF results. Our method applied to TNG50 and SDSS alike shows similar trends indicating that we are probing information content about a galaxy's accretion history present in the central integrated spectrum.

BaSTI isochrones. As a consequence, this could result in a sharp increase of the calculated ex-situ fraction, when the discretized weights are assigned to a certain accreted satellite galaxy mass based on the AMR.

In case of the BaSTI isochrones, the trend and scatter of ex-situ fractions from SDSS look qualitatively similar to the genuine ex-situ fractions predicted by TNG50, which makes us confident that these trends arise not purely due to the construction of our method, but genuinely probe information content about a galaxy's assembly history.

9.6 DISCUSSION AND OUTLOOK

We discuss some of the conclusions drawn from our results and the future investigations we plan with regards to stellar populations extracted from observations and predicted by simulations. We comment

on the feasibility of observationally quantifying merger events from integrated spectra alone.

9.6.1 Are TNG50 galaxies too metal-rich or observations too metal-poor?

We extracted stellar population properties via full spectral fitting of realistic SDSS-like mock spectra from a matched sample of TNG50 galaxies, thus taking into account multiple observational effects. Even then, TNG50 galaxies below $\sim 10^{10}\,M_\odot$ are more metal-rich in their centers by $0.25-0.5$ dex than their SDSS counterparts, which we fitted with the exact same method (see Figure 9.8). We have identified that this discrepancy mainly arises in star forming galaxies (see Figure 9.10), which could point towards simulations not being able to capture certain aspects of star formation. Especially at the low mass end, galaxies should have a low efficiency in making stars, resulting in a slow chemical enrichment, which could be easily affected by the particular prescription of stellar feedback used in the simulation as well as the resolution (e.g. Hopkins et al., 2013b; Smith et al., 2018). Vice versa, observed lower mass galaxies have typically lower signal-to-noise, and star forming galaxies will have emission lines present on top of that, which could bias the observed metallicities as well.

The ages and metallicities of quenched galaxies from TNG50 and SDSS are in excellent in agreement with each other, at least within the limitations of the SSP models that are used to construct and fit the (mock) integrated spectra. The maximum metallicity of $0.2-0.4$ dex of currently available SSP models prevents us from modelling the true metallicity distribution present in the TNG50 simulation, as many stellar particles reach higher metallicities than this. Thus, any metallicity recovered with observational techniques from mock spectra will have lower metallicities than the genuine output from the simulation *by construction*, and *not* necessarily due to the biases introduced by the observational method. This is partially an explanation, for the offset reported by Nelson et al. (2018), who compared luminosity weighted, but *intrinsic* metallicities from TNG100 with metallicities recovered from SDSS mock spectra in a mass regime of $10^{8-10.5}\,M_\odot$[139]. In particular for galaxies $> 10^{10}\,M_\odot$ the reported offset is constant and on the order of 0.2 dex, which is exactly the offset between the intrinsic TNG50 metallicities and the ones assigned through the PADOVA00 isochrones (see Figure 9.3), which were also used in Nelson et al. (2018). The offset between instrinsic and recovered TNG50 metallicities in Nelson et al. (2018) is larger by around 0.5 dex for galaxies $< 10^{9}\,M_\odot$, which indeed hints at a bias due to the observational modelling technique, as the SSP models sufficiently represent the underlying true metallicities of TNG50 in this regime (see Figure 9.3). A reason could be that the technique used in Nelson et al. (2018) also assumes a constant metallicity over time, similarly to Gallazzi et al. (2021). In Figure 9.4 we see the same offset of 0.5 dex at $10^{9}\,M_\odot$ for the PADOVA00 isochrones between our FSF approach, which allows for different metallicities at different

139: Note that metallicities were averaged over a 4 kpc aperture in Nelson et al. (2018), thus the absolute metallicitites are slightly lower than reported here, due to negative metallicity gradient present in galaxies.

ages, and the metallicities from Gallazzi et al. (2021). To provide a definite answer, we plan to apply the approach of Gallazzi et al. (2021) to our mock spectra, which is already planned.

On one hand, due to the boundaries of the SSP models, we also would not be able to tell, if observed galaxies are in reality more metal-rich. This could be the case at least for the high mass end, as SSP models based on empirical spectra are limited by the highest metallicity stars produced by the Milky Way. On the other hand, metallicity measurements of *individual* stars in Local Group dwarfs clearly show lower metallicites (McConnachie et al., 2005; McConnachie, 2012; Kirby et al., 2013; Leaman et al., 2013)[140]. Some zoom-in simulations (e.g. Buck et al., 2021; Grand et al., 2021) can indeed reproduce these low metallicities for dwarf galaxies ($< 10^9\,M_\odot$). So a promising avenue to understand the true discrepancy between simulations and observations could be to perform zoom-in simulation with the TNG model and apply the same observational techniques presented here.

140: But then again those averages are not necessarily directly comparable to averages from integrated spectra. Especially since they measure [Fe/H] and not the total metallicity as probed here.

All in all, we need to investigate the observed and simulated mass-metallicity relation in more detail, as discrepancies between the two are impacted by different effects influencing the metallicity in different ways across the mass range of the galaxy population. In particular, we need to check two assumptions made so far in our matching of SDSS and TNG50 galaxies. Firstly, we used the $z = 0$ snapshot for TNG50 galaxies, whereas the SDSS are at $0.01 < z < 0.02$. Thus, the TNG50 galaxies are ~ 200 Myr more evolved than their SDSS counterparts. This will influence the stellar populations properties, especially if the galaxy is actively forming stars. Even though TNG50 has snapshots available at $z \approx 0.01$ and $z \approx 0.02$, we used the $z = 0$ snapshot, because the post-processed radiative transfer images are only available at $z = 0$ and $z = 0.05$. To investigate the relative impact of this assumption, we plan to match the SDSS galaxies to the $z = 0.05$ snapshot with the available SKIRT images. Secondly, we did not extract the stellar population quantities of TNG50 galaxies from the exact same aperture as the SDSS galaxies. We used a fixed 500 pc aperture for TNG50, whereas the one for SDSS varies between $\sim 0.3 - 0.6$ kpc. This was to avoid expensive remaking of the TNG50 mock spectra, when considering different matching criteria. Even though we do not expect significant change of stellar populations in such a small radial extent, we will explicitly test this.

9.6.2 Stellar population properties from indices or full spectral fitting?

From Section 9.4.1.2 we have seen that light-weighted ages and metallicities derived from our FSF approach and taken from Gallazzi et al. (2021) are not the same (focussing on the PADOVA00 isochrones). This difference arises because of the different assumptions on star formation and chemical enrichment histories as well as the different parts of the spectrum that were used to extract this information. In case of the FSF approach, we have extensively tested the variations and biases

introduced by different SSP models and wavelength coverage as well as the modelling technique itself, by comparison to the underlying truth known from TNG50 (see Section 9.4.1.3). We now need to repeat this analysis for the approach used by Gallazzi et al. (2021) to understand the exact trends and differences between the two methods. Once these biases are also understood, we can more accurately interpret observations with respect to physical processes that drive the scaling relations of average stellar population properties.

Furthermore, it will also be important to compare average stellar population properties of individual galaxies derived with the two approaches. Can we achieve consistent placements of galaxies on the scaling relations measured with the technique of Gallazzi et al. (2021) and the FSF approach? For example, are galaxies, that are more metal-poor than the average galaxy at fixed mass for one approach, in the same regime with the other method? Our initial tests show that this is not necessarily the case, which would imply an even more complex mapping between different observational techniques than just constant bulk offsets.

Still, measurements based on absorption indices will likely not be able to accommodate for a more complex model of a galaxy's star formation and chemical enrichment history, as only a few data points are used to constrain this model. While it is not per se a disadvantage to focus on specific places in the integrated spectrum, traditional index measurements average the flux over a narrow passband. This means that the information encoded in the specific shape of the spectral line is lost, which makes it also prone to artifacts caused by, for example, an inaccurate subtraction of emission lines. An alternative hybrid approach is to fit every spectral pixel in the passband of traditional indices, as done in Martín-Navarro et al. (2019, 2021b).

On the other hand, the flexibility of pPXF and the usual degeneracies of stellar population parameters make it sometimes hard to gauge, whether the recovered age-metallicity distribution is reliable. Thus, more studies that compare resolved and integrated light would be beneficial to understand this (e.g. Ruiz-Lara et al., 2015; Boecker et al., 2020b). On top of that, the calibration of the regularization parameter in pPXF often appears to be rather obscure, i.e. it is not behaving in the same way for different isochrones, neither for the recovery of observed nor mock spectra. In fact, the implementation of the regularization itself is not necessarily physically meaningful. A given weight associated with an age and metallicity is smoothed out in a manner that is not physically motivated by our understanding of galactic chemical enrichment. Some prior information could help with this and perhaps circumvent the calibration of the regularization parameter. Furthermore, a fully Bayesian treatment would allow for a (better) derivation of associated errors (e.g. Johnson et al., 2021). At the moment pPXF does not output errors for the derived age-metallicity distribution, which have to be estimated with Monte Carlo simulations (see e.g. Boecker et al., 2020b).

In conclusion, it is now timely to test observational methods that derive stellar population parameters with cosmological hydrodynami-

cal simulations in order to understand biases and continue to improve the existing methods. For example, we plan to incorporate tests of the recovery of [α/Fe] from TNG50 mock spectra in the future.

9.6.3 Does it matter which SSP models we use?

Usually, we would advocate that it does not matter which SSP models are used to measure stellar population parameters. As long as the same models are used throughout a sample or across different ones, the uncertainties associated with unknowns in stellar evolutionary synthesis will be same. Thus, physical interpretations about the formation and evolution of a certain stellar system can be made differentially. However, this assumption starts to crumble, when we then apply other techniques that use these measured ages and metallicities as an input to derive other quantities all together. This is especially the case when those methods rely on the joint combination of ages and metallicities and are calibrated on other relations that were derived with different SSP models. We partially see this effect for our accretion history method, as the derived ex-situ fractions behave quite differently for the BaSTI and PADOVA00 isochrones (see Figure 9.12). To be perfectly self-consistent we would need to construct different AMRs for the two isochrone sets.

The differences between the BaSTI and PADOVA00 isochrones mainly arise in age, especially for lower mass galaxies ($< 10^{10}\,M_\odot$), where an inversion of the mass-age relation becomes apparent for the BaSTI isochrones (using the E-MILES models, see Figures 9.4 and 9.10). Thus, BaSTI isochrones have to have a bluer turn-off point than the PADOVA00 isochrones at the same age, to fit the observed SDSS spectra equally well with older ages compared to the PADOVA00 ones. The (E-)MILES models (Vazdekis et al., 2015, 2016) use the non-canonical variation of BaSTI isochrones, which include convective overshooting as opposed to the canonical version. The particular treatment of overshooting is different from the one adopted for the PADOVA00 isochrones, which causes a 2 Gyr PADOVA00 isochrone to appear like a 3 Gyr old BaSTI isochrone (see Gallart et al., 2008, Figure 1). The differences disappear for genuinely old stellar populations. This could explain the different behaviour for the ages between the two isochrone sets (see also Gallart et al., 2005).

Hence, it is perhaps advisable to extract stellar population properties with at least two different sets of SSP models, if the knowledge of the absolute age and metallicity is required.

9.6.4 Towards observationally quantifying galaxy accretion histories from their centers

Just recently, we undoubtedly understood that the Milky Way underwent an ancient merger (Helmi et al., 2018; Belokurov et al., 2018). These merger events are a key prediction of our current standard

cosmological model. Thus, it is essential to build statistical samples of quantifying past merger events to constrain the ΛCDM model together with the formation of galaxies. Much of our current understanding about accretion events stems from the faint stellar halo of galaxies, traced through individually resolved stars of a few nearby systems (Bell et al., 2008; McConnachie et al., 2009; Carollo et al., 2010; Courteau et al., 2011; Radburn-Smith et al., 2011; Ibata et al., 2014; Monachesi et al., 2016; Crnojević et al., 2016; Iorio et al., 2018; D'Souza & Bell, 2018a), other deep photometric studies of integrated light (Martínez-Delgado et al., 2010; Merritt et al., 2016; Iodice et al., 2016; Huang et al., 2016b; Spavone et al., 2017; Huang et al., 2018; Hood et al., 2018; Spavone et al., 2020) or globular clusters (Tonini, 2013; Leaman et al., 2013; Kruijssen et al., 2018; Beasley et al., 2018; Hughes et al., 2018; Mackey et al., 2019).

Encouraged by results from simulations (see Chapter 7 and also Pillepich et al., 2018b; Zhu et al., 2022b), predicting the presence of substantial accreted material also in the center of galaxies, we demonstrated a first attempt of extracting information about a galaxy's merger history from its central 500 pc. The radius of this extent is 200 times smaller than what is typically probed with stellar halos (see also Davison et al., 2021; Martig et al., 2021; Zhu et al., 2022a, that probe merger events on kpc scales with IFU observations).

The method of Boecker et al. (2020a) applied to realistic SDSS-like mock spectra of TNG50 galaxies shows that this is indeed possible. Even though the accreted fractions for the majority of TNG50 galaxies are overestimated, as the method provides a hard upper limit, there seems to be at least some decent constraint on the mass of the most massive accreted satellite galaxy in the center. The AMR templates are constructed from empirical findings, which explains partially the overprediction of the ex-situ fraction, as TNG50 galaxies are more metal-rich than observations. In that sense, it may be even surprising that this works at all, given that this method is not informed by simulations in any way. Perhaps even more support is gained from the application to actual SDSS observations, in which we recover nearly similar trends compared to the TNG50 mocks. The similar scatter in the derived ex-situ fraction at fixed galaxy mass from SDSS and TNG50 (for the BaSTI isochrones) is perhaps hard to reconcile, if these results were purely due to the construction of the method.

Naturally however, we plan to invest more time into making the method more sophisticated and robust. The differences in the derived ex-situ fractions for the two sets of isochrones calls for the calibration of the AMR templates specifically for each isochrone due to differences in the age and metallicity grid. More importantly, we need to address actual astrophysical effects. Those are the overlap of in-situ and ex-situ stars, especially at the old ages, where in-situ stars can be equally metal-poor (see Figure 7.9). Furthermore, galaxies display a metallicity gradient (Zhuang et al., 2019) due to lower star formation efficiency in the outskirts. This is unlikely a major concern for the central 500 pc, but could cause line-of-sight overlap with the more metal-poor outskirts, especially if the galaxy is star forming and viewed edge-on. A

first extension of our model that takes into account the contamination due to in-situ stellar population gradients was explored by Davison et al. (2021), who found only a slight dependence, although this was only applied to early-type galaxies. Still, it shows that it is feasible to consider this effect, as metallicity gradients are after all a manifestation of a local mass-metallicity relation (Zhuang et al., 2019). Another possible source for concern, in particular for the central 500 pc, are star-forming nuclear rings, which are found to be very young and metal-poor (Bittner et al., 2020). As barred galaxies in particular show this feature, a comparison between barred and unbarred galaxies with respect to their derived stellar population properties and accretion fractions could help gain insight into this effect.

To conclude, we showed that extracting accretion histories from integrated spectra focused on the center of galaxies has great potential, which was only possible by comparing and testing our method with realistic, SDSS-like mock spectra of galaxies from the TNG50 simulation. We plan to extend the TNG mock spectra to the full SDSS sample to test and refine our method. The majority of galaxies observed with SDSS have a redshift of $z = 0.1$, which translates to an aperture of 2 kpc in radius that is covered by the fiber. This should allow for a larger contribution of ex-situ stars as well as the possibility to use the bigger TNG volume, TNG100, in order to sample even more unique merger histories and galaxy characteristics. After taking into account the aforementioned improvements and the continued exploration of and cross-checking with simulations, we could in principle apply this to readily available, good quality integrated spectra, of which we have 60000 from SDSS alone (Gallazzi et al., 2021), a sample size that will hardly be achievable for stellar halos.

9.7 SUMMARY

The assembly histories of the central 500 pc of galaxies, as predicted by the cosmological, hydrodynamical simulation TNG50, are diverse and closely connected to a galaxy's individual history of interactions with others (Boecker et al. submitted, see Chapter 7). Encouraged by the prospect that information about the hierarchical growth of structures is encoded in the brightest region of galaxies, we make a first comparison to observations of nearby ($0.01 < z < 0.02$) galaxies from SDSS covering stellar masses between 10^9 and $10^{11}\,M_\odot$.

To account for sample selection and projection effects, we find for each SDSS galaxy a TNG50 analogue at $z = 0$, that is matched in stellar mass, half-light radius and ellipticity measured in the SDSS r-band. The TNG50 measurements are extracted from mock images created with the radiative transfer code SKIRT with the inclusion of dust in order to mimic the actual SDSS measurements as closely as possible.

We then use full spectral fitting to extract information about the ages, metallicities and α-abundances of SDSS galaxies. Overall, the full spectral fitting approach generally suggests older ages across the galaxy mass range, higher metallicities for galaxies $< 10^{10}\,M_\odot$, a flatter [α/Fe]

relation and smaller galaxy-to-galaxy variation at fixed mass in comparison to results using absorption indices (Gallazzi et al., 2021). Those trends move towards a better agreement with intrinsic predictions from TNG50. By using single stellar population models with different isochrones and wavelength coverage for the full spectral fitting approach, we detect systematic changes mainly in the average ages, which hint towards biases introduced at the low mass end of the galaxy population in case of the index measurements (see Figures 9.4 and 9.5).

To ensure a comparison, as self-consistent as possible, between observations and simulation, we additionally construct mock integrated absorption spectra from stellar particles in the central 500 pc of TNG50 galaxies at $z = 0$. The mock spectra include galaxy specific dust attenuation caused by the gas column density along the line-of-sight and instrumental effects, such as SDSS-like spectral resolution and signal-to-noise. Applying the exact same full spectral fitting approach to the TNG50 mock spectra, reveals that the average age distributions across SDSS and TNG50 galaxies are in excellent agreement with each other, whereas a discrepancy between the average metallicities of around $0.25 - 0.5\,M_\odot$ for galaxies $< 10^{10}\,M_\odot$ persists (see Figure 9.8).

As the full spectral fitting method can recover *distributions* of ages and metallicities for individual galaxies, we confirm that low mass, star forming galaxies from SDSS indeed have metal-rich populations present in their spectra, which are however dominated by the simultaneous presence of very metal-poor (~ -2 dex) populations. A further investigation in this direction will help us understand the apparent discrepancy between observations and simulations (see Figure 9.10).

The age-metalliciy distributions of quenched galaxies extracted from SDSS and TNG50 spectra are in excellent agreement with each other, and show in fact the presence of old, metal-poor populations - a sign of past accretion events. We use the method developed in Boecker et al. (2020a) to quantify the fraction of accreted stars and the mass of the most massive accreted satellite galaxy from the central 500 pc alone. Initial results are promising and show that we can indeed obtain information on a galaxy's merger history from its center, but the method still needs further improvement (see Figure 9.12).

This study highlights the synergy and co-dependence of observations and simulations. Most importantly, we can check with mock observations of simulations the reliability of our observational techniques, discover introduced biases and work towards improving them (see Figures 9.3, 9.6, 9.7, 9.9 and 9.11). This is essential in understanding true mismatches between our theoretical knowledge of galaxy formation and the empirical evidence we have. Furthermore, it allows us to broaden our horizon beyond established observational methods and look for new signatures. The one presented here points towards a new avenue in extracting information about merger histories of statistical samples of individual galaxies from their bright, central regions.

APPENDIX C

Supplementary material for the study conducted in Chapter 9.

Contents

C.1 MODELLED EMISSION LINES

In Table C.1 we provide a list of all the emission lines that we included in the pPXF fits to the SDSS galaxies. The central wavelength of each line is given in *air*. See Section 9.3.3.1 for details on how exactly they were modelled during the fitting procedure.

Table C.1. List of emission lines used in fitting the SDSS spectra. The ratios of the [OI] and [NII] doublets are fixed to their theoretical values of one third. The wavelengths are given in air.

LINE NAME	WAVELENGTH [Å]
H_{9}	3797.90
H_{η}	3835.39
NeIII 3868	3868.76
H_{ζ}	3889.05
NeIII 3970	3967.47
H_{ϵ}	3970.07
[SII] 4068	4068.60
[SII] 4076	4076.30
H_{δ}	4101.76
H_{γ}	4340.47
[OIII] 4363	4363.20
H_{β}	4861.33
[OIII] 4959	4958.92
[OIII] 5007	5006.84
[NI] 5200	5200.26
[OI] 5577	5577.30
HeI 5876	5876.62
[OI] 6300	6300.30
[SIII] 6312	6312.06
[OI] 6363	6363.67
[NII] 6548	6548.03
H_{α}	6562.80
[NII] 6583	6583.41
[SII] 6716	6716.47
[SII] 6731	6730.85
HeI 7065	7065.20
ArIII 7135	7135.80
[OII] 7320	7319.99
[OII] 7330	7330.73
[SIII] 9068	9068.60

C.2 UNREGULARIZED SOLUTIONS FROM PPXF FOR SDSS GALAXIES

We show results for stellar population properties of SDSS galaxies that are obtained using full spectral fitting with pPXF *without* regularization. They are referenced throughout the main text in order to understand the impact of regularization on the derived average ages, metallicities and α-abundances (see Section 9.4.1), as well as the age-metallicity distributions (see Section 9.4.2).

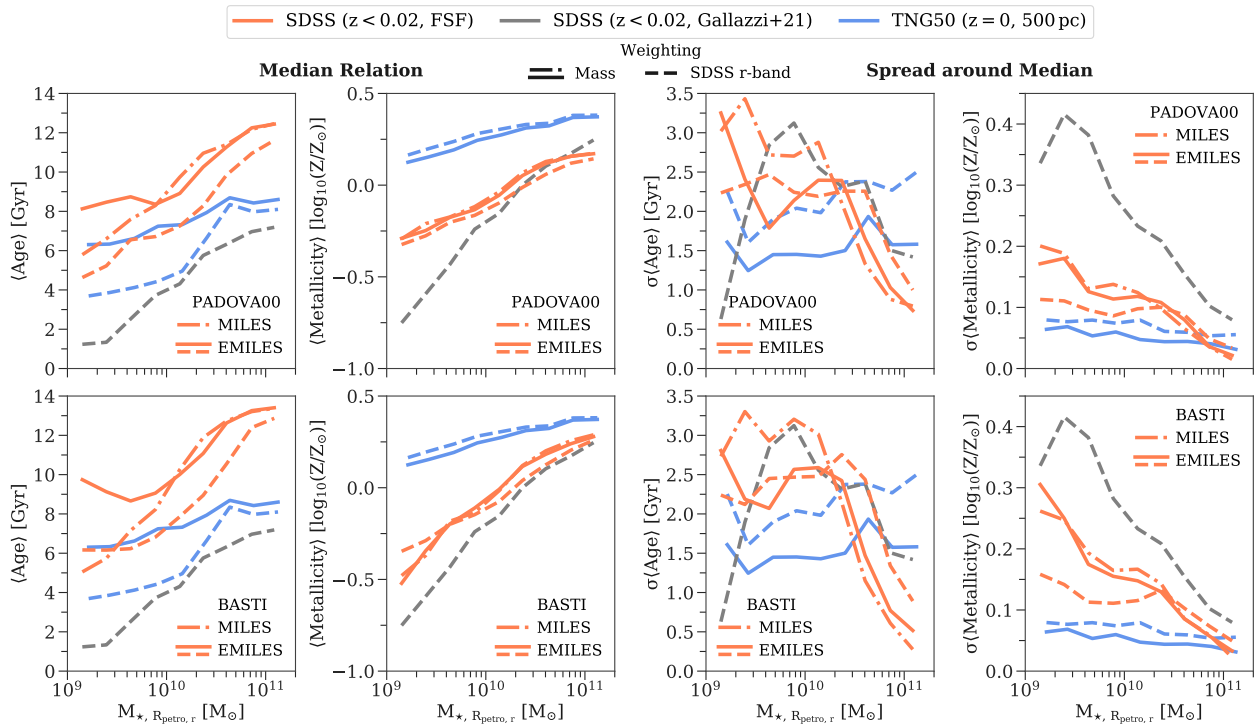

Figure C.1. Same as Figure 9.4, except that we show stellar population properties derived from unregularized full spectral fitting. *Left panel*: Running median trends for average ages (*left column*) and metallicities (*right column*) as a function of galaxy mass derived from SDSS observations via full spectral fitting (FSF; *orange*) and absorption indices (Gallazzi et al., 2021, *grey*) as well as values from TNG50 galaxies (*blue*). Solid lines refer to mass-weighted averages, whereas dashed lines are weighted by the luminosity in the SDSS r-band. Additionally, stellar population quantities derived via FSF are shown for the application of "baseFe" (E-)MILES SSP models using BaSTI (*top row*) and PADOVA00 (*bottom row*) respectively. The dashed dotted orange lines show the mass-weighted averages derived from the MILES models, which only extend up to 7410 Å, whereas the solid and dashed orange lines show the mass- and light-weighted averages derived from the E-MILES models, which cover the whole SDSS wavelength range. *Right panel*: The same as the left panel, but now the spread (σ) of the median relations are shown to understand the scatter in stellar population properties across galaxy stellar mass. The spread is calculated as the mean of the 16th and 84th percentile. Note that this does not include errors on the observed quantities.

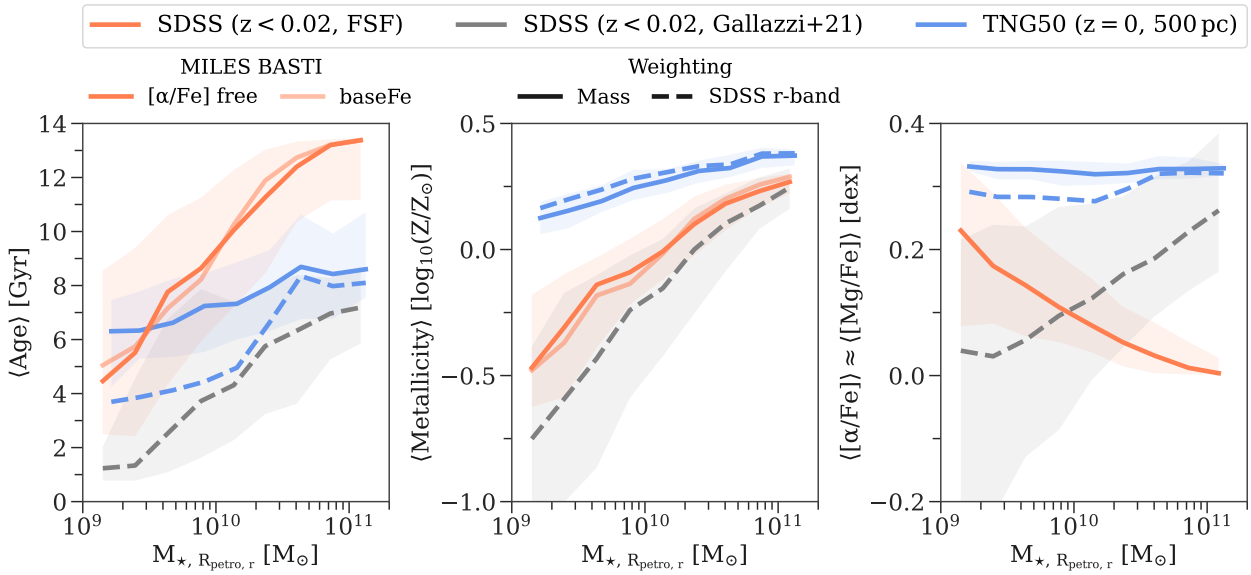

Figure C.2. Same as Figure 9.5, except that we show stellar population properties derived from unregularized full spectral fitting. *From left to right*: Running median trends for average ages, metallicities and [α/Fe] (for SDSS) ≈ [Mg/Fe] (for TNG50) as a function of galaxy mass. Quantities derived from SDSS observations via full spectral fitting (FSF) are shown in orange and absorption indices from Gallazzi et al. (2021) are in grey. Values from TNG50 are in blue. The shaded region displays the 16th and 84th percentile range. Solid lines refer to mass-weighted averages, whereas dashed lines are weighted by the luminosity in the SDSS r-band. Stellar population quantities derived via FSF are shown for MILES BASTI SSP models with [α/Fe] = 0 and 0.4 dex, i.e. [α/Fe] is free during the fit (*dark orange*), as well as for the "baseFe" models as a reference (*lighter orange*, same as the dashed dotted lines in Figure 9.4).

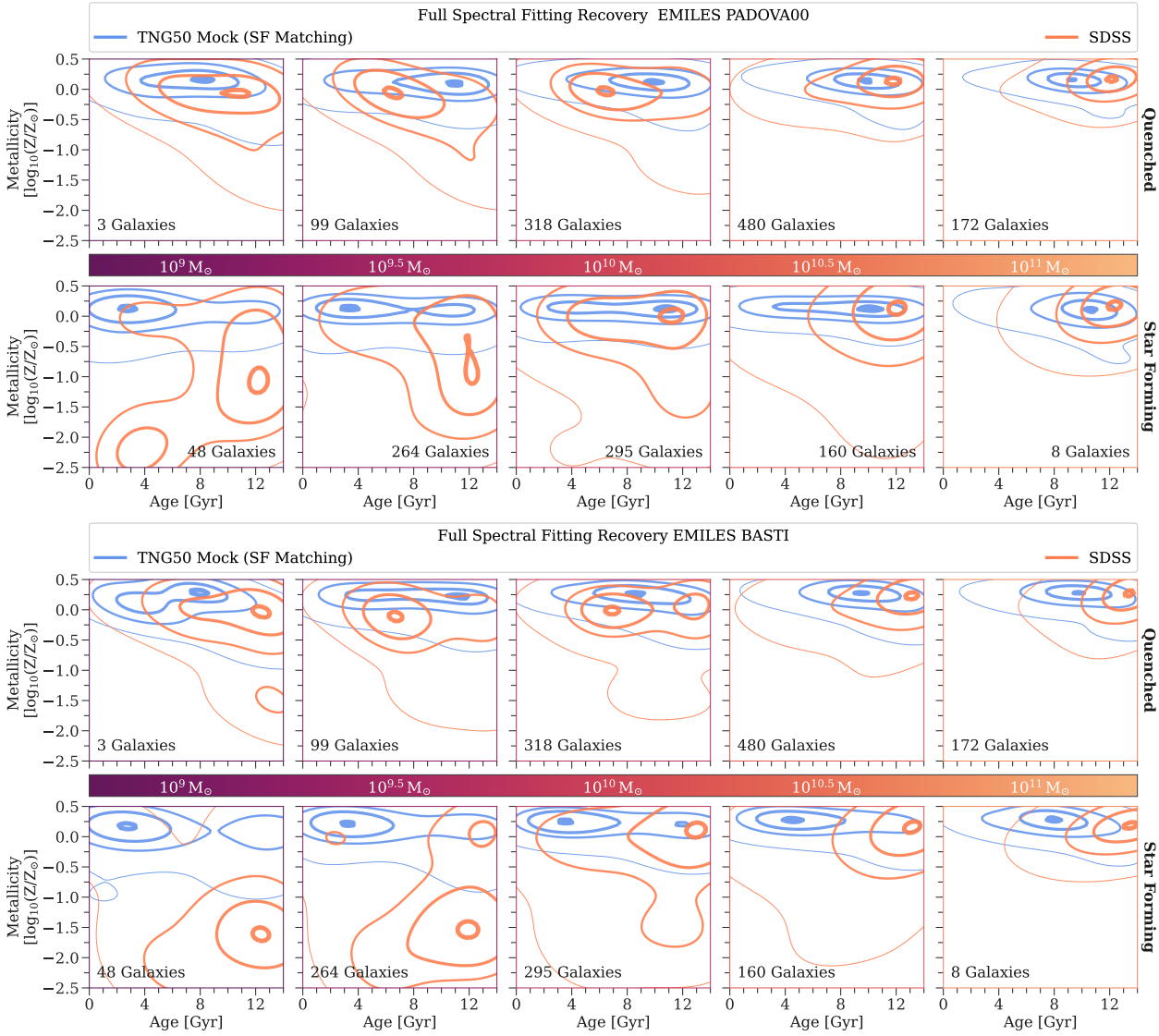

Figure C.3. Same as Figure 9.10, except that we show stellar population properties derived from unregularized full spectral fitting. Gaussian kernel density estimates of age-metallicity distributions encompassing 1%, 20%, 50% and 90% of all central stellar mass in stacks of galaxy stellar mass bins with a width of 0.5 dex are shown increasing from left to right as depicted by the colorbar. The panels above and below the colorbar show quenched and star forming galaxies separately. The distributions show the *unregularized* solution from FSF of TNG50 mock integrated spectra (*blue*) and SDSS observations (*orange*). The top and bottom panels show results using the PADOVA00 and BaSTI isochrones respectively. Prior to stacking, the age-metallicity distribution of each galaxy is normalized. TNG50 galaxies are matched to SDSS galaxies by splitting the galaxy samples first according to their star formation status. In each panel, the number of galaxies in the corresponding stellar mass bin is indicated

Part V

MOVING FORWARD

10 SUMMARY AND IMPLICATIONS

Galaxies are complex as seen in Chapter 3. Still, the build-up of their stellar mass through cosmic time can be largely divided into two categories: in-situ and ex-situ. The former is dictated by baryonic processes that convert gas into stars, while the latter is dictated by galaxy mergers, a direct consequence of cosmology. Unfortunately, quantification of the contribution of accreted stars to a galaxy's total stellar mass budget for statistical samples of galaxies is still missing. Throughout this thesis I presented a first foundation to carry out such measurements by extracting stellar population information from widely available integrated spectra that focus on the central regions of galaxies.

Summary

The three main results of this thesis are :

1. Complex star formation and chemical enrichment histories, encoded in the 2D distribution of ages and metallicities, can be robustly recovered from integrated spectra and proved to be in agreement with measurements of individually resolved stars.

2. The cosmological, hydrodynamical simulation TNG50 predicts a diverse assembly history across various galaxies even in their most central (500 pc) regions reflecting the hierarchical structure formation in a ΛCDM universe.

3. Age-metallicity distributions measured from galaxy centers observed with SDSS reveal a similar complexity hinting at the feasibility to extend the quantification of individual merger histories to large statistical samples of galaxies.

Contents

10.1 OBSERVATIONAL EFFORTS

In Chapter 5, I modelled the integrated spectrum of M 54, the nucleus of the Sagittarius dwarf spheroidal galaxy, by fitting its full spectrum with SSP models (see Chapter 4) to derive its complex distribution of stellar populations with different ages and metallicities. Due to its vicinity and the capabilities of the MUSE IFU instrument, I could compare the age-metallicity distribution from integrated light to the ages and metallicities of individually resolved stars (Alfaro-Cuello et al., 2019). I showed that the integrated and resolved light analyses, are in excellent agreement with each other, revealing a young ($\sim 1-2\,$Gyr), metal-rich ($\sim 0.0\,$dex) and an old ($\sim 8-14\,$Gyr), metal-poor ($\sim -1.5\,$dex) component. By including or excluding certain stars in the construction of M54's integrated spectrum, I could perform extensive tests to understand the robustness of the integrated light method. In particular, I showed that M54's blue horizontal branch (HB) stars do not induce the recovery of spurious young stellar populations, nor is the method particularly sensitive to the adopted magnitude limit of stars included in the integrated spectrum. The former was also confirmed with data from the WAGGS survey, that covers even bluer wavelengths than MUSE. However, the brightest stars can induce spurious old and metal-rich stellar populations, if they dominate a certain percentage of the total flux.

Nevertheless, I discussed that degeneracies and uncertainties in stellar population modelling influences the ages and metallicities of *both* the integrated and resolved light analysis. Crucially however, the integrated light method probes better the underlying mass distribution, which cannot be achieved so straightforwardly with resolved stars due to selection effects. Furthermore, the integrated light analysis performed on each MUSE pointing individually was able to measure an increase of the fraction of young, metal-rich population towards the center of M 54 in concordance with results of the resolved stars. The increased contribution of young, metal-rich stars decreases the M/L ratio in the center compared to the outskirts of M 54, which can be used as valuable input for dynamical models to help break degeneracies with unseen mass (Aros et al., 2020).

This study showed that full spectral fitting methods of integrated spectra can robustly extract more information than just the mean age and metallicity of the underlying stellar populations. Thus, we are now in an era - data and modelling wise - that can move towards extracting age-metallicity *distributions* for many extragalactic systems, which will be crucial to understand their formation pathways.

10.2 THEORETICAL EFFORTS

In Chapter 7, I used TNG50, a cosmological, hydrodynamical simulation (see Chapter 6) that allows the study of the stellar mass assembly of the central $\sim 500\,$pc of galaxies in the stellar mass range of $10^{9-12}\,M_\odot$ in a ΛCDM universe. I determined the origin of stars found

in the center of galaxies at $z = 0$ to be either in-situ (formed in the center), migrated (formed inside the $z = 0$ galaxy, but outside the center) or ex-situ (brought in through galaxy mergers). While the in-situ stars dominate on average the mass in the center of galaxies (70%), it is rare to find galaxies - low and high mass galaxies alike - without any ex-situ stars in their centers. The average fraction of ex-situ stars in the centers of galaxies with stellar masses $> 10^{11}\,M_\odot$ rises to 10%. This provides evidence that mergers contribute stars to a galaxy's mass build-up on sub-kpc scales. Migrated stars constitute on average 20% to the stellar mass in the center travelling distances of 1-10 kpc to the center, either individually or in clusters, from their birth radii. Due to the unique assembly history of each galaxy, the exact fraction of in-situ, migrated and ex-situ stars can vary significantly from galaxy to galaxy, even at a fixed galaxy mass. Splitting galaxies into the different bulk properties that they show at $z = 0$ shows that star forming galaxies tend to have more ex-situ stars in their centers on average than their quenched counterparts - in contrast to what is usually thought.

I also characterized the stellar populations - ages, metallicities and [Mg/Fe] - and dynamics - the type of orbit - of central stars with different origins in TNG50 galaxies. Ex-situ stars are on average the oldest, most metal-poor, most magnesium enhanced and most dispersion dominated stars in the center. Migrated stars are typically the youngest stars with still a significant amount of rotational support in both disk and bulge dominated galaxies with stellar masses of $\sim 10^{10}\,M_\odot$. In-situ stars have intermediate ages between ex-situ and migrated stars, are the most metal-rich and on orbits dominated by random motion. These measurable differences make it promising to quantify stars of different origins in the bright centers of galaxies.

Furthermore, I demonstrated that episodes of bursts of in-situ star formation, formation of stellar clumps, migration to the center and quenching of the center, can be tied almost exclusively to galaxy interaction events. These events include galaxy mergers or infall into galaxy clusters, which can trigger star formation, exert torques to make stars migrate, funnel gas onto the SMBH triggering AGN activity or completely quench the host galaxy. Thus, the influence of a ΛCDM cosmology cannot be neglected even in the most central part of galaxies. This could provide a new view on proposed formation pathways for central structures of galaxies, such as bulges or even NSCs, as the significance of mergers to the central stellar mass build-up is quite stochastic, but increases overall with galaxy stellar mass.

This study highlights that the brightest region of a galaxy encodes information about its assembly history in a ΛCDM universe, which provides an alternative to look for past accretion events at the center of galaxies instead of their faint stellar halos.

10.3 COMBINED EFFORTS

In Chapter 9, I used and combined the results of the two previous studies. I applied the method tested in Chapter 5 to integrated spectra

of ~ 2000 galaxies from SDSS. The redshift of the galaxies, $0.01z < 0.02$, was chosen such that they cover a similar physical aperture (~ 500 pc) as the theoretical study from Chapter 7. By matching an observed SDSS galaxy based on its stellar mass, half-light radius and ellipticity measured in the r-band to its closest analogue in TNG50, I took care of selection and projection effects. I could then compare the mass-age, mass-metallicity and mass-[α/Fe] relation of galaxies derived from full spectral fitting (FSF) of SDSS galaxies with the predictions from TNG50. While the slopes of all the trends are overall similar, the mass-metallicity relation from TNG50 seems to be shifted by a constant of 0.5 dex towards higher metallicities. The scaling relations from full spectral fitting (FSF) show different trends than those measured with absorption indices from Gallazzi et al. (2021), especially at the low mass end, which requires further investigation, as this has implications on the interpretation of galaxy formation pathways. Additional tests with SSP models based on different isochrones and wavelength coverage, shows that these are mostly affecting age measurements, whereas the mean metallicity is relatively robust.

To eliminate the biases introduced from the observational FSF method, I apply the exact same method to realistic, SDSS-like mock spectra constructed from TNG50. While the recovered ages match between TNG50 and SDSS, the metallicity is around $0.25 - 0.5$ dex lower for SDSS galaxies with masses $< 10^{10}\,M_\odot$. For higher mass galaxies, the inherent upper metallicity boundary of available SSP models makes it impossible that the intrinsic stellar populations as output by TNG50 are accurately represented in the mock integrated spectra. This causes a flattening of the mass-metallicity relation recovered from the mock spectra and the genuine TNG50 output, which is not due to the adopted observational technique.

By comparing the distribution of ages and metallicites derived from FSF for each TNG50 and SDSS galaxy, I show that star forming galaxies seem to drive the discrepancy in the mean metallicities by exhibiting atypical metal-poor (~ -2.0 dex) components. Such a diagnostic gives us a good direction for future work to identify whether the mismatch of metallicities at the low mass end is driven by problems in the observations or simulations (or both). This is essential to understand, as the mass-metallicity relation is a fundamental manifestation of the cosmic baryon cycle, which drives galaxy evolution.

Nevertheless, I was encouraged by the excellent agreement of TNG50 and SDSS in age and metallicity space for quenched galaxies; especially with regard to contributions of metal-poor populations at old ages, which are reminiscent of past merger events. I applied my developed method, showcased in Chapter 8, which can extract the ex-situ fraction and the mass of the most massive accreted satellite galaxy from age-metallicity distributions recovered from integrated spectra. The recovered ex-situ fraction increases with stellar mass in SDSS galaxies showing qualitatively the same trend and scatter found when applying the method to TNG50 mock spectra. However, a comparison between these results and to the underlying true accretion fraction known from TNG50 shows that they are overestimated for most galaxies, requiring

a revision of the accretion history method.

These first results are still promising that information about a galaxy's merger history is encoded in its central region, which can be detected through observations with integrated spectra. Refinement and eventual application of such a technique to available large spectroscopic surveys would make it possible to understand the accretion history of individual galaxies for statistical samples, which would put strong constraints on galaxy formation in a ΛCDM cosmology.

11 DISCUSSION AND OUTLOOKS

Naturally, the analysis conducted in this thesis needs to be followed up to improve our observational evidence and theoretical understanding. I discuss possibilities to extend the adopted observational modelling techniques, point towards interesting aspects that can be probed further with the simulations and give exciting applications to current and future observations.

Summary

There are several projects which I am already working on:

Observations : Extracting spatially resolved ex-situ fractions for galaxies from the SAMI IFU survey, which are also covered with deep photometric observations to reveal their faint stellar halos.

Simulations : Quantifying the exact properties of mergers that contribute stars the center of galaxies and connecting them to peaks of in-situ star formation and migration times.

Combined : Making mock spectra from TNG50 for the complete SDSS sample to shed light on the discrepancy of the mass-metallicity relation and to improve the extraction of ex-situ fractions from integrated spectra.

Contents

11.1 EXTENSIONS OF CURRENT MODELS

The two observational methods used in this thesis would both benefit from certain methodological extensions. It is crucial to test and further develop these techniques, which can extract star formation and chemical enrichment histories from integrated spectroscopy, as even the newest generation of telescopes, such as JWST and ELT, will only reach individually resolved (red clump) stars for distances smaller than $\sim$ 10 Mpc (Tolstoy, 2019). Despite the fact that CMDs of individually resolved stars count as the most reliable observational measurement to extract star formation histories (e.g Gallart et al., 2019), we need to measure stellar population properties in samples of thousands of galaxies and more across various redshifts, to fully understand the assembly of galaxies in a cosmological context.

11.1.1 Deriving age-metallicity distributions

In Chapter 5 we have demonstrated that the recovery of age-metallicity distributions from integrated spectra is in agreement with measurements from individually resolved stars, and is also largely robust with respect to certain suspected troublemakers such as horizontal branch (HB) stars and the adopted magnitude limit. Still, this application was performed on only one specific stellar system. In Chapter 9 we did reveal certain biases that were introduced in recovering age-metallicity distributions with the adopted full spectral fitting technique by comparison to the known true underlying distribution from many different TNG50 galaxies ranging from 10^{9-11} $M_\odot$. In addition, the absolute values of stellar populations properties can be highly dependent on the SSP models used to derive them. Assumptions and unknowns in the SSP models and biases introduced through these are quite separate from how the adopted technique itself models the integrated spectrum. Hence we ask three questions:

1. How can we extend SSP models and handle the uncertainties due to the different assumptions made in creating them?
2. How can we improve the full spectral fitting method itself?
3. Can we find more systems, where a comparison between age-metallicity distributions recovered from resolved and integrated light is possible with current data?

11.1.1.1 *Extensions of SSP models*

In Chapter 9, we showed that metallicities for most stellar particles in the center of galaxies ($> 10^9$ $M_\odot$) produced by the TNG simulation, are substantially higher (> 0.4 dex) than what we can model with current SSP models. This makes it impossible to construct mock integrated spectra reflecting the actual distributions of stellar populations that were genuinely produced by the simulation. Hence, this makes it

complicated to test the robustness of methods that rely on the preservation of the accurate mapping of age-metallicitiy distributions, such as the methoid I developed to identify the fraction of accreted material in galaxies (see Chapter 8). In addition, observations are also subjected to the inherent grid boundaries of SSP models, such that it is non-trivial to assess, if discrepancies seen between observations and predictions from simulations are "true" or just due to the limitations of the SSP models.

Extending SSP models to higher metallicities or adding more grid points in general is not exactly trivial. When these models are based on empirical stellar libraries, which is the case for the SSPs used here, they sample stars in the solar neighbourhood, which will thus represent ages and metallicities typical for a star forming, disk galaxy with a stellar mass of $\sim 10^{10}\,M_\odot$. Thus, it is hard to sample isochrones of a certain metallicity with enough stellar spectra to make up the SSP model. This is not only the case for high metallicity stars, but also for the lowest metallicities (~ 2.0 dex), especially for young ages[141]. In addition, the wavelength coverage and spectral resolution of SSPs based empirical stellar libraries are fixed through the spectrograph that obtained the spectra in the first place. We have seen in Chapter 9 that the wavelength coverage can influence the derived ages for low mass galaxies. Theoretical stellar spectra can help eliminate the insufficient parameter sampling of isochrones, as well as the instrumental limitations (e.g. Maraston & Strömbäck, 2011; Villaume et al., 2017), however they are subjected to their own uncertainties due to the complexity of stellar atmospheres (see Section 4.1.3).

141: See e.g. the ranges of ages and metallicities for the MILES SSP models, which are uncertain: http://research.iac.es/proyecto/miles/pages/ssp-models/safe-ranges.php.

A way forward is certainly to observe more stellar spectra to better cover the parameter space of isochrones. For example, the recently released completed MaStar library (Yan et al., 2019; Abdurro'uf et al., 2022) from SDSS-IV, covers around 10000 stellar spectra in the optical as opposed to 1000 stars included in the MILES library (Sánchez-Blázquez et al., 2006). Moreover, an increasing number of spectra with higher resolution ($R \sim 10000$ as opposed to $R \sim 2000 - 3000$) and extended wavelength coverage towards the IR are being produced (e.g. the XShooter Spectral Library: Chen et al., 2014; Gonneau et al., 2020; Verro et al., 2021). The latter is especially important to understand the contribution of cool, low mass stars[142].

142: Most empirical stellar libraries are in the optical, as it is easier to observe.

Also other surveys that are designed to deliver detailed individual element abundances for several hundred thousands of MW stars (e.g. APOGEE: Majewski et al., 2017; GALAH: Buder et al., 2018; LAMOST: Zhao et al., 2012; Gaia-ESO: Gilmore et al., 2012 and together with those planned through SDSS-V: (Kollmeier et al., 2017); 4MOST: de Jong et al., 2019; WEAVE: Dalton et al., 2020) will help expand our knowledge of stellar parameters outside the solar neighbourhood as well as improve our theoretical understanding of stellar atmospheres (see e.g. Ashok et al., 2021, for SSP models build from APOGEE stars).

Other effects that influence the recovery of ages and metallicities with SSP models are [α/Fe] (or even more general individual element abundances) and the IMF. The former can be taken into account in full spectral fitting techniques that recover the whole age-metallicity dis-

tribution (see Chapter 9), but are limited again by the available grid points (which are two in our case, but see Knowles et al., 2021, for an extension of covered values for the MILES library). Individual element abundances are only considered so far in full spectral fitting by modelling the SFH as a single burst or at most made out of two components (i.e. an old and young population; see e.g. Conroy et al., 2014; Vaughan et al., 2018). Apart from the expense[143] in producing (theoretical) spectra with individual element abundances (Conroy et al., 2018), the isochrones also have to be adapted to the varying element abundances to ensure self-consistency; especially elements like oxygen can have a large impact on the placement of the isochrones in $\log g - T_{eff}$ space and can thus mimic changes in age, if not taken into account (VandenBerg et al., 2012). More flexible SSP generation tools like FSPS (Conroy et al., 2009, 2010; Conroy & Gunn, 2010) aim to account for these effects.

143: The parameter space grows exponentially with the number of different elements.

Similarly, the IMF is rarely changed from the canonical form when age-metallicity distributions are derived form full spectral fitting. However, we know that the IMF is bottom-heavy, in particular for galaxies at the high mass end (see Section 4.1.1). The MILES SSP models come with a variety of IMF slopes, so this effect could be included in theory in the full spectral fitting method. However, this is complicated by the fact that spectral features that are influenced by the slope of the IMF are also influenced by individual element abundances (e.g. sodium and titanium). Leaving all these parameters free while attempting to recover a distribution of ages and metallicities will be highly degenerate and computationally expensive. A way forward might be to first constrain the IMF with methods that are tailored to that task (e.g. Conroy & van Dokkum, 2012a,b; Martín-Navarro et al., 2019, 2021b) and then keep the derived IMF slope fixed to fit for the age-metallicity distribution.

All in all, it is crucial to be aware of the influence of SSP models, which are based on different isochrones and stellar libraries, as well as the biases introduced by simplifying assumptions about the IMF or other element abundances, when deriving stellar population parameters. The continuous extension of SSP models facilitated by ever growing surveys, updates of theoretical calculations and testing of different models to the same data (see also Neumann et al., 2022) will help us understand derived stellar populations properties of galaxies.

11.1.1.2 *Improving the full spectral fitting method*

Undoubtedly, the full spectral fitting method to derive distributions in ages and metallicities would benefit from a Bayesian approach. This would help to understand degeneracies better, and would allow for an uncertainty quantification on the recovered age-metallicity distribution as well as the inclusion of priors. Especially, the latter could improve the current implementation of the regularization, as the smoothing of the weights associated with an age-metalliciy bin are not done in physically meaningful way. For example, changes in age and metallicity of a mass weight should follow an age-metallicity relation and not be done in an equal amount in all four directions of the age-metallicity grid.

Meanwhile the Bayesian "revolution" has already arrived in SED fitting (Noll et al., 2009; Chevallard & Charlot, 2016; Leja et al., 2017; Carnall et al., 2018; Johnson et al., 2021, and see also see Section 4.2.1) including non-parametric SFH (Leja et al., 2019). Especially, the Prospector code by Johnson et al. (2021) is promising for a direct extension of our adopted full spectral fitting technique, since it can already handle spectroscopic data (see e.g. Oyarzún et al., 2019, for an application to MaNGA data).

Nevertheless, none of these codes so far can fit for a non-parametric distribution in age *and* metallicity; all of them assume a constant metallicity at all ages. However, it is crucial to take this into account, as galaxies enrich in metals over time and do so with different efficiencies depending on their stellar mass, which we exploit to estimate the accretion history. In addition, the increased computational cost also has to be taken care of, since full spectral fitting includes the modelling of several thousands of data points (i.e. each spectral pixel) as opposed to SEDs, which perhaps fits on the order of ten photometric filters. A Bayesian full spectral fitting approach still needs to be fast enough, since data sets from IFU or other large spectroscopic surveys provide several (ten)thousands of integrated spectra.

In summary, more time needs to be invested into developing Bayesian tools for deriving age-metallicity distributions from integrated spectra.

11.1.1.3 *More test systems with integrated and resolved light measurements*

The study conducted in Chapter 5 could be extended to other MW globular clusters (GCs) observed with MUSE (Kamann et al., 2018). Especially, the application to Omega Centauri (see Section 3.3.3.5), could be interesting, as it has a large spread in metallicity (Villanova et al., 2014). However, its individual light element abundances are also much more complex than in M 54 (Milone et al., 2017). These can significantly influence the age determination, but are not trivially taken into account for full spectral fitting approaches that derive age-metallicity distributions (see the earlier Section 11.1.1.1).

Another possibility could be to observe parts of the Milky Way as if it were an extragalactic system. This idea was inspired by a recent study of Xiang & Rix (2022), who studied ages, metallicities and [α/Fe] for $\sim$ 250000 (sub-giant branch)[144] stars, which are both measured with Gaia and LAMOST. The 6D phase-space information provided by Gaia would make it possible to project the observer outside the MW, whereas the spectra taken with LAMOST closely match the wavelength range ($3700 - 9000$Å) and spectral resolution ($R \sim 1800$) usually available for extragalactic systems. From this we could construct an integrated spectrum and derive the age-metallicity distribution, which could then be compared to results from Xiang & Rix (2022). This is particularly intriguing, since the ancient merger of the MW (Helmi et al., 2018; Belokurov et al., 2018) was evident in their recovered age-metallicity distribution, which could provide a test case for our accretion history method from Chapter 8.

144: Some care would need to be taken here, as only stars in a certain stellar evolutionary phase were selected, which will not be the case for integrated spectra of extragalactic systems.

11.1.2 Deriving accretion histories

There are several methodological updates that need to be considered for deriving accretion histories of galaxies from their integrated spectra (see also Section 9.6.4), in particular when we want to apply this method to spatially resolved studies with IFU observations (see also Section 11.2.2). These updates are connected to in-situ stellar population gradients, which contribute metal-poor stars at fixed age due to lower star formation efficiency in the outskirts of galaxies; and hence could be detected as having an ex-situ origin with our method. This will be problematic especially for galaxies with on-going star formation. A first extension in this direction has been done in Davison et al. (2021). Secondly, the determination of the most massive accreted satellite galaxy becomes more complex, when the underlying integrated spectrum does not sample the majority of the host galaxy's stellar mass. Hence, it would be crucial to understand the number and masses of mergers that contribute to the host's stellar mass as function of position within the host galaxy. We plan to investigate this with the TNG simulation for the galaxy population as a whole (see Section 11.2.2 for further discussion).

Apart from investigations in this direction, my collaborator Ryan Leaman and I, have also started to work on a different approach. Instead of first deriving age-metallicity distribution from integrated spectra and then associating past merger events with empirical age-metallicity relations (AMRs), we pursue to build a large library of integrated spectra constructed from stochastically sampled AMRs for different accretion histories. This would have a number of advantages. Firstly, it takes into account the overlap of different accretion events and the in-situ host in age-metallicity space. This will be particularly the case at old ages for a range of accreted satellite galaxies, since galaxies start their chemical evolution from low metallicity gas. The most severe overlap however will be present for major mergers events, as both galaxies will have a very similar in-situ chemical enrichment (see Figure 7.9), which can thus be treated better with this forward approach. Secondly, it imposes a more realistic age-metallicity relation for galaxies, as opposed to the regularization as discussed in Section 11.1.1.2; in fact, this type of modelling would skip the inversion, i.e. going from integrated spectra to age-metallicity distributions, all together. While the work is still in the early stages, this method appears as a promising way forward to make the current method more sophisticated.

11.2 FOLLOW-UP WORK WITH THE TNG SIMULATION

There is some follow-up work that I am envisioning with the TNG simulations in the context of this thesis.

11.2.1 Formation mechanisms to build-up of galaxy centers

The first project is a direct extension of the study conducted in Chapter 7. In particular, by looking at Figure 7.11 it is intriguing to think that almost every aspect and mechanism that influences the mass build-up of galaxy centers is connected to galaxy interactions. From there, three main questions arise:

1. Which exact types of mergers deposit stars in the centers of galaxies?
2. Are in-situ star formation episodes in the center, or episodes of stellar migration to the center, entirely dictated by mergers and flybys?
3. How are mergers connected to gas inflow, SMBHs, AGN feedback and quenching?

11.2.1.1 *Characterization of merger events*

To answer question 1., I have already done some calculations, which characterize the morphological and orbital properties of the primary and secondary during the merger process, as described in Section 6.3.1. Such a study allows for a statistical investigation of merger properties in a fully cosmological context, as opposed to studies that treat the merger process in isolation (Di Matteo et al., 2007; Renaud et al., 2009). Importantly, this would let us understand the scatter of the central ex-situ mass at fixed galaxy mass (Figure 7.5) as well as the differences thereof for different galaxy types (Figure 7.6).

Some initial results are shown in Figure 11.1. They indicate that mergers, which contribute stars to the central 500 pc, are preferentially gas-rich, major mergers that are on low eccentricity orbits, as compared to mergers, which do not deposit stars in the center. Nearly equal mass mergers allow the secondary galaxy to actually retain its stars for long enough to sink towards the center, before being completely disrupted by tidal forces. A low eccentricity orbit ensures that the first pericenter is at larger distances as compared to more radial orbits. This also decreases the tidal forces, which act upon the secondary, making it possible to retain more stars until the primary's center. I also studied other parameters such as the spin-orbit alignment and the impact angle, i.e. how the "disks" of the two merging galaxy are aligned with respect to each other, but did not find any difference between mergers, which contribute stars to the centers and which do not.

I plan to further investigate, how these merger characteristics are connected to properties of the $z = 0$ host galaxy, and if there is a detectable imprint in the stellar population or dynamical properties, which we could derive from observations. This could give us insights on how different merger events result in a unique assembly history for each individual galaxy, while still leading to similar morphological galaxy types.

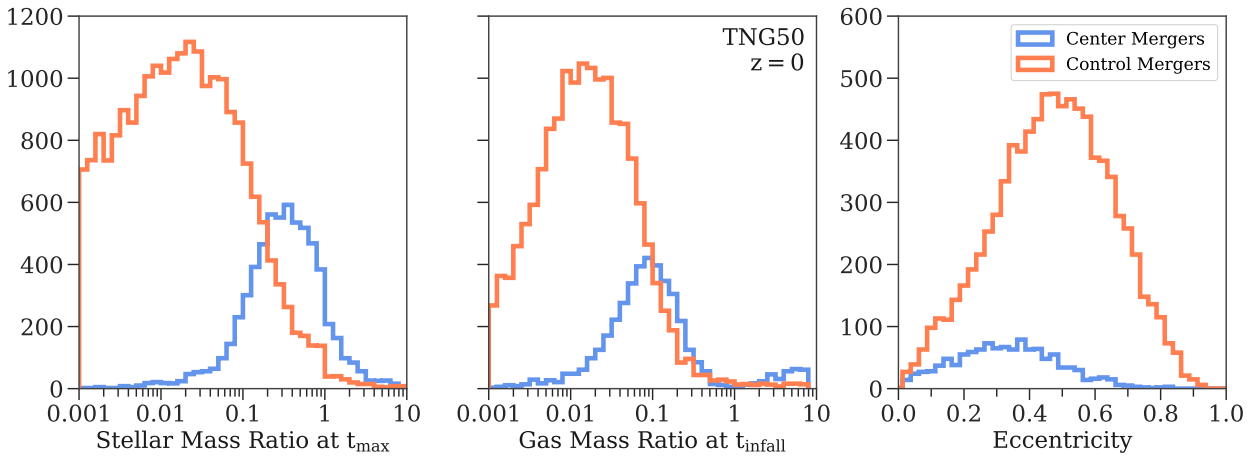

Figure 11.1. Characterization of mergers from TNG50 galaxies at $z = 0$ analyzed in Chapter 7. *From left to right*: Distribution of stellar merger mass ratios, gas mass ratios and eccentricities of mergers that deposited stars in the central 500 pc of their $z = 0$ host (*blue*) and of ones that did not (*orange*). The stellar mass ratios, i.e. the ratio of the stellar mass of the secondary to the primary galaxy, were taken at time t_{max}, when the secondary reached its maximum stellar mass (Rodriguez-Gomez et al., 2016). The gas mass ratios were taken at the time of infall t_{infall}, i.e. when the secondary entered the virial radius of the primary galaxy. The eccentricities are calculated by considering the peri- and apocenter at first approach following Joshi et al. (2020). Mergers that contribute stars to the centers of their host galaxies are preferentially gas-rich, major mergers on low eccentricity orbits.

11.2.1.2 *Connecting the formation and migration times of central stars with galaxy interactions*

Mergers or flybys can trigger star formation in the center, as gas is funnelled and compressed via torques exerted by the on-going galaxy interaction (e.g. Hernquist, 1989; Mihos & Hernquist, 1994a,b, 1996). Figure 7.11 shows that peaks of in-situ star formation occur primarily during pericenter or coalescence of mergers. This can also happen for flybys, or at pericenter around the central galaxy, in the case of satellite galaxies. We can quantify this interaction history by calculating the tidal parameter (Di Matteo et al., 2007) between the primary, $z = 0$ host galaxy and the interacting secondary galaxy over the time of the interaction period:

$$T = \frac{M_1 M_2}{(M_1 + M_2)^2} \left(\frac{R_1 R_2}{D^2} \right)^3 , \tag{11.1}$$

where M_1 and M_2 are the total masses, and R_1 and R_2 are the half-mass radii of the primary and secondary respectively. The separation between the two galaxies is D.

As multiple mergers or interactions can occur at the same time, we calculate $T_{max} = \max_{i \in N_{sat}} T_i$, i.e. the maximum tidal parameter of all interacting satellite galaxies present at a given time. This gives us an approximation of which interacting galaxy is exerting the most tidal forces onto the primary as a function of time.

We compare T_{max} and the in-situ mass formed in the center as a function of time for a Milky Way like galaxy in Figure 11.2. This galaxy has in fact *no* ex-situ stars in its center. Still, it is apparent that the central in-situ star formation episodes follow closely the shape of T_{max} lagging behind ≈ 600 Myr.

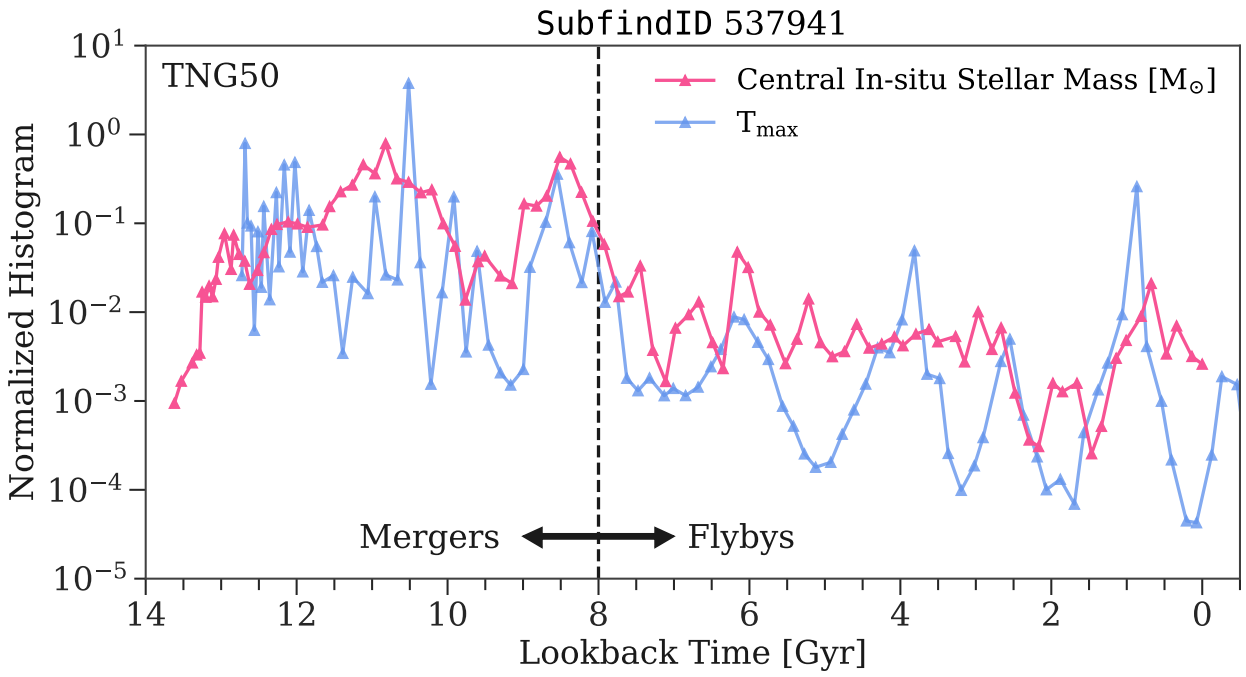

Figure 11.2. The connection between in-situ star formation and galaxy interactions. The pink line shows the stellar mass assembly of in-situ stars in the central 500 pc of a Milky Way like galaxy from TNG50 (`SubfindID` 537941). The blue line shows the maximum tidal parameter (T_{max}) as defined according to Equation 11.1, which has been shifted by 600 Myr to smaller lookback times to show the correspondence of peaks in both curves. At lookback times > 8 Gyr, the values of T_{max} are driven by mergers, whereas flybys dominate T_{max} at more recent times. Peaks of star formation match peaks of T_{max}. The merger that coalesced 8 Gyr ago triggered the kinetic AGN feedback, which explains the sharp decrease of central in-situ star formation.

This can be quantified for each galaxy in the sample of my study in Chapter 7 via cross-correlation, such that we can understand how frequently peaks of star formation are a consequence of galaxy interaction events. Star formation histories are measurable from observations with methods presented in this thesis, and thus insights gained from this new analysis could help interpret observed peaks of star formation episodes in the context of past and recent galaxy interactions[145] (see e.g. Ruiz-Lara et al., 2020, for a similar study in the case of the interaction between the MW and the Sagittarius dSph). Furthermore, this analysis could also help understand, if in fact the majority of the in-situ stars are formed during galaxy interactions, as opposed to more "quiet" or secular phases, which are thought to be important for the evolution of star forming galaxies (see Section 3.3.3.3).

145: This will particularly be possible for young star formation episodes, as the observational errors in age for old ages will likely be too large.

Similar analysis can be conducted for the migrated stars to understand how episodes of stars migrating to the center correlate with galaxy interactions. The latter will cause non-axisymmetric features in the matter distribution, which can promote stars to change their orbits. Thus, a Fourier decomposition of the mass distribution of gas and stars as a function of time can help quantify such non-axisymmetries and therefore provide a physical connection between migration and merger events.

Such an investigation will also be important for understanding bars and their impact on the mass build-up in galaxy centers (see Section 3.3.3.4). While the properties and evolution of bars are now stud-

ied with cosmological, hydrodynamical simulations (Fragkoudi et al., 2020; Rosas-Guevara et al., 2020, 2021), we still lack comprehensive studies of why they were created in the first place using such simulations. With TNG50, we can connect the formation of bars to the exact type of galaxy interactions that created (or perhaps also destroyed) them, and understand why other interactions do not create bars. This will then also extend our knowledge of processes that are thought to be linked to the presence of bars, such as radial migration in the outer disk (see Section 3.3.3.2). Hence, follow-up work in this direction can connect migration events at various radii across galactic disks and help us to better understand the interplay between merger events and bar driven secular evolution.

11.2.1.3 *Processes involving gas inflow, SMBHs and quenching*

Galaxy mergers cannot only funnel gas to the center causing star formation, but also trigger AGN activity due to the presence of SMBHs at the centers of galaxies (see Section 3.3.3.6). Moreover, if the merging galaxy is massive enough, it could also contain a SMBH on its own, which would ultimately result in a SMBH merger. The AGN feedback will quench the galaxy from inside out (Nelson et al., 2021). However, not every galaxy that is found today below the star forming main sequence is quenched because of the AGN due to environmental processes (see Donnari et al., 2021a and Section 3.4). At the same time, there are galaxies in TNG50 that are quenched in the center, but remain on the star forming main sequence for multiple Gyr. What causes complete quenching with active AGN feedback in some, but not all galaxies? More complicated even, some mergers in TNG50 are able to bring gas to the center, rejuvenating star formation for short periods of time (see e.g. Martín-Navarro et al., 2022, for observational evidence). While it is clear that this gas must come from the merging galaxy for completely quenched (essentially gas free) galaxies, it poses the question if this is also the case for star forming galaxies. The stars formed through gas brought in by mergers are technically counted as in-situ in TNG50, but they should follow the chemistry of the accreted galaxy and not the host. How large is the fraction of such stars in the center of galaxies? Measuring this would be an effort (but doable) in TNG, since the gas accretion can only be followed through tracer particles as the hydrodynamics are solved using the Lagrangian approach (see Chapter 6). Still, it would be intriguing to follow-up on this connection between mergers, star formation and AGN activity, since it is fundamental to understand how galaxies move between different states of star formation activity (see Section 3.2.2).

11.2.2 Extension to larger radii

It is straightforward to extend the finished and on-going analysis with TNG, which now focus on the centers of galaxies, to larger radii. This will be necessary with regard to the study done in Chapter 9, such that

we can compare a larger sample of SDSS and TNG galaxies.

The median redshift of the SDSS galaxies studied in Gallazzi et al. (2021) is approximately $z = 0.1$, which translates to an extent of roughly 4 kpc covered with the SDSS fiber. This allows us to also include comparisons to the larger volume runs of TNG50, which are TNG100 and TNG300. With the larger boxes we can probe even better the diversity of merger histories of individual galaxies, particularly at the high mass end ($> 10^{11}\,M_\odot$). This will ensure that more TNG galaxies are uniquely matched to SDSS, which is currently not the case with TNG50. The limited volume includes much less high mass galaxies than what is preferentially observed with SDSS, and thus we may not be sampling enough different assembly pathways in this regime with TNG50 alone.

In addition, the larger aperture will include by construction more ex-situ material, which is beneficial for the recovery of ex-situ fractions from observations. On the contrary, this could also be complicated by the effect of mixing in an increasing gradient of in-situ stellar populations (as discussed in Section 9.6.4). Studying these effects with TNG, will reveal which of the two will be more dominant and have a stronger impact on the derivation of the accreted fractions. Additionally, the extended sample size might give us a better understanding of why and how the discrepancy in the mass-metallicity relation between observations and simulations arises (see Section 9.6.1).

Even more general, we can study the ex-situ fraction, and the number and types of mergers contributed in different parts of the $z = 0$ host galaxy, in a spatially resolved manner with TNG. Doing so across the whole galaxy population will give us complete demographics of where and when mergers are deposited, as well as what imprints they leave in observable quantities such as stellar population and dynamical properties of the $z = 0$ host galaxy. More so, such a study will be valuable for applying and extending the accretion history method from Boecker et al. (2020a) to IFU surveys. A first application to MUSE data was performed in Davison et al. (2021), which was done, however, only for a few (early-type) galaxies. Because IFU surveys now cover increasingly large samples of galaxies, such as the just completed MaNGA survey (~ 10000 galaxies; Bundy et al., 2015; Abdurro'uf et al., 2022), and the final data release of the SAMI survey (~ 3000 galaxies; Allen et al., 2015; Croom et al., 2021), we need to know precisely that we can derive spatially resolved ex-situ fraction (or even the whole accreted galaxy mass function) with this method in a robust and automated way. Considering the complications discussed above, such as in-situ stellar population gradients and the determination of the stopping point of the most massive accreted satellite galaxy (see Section 9.5.1), an exploration of these effects with the TNG simulations will let us develop the necessary enhancements, as well as test the reliability of our method with IFU mock observations (see e.g. Nanni et al., 2022, for mock MaNGA observations from TNG).

In addition, such a complete study of spatially resolved merger demographics will also be informative for other works that illuminate past merger events from deep photometry of stellar halos (Merritt et al., 2020) or chemo-dynamical Schwarzschild models (Zhu et al.,

2022a,b). The latter method measures circularities of stellar orbits, while simultaneously tagging them with observed stellar population properties (Poci et al., 2019; Zhu et al., 2020). Therefore, this technique can produce Figure 7.10 observationally, which shows that stars of different origins are separated in age-circularity space. Applying chemo-dynamical Schwarzschild models and the spectroscopic accretion history method from Chapter 8 to the same IFU data sets can hence detect past merger events with two independent, but complementary methods. This can be used to understand, if both (chemo-)dynamical and purely stellar population based models give consistent results on the derived mass of, for example, the most massive accreted satellite galaxy, in comparison to results derived from mock observations of simulations.

11.3 APPLICATIONS TO MORE OBSERVATIONS

Apart from the already mentioned extension of the analysis performed in Chapter 9 to the entire SDSS sample from Gallazzi et al. (2021), there are other current and future observational data sets that are optimal for deriving age-metallicity distributions and accretion histories from integrated spectra. Applying these methods to statistical samples of galaxies across different redshifts will let us understand better the emergence and evolution of scaling relations and galaxy-to-galaxy variations at fixed mass (see Section 3.2.3 and e.g. Martín-Navarro et al., 2018b; Barone et al., 2018, 2020; Davison et al., 2020; Scholz-Díaz et al., 2022). A low redshifts, IFU surveys make it even possible to explore age-metallicity distributions and ex-situ fraction as a function of spatial position within galaxies (e.g. Zibetti et al., 2020; Neumann et al., 2021).

11.3.1 Current data for studying accretion histories

While new data is always exciting, it is also crucial to exploit current data sets to their fullest. This is especially true for the application of newer observational techniques, since current data is usually well studied, and is in some cases also complemented by ancillary data. Thus results of new and existing methods can be checked for consistency, differences can be understood and improvements made pioneering for future data at even higher redshifts.

11.3.1.1 *Combining deep photometery with IFU*

I have planned and started first measurements of spatially resolved ex-situ fractions of a few galaxies from the SAMI IFU survey (Allen et al., 2015; Croom et al., 2021), which are shown in Figure 11.3. This work was initiated by and is done in collaboration with Thomas Jackson, who analyzed stellar population gradients of these galaxies for his thesis, and characterized their faint stellar halos (see Section 3.3.3.1) by us-

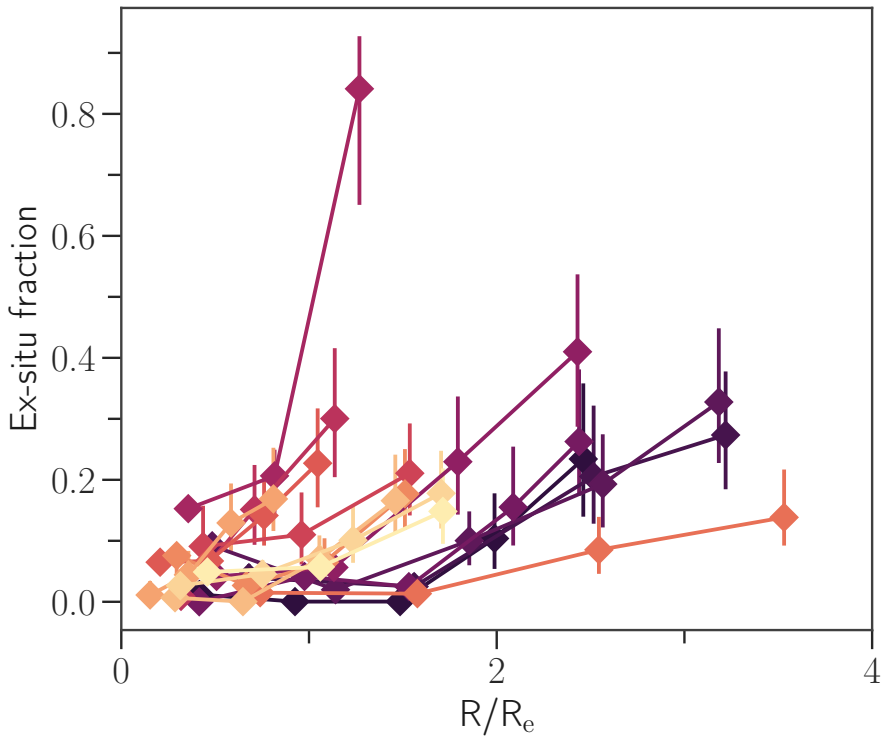

Figure 11.3. Ex-situ fraction profiles for 12 early-type galaxies with stellar masses $\sim 10^{10.5}\,M_\odot$ extracted from the SAMI IFU survey obtained with the method from Chapter 8. The radius is given as a fraction of the effective radius. Each color represents a different galaxy. The ex-situ fraction increases as a function of radius, as expected from the accretion of lower mass galaxies (Cooper et al., 2010). The diversity of the profiles at fixed radius reflects the stochasticity of merger events. For example, the galaxy with an ex-situ fraction of 80% at 1 R_e has a prominent substructure in its stellar halo detected in the HSC-SSP data.

ing data from the Hyper Suprime-Cam Subaru Strategic Programme[146] (HSC-SSP; Aihara et al., 2018).

We now plan to extend this preliminary analysis of 12 galaxies to ~ 500, facilitated by the newest HSC-SSP data release (Aihara et al., 2022). The galaxies are cross-matched with the SAMI survey as well as the catalogue of Gallazzi et al. (2021), providing a sample twice as large as other deep photometric surveys that are simultaneously covered by IFU observations (e.g. MATLAS: Duc et al., 2015; Duc, 2020; Bílek et al., 2020 and ATLAS3D: Cappellari et al., 2011a; FDS: Iodice et al., 2016, 2019a; Spavone et al., 2020 and Fornax3D Sarzi et al., 2018; Iodice et al., 2019b; VEGAS: Capaccioli et al., 2015; Spavone et al., 2017 and M3G: Krajnović et al., 2018; Spavone et al., 2021). We have completed visual classification of all galaxies to determine whether they show either substructures in the forms of streams and shells, a diffuse halo or whether they are indeed featureless.

This sample is ideal to understand accreted fractions in the inner regions from the spectroscopic measurements, by using the methods outlined in this thesis, and from their faint stellar halos following Jackson et al. (2021) for a statistical sample of *individual*[147] galaxies. Crucially, the method employed in Jackson et al. (2021) obtains stellar mass maps until ten effective radii via Voronoi binning and SED fitting. This provides more reliable stellar mass estimates and preserves the structures seen in the stellar halo, as opposed to usual isophotal measurements, which tend to smooth out observed features.

Thus, for this study the planned follow-up work with the TNG simulation as outlined in Section 11.2.2 will be essential to a) optimize our spectroscopic accretion history method for spatially resolved studies and b) to compare observational results with the predictions from

146: The HSC-SSP provides deep photometry in five broad bands (grizy) reaching r ~ 26, 27 and 28 mag for 1400, 27 and 3.5 deg^2 of the sky respectively. Explore the stunning data at `https://hsc-release.mtk.nao.ac.jp/hscMap-pdr3/`.

147: Note that, up until recently, images had to be stacked to achieve the necessary signal at large radii (e.g. La Barbera et al., 2012; D'Souza et al., 2014), which makes it impossible to study details about individual merger events.

TNG. The latter will make it possible to understand the deposit of different accretion events at different radii from simulations *and* observations. Furthermore, it might give insight into the "missing outskirt problem" put forward by Merritt et al. (2020), who showed that stellar halos of Milky Way like galaxies from the Dragonfly survey (Merritt et al., 2016) are less massive than their counterparts in the TNG100 simulation.

11.3.1.2 *Merger histories until* $z = 1$

There exist mainly two data sets that currently allow for the study of stellar populations from integrated spectra at redshifts higher than those reached by SDSS and by the other low redshift IFU surveys mentioned above.

The first one is the MAGPI survey (Foster et al., 2021), which uses MUSE to spatially resolve ~ 200 galaxies at $z \approx 0.3$ ranging from low- to high-density environments. The other, is the LEGA-C survey (van der Wel et al., 2016, 2021), which provides long-slit spectra from VIMOS for ~3500 galaxies at $0.6 \leqslant z \leqslant 1$. The sample size and survey footprint of LEGA-C are large enough to probe a range of galaxy masses, star-forming rates and environments (Cole et al., 2020), and provide high quality stellar continuum data to study kinematics (Bezanson et al., 2018; van Houdt et al., 2021) and stellar populations (Wu et al., 2018; Chauke et al., 2018; Barone et al., 2022).

Recovering merger histories from integrated spectra of these higher redshift data is ideal for several reasons. Firstly, we only need to consider galaxy evolution up to $3-4\,\mathrm{Gyr}$ ago for the MAGPI and up to $7-8\,\mathrm{Gyr}$ ago for the LEGA-C survey respectively. Especially the later, alleviates the poor age resolution of stellar population models at old ages ($> 8\,\mathrm{Gyr}$), that we currently face at $z = 0$. Thus, we can hope to better resolve star formation episodes that happened early on and are likely connected to the first merger events that took place at $z > 1$. Secondly, we can connect the derived merger statistics with morphology, dynamical and star formation state of the galaxies to understand the role past accretion events have played in determining those properties. Comparisons to locally observed galaxies can then provide hints on whether morphological transformations happening after $z = 1$ are still driven by mergers or other processes, such as AGN feedback and environmental quenching.

These merger statistics and their correlations with global galaxy properties can also be compared to predictions of cosmological simulations. As the subgrid physics in cosmological, hydrodynamical simulations is calibrated to observed relations at $z = 0$, the properties of galaxies at higher redshifts in different simulations can be very discrepant (see e.g. Habouzit et al., 2022, in the case of SMBHs). Thus, these measurements will also provide new constraints to our current theoretical understanding of galaxy formation.

11.3.2 Upcoming instruments and telescopes

There are a number of upcoming instruments and telescopes, which will provide integrated spectra reaching the stellar continuum for galaxies at $z > 1$. The newest generation instrument for the VLT, MOONS (Multi Object Optical and Near-infrared Spectrograph), is planned to see first light in 2023 and aims to complement SDSS ($z < 0.2$) by surveying several hundred thousands of galaxies at redshifts $0.8 < z < 1.8$ (Maiolino et al., 2020) with spectral resolution $R \sim 4000 - 6000$. Also, the James Webb Space Telescope (JWST) and its instrument NIRSpec (Jakobsen et al., 2022) will provide integrated spectra for galaxies at $z > 1$. Thus, it is now very timely to perfect the methods presented in this thesis with current SDSS observations, such that we can derive distributions of stellar population properties and accretion fraction for these higher redshift galaxies. This would enable us to understand the evolution of accreted stellar mass over cosmic time in analogy to the cosmic star formation rate density (Madau & Dickinson, 2014). Just recently, observations of the molecular gas mass were possible at high redshifts ($z \sim 2$) thanks to ALMA (Walter et al., 2020). Producing similar measurements for the accreted stellar mass of galaxies could let us understand the interplay between star formation and merger processes in the evolution of galaxies. This can then put our theoretical knowledge of galaxy formation to the test, thanks to comparison to predictions from simulations (see Figure 11.4).

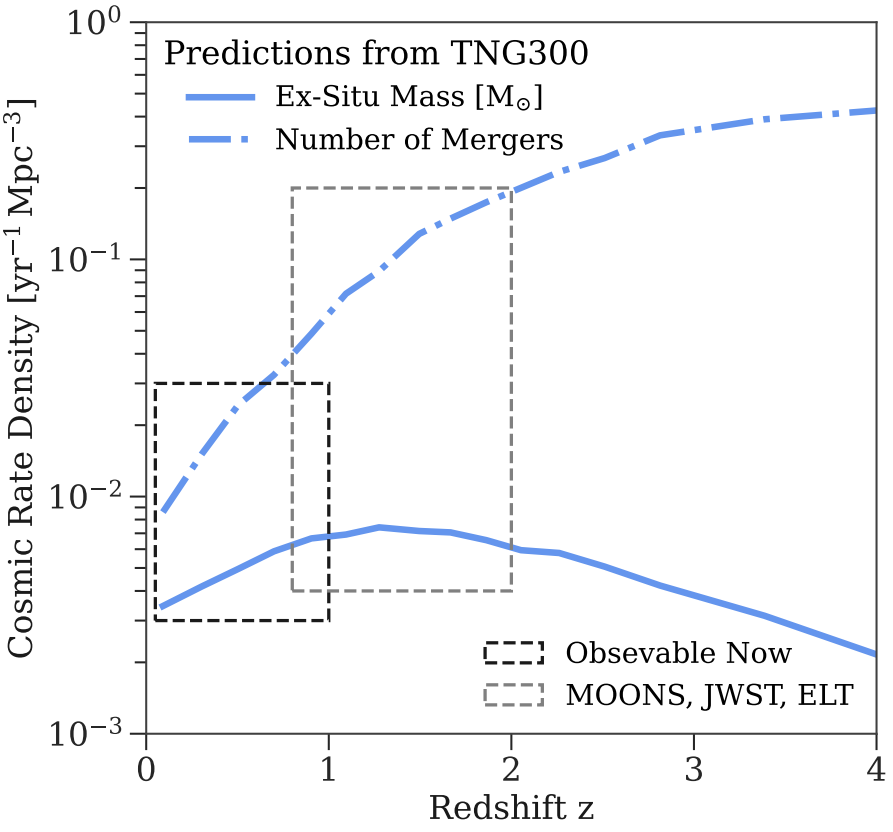

Figure 11.4. The cosmic rate density of ex-situ stellar mass (*blue solid line*) and the number of mergers (*blue dashed-dotted line*) as predicted by TNG300. Techniques presented in this thesis can provide measurements on ex-situ fractions for low redshifts galaxies with current spectroscopic and IFU observations (*black dashed box*). This prepares for upcoming instruments and telescopes, providing integrated spectra of galaxies, that reach the stellar continuum at $z > 1$ (*grey dashed box*).

Furthermore, the IFU capabilities of NIRSpec as well as HARMONI (Thatte et al., 2021), the first light IFU instrument planned for the Extremely Large Telescope (ELT), will provide spatially resolved spectroscopic information for the nuclear regions of galaxies. The studies performed in this thesis, both via observational and theoretical models, provide an ideal preparation to analyse and interpret of such new measurements.

12 CONCLUSION

In this thesis I combined modelling techniques, observations and simulations to build the foundation towards illuminating past merger events of individual galaxies by extracting their complex stellar population properties from their bright central regions. These accretion events are not only an integral part of galaxy formation and evolution itself, but also a key prediction of the cosmology galaxies form in. Therefore, the contribution of past mergers events to a galaxy's stellar mass build-up needs to be quantified for statistical samples of galaxies, which I showed is possible by using widely available integrated spectra. The work presented in this thesis is therefore able to answer the three questions presented in the introduction:

1) How reliable are current techniques in recovering distributions of ages and metallicities from integrated spectra to understand the mass assembly of galaxies?

Current techniques are able to extract distributions of ages and metallicities from integrated spectra, with results comparable to those retrieved from individually resolved stars. Nevertheless, due to the intrinsic degeneracies and uncertainties connected to stellar population models, the full spectral fitting method used throughout this thesis would benefit from a better statistical modelling approach.

2) How much is the stellar assembly in the center of galaxies influenced by the individual galaxy's merger history?

The state-of-the-art, high resolution cosmological hydrodynamical simulation TNG50 predicts a diverse assembly history for central regions of all galaxies, closely connected with each unique galaxy merger history and interaction pathway.

3) Are the properties of stars of different origins as predicted by simulations different enough to be detected from currently available integrated spectra?

A first application to galaxies from SDSS shows indeed signatures in their distributions of ages and metallicities that point towards past accretion events. However, the method for quantifying individual accretion fraction of galaxies needs to be refined further and continuously tested with realistic mock observations from simulations.

Current public data sets of large spectroscopic and IFU surveys can already facilitate the measurement of age-metallicity distributions and

accretion histories of nearby galaxies, which will be expanded even more in the near future for higher redshifts with upcoming instruments. Thus, it is now crucial to continue to perfect these applications, which will only be possible through synergies between observations and simulations as demonstrated in this thesis. Together, this will provide an unprecedented view on the emergence of the diverse galaxy population embedded in a cosmological context.

MY PUBLICATIONS

First Author

Boecker A., Alfaro-Cuello M., Neumayer N., Martín-Navarro I., Leaman R., 2020b, ApJ, 896, 13
Used in this Thesis in Chapter 5

Boecker A., Leaman R., van de Ven G., Norris M. A., Mackereth, J. T., Crain, R. A., 2020a, MNRAS, 491, 823
Used partially in this Thesis in Chapter 8

Co-authored

Davison T. A., Norris M. A., Leaman R., Kuntschner H., Boecker A., van de Ven G., 2021, MNRAS, 507, 3089
Not used in this Thesis

Leaman R., Ruiz-Lara T., Cole A. A., Beasley M. A., Boecker A., Fahrion K., Bianchini P., Falcón-Barroso J., Webb J., Sills A., Mastrobuono-Battisti A., Neumayer N., Sippel A., 2020, MNRAS, 492, 5102
Not used in this Thesis

REFERENCES

Aarseth S. J., Gott J. R. I., Turner E. L., 1979, ApJ, 228, 664

Abadi M. G., Moore B., Bower R. G., 1999, MNRAS, 308, 947

Abadi M. G., Navarro J. F., Steinmetz M., Eke V. R., 2003, ApJ, 597, 21

Abazajian K. N., et al., 2009, ApJS, 182, 543

Abbott B. P., et al., 2016, Phys. Rev. Lett., 116, 061102

Abbott B. P., et al., 2017, ApJ, 848, L12

Abdurro'uf et al., 2022, ApJS, 259, 35

Abell G. O., 1958, ApJS, 3, 211

Abell G. O., Corwin Harold G. J., Olowin R. P., 1989, ApJS, 70, 1

Agarwal M., Milosavljević M., 2011, ApJ, 729, 35

Agertz O., et al., 2007, MNRAS, 380, 963

Agertz O., Kravtsov A. V., Leitner S. N., Gnedin N. Y., 2013, ApJ, 770, 25

Agertz O., et al., 2020, MNRAS, 491, 1656

Aguerri J. A. L., Balcells M., Peletier R. F., 2001, A&A, 367, 428

Aguerri J. A. L., Méndez-Abreu J., Corsini E. M., 2009, A&A, 495, 491

Aharon D., Perets H. B., 2015, ApJ, 799, 185

Aihara H., et al., 2018, PASJ, 70, S4

Aihara H., et al., 2022, PASJ, 74, 247

Alfaro-Cuello M., et al., 2019, ApJ, 886, 57

Alfaro-Cuello M., et al., 2020, ApJ, 892, 20

Allen J. T., et al., 2015, MNRAS, 446, 1567

Alpher R. A., Herman R., 1948, Nature, 162, 774

Alpher R. A., Bethe H., Gamow G., 1948, Physical Review, 73, 803

Anderson L., et al., 2012, MNRAS, 427, 3435

Andredakis Y. C., Peletier R. F., Balcells M., 1995, MNRAS, 275, 874

Antonini F., 2013, ApJ, 763, 62

Antonini F., Capuzzo-Dolcetta R., Mastrobuono-Battisti A., Merritt D., 2012, ApJ, 750, 111

Antonini F., Barausse E., Silk J., 2015, ApJ, 812, 72

Antonucci R., 1993, ARA&A, 31, 473

Arca-Sedda M., Capuzzo-Dolcetta R., 2014, MNRAS, 444, 3738

Arentsen A., et al., 2020, MNRAS, 491, L11

Armillotta L., Fraternali F., Marinacci F., 2016, MNRAS, 462, 4157

Arnold J. A., et al., 2014, ApJ, 791, 80

Aros F. I., Sippel A. C., Mastrobuono-Battisti A., Askar A., Bianchini P., van de Ven G., 2020, MNRAS, 499, 4646

Arp H., 1966, ApJS, 14, 1

Asa'd R. S., Vazdekis A., Cerviño M., Noël N. E. D., Beasley M. A., Kassab M., 2017, MNRAS, 471, 3599

Ashok A., et al., 2021, AJ, 161, 167

Asplund M., Grevesse N., Sauval A. J., Scott P., 2009, ARA&A, 47, 481

Athanassoula E., 1992, MNRAS, 259, 345

Athanassoula E., 2003, MNRAS, 341, 1179

Athanassoula E., 2005, MNRAS, 358, 1477

Athanassoula E., Machado R. E. G., Rodionov S. A., 2013, MNRAS, 429, 1949

Bañados E., et al., 2018, Nature, 553, 473

Babusiaux C., et al., 2010, A&A, 519, A77

Bacon R., et al., 2001, MNRAS, 326, 23

Bacon R., et al., 2014, The Messenger, 157, 13

Baes M., Verstappen J., De Looze I., Fritz J., Saftly W., Vidal Pérez E., Stalevski M., Valcke S., 2011, ApJS, 196, 22

Bakos J., Trujillo I., Pohlen M., 2008, ApJ, 683, L103

Balcells M., Peletier R. F., 1994, AJ, 107, 135

Balcells M., Quinn P. J., 1990, ApJ, 361, 381

Balcells M., Graham A. W., Domínguez-Palmero L., Peletier R. F., 2003, ApJ, 582, L79

Balcells M., Graham A. W., Peletier R. F., 2007, ApJ, 665, 1084

Baldry I. K., Glazebrook K., Brinkmann J., Ivezić Ž., Lupton R. H., Nichol R. C., Szalay A. S., 2004, ApJ, 600, 681

Baldry I. K., Balogh M. L., Bower R. G., Glazebrook K., Nichol R. C., Bamford S. P., Budavari T., 2006, MNRAS, 373, 469

Baldwin C., McDermid R. M., Kuntschner H., Maraston C., Conroy C., 2018, MNRAS, 473, 4698

Balogh M. L., Navarro J. F., Morris S. L., 2000, ApJ, 540, 113

Bania T. M., Rood R. T., Balser D. S., 2002, Nature, 415, 54

Barazza F. D., Jogee S., Marinova I., 2008, ApJ, 675, 1194

Barbuy B., Chiappini C., Gerhard O., 2018, ARA&A, 56, 223

Barmby P., et al., 2006, ApJ, 650, L45

Barnes J. E., 1988, ApJ, 331, 699

Barnes J. E., Hernquist L. E., 1991, ApJ, 370, L65

Barnes J. E., Hernquist L., 1996, ApJ, 471, 115

Barnes J., Hut P., 1986, Nature, 324, 446

Barone T. M., et al., 2018, ApJ, 856, 64

Barone T. M., D'Eugenio F., Colless M., Scott N., 2020, ApJ, 898, 62

Barone T. M., et al., 2022, MNRAS, 512, 3828

Bastian N., Covey K. R., Meyer M. R., 2010, ARA&A, 48, 339

Baumgardt H., Hilker M., 2018, MNRAS, 478, 1520

Beasley M. A., Trujillo I., Leaman R., Montes M., 2018, Nature, 555, 483

Bekki K., Freeman K. C., 2003, MNRAS, 346, L11

Bekki K., Couch W. J., Shioya Y., 2006, ApJ, 642, L133

Bell E. F., McIntosh D. H., Katz N., Weinberg M. D., 2003, ApJS, 149, 289

Bell E. F., et al., 2004, ApJ, 608, 752

Bell E. F., et al., 2008, ApJ, 680, 295

Bellazzini M., et al., 2008, AJ, 136, 1147

Belokurov V., et al., 2007, ApJ, 654, 897

Belokurov V., Erkal D., Evans N. W., Koposov S. E., Deason A. J., 2018, MNRAS, 478, 611

Bender R., Doebereiner S., Moellenhoff C., 1988, A&AS, 74, 385

Bennett C. L., et al., 2013, ApJS, 208, 20

Berger M. J., Colella P., 1989, Journal of Computational Physics, 82, 64

Bertelli G., Bressan A., Chiosi C., Fagotto F., Nasi E., 1994, A&AS, 106, 275

Bethe H. A., 1939, Physical Review, 55, 434

Bezanson R., et al., 2018, ApJ, 858, 60

Bigiel F., Leroy A., Walter F., Brinks E., de Blok W. J. G., Madore B., Thornley M. D., 2008, AJ, 136, 2846

Bílek M., et al., 2020, MNRAS, 498, 2138

Binggeli B., Sandage A., Tammann G. A., 1985, AJ, 90, 1681

Binney J., 1978, Comments on Astrophysics, 8, 27

Binney J., Tremaine S., 2008, Galactic Dynamics: Second Edition

Bird J. C., Kazantzidis S., Weinberg D. H., Guedes J., Callegari S., Mayer L., Madau P., 2013, ApJ, 773, 43

Birnboim Y., Dekel A., 2003, MNRAS, 345, 349

Bittner A., et al., 2020, A&A, 643, A65

Blakeslee J. P., Tonry J. L., Metzger M. R., 1997, AJ, 114, 482

Bland-Hawthorn J., Gerhard O., 2016, ARA&A, 54, 529

Blanton M. R., et al., 2003, ApJ, 592, 819

de Blok W. J. G., 2010, Advances in Astronomy, 2010, 789293

Blumenthal G. R., Faber S. M., Primack J. R., Rees M. J., 1984, Nature, 311, 517

Blumenthal G. R., Faber S. M., Flores R., Primack J. R., 1986, ApJ, 301, 27

Bocquet S., Saro A., Dolag K., Mohr J. J., 2016, MNRAS, 456, 2361

Boecker A., Leaman R., van de Ven G., Norris M. A., Mackereth J. T., Crain R. A., 2020a, MNRAS, 491, 823

Boecker A., Alfaro-Cuello M., Neumayer N., Martín-Navarro I., Leaman R., 2020b, ApJ, 896, 13

de Boer T. J. L., Belokurov V., Beers T. C., Lee Y. S., 2014, MNRAS, 443, 658

de Boer T. J. L., Belokurov V., Koposov S., 2015, MNRAS, 451, 3489

Bois M., et al., 2011, MNRAS, 416, 1654

Böker T., Laine S., van der Marel R. P., Sarzi M., Rix H.-W., Ho L. C., Shields J. C., 2002, AJ, 123, 1389

Böker T., Sarzi M., McLaughlin D. E., van der Marel R. P., Rix H.-W., Ho L. C., Shields J. C., 2004, AJ, 127, 105

Bond J. R., Efstathiou G., 1984, ApJ, 285, L45

Bond J. R., Kofman L., Pogosyan D., 1996, Nature, 380, 603

van den Bosch F. C., 2001, MNRAS, 327, 1334

van den Bosch R. C. E., 2016, ApJ, 831, 134

van den Bosch F. C., Burkert A., Swaters R. A., 2001, MNRAS, 326, 1205

van den Bosch R. C. E., van de Ven G., Verolme E. K., Cappellari M., de Zeeuw P. T., 2008a, MNRAS, 385, 647

van den Bosch F. C., Aquino D., Yang X., Mo H. J., Pasquali A., McIntosh D. H., Weinmann S. M., Kang X., 2008b, MNRAS, 387, 79

Boselli A., Gavazzi G., 2006, PASP, 118, 517

Bottema R., 2003, MNRAS, 344, 358

Bournaud F., Combes F., Semelin B., 2005, MNRAS, 364, L18

Bournaud F., Elmegreen B. G., Elmegreen D. M., 2007, ApJ, 670, 237

Bournaud F., et al., 2014, ApJ, 780, 57

Bovy J., Rix H.-W., 2013, ApJ, 779, 115

Bovy J., Rix H.-W., Liu C., Hogg D. W., Beers T. C., Lee Y. S., 2012, ApJ, 753, 148

Bovy J., Rix H.-W., Schlafly E. F., Nidever D. L., Holtzman J. A., Shetrone M., Beers T. C., 2016, ApJ, 823, 30

Bower R. G., Benson A. J., Malbon R., Helly J. C., Frenk C. S., Baugh C. M., Cole S., Lacey C. G., 2006, MNRAS, 370, 645

Bremer M. N., et al., 2018, MNRAS, 476, 12

Bressan A., Marigo P., Girardi L., Salasnich B., Dal Cero C., Rubele S., Nanni A., 2012, MNRAS, 427, 127

Brinchmann J., Charlot S., White S. D. M., Tremonti C., Kauffmann G., Heckman T., Brinkmann J., 2004, MNRAS, 351, 1151

Brodie J. P., Strader J., 2006, ARA&A, 44, 193

den Brok M., et al., 2014, MNRAS, 445, 2385

Bromm V., Larson R. B., 2004, ARA&A, 42, 79

Brook C. B., Kawata D., Gibson B. K., Freeman K. C., 2004, ApJ, 612, 894

Brook C. B., Stinson G., Gibson B. K., Roškar R., Wadsley J., Quinn T., 2012, MNRAS, 419, 771

Brooks A. M., Governato F., Quinn T., Brook C. B., Wadsley J., 2009, ApJ, 694, 396

Brown G., Gnedin O. Y., Li H., 2018, ApJ, 864, 94

Bruzual G., Charlot S., 2003, MNRAS, 344, 1000

Bryant J. J., et al., 2015, MNRAS, 447, 2857

Buck T., Macciò A. V., Obreja A., Dutton A. A., Domínguez-Tenreiro R., Granato G. L., 2017, MNRAS, 468, 3628

Buck T., Macciò A. V., Dutton A. A., Obreja A., Frings J., 2019, MNRAS, 483, 1314

Buck T., Obreja A., Macciò A. V., Minchev I., Dutton A. A., Ostriker J. P., 2020, MNRAS, 491, 3461

Buck T., Rybizki J., Buder S., Obreja A., Macciò A. V., Pfrommer C., Steinmetz M., Ness M., 2021, MNRAS, 508, 3365

Buder S., et al., 2018, MNRAS, 478, 4513

Bullock J. S., Johnston K. V., 2005, ApJ, 635, 931

Bullock J. S., Kolatt T. S., Sigad Y., Somerville R. S., Kravtsov A. V., Klypin A. A., Primack J. R., Dekel A., 2001a, MNRAS, 321, 559

Bullock J. S., Dekel A., Kolatt T. S., Kravtsov A. V., Klypin A. A., Porciani C., Primack J. R., 2001b, ApJ, 555, 240

Bundy K., et al., 2015, ApJ, 798, 7

Burbidge E. M., Burbidge G. R., Fowler W. A., Hoyle F., 1957, Reviews of Modern Physics, 29, 547

Butcher H., Oemler A. J., 1978, ApJ, 219, 18

Calabrò A., et al., 2019, A&A, 632, A98

Calzetti D., Kinney A. L., Storchi-Bergmann T., 1994, ApJ, 429, 582

Camps P., Baes M., 2015, Astronomy and Computing, 9, 20

Capaccioli M., et al., 2015, A&A, 581, A10

Cappellari M., 2008, MNRAS, 390, 71

Cappellari M., 2017, MNRAS, 466, 798

Cappellari M., 2020, MNRAS, 494, 4819

Cappellari M., Emsellem E., 2004, PASP, 116, 138

Cappellari M., et al., 2006, MNRAS, 366, 1126

Cappellari M., et al., 2011a, MNRAS, 413, 813

Cappellari M., et al., 2011b, MNRAS, 416, 1680

Cappellari M., et al., 2012, Nature, 484, 485

Cappellari M., et al., 2013a, MNRAS, 432, 1709

Cappellari M., et al., 2013b, MNRAS, 432, 1862

Cardelli J. A., Clayton G. C., Mathis J. S., 1989, ApJ, 345, 245

Carnall A. C., 2017, arXiv e-prints, p. arXiv:1705.05165

Carnall A. C., McLure R. J., Dunlop J. S., Davé R., 2018, MNRAS, 480, 4379

Carnall A. C., Leja J., Johnson B. D., McLure R. J., Dunlop J. S., Conroy C., 2019, ApJ, 873, 44

Carollo C. M., Stiavelli M., de Zeeuw P. T., Mack J., 1997, AJ, 114, 2366

Carollo D., et al., 2010, ApJ, 712, 692

Carretta E., et al., 2010a, A&A, 520, A95

Carretta E., et al., 2010b, ApJ, 714, L7

Carson D. J., Barth A. J., Seth A. C., den Brok M., Cappellari M., Greene J. E., Ho L. C., Neumayer N., 2015, AJ, 149, 170

Carter D., et al., 2009, MNRAS, 397, 695

Cavaliere A. G., Gursky H., Tucker W. H., 1971, Nature, 231, 437

Cenarro A. J., Cardiel N., Gorgas J., Peletier R. F., Vazdekis A., Prada F., 2001, MNRAS, 326, 959

Chabrier G., 2003, PASP, 115, 763

Charbonnel C., Primas F., 2005, A&A, 442, 961

Charlot S., Fall S. M., 2000, ApJ, 539, 718

Chauke P., et al., 2018, ApJ, 861, 13

Chen Y.-P., Trager S. C., Peletier R. F., Lançon A., Vazdekis A., Prugniel P., Silva D. R., Gonneau A., 2014, A&A, 565, A117

Chen Z., et al., 2020, ApJ, 897, 102

Cheung E., et al., 2013, ApJ, 779, 162

Chevallard J., Charlot S., 2016, MNRAS, 462, 1415

Choi J., Dotter A., Conroy C., Cantiello M., Paxton B., Johnson B. D., 2016, ApJ, 823, 102

Cid Fernandes R., González Delgado R. M., 2010, MNRAS, 403, 780

Cid Fernandes R., Mateus A., Sodré L., Stasińska G., Gomes J. M., 2005, MNRAS, 358, 363

Cid Fernandes R., et al., 2013, A&A, 557, A86

Ciddor P. E., 1996, Appl. Opt., 35, 1566

Cisternas M., et al., 2011, ApJ, 726, 57

Clayton D. D., Fowler W. A., Hull T. E., Zimmerman B. A., 1961, Annals of Physics, 12, 331

Coelho P. R. T., 2014, MNRAS, 440, 1027

Cole S., et al., 2001, MNRAS, 326, 255

Cole S., et al., 2005, MNRAS, 362, 505

Cole J., et al., 2020, ApJ, 890, L25

Colless M., et al., 2001, MNRAS, 328, 1039

Colucci J. E., Bernstein R. A., Cameron S., McWilliam A., Cohen J. G., 2009, ApJ, 704, 385

Combes F., Young L. M., Bureau M., 2007, MNRAS, 377, 1795

Comparat J., et al., 2017, arXiv e-prints, p. arXiv:1711.06575

Conroy C., 2013, ARA&A, 51, 393

Conroy C., Gunn J. E., 2010, ApJ, 712, 833

Conroy C., van Dokkum P., 2012a, ApJ, 747, 69

Conroy C., van Dokkum P. G., 2012b, ApJ, 760, 71

Conroy C., Gunn J. E., White M., 2009, ApJ, 699, 486

Conroy C., White M., Gunn J. E., 2010, ApJ, 708, 58

Conroy C., Graves G. J., van Dokkum P. G., 2014, ApJ, 780, 33

Conroy C., Villaume A., van Dokkum P. G., Lind K., 2018, ApJ, 854, 139

Cooper M. C., et al., 2007, MNRAS, 376, 1445

Cooper A. P., et al., 2010, MNRAS, 406, 744

Côté P., et al., 2006, ApJS, 165, 57

Côté P., et al., 2007, ApJ, 671, 1456

Courteau S., Dutton A. A., van den Bosch F. C., MacArthur L. A., Dekel A., McIntosh D. H., Dale D. A., 2007, ApJ, 671, 203

Courteau S., Widrow L. M., McDonald M., Guhathakurta P., Gilbert K. M., Zhu Y., Beaton R. L., Majewski S. R., 2011, ApJ, 739, 20

Cox T. J., Dutta S. N., Di Matteo T., Hernquist L., Hopkins P. F., Robertson B., Springel V., 2006, ApJ, 650, 791

Cox T. J., Jonsson P., Somerville R. S., Primack J. R., Dekel A., 2008, MNRAS, 384, 386

Crain R. A., et al., 2015, MNRAS, 450, 1937

Crnojević D., et al., 2016, ApJ, 823, 19

Croom S. M., et al., 2021, MNRAS, 505, 991

Croton D. J., et al., 2006, MNRAS, 365, 11

Curtis H. D., 1917, PASP, 29, 206

Cyburt R. H., Fields B. D., Olive K. A., Yeh T.-H., 2016, Reviews of Modern Physics, 88, 015004

D'Souza R., Bell E. F., 2018a, Nature Astronomy, 2, 737

D'Souza R., Bell E. F., 2018b, MNRAS, 474, 5300

D'Souza R., Kauffman G., Wang J., Vegetti S., 2014, MNRAS, 443, 1433

Daddi E., et al., 2007, ApJ, 670, 156

Dahmer-Hahn L. G., Riffel R., Rodríguez-Ardila A., Martins L. P., Kehrig C., Heckman T. M., Pastoriza M. G., Dametto N. Z., 2018, MNRAS, 476, 4459

Dalcanton J. J., 2007, ApJ, 658, 941

Dalgleish H., et al., 2020, MNRAS, p. 143

Dalton G., et al., 2020, in Society of Photo-Optical Instrumentation Engineers (SPIE) Conference Series. p. 1144714, doi:10.1117/12.2561067

Darvish B., Mobasher B., Sobral D., Rettura A., Scoville N., Faisst A., Capak P., 2016, ApJ, 825, 113

Davé R., Anglés-Alcázar D., Narayanan D., Li Q., Rafieferantsoa M. H., Appleby S., 2019, MNRAS, 486, 2827

Davies R. L., Efstathiou G., Fall S. M., Illingworth G., Schechter P. L., 1983, ApJ, 266, 41

Davies R. L., Sadler E. M., Peletier R. F., 1993, MNRAS, 262, 650

Davis M., Efstathiou G., Frenk C. S., White S. D. M., 1985, ApJ, 292, 371

Davis B. L., Graham A. W., Cameron E., 2019, ApJ, 873, 85

Davison T. A., Norris M. A., Pfeffer J. L., Davies J. J., Crain R. A., 2020, MNRAS, 497, 81

Davison T. A., Norris M. A., Leaman R., Kuntschner H., Boecker A., van de Ven G., 2021, MNRAS, 507, 3089

Dawson K. S., et al., 2013, AJ, 145, 10

De Lucia G., et al., 2007, MNRAS, 374, 809

Dekel A., Krumholz M. R., 2013, MNRAS, 432, 455

Dekel A., Silk J., 1986, ApJ, 303, 39

Dekel A., Sari R., Ceverino D., 2009, ApJ, 703, 785

Dekel A., Mandelker N., Bournaud F., Ceverino D., Guo Y., primack J., 2021, arXiv e-prints, p. arXiv:2107.13561

Di Matteo T., Springel V., Hernquist L., 2005, Nature, 433, 604

Di Matteo P., Combes F., Melchior A. L., Semelin B., 2007, A&A, 468, 61

Di Matteo P., Bournaud F., Martig M., Combes F., Melchior A. L., Semelin B., 2008, A&A, 492, 31

Di Matteo P., Pipino A., Lehnert M. D., Combes F., Semelin B., 2009, A&A, 499, 427

Di Valentino E., et al., 2021, Classical and Quantum Gravity, 38, 153001

Díaz-García S., Salo H., Laurikainen E., Herrera-Endoqui M., 2016a, A&A, 587, A160

Díaz-García S., Salo H., Laurikainen E., 2016b, A&A, 596, A84

Dicke R. H., Peebles P. J. E., Roll P. G., Wilkinson D. T., 1965, ApJ, 142, 414

Djorgovski S., Davis M., 1987, ApJ, 313, 59

Do T., Ghez A. M., Morris M. R., Lu J. R., Matthews K., Yelda S., Larkin J., 2009, ApJ, 703, 1323

Do T., Lu J. R., Ghez A. M., Morris M. R., Yelda S., Martinez G. D., Wright S. A., Matthews K., 2013, ApJ, 764, 154

Do T., David Martinez G., Kerzendorf W., Feldmeier-Krause A., Arca Sedda M., Neumayer N., Gualandris A., 2020, ApJ, 901, L28

Dobbs C., Baba J., 2014, Publ. Astron. Soc. Australia, 31, e035

van Dokkum P. G., 2008, ApJ, 674, 29

van Dokkum P. G., Conroy C., 2010, Nature, 468, 940

van Dokkum P. G., Franx M., 2001, ApJ, 553, 90

van Dokkum P. G., et al., 2008, ApJ, 677, L5

van Dokkum P. G., et al., 2010, ApJ, 709, 1018

Donnari M., et al., 2019, MNRAS, 485, 4817

Donnari M., et al., 2021a, MNRAS, 500, 4004

Donnari M., Pillepich A., Nelson D., Marinacci F., Vogelsberger M., Hernquist L., 2021b, MNRAS, 506, 4760

Dotter A., 2016, ApJS, 222, 8

Dotter A., Chaboyer B., Jevremović D., Kostov V., Baron E., Ferguson J. W., 2008, ApJS, 178, 89

Dressler A., 1980, ApJ, 236, 351

Dressler A., Gunn J. E., 1983, ApJ, 270, 7

Dressler A., et al., 1997, ApJ, 490, 577

Dressler A., Smail I., Poggianti B. M., Butcher H., Couch W. J., Ellis R. S., Oemler Augustus J., 1999, ApJS, 122, 51

Dreyer J. L. E., 1888, Mem. RAS, 49, 1

Dreyer J. L. E., 1895, Mem. RAS, 51, 185

Dreyer J. L. E., 1910, Mem. RAS, 59, 105

Drinkwater M. J., Jones J. B., Gregg M. D., Phillipps S., 2000, Publ. Astron. Soc. Australia, 17, 227

Drinkwater M. J., Gregg M. D., Hilker M., Bekki K., Couch W. J., Ferguson H. C., Jones J. B., Phillipps S., 2003, Nature, 423, 519

Du M., Ho L. C., Debattista V. P., Pillepich A., Nelson D., Zhao D., Hernquist L., 2020, ApJ, 895, 139

Dubois Y., et al., 2014, MNRAS, 444, 1453

Dubois Y., Peirani S., Pichon C., Devriendt J., Gavazzi R., Welker C., Volonteri M., 2016, MNRAS, 463, 3948

Duc P.-A., 2020, arXiv e-prints, p. arXiv:2007.13874

Duc P.-A., et al., 2015, MNRAS, 446, 120

Durrell P. R., et al., 2014, ApJ, 794, 103

Dutton A. A., van den Bosch F. C., Dekel A., 2010, MNRAS, 405, 1690

Eckert D., Gaspari M., Gastaldello F., Le Brun A. M. C., O'Sullivan E., 2021, Universe, 7, 142

Eddington A. S., 1926, The Internal Constitution of the Stars

Edmunds M. G., 1990, MNRAS, 246, 678

Efstathiou G., Jones B. J. T., 1979, MNRAS, 186, 133

Eggen O. J., Lynden-Bell D., Sandage A. R., 1962, ApJ, 136, 748

Einstein A., 1917, Sitzungsberichte der Königlich Preußischen Akademie der Wissenschaften (Berlin), pp 142–152

Eisenstein D. J., et al., 2005, ApJ, 633, 560

Eldridge J. J., Stanway E. R., Xiao L., McClelland L. A. S., Taylor G., Ng M., Greis S. M. L., Bray J. C., 2017, Publ. Astron. Soc. Australia, 34, e058

Elmegreen B. G., 1990, Annals of the New York Academy of Sciences, 596, 40

Elmegreen D. M., Elmegreen B. G., Ravindranath S., Coe D. A., 2007, ApJ, 658, 763

Elmegreen B. G., Bournaud F., Elmegreen D. M., 2008, ApJ, 688, 67

Elmegreen D. M., Elmegreen B. G., Marcus M. T., Shahinyan K., Yau A., Petersen M., 2009, ApJ, 701, 306

Elmegreen D. M., et al., 2011, ApJ, 737, 32

Emsellem E., et al., 2007, MNRAS, 379, 401

Emsellem E., et al., 2011, MNRAS, 414, 888

Engler C., et al., 2021, MNRAS, 507, 4211

Erwin P., 2005, MNRAS, 364, 283

Erwin P., 2018, MNRAS, 474, 5372

Event Horizon Telescope Collaboration et al., 2019, ApJ, 875, L1

Faber S. M., Jackson R. E., 1976, ApJ, 204, 668

Fabian A. C., 2012, ARA&A, 50, 455

Fabricius M. H., Saglia R. P., Fisher D. B., Drory N., Bender R., Hopp U., 2012, ApJ, 754, 67

Fahrion K., et al., 2021, A&A, 650, A137

Falcón-Barroso J., et al., 2004, MNRAS, 350, 35

Fall S. M., Efstathiou G., 1980, MNRAS, 193, 189

Fan Z., de Grijs R., Chen B., Jiang L., Bian F., Li Z., 2016, AJ, 152, 208

Fanidakis N., Baugh C. M., Benson A. J., Bower R. G., Cole S., Done C., Frenk C. S., 2011, MNRAS, 410, 53

Farouki R., Shapiro S. L., 1981, ApJ, 243, 32

Faucher-Giguère C.-A., Lidz A., Zaldarriaga M., Hernquist L., 2009, ApJ, 703, 1416

Feldmeier-Krause A., et al., 2015, A&A, 584, A2

Feldmeier-Krause A., Kerzendorf W., Neumayer N., Schödel R., Nogueras-Lara F., Do T., de Zeeuw P. T., Kuntschner H., 2017a, MNRAS, 464, 194

Feldmeier-Krause A., Zhu L., Neumayer N., van de Ven G., de Zeeuw P. T., Schödel R., 2017b, MNRAS, 466, 4040

Feldmeier-Krause A., et al., 2020, MNRAS, 494, 396

Feldmeier A., et al., 2014, A&A, 570, A2

Fellhauer M., Kroupa P., 2002, MNRAS, 330, 642

Ferrarese L., et al., 2006a, ApJS, 164, 334

Ferrarese L., et al., 2006b, ApJ, 644, L21

Fisher D. B., 2006, ApJ, 642, L17

Fisher D. B., Drory N., 2008, AJ, 136, 773

Fisher D. B., Drory N., 2010, ApJ, 716, 942

Fisher D. B., Drory N., 2011, ApJ, 733, L47

Fitzpatrick E. L., 1999, PASP, 111, 63

Fixsen D. J., Cheng E. S., Gales J. M., Mather J. C., Shafer R. A., Wright E. L., 1996, ApJ, 473, 576

Forbes D. A., Brodie J. P., Grillmair C. J., 1997, AJ, 113, 1652

Foster C., et al., 2021, Publ. Astron. Soc. Australia, 38, e031

Fragkoudi F., et al., 2020, MNRAS, 494, 5936

Frankel N., Sanders J., Ting Y.-S., Rix H.-W., 2020, ApJ, 896, 15

Frankel N., et al., 2022, arXiv e-prints, p. arXiv:2201.08406

Franx M., Illingworth G., Heckman T., 1989, ApJ, 344, 613

Freeman K. C., 1970, ApJ, 160, 811

Frenk C. S., White S. D. M., Davis M., 1983, ApJ, 271, 417

Friedmann A., 1922, Zeitschrift fur Physik, 10, 377

Gadotti D. A., 2009, MNRAS, 393, 1531

Gadotti D. A., Kauffmann G., 2009, MNRAS, 399, 621

Gadotti D. A., dos Anjos S., 2001, AJ, 122, 1298

Gadotti D. A., et al., 2020, A&A, 643, A14

Gaia Collaboration et al., 2018a, A&A, 616, A1

Gaia Collaboration et al., 2018b, A&A, 616, A10

Gallart C., Zoccali M., Aparicio A., 2005, ARA&A, 43, 387

Gallart C., Aparicio A., Cassisi S., Hidalgo S. L., Monelli M., Noël N. E. D., Zoccali M., 2008, Mem. Soc. Astron. Italiana, 79, 324

Gallart C., Bernard E. J., Brook C. B., Ruiz-Lara T., Cassisi S., Hill V., Monelli M., 2019, Nature Astronomy, 3, 932

Gallazzi A., Charlot S., Brinchmann J., White S. D. M., Tremonti C. A., 2005, MNRAS, 362, 41

Gallazzi A., Charlot S., Brinchmann J., White S. D. M., 2006, MNRAS, 370, 1106

Gallazzi A. R., Pasquali A., Zibetti S., Barbera F. L., 2021, MNRAS, 502, 4457

Gamow G., 1946, Physical Review, 70, 572

García-Benito R., et al., 2015, A&A, 576, A135

Gargiulo I. D., et al., 2021, arXiv e-prints, p. arXiv:2111.13712

Garnett D. R., 2002, ApJ, 581, 1019

Ge J., Yan R., Cappellari M., Mao S., Li H., Lu Y., 2018, MNRAS, 478, 2633

Ge J., Mao S., Lu Y., Cappellari M., Yan R., 2019, MNRAS, 485, 1675

Geller M. J., Huchra J. P., 1989, Science, 246, 897

Genel S., et al., 2012, ApJ, 745, 11

Genel S., et al., 2014, MNRAS, 445, 175

Genel S., et al., 2018, MNRAS, 474, 3976

Genzel R., et al., 2010, MNRAS, 407, 2091

Georgiev I. Y., Böker T., 2014, MNRAS, 441, 3570

Georgiev I. Y., Hilker M., Puzia T. H., Goudfrooij P., Baumgardt H., 2009, MNRAS, 396, 1075

Georgiev I. Y., Puzia T. H., Goudfrooij P., Hilker M., 2010, MNRAS, 406, 1967

Georgiev I. Y., Goudfrooij P., Puzia T. H., 2012, MNRAS, 420, 1317

Georgiev I. Y., Böker T., Leigh N., Lützgendorf N., Neumayer N., 2016, MNRAS, 457, 2122

Gerhard O. E., 1993, MNRAS, 265, 213

Ghez A. M., et al., 2008, ApJ, 689, 1044

Gilman D., Birrer S., Nierenberg A., Treu T., Du X., Benson A., 2020, MNRAS, 491, 6077

Gilmore G., Reid N., 1983, MNRAS, 202, 1025

Gilmore G., et al., 2012, The Messenger, 147, 25

Gingold R. A., Monaghan J. J., 1977, MNRAS, 181, 375

Giocoli C., Tormen G., van den Bosch F. C., 2008, MNRAS, 386, 2135

Girardi L., Bressan A., Bertelli G., Chiosi C., 2000, A&AS, 141, 371

Gnedin O. Y., Kravtsov A. V., Klypin A. A., Nagai D., 2004, ApJ, 616, 16

Gnedin O. Y., Ostriker J. P., Tremaine S., 2014, ApJ, 785, 71

Goddard D., et al., 2017, MNRAS, 466, 4731

Gonneau A., et al., 2020, A&A, 634, A133

González Delgado R. M., Cid Fernandes R., 2010, MNRAS, 403, 797

González Delgado R. M., Cerviño M., Martins L. P., Leitherer C., Hauschildt P. H., 2005, MNRAS, 357, 945

González Delgado R. M., et al., 2014, A&A, 562, A47

González Delgado R. M., et al., 2015, A&A, 581, A103

Gonzalez O. A., et al., 2011, A&A, 530, A54

Goto T., Yamauchi C., Fujita Y., Okamura S., Sekiguchi M., Smail I., Bernardi M., Gomez P. L., 2003, MNRAS, 346, 601

Gott J. Richard I., Melott A. L., Dickinson M., 1986, ApJ, 306, 341

Goudfrooij P., Hansen L., Jorgensen H. E., Norgaard-Nielsen H. U., 1994, A&AS, 105, 341

Governato F., et al., 2009, MNRAS, 398, 312

Graham A. W., Guzmán R., 2003, AJ, 125, 2936

Grand R. J. J., Springel V., Gómez F. A., Marinacci F., Pakmor R., Campbell D. J. R., Jenkins A., 2016, MNRAS, 459, 199

Grand R. J. J., et al., 2017, MNRAS, 467, 179

Grand R. J. J., et al., 2021, MNRAS, 507, 4953

Gratton R. G., Carretta E., Bragaglia A., Lucatello S., D'Orazi V., 2010, A&A, 517, A81

Greene J. E., Murphy J. D., Comerford J. M., Gebhardt K., Adams J. J., 2012, ApJ, 750, 32

Greene J. E., Murphy J. D., Graves G. J., Gunn J. E., Raskutti S., Comerford J. M., Gebhardt K., 2013, ApJ, 776, 64

Gregory S. A., Thompson L. A., 1978, ApJ, 222, 784

Guedes J., Callegari S., Madau P., Mayer L., 2011, ApJ, 742, 76

Guedes J., Mayer L., Carollo M., Madau P., 2013, ApJ, 772, 36

Guérou A., et al., 2017, A&A, 608, A5

Guillard N., Emsellem E., Renaud F., 2016, MNRAS, 461, 3620

Gunn J. E., Gott J. Richard I., 1972, ApJ, 176, 1

Guo Q., et al., 2011, MNRAS, 413, 101

Guo Y., et al., 2015, ApJ, 800, 39

Gursky H., Kellogg E., Murray S., Leong C., Tananbaum H., Giacconi R., 1971, ApJ, 167, L81

Guth A. H., 1981, Phys. Rev. D, 23, 347

Habouzit M., et al., 2022, MNRAS, 511, 3751

Häring N., Rix H.-W., 2004, ApJ, 604, L89

Harris W. E., 1976, AJ, 81, 1095

Harris W. E., 1996, AJ, 112, 1487

Harris W. E., 2010, arXiv e-prints, p. arXiv:1012.3224

Harris W. E., Harris G. L. H., Alessi M., 2013, ApJ, 772, 82

Hartmann M., Debattista V. P., Seth A., Cappellari M., Quinn T. R., 2011, MNRAS, 418, 2697

Hasan H., Norman C., 1990, ApJ, 361, 69

Hayden M. R., et al., 2015, ApJ, 808, 132

Hayward C. C., Hopkins P. F., 2017, MNRAS, 465, 1682

Helmi A., Babusiaux C., Koppelman H. H., Massari D., Veljanoski J., Brown A. G. A., 2018, Nature, 563, 85

Hernquist L., 1989, Nature, 340, 687

Hernquist L., 1992, ApJ, 400, 460

Hernquist L., 1993a, ApJS, 86, 389

Hernquist L., 1993b, ApJ, 409, 548

Hernquist L., Katz N., 1989, ApJS, 70, 419

Herschel W., 1785, Philosophical Transactions of the Royal Society of London Series I, 75, 213

Herschel W., 1786, Philosophical Transactions of the Royal Society of London Series I, 76, 457

Herschel W., 1789, Philosophical Transactions of the Royal Society of London Series I, 79, 212

Herschel W., 1802, Philosophical Transactions of the Royal Society of London Series I, 92, 477

Hertzsprung E., 1911, Publikationen des Astrophysikalischen Observatoriums zu Potsdam, 63

Hilker M., Infante L., Vieira G., Kissler-Patig M., Richtler T., 1999, A&AS, 134, 75

Hilz M., Naab T., Ostriker J. P., 2013, MNRAS, 429, 2924

Hirschmann M., Dolag K., Saro A., Bachmann L., Borgani S., Burkert A., 2014, MNRAS, 442, 2304

Hockney R. W., Eastwood J. W., 1988, Computer simulation using particles

Hogg D. W., Baldry I. K., Blanton M. R., Eisenstein D. J., 2002, arXiv e-prints, pp astro–ph/0210394

Holmberg E., 1941, ApJ, 94, 385

Holmberg E., 1958, Meddelanden fran Lunds Astronomiska Observatorium Serie II, 136, 1

Hood C. E., Kannappan S. J., Stark D. V., Dell'Antonio I. P., Moffett A. J., Eckert K. D., Norris M. A., Hendel D., 2018, ApJ, 857, 144

Hopkins P. F., 2013, MNRAS, 430, 1653

Hopkins P. F., Hernquist L., Cox T. J., Di Matteo T., Robertson B., Springel V., 2006, ApJS, 163, 1

Hopkins P. F., Hernquist L., Cox T. J., Kereš D., 2008, ApJS, 175, 356

Hopkins P. F., Cox T. J., Dutta S. N., Hernquist L., Kormendy J., Lauer T. R., 2009a, ApJS, 181, 135

Hopkins P. F., Lauer T. R., Cox T. J., Hernquist L., Kormendy J., 2009b, ApJS, 181, 486

Hopkins P. F., et al., 2009c, MNRAS, 397, 802

Hopkins P. F., Cox T. J., Younger J. D., Hernquist L., 2009d, ApJ, 691, 1168

Hopkins P. F., et al., 2010, ApJ, 715, 202

Hopkins P. F., Quataert E., Murray N., 2012a, MNRAS, 421, 3522

Hopkins P. F., Kereš D., Murray N., Quataert E., Hernquist L., 2012b, MNRAS, 427, 968

Hopkins P. F., Cox T. J., Hernquist L., Narayanan D., Hayward C. C., Murray N., 2013a, MNRAS, 430, 1901

Hopkins P. F., Narayanan D., Murray N., 2013b, MNRAS, 432, 2647

Hopkins P. F., et al., 2018, MNRAS, 480, 800

van Houdt J., et al., 2021, ApJ, 923, 11

Hoyer N., Neumayer N., Georgiev I. Y., Seth A. C., Greene J. E., 2021, MNRAS, 507, 3246

Hoyle F., 1946, MNRAS, 106, 343

Hoyle F., 1948, MNRAS, 108, 372

Hoyle F., 1954, ApJS, 1, 121

Hoyle F., Fowler W. A., 1960, ApJ, 132, 565

Huang G., Noschese S., Reichel L., 2016a, arXiv e-prints, p. arXiv:1602.03318

Huang S., Ho L. C., Peng C. Y., Li Z.-Y., Barth A. J., 2016b, ApJ, 821, 114

Huang S., Leauthaud A., Greene J. E., Bundy K., Lin Y.-T., Tanaka M., Miyazaki S., Komiyama Y., 2018, MNRAS, 475, 3348

Hubble E. P., 1926, ApJ, 64, 321

Hubble E., 1929a, Proceedings of the National Academy of Science, 15, 168

Hubble E. P., 1929b, ApJ, 69, 103

Hubble E., Humason M. L., 1931, ApJ, 74, 43

Hubeny I., Mihalas D., 2014, Theory of Stellar Atmospheres

Hughes M. E., Pfeffer J., Martig M., Bastian N., Crain R. A., Kruijssen J. M. D., Reina-Campos M., 2018, MNRAS,

Husser T. O., Wende-von Berg S., Dreizler S., Homeier D., Reiners A., Barman T., Hauschildt P. H., 2013, A&A, 553, A6

Ibata R. A., Gilmore G., Irwin M. J., 1994, Nature, 370, 194

Ibata R. A., et al., 2014, ApJ, 780, 128

Ilbert O., et al., 2013, A&A, 556, A55

Illingworth G., 1977, ApJ, 218, L43

Immeli A., Samland M., Gerhard O., Westera P., 2004, A&A, 413, 547

Iodice E., et al., 2016, ApJ, 820, 42

Iodice E., et al., 2019a, A&A, 623, A1

Iodice E., et al., 2019b, A&A, 627, A136

Iorio G., Belokurov V., Erkal D., Koposov S. E., Nipoti C., Fraternali F., 2018, MNRAS, 474, 2142

Jáchym P., et al., 2019, ApJ, 883, 145

Jackson T. M., Pasquali A., La Barbera F., More S., Grebel E. K., 2021, arXiv e-prints, p. arXiv:2102.02241

Jakobsen P., et al., 2022, arXiv e-prints, p. arXiv:2202.03305

Jeans J. H., 1915, MNRAS, 76, 70

Jeřábková T., Hasani Zonoozi A., Kroupa P., Beccari G., Yan Z., Vazdekis A., Zhang Z. Y., 2018, A&A, 620, A39

Jiang F., van den Bosch F. C., 2016, MNRAS, 458, 2848

Johnson B. D., Leja J., Conroy C., Speagle J. S., 2021, ApJS, 254, 22

de Jong R. S., et al., 2019, The Messenger, 175, 3

Jorgensen I., Franx M., Kjaergaard P., 1996, MNRAS, 280, 167

Joshi G. D., Pillepich A., Nelson D., Marinacci F., Springel V., Rodriguez-Gomez V., Vogelsberger M., Hernquist L., 2020, MNRAS, 496, 2673

Jurić M., et al., 2008, ApJ, 673, 864

Kacharov N., Neumayer N., Seth A. C., Cappellari M., McDermid R., Walcher C. J., Böker T., 2018, MNRAS, 480, 1973

Kamann S., Wisotzki L., Roth M. M., 2013, A&A, 549, A71

Kamann S., et al., 2018, MNRAS, 473, 5591

Kannan R., Garaldi E., Smith A., Pakmor R., Springel V., Vogelsberger M., Hernquist L., 2022, MNRAS, 511, 4005

Kant I., 1755, Allgemeine Naturgeschichte und Theorie des Himmels

Kapteyn J. C., 1922, ApJ, 55, 302

Katz N., 1992, ApJ, 391, 502

Kenney J. D. P., Koopmann R. A., 1999, AJ, 117, 181

Kennicutt R. C. J., 1981, AJ, 86, 1847

Kennicutt Robert C. J., 1989, ApJ, 344, 685

Kennicutt Robert C. J., 1998, ApJ, 498, 541

Kereš D., Katz N., Weinberg D. H., Davé R., 2005, MNRAS, 363, 2

Kimmig B., Seth A., Ivans I. I., Strader J., Caldwell N., Anderton T., Gregersen D., 2015, AJ, 149, 53

Kirby E. N., Cohen J. G., Smith G. H., Majewski S. R., Sohn S. T., Guhathakurta P., 2011, ApJ, 727, 79

Kirby E. N., Cohen J. G., Guhathakurta P., Cheng L., Bullock J. S., Gallazzi A., 2013, ApJ, 779, 102

Knowles A. T., Sansom A. E., Allende Prieto C., Vazdekis A., 2021, MNRAS, 504, 2286

Kobayashi C., 2004, MNRAS, 347, 740

Koleva M., Prugniel P., Bouchard A., Wu Y., 2009, A&A, 501, 1269

Kollatschny W., Weilbacher P. M., Ochmann M. W., Chelouche D., Monreal-Ibero A., Bacon R., Contini T., 2020, A&A, 633, A79

Kollmeier J. A., et al., 2017, arXiv e-prints, p. arXiv:1711.03234

Komatsu E., et al., 2011, ApJS, 192, 18

Kormendy J., 1977, ApJ, 218, 333

Kormendy J., 1985, ApJ, 295, 73

Kormendy J., Bender R., 2012, ApJS, 198, 2

Kormendy J., Ho L. C., 2013, ARA&A, 51, 511

Kormendy J., Illingworth G., 1982, ApJ, 256, 460

Kormendy J., Kennicutt Robert C. J., 2004, ARA&A, 42, 603

Kormendy J., Fisher D. B., Cornell M. E., Bender R., 2009, ApJS, 182, 216

Krajnović D., et al., 2011, MNRAS, 414, 2923

Krajnović D., Emsellem E., den Brok M., Marino R. A., Schmidt K. B., Steinmetz M., Weilbacher P. M., 2018, MNRAS, 477, 5327

Krajnović D., et al., 2020, A&A, 635, A129

Kraljic K., Bournaud F., Martig M., 2012, ApJ, 757, 60

Kravtsov A. V., 2013, ApJ, 764, L31

Kravtsov A. V., Borgani S., 2012, ARA&A, 50, 353

Kravtsov A. V., Klypin A. A., Khokhlov A. M., 1997, ApJS, 111, 73

Kroupa P., 2001, MNRAS, 322, 231

Kroupa P., Tout C. A., Gilmore G., 1993, MNRAS, 262, 545

Kruijssen J. M. D., Pfeffer J. L., Reina-Campos M., Crain R. A., Bastian N., 2018, MNRAS,

Krumholz M. R., McKee C. F., 2005, ApJ, 630, 250

Krumholz M. R., Dekel A., McKee C. F., 2012, ApJ, 745, 69

Kuhlen M., Vogelsberger M., Angulo R., 2012, Physics of the Dark Universe, 1, 50

Kuncarayakti H., Galbany L., Anderson J. P., Krühler T., Hamuy M., 2016, A&A, 593, A78

Kuntschner H., Lucey J. R., Smith R. J., Hudson M. J., Davies R. L., 2001, MNRAS, 323, 615

Kuntschner H., et al., 2010, MNRAS, 408, 97

Kurucz R. L., 1970, SAO Special Report, 309

Kurucz R. L., 1979, ApJS, 40, 1

La Barbera F., Ferreras I., de Carvalho R. R., Bruzual G., Charlot S., Pasquali A., Merlin E., 2012, MNRAS, 426, 2300

La Barbera F., Ferreras I., Vazdekis A., de la Rosa I. G., de Carvalho R. R., Trevisan M., Falcón-Barroso J., Ricciardelli E., 2013, MNRAS, 433, 3017

La Barbera F., Vazdekis A., Ferreras I., Pasquali A., Cappellari M., Martín-Navarro I., Schönebeck F., Falcón-Barroso J., 2016, MNRAS, 457, 1468

Lapiner S., Dekel A., Dubois Y., 2021, MNRAS, 505, 172

Larson R. B., 1974, MNRAS, 169, 229

Larson R. B., 1981, MNRAS, 194, 809

Larson R. B., 2005, MNRAS, 359, 211

Larson R. B., Tinsley B. M., Caldwell C. N., 1980, ApJ, 237, 692

Läsker R., Greene J. E., Seth A., van de Ven G., Braatz J. A., Henkel C., Lo K. Y., 2016, ApJ, 825, 3

Laurikainen E., Salo H., 2002, MNRAS, 337, 1118

Laurikainen E., Peletier R., Gadotti D., eds, 2016, Galactic Bulges Astrophysics and Space Science Library Vol. 418, doi:10.1007/978-3-319-19378-6.

Le Borgne J. F., et al., 2003, A&A, 402, 433

Le Borgne D., Rocca-Volmerange B., Prugniel P., Lançon A., Fioc M., Soubiran C., 2004, A&A, 425, 881

Leaman R., van de Ven G., 2021, MNRAS,

Leaman R., VandenBerg D. A., Mendel J. T., 2013, MNRAS, 436, 122

Leaman R., et al., 2017, MNRAS, 472, 1879

Lee Y.-W., Demarque P., Zinn R., 1994, ApJ, 423, 248

Lee Y. W., Joo J. M., Sohn Y. J., Rey S. C., Lee H. C., Walker A. R., 1999, Nature, 402, 55

Lee H.-c., Yoon S.-J., Lee Y.-W., 2000, AJ, 120, 998

Lee H., Skillman E. D., Cannon J. M., Jackson D. C., Gehrz R. D., Polomski E. F., Woodward C. E., 2006, ApJ, 647, 970

Leitherer C., et al., 1999, ApJS, 123, 3

Leja J., Johnson B. D., Conroy C., van Dokkum P. G., Byler N., 2017, ApJ, 837, 170

Leja J., Carnall A. C., Johnson B. D., Conroy C., Speagle J. S., 2019, ApJ, 876, 3

Lejeune T., Cuisinier F., Buser R., 1997, A&AS, 125, 229

Lelli F., McGaugh S. S., Schombert J. M., 2016, ApJ, 816, L14

Lemaître G., 1927, Annales de la Société Scientifique de Bruxelles, 47, 49

Lemaître G., 1931, Nature, 127, 706

Lequeux J., Peimbert M., Rayo J. F., Serrano A., Torres-Peimbert S., 1979, A&A, 80, 155

Leroy A. K., Walter F., Brinks E., Bigiel F., de Blok W. J. G., Madore B., Thornley M. D., 2008, AJ, 136, 2782

Leung G. Y. C., et al., 2018, MNRAS, 477, 254

Leung G. Y. C., Leaman R., Battaglia G., van de Ven G., Brooks A. M., Peñarrubia J., Venn K. A., 2021, MNRAS, 500, 410

Lewis I., et al., 2002, MNRAS, 334, 673

Lin C. C., Shu F. H., 1964, ApJ, 140, 646

Lin J., Dotter A., Ting Y.-S., Asplund M., 2018, MNRAS, 477, 2966

Lotz J. M., Telford R., Ferguson H. C., Miller B. W., Stiavelli M., Mack J., 2001, ApJ, 552, 572

Lucy L. B., 1977, AJ, 82, 1013

Lyubenova M., Tsatsi A., 2019, A&A, 629, A44

Macciò A. V., Dutton A. A., van den Bosch F. C., Moore B., Potter D., Stadel J., 2007, MNRAS, 378, 55

Maciejewski W., 2004, MNRAS, 354, 892

Mackereth J. T., et al., 2019, MNRAS, 482, 3426

Mackey A. D., et al., 2019, MNRAS, 484, 1756

Madau P., Dickinson M., 2014, ARA&A, 52, 415

Maiolino R., et al., 2020, The Messenger, 180, 24

Majewski S. R., et al., 2017, AJ, 154, 94

Malbon R. K., Baugh C. M., Frenk C. S., Lacey C. G., 2007, MNRAS, 382, 1394

Malmquist K. G., 1922, Meddelanden fran Lunds Astronomiska Observatorium Serie I, 100, 1

Malmquist K. G., 1925, Meddelanden fran Lunds Astronomiska Observatorium Serie I, 106, 1

Mandelker N., Dekel A., Ceverino D., Tweed D., Moody C. E., Primack J., 2014, MNRAS, 443, 3675

Mandelker N., Dekel A., Ceverino D., DeGraf C., Guo Y., Primack J., 2017, MNRAS, 464, 635

Mannucci F., Cresci G., Maiolino R., Marconi A., Gnerucci A., 2010, MNRAS, 408, 2115

Maraston C., 2005, MNRAS, 362, 799

Maraston C., Strömbäck G., 2011, MNRAS, 418, 2785

Maraston C., Daddi E., Renzini A., Cimatti A., Dickinson M., Papovich C., Pasquali A., Pirzkal N., 2006, ApJ, 652, 85

Maraston C., et al., 2020, MNRAS, 496, 2962

Marchesini D., van Dokkum P. G., Förster Schreiber N. M., Franx M., Labbé I., Wuyts S., 2009, ApJ, 701, 1765

van der Marel R. P., 1994, MNRAS, 270, 271

Marinacci F., Binney J., Fraternali F., Nipoti C., Ciotti L., Londrillo P., 2010, MNRAS, 404, 1464

Marinacci F., Pakmor R., Springel V., 2014, MNRAS, 437, 1750

Marinacci F., et al., 2018, MNRAS, 480, 5113

Martig M., et al., 2021, MNRAS, 508, 2458

Martín-Navarro I., La Barbera F., Vazdekis A., Falcón-Barroso J., Ferreras I., 2015a, MNRAS, 447, 1033

Martín-Navarro I., et al., 2015b, ApJ, 806, L31

Martín-Navarro I., Vazdekis A., Falcón-Barroso J., La Barbera F., Yıldırım A., van de Ven G., 2018a, MNRAS, 475, 3700

Martín-Navarro I., Brodie J. P., Romanowsky A. J., Ruiz-Lara T., van de Ven G., 2018b, Nature, 553, 307

Martín-Navarro I., et al., 2019, A&A, 626, A124

Martín-Navarro I., Pillepich A., Nelson D., Rodriguez-Gomez V., Donnari M., Hernquist L., Springel V., 2021a, Nature, 594, 187

Martín-Navarro I., et al., 2021b, A&A, 654, A59

Martín-Navarro I., Shankar F., Mezcua M., 2022, MNRAS, 513, L10

Martin D. C., et al., 2007, ApJS, 173, 342

Martínez-Delgado D., et al., 2010, AJ, 140, 962

Masters K. L., et al., 2011, MNRAS, 411, 2026

Mateo M. L., 1998, ARA&A, 36, 435

Mathiesen B. F., Evrard A. E., 2001, ApJ, 546, 100

Mayer L., Tamburello V., Lupi A., Keller B., Wadsley J., Madau P., 2016, ApJ, 830, L13

McConnachie A. W., 2012, AJ, 144, 4

McConnachie A. W., Irwin M. J., Ferguson A. M. N., Ibata R. A., Lewis G. F., Tanvir N., 2005, MNRAS, 356, 979

McConnachie A. W., et al., 2009, Nature, 461, 66

McDermid R. M., et al., 2006, MNRAS, 373, 906

McDermid R. M., et al., 2015, MNRAS, 448, 3484

McKee C. F., Ostriker J. P., 1977, ApJ, 218, 148

McKee C. F., Ostriker E. C., 2007, ARA&A, 45, 565

McKinnon R., Torrey P., Vogelsberger M., 2016, MNRAS, 457, 3775

Melnick J., Sargent W. L. W., 1977, ApJ, 215, 401

Méndez-Abreu J., et al., 2017, A&A, 598, A32

Meneghetti M., et al., 2017, MNRAS, 472, 3177

Mennekens N., Vanbeveren D., De Greve J. P., De Donder E., 2010, A&A, 515, A89

Merritt A., van Dokkum P., Abraham R., Zhang J., 2016, ApJ, 830, 62

Merritt A., Pillepich A., van Dokkum P., Nelson D., Hernquist L., Marinacci F., Vogelsberger M., 2020, MNRAS, 495, 4570

Messier C., 1781, Catalogue des Nébuleuses et des Amas d'Étoiles (Catalog of Nebulae and Star Clusters), Connoissance des Temps ou des Mouvements Célestes

Mihalas D., 1978, Stellar atmospheres

Mihos J. C., Hernquist L., 1994a, ApJ, 425, L13

Mihos J. C., Hernquist L., 1994b, ApJ, 431, L9

Mihos J. C., Hernquist L., 1996, ApJ, 464, 641

Miller G. E., Scalo J. M., 1979, ApJS, 41, 513

Miller Bertolami M. M., 2016, A&A, 588, A25

Milne E. A., 1928, The Observatory, 51, 88

Milone A. D. C., Sansom A. E., Sánchez-Blázquez P., 2011, MNRAS, 414, 1227

Milone A. P., et al., 2017, MNRAS, 464, 3636

Minchev I., Famaey B., 2010, ApJ, 722, 112

Minchev I., Chiappini C., Martig M., 2013, A&A, 558, A9

Minchev I., Chiappini C., Martig M., 2014, A&A, 572, A92

Mo H. J., Mao S., White S. D. M., 1998, MNRAS, 295, 319

Mo H., Van den Bosch F., White S., 2010, Galaxy formation and evolution. Cambridge University Press

Monachesi A., Bell E. F., Radburn-Smith D. J., Bailin J., de Jong R. S., Holwerda B., Streich D., Silverstein G., 2016, MNRAS, 457, 1419

Monaghan J. J., 1992, ARA&A, 30, 543

Moore B., Katz N., Lake G., Dressler A., Oemler A., 1996, Nature, 379, 613

Moore B., Lake G., Quinn T., Stadel J., 1999, MNRAS, 304, 465

Morganti R., et al., 2006, MNRAS, 371, 157

Moster B. P., Naab T., White S. D. M., 2013, MNRAS, 428, 3121

Muñoz-Cuartas J. C., Macciò A. V., Gottlöber S., Dutton A. A., 2011, MNRAS, 411, 584

Mucciarelli A., Bellazzini M., Ibata R., Romano D., Chapman S. C., Monaco L., 2017, A&A, 605, A46

Naab T., Burkert A., 2003, ApJ, 597, 893

Naab T., Ostriker J. P., 2017, ARA&A, 55, 59

Naab T., Jesseit R., Burkert A., 2006, MNRAS, 372, 839

Naab T., Johansson P. H., Ostriker J. P., 2009, ApJ, 699, L178

Naiman J. P., et al., 2018, MNRAS, 477, 1206

Nanni L., et al., 2022, arXiv e-prints, p. arXiv:2203.11575

Navarro J. F., Benz W., 1991, ApJ, 380, 320

Navarro J. F., Steinmetz M., 2000, ApJ, 538, 477

Navarro J. F., White S. D. M., 1994, MNRAS, 267, 401

Navarro J. F., Frenk C. S., White S. D. M., 1996, ApJ, 462, 563

Navarro J. F., et al., 2010, MNRAS, 402, 21

Nelson E. J., et al., 2012, ApJ, 747, L28

Nelson D., Vogelsberger M., Genel S., Sijacki D., Kereš D., Springel V., Hernquist L., 2013, MNRAS, 429, 3353

Nelson E. J., et al., 2016, ApJ, 828, 27

Nelson D., et al., 2018, MNRAS, 475, 624

Nelson D., et al., 2019a, Computational Astrophysics and Cosmology, 6, 2

Nelson D., et al., 2019b, MNRAS, 490, 3234

Nelson E. J., et al., 2021, MNRAS, 508, 219

Ness M., et al., 2013, MNRAS, 432, 2092

Netzer H., 2015, ARA&A, 53, 365

Neumann J., et al., 2021, MNRAS, 508, 4844

Neumann J., et al., 2022, arXiv e-prints, p. arXiv:2202.04082

Neumayer N., Walcher C. J., Andersen D., Sánchez S. F., Böker T., Rix H.-W., 2011, MNRAS, 413, 1875

Neumayer N., Seth A., Böker T., 2020, A&ARv, 28, 4

Noeske K. G., et al., 2007, ApJ, 660, L43

Noguchi M., 1999, ApJ, 514, 77

Nogueras-Lara F., et al., 2020, Nature Astronomy, 4, 377

Nogueras-Lara F., Schödel R., Neumayer N., 2021, ApJ, 920, 97

Noll S., Burgarella D., Giovannoli E., Buat V., Marcillac D., Muñoz-Mateos J. C., 2009, A&A, 507, 1793

O'Meara J. M., Tytler D., Kirkman D., Suzuki N., Prochaska J. X., Lubin D., Wolfe A. M., 2001, ApJ, 552, 718

Obreja A., et al., 2019, MNRAS, 487, 4424

Ocvirk P., 2010, ApJ, 709, 88

Ocvirk P., Pichon C., Lançon A., Thiébaut E., 2006a, MNRAS, 365, 46

Ocvirk P., Pichon C., Lançon A., Thiébaut E., 2006b, MNRAS, 365, 74

Ocvirk P., et al., 2016, MNRAS, 463, 1462

Oemler Augustus J., 1974, ApJ, 194, 1

Oesch P. A., et al., 2016, ApJ, 819, 129

Offner S. S. R., Clark P. C., Hennebelle P., Bastian N., Bate M. R., Hopkins P. F., Moreaux E., Whitworth A. P., 2014, in , Protostars and Planets VI. University of Arizona Press, doi:10.2458/azu_uapress_9780816531240-ch003, https://doi.org/10.2458%2Fazu_uapress_9780816531240-ch003

Okamoto T., 2013, MNRAS, 428, 718

Oklopčić A., Hopkins P. F., Feldmann R., Kereš D., Faucher-Giguère C.-A., Murray N., 2017, MNRAS, 465, 952

Olive K. A., Skillman E. D., 2004, ApJ, 617, 29

Oser L., Naab T., Ostriker J. P., Johansson P. H., 2012, ApJ, 744, 63

Oyarzún G. A., et al., 2019, ApJ, 880, 111

Pacifici C., Oh S., Oh K., Lee J., Yi S. K., 2016a, ApJ, 824, 45

Pacifici C., et al., 2016b, ApJ, 832, 79

Pakmor R., Springel V., 2013, MNRAS, 432, 176

Pakmor R., Bauer A., Springel V., 2011, MNRAS, 418, 1392

Pakmor R., Springel V., Bauer A., Mocz P., Munoz D. J., Ohlmann S. T., Schaal K., Zhu C., 2016, MNRAS, 455, 1134

Partridge R. B., Peebles P. J. E., 1967, ApJ, 147, 868

Peebles P. J. E., 1969, ApJ, 155, 393

Peebles P. J. E., 1982, ApJ, 263, L1

Peebles P. J. E., Yu J. T., 1970, ApJ, 162, 815

Peletier R. F., Balcells M., 1996, AJ, 111, 2238

Peletier R. F., Davies R. L., Illingworth G. D., Davis L. E., Cawson M., 1990, AJ, 100, 1091

Peletier R. F., et al., 2007, MNRAS, 379, 445

Peng C. Y., Ho L. C., Impey C. D., Rix H.-W., 2002, AJ, 124, 266

Peng E. W., et al., 2006, ApJ, 639, 95

Peng C. Y., Ho L. C., Impey C. D., Rix H.-W., 2010, AJ, 139, 2097

Peng Y., Maiolino R., Cochrane R., 2015, Nature, 521, 192

Penzias A. A., Wilson R. W., 1965, ApJ, 142, 419

Perets H. B., Mastrobuono-Battisti A., 2014, ApJ, 784, L44

Pérez E., et al., 2013, ApJ, 764, L1

Perlmutter S., et al., 1999, ApJ, 517, 565

Peschken N., Łokas E. L., 2019, MNRAS, 483, 2721

Pfeffer J., Baumgardt H., 2013, MNRAS, 433, 1997

Pickles A. J., 1998, PASP, 110, 863

Piersanti L., Straniero O., Cristallo S., 2007, A&A, 462, 1051

Pietrinferni A., Cassisi S., Salaris M., Castelli F., 2004, ApJ, 612, 168

Pietrinferni A., Cassisi S., Salaris M., Castelli F., 2006, ApJ, 642, 797

Pillepich A., et al., 2018a, MNRAS, 473, 4077

Pillepich A., et al., 2018b, MNRAS, 475, 648

Pillepich A., et al., 2019, MNRAS, 490, 3196

Pinna F., et al., 2019a, A&A, 623, A19

Pinna F., et al., 2019b, A&A, 625, A95

Pinna F., et al., 2021, ApJ, 921, 8

Planck Collaboration et al., 2014a, A&A, 571, A1

Planck Collaboration et al., 2014b, A&A, 571, A16

Planck Collaboration et al., 2016, A&A, 594, A13

Planck Collaboration et al., 2020, A&A, 641, A6

Poci A., McDermid R. M., Zhu L., van de Ven G., 2019, MNRAS, 487, 3776

Poggianti B. M., 1997, A&AS, 122, 399

Poggianti B. M., Barbaro G., 1997, A&A, 325, 1025

Pohlen M., Trujillo I., 2006, A&A, 454, 759

Pont F., Eyer L., 2004, MNRAS, 351, 487

Posti L., Fraternali F., Marasco A., 2019, A&A, 626, A56

Powell L. C., Bournaud F., Chapon D., Teyssier R., 2013, MNRAS, 434, 1028

Power C., Navarro J. F., Jenkins A., Frenk C. S., White S. D. M., Springel V., Stadel J., Quinn T., 2003, MNRAS, 338, 14

Press W. H., 2007, Numerical recipes 3rd edition: The art of scientific computing. Cambridge university press

Press W. H., Schechter P., 1974, ApJ, 187, 425

Prugniel P., Soubiran C., 2001, A&A, 369, 1048

Prugniel P., Soubiran C., 2004, arXiv e-prints, pp astro–ph/0409214

Prugniel P., Soubiran C., Koleva M., Le Borgne D., 2007, arXiv e-prints, pp astro–ph/0703658

Przybylski A., 1957, MNRAS, 117, 483

Pulsoni C., et al., 2018, A&A, 618, A94

Pulsoni C., Gerhard O., Arnaboldi M., Pillepich A., Rodriguez-Gomez V., Nelson D., Hernquist L., Springel V., 2021, A&A, 647, A95

Radburn-Smith D. J., et al., 2011, ApJS, 195, 18

Raha N., Sellwood J. A., James R. A., Kahn F. D., 1991, Nature, 352, 411

Rees M. J., Ostriker J. P., 1977, MNRAS, 179, 541

Reines A. E., Volonteri M., 2015, ApJ, 813, 82

Rejkuba M., Harris W. E., Greggio L., Harris G. L. H., 2011, A&A, 526, A123

Remus R.-S., Forbes D. A., 2021, arXiv e-prints, p. arXiv:2101.12216

Renaud F., 2010, PhD thesis, Universite de Strasbourg Louis Pasteur, France

Renaud F., Boily C. M., Naab T., Theis C., 2009, ApJ, 706, 67

Richard J., et al., 2019, arXiv e-prints, p. arXiv:1906.01657

Richards G. T., et al., 2006, AJ, 131, 2766

Riess A. G., et al., 1998, AJ, 116, 1009

Robertson B., Bullock J. S., Cox T. J., Di Matteo T., Hernquist L., Springel V., Yoshida N., 2006, ApJ, 645, 986

Robin A. C., Reylé C., Derrière S., Picaud S., 2003, A&A, 409, 523

Rodriguez-Gomez V., et al., 2015, MNRAS, 449, 49

Rodriguez-Gomez V., et al., 2016, MNRAS, 458, 2371

Rodriguez-Gomez V., et al., 2017, MNRAS, 467, 3083

Rodriguez-Gomez V., et al., 2019, MNRAS, 483, 4140

Romano-Díaz E., Shlosman I., Heller C., Hoffman Y., 2008, ApJ, 687, L13

Rosales-Ortega F. F., Sánchez S. F., Iglesias-Páramo J., Díaz A. I., Vílchez J. M., Bland-Hawthorn J., Husemann B., Mast D., 2012, ApJ, 756, L31

Rosas-Guevara Y., et al., 2020, MNRAS, 491, 2547

Rosas-Guevara Y., et al., 2021, arXiv e-prints, p. arXiv:2110.04537

Rosati P., Borgani S., Norman C., 2002, ARA&A, 40, 539

Rossa J., van der Marel R. P., Böker T., Gerssen J., Ho L. C., Rix H.-W., Shields J. C., Walcher C.-J., 2006, AJ, 132, 1074

Rosse T. E. O., 1850, Philosophical Transactions of the Royal Society of London Series I, 140, 499

Rubin V. C., Ford W. Kent J., 1970, ApJ, 159, 379

Rubin V. C., Ford W. K. J., Thonnard N., 1980, ApJ, 238, 471

Ruiter A. J., Belczynski K., Sim S. A., Hillebrandt W., Fryer C. L., Fink M., Kromer M., 2011, MNRAS, 417, 408

Ruiz-Lara T., et al., 2015, A&A, 583, A60

Ruiz-Lara T., et al., 2018, A&A, 617, A18

Ruiz-Lara T., Gallart C., Bernard E. J., Cassisi S., 2020, Nature Astronomy, 4, 965

Russell H. N., 1914, Popular Astronomy, 22, 275

Sahu N., Graham A. W., Davis B. L., 2019, ApJ, 876, 155

Sakamoto K., Okumura S. K., Ishizuki S., Scoville N. Z., 1999, ApJ, 525, 691

Salaris M., Cassisi S., 2005, Evolution of Stars and Stellar Populations

Salim S., 2014, Serbian Astronomical Journal, 189, 1

Salim S., et al., 2007, ApJS, 173, 267

Salo H., et al., 2015, ApJS, 219, 4

Salpeter E. E., 1955, ApJ, 121, 161

Salpeter E. E., 1964, ApJ, 140, 796

Salvato M., Ilbert O., Hoyle B., 2019, Nature Astronomy, 3, 212

Sánchez-Blázquez P., et al., 2006, MNRAS, 371, 703

Sánchez-Blázquez P., Ocvirk P., Gibson B. K., Pérez I., Peletier R. F., 2011, MNRAS, 415, 709

Sánchez-Janssen R., et al., 2019, ApJ, 878, 18

Sánchez S. F., et al., 2012, A&A, 538, A8

Sandage A., 1961, The Hubble Atlas of Galaxies

Sandage A. R., Eggen O. J., 1959, MNRAS, 119, 278

Sandage A., Visvanathan N., 1978, ApJ, 225, 742

Sandage A., Freeman K. C., Stokes N. R., 1970, ApJ, 160, 831

van de Sande J., et al., 2019, MNRAS, 484, 869

Sani E., Marconi A., Hunt L. K., Risaliti G., 2011, MNRAS, 413, 1479

Sarajedini A., et al., 2007, AJ, 133, 1658

Sarazin C. L., 2002, The Physics of Cluster Mergers. Springer Netherlands, Dordrecht, pp 1–38, doi:10.1007/0-306-48096-4_1, https://doi.org/10.1007/0-306-48096-4_1

Sarzi M., et al., 2006, MNRAS, 366, 1151

Sarzi M., et al., 2018, A&A, 616, A121

Sawala T., et al., 2016, MNRAS, 457, 1931

Scalo J. M., 1986, Fundamentals Cosmic Phys., 11, 1

Schaye J., Dalla Vecchia C., 2008, MNRAS, 383, 1210

Schaye J., et al., 2015, MNRAS, 446, 521

Schechter P., 1976, ApJ, 203, 297

Schiavon R. P., 2007, ApJS, 171, 146

Schiavon R. P., Faber S. M., Rose J. A., Castilho B. V., 2002, ApJ, 580, 873

Schiavon R. P., Rose J. A., Courteau S., MacArthur L. A., 2004, ApJ, 608, L33

Schinnerer E., Böker T., Meier D. S., Calzetti D., 2008, ApJ, 684, L21

Schmidt M., 1959, ApJ, 129, 243

Schmidt M., 1963, Nature, 197, 1040

Schmidt B. P., et al., 1998, ApJ, 507, 46

Scholz-Díaz L., Martín-Navarro I., Falcón-Barroso J., 2022, MNRAS, 511, 4900

Schultheis M., et al., 2021, A&A, 650, A191

Schulze F., Remus R.-S., Dolag K., Burkert A., Emsellem E., van de Ven G., 2018, MNRAS, 480, 4636

Schulze F., Remus R.-S., Dolag K., Bellstedt S., Burkert A., Forbes D. A., 2020, MNRAS, 493, 3778

Schwarzschild M., 1979, ApJ, 232, 236

Schweizer F., Seitzer P., Whitmore B. C., Kelson D. D., Villanueva E. V., 2018, ApJ, 853, 54

Scott N., Graham A. W., 2013, ApJ, 763, 76

Searle L., Zinn R., 1978, ApJ, 225, 357

Seeger P. A., Fowler W. A., Clayton D. D., 1965, ApJS, 11, 121

Segers M. C., Schaye J., Bower R. G., Crain R. A., Schaller M., Theuns T., 2016, MNRAS, 461, L102

Seigar M. S., Graham A. W., Jerjen H., 2007, MNRAS, 378, 1575

Sellwood J. A., Binney J. J., 2002, MNRAS, 336, 785

Sellwood J. A., Wilkinson A., 1993, Reports on Progress in Physics, 56, 173

Seo W.-Y., Kim W.-T., Kwak S., Hsieh P.-Y., Han C., Hopkins P. F., 2019, ApJ, 872, 5

Serra P., Trager S. C., 2007, MNRAS, 374, 769

Sérsic J. L., 1968, Atlas de Galaxias Australes

Seth A. C., Dalcanton J. J., Hodge P. W., Debattista V. P., 2006, AJ, 132, 2539

Seth A. C., Blum R. D., Bastian N., Caldwell N., Debattista V. P., 2008, ApJ, 687, 997

Seth A. C., et al., 2014, Nature, 513, 398

Seyfert C. K., 1943, ApJ, 97, 28

Shapiro P. R., Field G. B., 1976, ApJ, 205, 762

Shapley H., 1918, ApJ, 48, 154

Shen J., Sellwood J. A., 2004, ApJ, 604, 614

Shen S., Mo H. J., White S. D. M., Blanton M. R., Kauffmann G., Voges W., Brinkmann J., Csabai I., 2003, MNRAS, 343, 978

Sheth K., et al., 2008, ApJ, 675, 1141

Shibuya T., Ouchi M., Harikane Y., 2015, ApJS, 219, 15

Siegel M. H., et al., 2007, ApJ, 667, L57

Siegel M. H., et al., 2011, ApJ, 743, 20

Silk J., 1968, ApJ, 151, 459

Silk J., 1997, ApJ, 481, 703

Silk J., Rees M. J., 1998, A&A, 331, L1

Simard L., Mendel J. T., Patton D. R., Ellison S. L., McConnachie A. W., 2011, ApJS, 196, 11

Simmons B. D., et al., 2014, MNRAS, 445, 3466

Smith M. C., 2021, MNRAS, 502, 5417

Smith M. C., Sijacki D., Shen S., 2018, MNRAS, 478, 302

Smith M. C., Bryan G. L., Somerville R. S., Hu C.-Y., Teyssier R., Burkhart B., Hernquist L., 2021, MNRAS, 506, 3882

Smoot G. F., et al., 1992, ApJ, 396, L1

Snyder G. F., et al., 2015, MNRAS, 454, 1886

Solanes J. M., Manrique A., García-Gómez C., González-Casado G., Giovanelli R., Haynes M. P., 2001, ApJ, 548, 97

Somerville R. S., Davé R., 2015, ARA&A, 53, 51

Somerville R. S., Primack J. R., 1999, MNRAS, 310, 1087

Somerville R. S., et al., 2008, ApJ, 672, 776

Somerville R. S., et al., 2018, MNRAS, 473, 2714

Sormani M. C., Tress R. G., Glover S. C. O., Klessen R. S., Battersby C. D., Clark P. C., Hatchfield H. P., Smith R. J., 2020, MNRAS, 497, 5024

Spavone M., et al., 2017, A&A, 603, A38

Spavone M., et al., 2020, A&A, 639, A14

Spavone M., Krajnović D., Emsellem E., Iodice E., den Brok M., 2021, A&A, 649, A161

Speagle J. S., Steinhardt C. L., Capak P. L., Silverman J. D., 2014, ApJS, 214, 15

Spergel D. N., et al., 2003, ApJS, 148, 175

Spiniello C., Trager S., Koopmans L. V. E., Conroy C., 2014, MNRAS, 438, 1483

Spitler L. R., Forbes D. A., 2009, MNRAS, 392, L1

Spolaor M., Kobayashi C., Forbes D. A., Couch W. J., Hau G. K. T., 2010, MNRAS, 408, 272

Springel V., 2000, MNRAS, 312, 859

Springel V., 2005, MNRAS, 364, 1105

Springel V., 2010a, ARA&A, 48, 391

Springel V., 2010b, MNRAS, 401, 791

Springel V., Hernquist L., 2003, MNRAS, 339, 289

Springel V., Hernquist L., 2005, ApJ, 622, L9

Springel V., White S. D. M., Tormen G., Kauffmann G., 2001, MNRAS, 328, 726

Springel V., Di Matteo T., Hernquist L., 2005a, MNRAS, 361, 776

Springel V., et al., 2005b, Nature, 435, 629

Springel V., Di Matteo T., Hernquist L., 2005c, ApJ, 620, L79

Springel V., Frenk C. S., White S. D. M., 2006, Nature, 440, 1137

Springel V., et al., 2008, MNRAS, 391, 1685

Springel V., et al., 2018, MNRAS, 475, 676

Springel V., Pakmor R., Zier O., Reinecke M., 2021, MNRAS, 506, 2871

Strateva I., et al., 2001, AJ, 122, 1861

Sunyaev R. A., Zeldovich Y. B., 1970, Ap&SS, 7, 3

Tacchella S., Dekel A., Carollo C. M., Ceverino D., DeGraf C., Lapiner S., Mandelker N., Primack Joel R., 2016, MNRAS, 457, 2790

Tacchella S., et al., 2019, MNRAS, 487, 5416

Tacconi L. J., et al., 2010, Nature, 463, 781

Tacconi L. J., et al., 2013, ApJ, 768, 74

Tacconi L. J., et al., 2018, ApJ, 853, 179

Tal T., van Dokkum P. G., 2011, ApJ, 731, 89

Teklu A. F., Remus R.-S., Dolag K., Beck A. M., Burkert A., Schmidt A. S., Schulze F., Steinborn L. K., 2015, ApJ, 812, 29

Teyssier R., 2002, A&A, 385, 337

Thater S., et al., 2022, MNRAS, 509, 5416

Thatte N., et al., 2021, The Messenger, 182, 7

Thomas D., Maraston C., Bender R., 2003, MNRAS, 339, 897

Thomas D., Maraston C., Korn A., 2004, MNRAS, 351, L19

Thomas D., Maraston C., Bender R., Mendes de Oliveira C., 2005, ApJ, 621, 673

Thomas D., Maraston C., Schawinski K., Sarzi M., Silk J., 2010, MNRAS, 404, 1775

Tifft W. G., Gregory S. A., 1976, ApJ, 205, 696

Tinsley B. M., 1979, ApJ, 229, 1046

Tinsley B. M., 1980, Fundamentals Cosmic Phys., 5, 287

Tolstoy E., 2019, IAU Symposium, 343, 49

Tolstoy E., Hill V., Tosi M., 2009, ARA&A, 47, 371

Tomczak A. R., et al., 2016, ApJ, 817, 118

Tonini C., 2013, ApJ, 762, 39

Toomre A., 1964, ApJ, 139, 1217

Toomre A., 1977, in Tinsley B. M., Larson Richard B. Gehret D. C., eds, Evolution of Galaxies and Stellar Populations. p. 401

Toomre A., Toomre J., 1972, ApJ, 178, 623

Torrey P., Vogelsberger M., Genel S., Sijacki D., Springel V., Hernquist L., 2014, MNRAS, 438, 1985

Torrey P., et al., 2015, MNRAS, 447, 2753

Torrey P., et al., 2019, MNRAS, 484, 5587

Tortora C., Napolitano N. R., Cardone V. F., Capaccioli M., Jetzer P., Molinaro R., 2010, MNRAS, 407, 144

Trager S. C., Somerville R. S., 2009, MNRAS, 395, 608

Trager S. C., Worthey G., Faber S. M., Burstein D., González J. J., 1998, ApJS, 116, 1

Trager S. C., Faber S. M., Worthey G., González J. J., 2000a, AJ, 119, 1645

Trager S. C., Faber S. M., Worthey G., González J. J., 2000b, AJ, 120, 165

Trayford J. W., et al., 2015, MNRAS, 452, 2879

Trayford J. W., et al., 2017, MNRAS, 470, 771

Tremblay B., Merritt D., 1996, AJ, 111, 2243

Tremonti C. A., et al., 2004, ApJ, 613, 898

Tress R. G., Sormani M. C., Glover S. C. O., Klessen R. S., Battersby C. D., Clark P. C., Hatchfield H. P., Smith R. J., 2020, MNRAS, 499, 4455

Tsatsi A., Macciò A. V., van de Ven G., Moster B. P., 2015, ApJ, 802, L3

Tsatsi A., Mastrobuono-Battisti A., van de Ven G., Perets H. B., Bianchini P., Neumayer N., 2017, MNRAS, 464, 3720

Tully R. B., Fisher J. R., 1977, A&A, 500, 105

Turner M. L., Côté P., Ferrarese L., Jordán A., Blakeslee J. P., Mei S., Peng E. W., West M. J., 2012, ApJS, 203, 5

Usher C., et al., 2017, MNRAS, 468, 3828

Valdes F., Gupta R., Rose J. A., Singh H. P., Bell D. J., 2004, ApJS, 152, 251

VandenBerg D. A., Bergbusch P. A., Dotter A., Ferguson J. W., Michaud G., Richer J., Proffitt C. R., 2012, ApJ, 755, 15

Vasiliev E., Valluri M., 2020, ApJ, 889, 39

de Vaucouleurs G., 1948, Annales d'Astrophysique, 11, 247

de Vaucouleurs G., 1959, Handbuch der Physik, 53, 275

Vaughan S. P., Davies R. L., Zieleniewski S., Houghton R. C. W., 2018, MNRAS, 479, 2443

Vazdekis A., Casuso E., Peletier R. F., Beckman J. E., 1996, ApJS, 106, 307

Vazdekis A., Salaris M., Arimoto N., Rose J. A., 2001, ApJ, 549, 274

Vazdekis A., Cenarro A. J., Gorgas J., Cardiel N., Peletier R. F., 2003, MNRAS, 340, 1317

Vazdekis A., Sánchez-Blázquez P., Falcón-Barroso J., Cenarro A. J., Beasley M. A., Cardiel N., Gorgas J., Peletier R. F., 2010, MNRAS, 404, 1639

Vazdekis A., Ricciardelli E., Cenarro A. J., Rivero-González J. G., Díaz-García L. A., Falcón-Barroso J., 2012, MNRAS, 424, 157

Vazdekis A., et al., 2015, MNRAS, 449, 1177

Vazdekis A., Koleva M., Ricciardelli E., Röck B., Falcón-Barroso J., 2016, MNRAS, 463, 3409

Velazquez H., White S. D. M., 1999, MNRAS, 304, 254

Venn K. A., Irwin M., Shetrone M. D., Tout C. A., Hill V., Tolstoy E., 2004, AJ, 128, 1177

Vernet J., et al., 2011, A&A, 536, A105

Verro K., et al., 2021, arXiv e-prints, p. arXiv:2110.10188

Villanova S., Geisler D., Gratton R. G., Cassisi S., 2014, ApJ, 791, 107

Villaume A., Conroy C., Johnson B., Rayner J., Mann A. W., van Dokkum P., 2017, ApJS, 230, 23

Vogelsberger M., et al., 2014a, MNRAS, 444, 1518

Vogelsberger M., et al., 2014b, Nature, 509, 177

Vogelsberger M., Marinacci F., Torrey P., Puchwein E., 2020, Nature Reviews Physics, 2, 42

Voggel K. T., et al., 2022, A&A, 658, A152

Volonteri M., 2010, A&ARv, 18, 279

Wadsley J. W., Stadel J., Quinn T., 2004, New Astron., 9, 137

Walch S., et al., 2015, MNRAS, 454, 238

Walcher C. J., Böker T., Charlot S., Ho L. C., Rix H. W., Rossa J., Shields J. C., van der Marel R. P., 2006, ApJ, 649, 692

Walcher C. J., Coelho P. R. T., Gallazzi A., Bruzual G., Charlot S., Chiappini C., 2015, A&A, 582, A46

Walter F., et al., 2020, ApJ, 902, 111

Wang L., et al., 2014, MNRAS, 439, 611

Wang L., Dutton A. A., Stinson G. S., Macciò A. V., Penzo C., Kang X., Keller B. W., Wadsley J., 2015, MNRAS, 454, 83

Wehner E. H., Harris W. E., 2006, ApJ, 644, L17

Weinberg D. H., Bullock J. S., Governato F., Kuzio de Naray R., Peter A. H. G., 2015, Proceedings of the National Academy of Science, 112, 12249

Weinberger R., et al., 2017, MNRAS, 465, 3291

Weinmann S. M., van den Bosch F. C., Yang X., Mo H. J., 2006, MNRAS, 366, 2

Weisz D. R., et al., 2011, ApJ, 739, 5

Weizsäcker C. F. V., 1935, Zeitschrift fur Physik, 96, 431

van der Wel A., et al., 2012, ApJS, 203, 24

van der Wel A., et al., 2014, ApJ, 788, 28

van der Wel A., et al., 2016, ApJS, 223, 29

van der Wel A., et al., 2021, ApJS, 256, 44

Werner N., et al., 2014, MNRAS, 439, 2291

Westera P., Lejeune T., Buser R., Cuisinier F., Bruzual G., 2002, A&A, 381, 524

Wetzel A. R., Hopkins P. F., Kim J.-h., Faucher-Giguère C.-A., Kereš D., Quataert E., 2016, ApJ, 827, L23

Whitaker K. E., van Dokkum P. G., Brammer G., Franx M., 2012, ApJ, 754, L29

White S. D. M., 1976, MNRAS, 177, 717

White S. D. M., 1978, MNRAS, 184, 185

White S. D. M., 1984, ApJ, 286, 38

White S. D. M., Rees M. J., 1978, MNRAS, 183, 341

Whitmore B. C., Kirshner R. P., Schechter P. L., 1979, ApJ, 234, 68

Whitmore B. C., Gilmore D. M., Jones C., 1993, ApJ, 407, 489

Wilkinson D. M., et al., 2015, MNRAS, 449, 328

Wilkinson D. M., Maraston C., Goddard D., Thomas D., Parikh T., 2017, MNRAS, 472, 4297

Woodward P., Colella P., 1984, Journal of Computational Physics, 54, 115

Worthey G., 1994, ApJS, 95, 107

Worthey G., Ottaviani D. L., 1997, ApJS, 111, 377

Worthey G., Faber S. M., Gonzalez J. J., Burstein D., 1994, ApJS, 94, 687

Worthey G., Tang B., Serven J., 2014, ApJ, 783, 20

Wu Y., Singh H. P., Prugniel P., Gupta R., Koleva M., 2011, A&A, 525, A71

Wu P.-F., et al., 2018, ApJ, 855, 85

Wu P.-F., et al., 2021, AJ, 162, 201

Xiang M., Rix H.-W., 2022, Nature, 603, 599

Yan R., et al., 2019, ApJ, 883, 175

Yang X., Mo H. J., van den Bosch F. C., Jing Y. P., 2005, MNRAS, 356, 1293

Yang X., Mo H. J., van den Bosch F. C., Pasquali A., Li C., Barden M., 2007, ApJ, 671, 153

Yi S., Demarque P., Kim Y.-C., Lee Y.-W., Ree C. H., Lejeune T., Barnes S., 2001, ApJS, 136, 417

Yi S. K., et al., 2005, ApJ, 619, L111

York D. G., et al., 2000, AJ, 120, 1579

Young L. M., et al., 2011, MNRAS, 414, 940

Yu S.-Y., Ho L. C., 2019, ApJ, 871, 194

Zabludoff A. I., Zaritsky D., Lin H., Tucker D., Hashimoto Y., Shectman S. A., Oemler A., Kirshner R. P., 1996, ApJ, 466, 104

Zahid H. J., Geller M. J., Kewley L. J., Hwang H. S., Fabricant D. G., Kurtz M. J., 2013, ApJ, 771, L19

Zahid H. J., Dima G. I., Kudritzki R.-P., Kewley L. J., Geller M. J., Hwang H. S., Silverman J. D., Kashino D., 2014, ApJ, 791, 130

Zehavi I., et al., 2011, ApJ, 736, 59

Zel'dovich Y. B., 1964, Soviet Physics Doklady, 9, 195

Zel'dovich Y. B., 1970, A&A, 5, 84

Zhang H.-X., Hunter D. A., Elmegreen B. G., Gao Y., Schruba A., 2012, AJ, 143, 47

Zhao G., Zhao Y.-H., Chu Y.-Q., Jing Y.-P., Deng L.-C., 2012, Research in Astronomy and Astrophysics, 12, 723

Zheng Z., et al., 2017, MNRAS, 465, 4572

Zhu L., van de Ven G., Méndez-Abreu J., Obreja A., 2018, MNRAS, 479, 945

Zhu L., et al., 2020, MNRAS, 496, 1579

Zhu L., et al., 2022a, arXiv e-prints, p. arXiv:2203.15822

Zhu L., et al., 2022b, A&A, 660, A20

Zhuang Y., Leaman R., van de Ven G., Zibetti S., Gallazzi A., Zhu L., Falcón-Barroso J., Lyubenova M., 2019, MNRAS, 483, 1862

Zibetti S., White S. D. M., Brinkmann J., 2004, MNRAS, 347, 556

Zibetti S., Gallazzi A. R., Hirschmann M., Consolandi G., Falcón-Barroso J., van de Ven G., Lyubenova M., 2020, MNRAS, 491, 3562

Zinger E., et al., 2020, MNRAS, 499, 768

Zoccali M., Hill V., Lecureur A., Barbuy B., Renzini A., Minniti D., Gómez A., Ortolani S., 2008, A&A, 486, 177

Zoccali M., et al., 2017, A&A, 599, A12

Zolotov A., et al., 2015, MNRAS, 450, 2327

Zwicky F., 1933, Helvetica Physica Acta, 6, 110

Zwicky F., 1957, Morphological astronomy